A novel travelling-wave Zeeman decelerator for production of cold radicals

Inauguraldissertation

zur

Erlangung der Würde eines Doktors der Philosophie

vorgelegt der

Philosophisch-Naturwissenschaftlichen Fakultät

der Universität Basel

von

Tomislav Damjanović

aus Kroatien

Basel, 2021

Genehmigt von der Philosophisch-Naturwissenschaftlichen Fakultät
auf Antrag von

Prof. Dr. Stefan Willitsch und Prof. Dr. Hendrick L. Bethlem

Basel, den 15.12.2020

Prof. Dr. Martin Spiess
Dekan

Abstract

Recent advances in producing samples of molecules at very low temperatures have been motivated by the prospects of studying collisions and chemical reactions with controllable collision energies, performing high resolution spectroscopy and precision measurements for fundamental physics, quantum information processing and quantum simulation. Methods based on the deceleration of supersonic molecular beams are particularly well suited for collision experiments since the final longitudinal velocity of the sample can be tuned over a wide range with narrow velocity spreads. Zeeman deceleration methods rely on the state-dependent interaction of neutral paramagnetic atoms or molecules with a time-dependent inhomogeneous magnetic fields. For this reason, the Zeeman deceleration technique is especially effective in open-shell systems such as molecular radicals or metastable atoms and molecules.

Here, an experimental realization of a novel travelling-wave Zeeman decelerator based on a double-helix wire geometry is presented. The decelerator is capable of decelerating samples of paramagnetic atoms and molecules from 560 m/s forward velocity down to an arbitrary final velocity. Compared to the conventional Zeeman or Stark decelerators, the presented decelerator exhibits full three-dimensional confinement of the molecules at a full range of velocities starting from the initial forward velocity down to the arbitrary final velocity, leading to an improvement of the overall phase-space acceptance compared to the conventional Zeeman and Stark decelerators. Operation of the decelerator is demonstrated by deceleration of a molecular beam of OH radicals from an initial velocity of 445 m/s down to a final velocity of 350 m/s. The experimental results are accompanied by numerical trajectory simulations confirming stable operation and showing phase-space stability of the decelerator.

These results pave the way for the future cold-collision experiments. In the future, the traveling-wave Zeeman decelerator will serve as a source of cold paramagnetic molecules for hybrid trapping experiments.

Acknowledgements

I would like to acknowledge the support and help of many exceptional people without whom this work would not be possible. First, I would like to thank Prof. Dr. Stefan Willitsch and Prof. Dr. Dongdong Zhang for giving me the opportunity to be a part of this exciting project. Their mentorship, guidance and infinite patience were invaluable. I am grateful to Dr. Hendrick L. Bethlem for kindly agreeing to review my work. I would like to thank Georg Holderied Salvisberg for all the help with the electronics, without him the decelerator would never work. I am grateful to Dr. Anatoly Johnson for all the help with the laser setup and to the members of the mechanical workshop: Grischa Martin and Philipp Knöpfel for their amazing work in transforming our rudimentary sketches with extraordinary precision into real-life objects. I am also grateful to Dr. Jutta Toscano for our discussions regarding the 2+1 REMPI of hydrogen. I would also like to thank all of the former and current members of the group who made the everyday work experience much more enjoyable. Special thanks goes to Dr. Claudio von Planta for all the fun times in the lab, Dr. Thomas Kierspel for all the scientific discussions, Patrik Stranak and Ludger Ploenes for their constant eagerness to help and Moritz Weegen for all the chess discussions. I would also like to thank all of my family members and friends, especially my brothers Krešimir and Zvonimir for always believing in me. Last but not least, I would like to thank Dijana for her unlimited support and for always encouraging me to be better. This thesis is dedicated to the memory of my mother, who instilled in me a sense of curiosity about the world and has always encouraged me to find my own path in life.

Contents

1 General Introduction **1**

1.1 Introduction 1

1.2 Stark deceleration 4

1.3 Zeeman deceleration 6

1.3.1 Zeeman deceleration experiments 8

1.4 Thesis outline 11

2 Theoretical Background **13**

2.1 Introduction 13

2.2 Atoms and molecules in a magnetic field 16

Zeeman effect in the 1 $^2S_{1/2}$ ground state of H 19

Zeeman effect in the n=2 state of H 21

Zeeman effect in the $X^2\Pi_{3/2}$ state of OH 24

Zeeman effect in the $A^2\Sigma^+$ state of OH 26

2.3 Energy level structure of OH 28

2.3.1 Hund's coupling cases a) and b) 31

2.3.2 The electronic ground state of OH 34

2.3.3 The first electronic excited state of OH 39

2.3.4 A←X transition in OH 40

2.4 Conclusions 42

3 Experimental setup **43**

3.1 Introduction 43

3.2 Pulsed dye laser setup for the production of 243 nm and 282 nm laser light . . . 44
3.3 The molecular beam source [1] . . . 47
3.4 Time-of-flight mass spectrometer . . . 57
3.4.1 Time-resolved detection with MCP detectors . . . 57
3.4.2 Design of the time-of-flight mass spectrometer . . . 62
3.5 Conclusions . . . 71

4 A travelling-wave Zeeman decelerator 73
4.1 Introduction . . . 73
4.2 Principles of operation of the travelling-wave Zeeman decelerator . 74
4.2.1 Mathematical description of our implementation of the travelling wave Zeeman decelerator . . . 74
4.3 Decelerator design . . . 86
4.3.1 Design of the deceleration modules . . . 86
4.3.2 General decelerator design . . . 89
4.3.3 Double-helix geometry . . . 93
4.3.4 Control and monitoring of the operation of the decelerator 98
Travelling-wave Zeeman decelerator control software . . . 99
Power supply control software . . . 101
Temperature monitoring software . . . 102
Pressure monitoring software . . . 104
4.4 Numerical trajectory simulations . . . 105
4.4.1 Numerical calculations of time-dependant inhomogeneous magnetic fields . . . 105
4.4.2 Numerical particle trajectory simulation program . . . 113
4.4.3 Evolutionary algorithm for optimization of numerical trajectory simulations . . . 117
4.5 Conclusions . . . 121

5 Power electronics 123
5.1 Introduction . . . 123

5.2 General considerations in the design of the high-power arbitrary-waveform current generators 124
5.3 Implementation of the power electronics in our travelling-wave Zeeman decelerator 129
5.3.1 Generation of current switching sequences 137
5.3.2 The power distribution system 140
5.4 The embedded software for controlling the production of arbitrary current waveforms 141
5.5 Conclusions 147

6 Guiding and deceleration of OH radicals 149
6.1 Introduction 149
6.2 Characterization of the phase-space stability of decelerated OH radicals 149
6.2.1 Longitudinal motion in the trap and 2-dimensional phase-space stability 153
6.2.2 Transverse motion in the trap and 6-dimensional phase-space stability 162
6.3 Guiding and deceleration of a molecular beam of OH radicals . . . 167
6.3.1 Guiding of a molecular beam of OH radicals 167
6.3.2 Deceleration of a molecular beam of OH radicals 172
6.4 Conclusions 176

7 Conclusions and outlook 179

A Matrix elements of the effctive Hamiltonian for OH in $X^2\Pi$ state in the Hund's case (a) basis 183

Bibliography 189

Chapter 1

General Introduction

1.1 Introduction

With the advances in the production of cold and ultra-cold molecules in recent years, there has been an increasing interest within the scientific community in better understanding the fundamental properties of such systems. Experiments with molecules in the gas phase at temperatures close to absolute zero offer new insights into cold and ultra-cold chemistry [2, 3, 4, 5, 6, 7], many-body physics [8, 9, 10], precision spectroscopy [11, 12, 13], a search for physics beyond the Standard Model with cold molecules [14, 15, 16, 17, 18, 19, 20, 21], quantum information processing and quantum computing [22, 23, 24, 25, 23], quantum simulation and quantum dynamics of complex systems [23, 26, 27, 28]. The term "cold", in a broader sense, refers to translational temperatures of the molecules between 1 mK - 1 K, while the term "ultra-cold " refers to translational temperatures below 1 mK. More rigorously, the "ultra-cold" temperature regime is defined as one where collision dynamics of the particles is dominated by single-partial-wave scattering, more generally s-wave scattering for collisions of bosons and p-wave scattering for collisions of identical fermions. The boundary between the cold and ultra-cold regime depends on the mass of the specific molecule and nature of the long-range interactions [29]. A range of astrophysical phenomena, such as formation of interstellar molecular clouds [30], arises in the near-cold (1 K$<$T$<$50 K) regime. Many aspects of the chemistry at these temperatures are still not well

understood. The thermal De Broglie wavelength of a particle is given by:

$$\Lambda = \frac{h}{\sqrt{2\pi m k_{\mathrm{B}} T}}, \tag{1.1}$$

where m is the mass of the molecule, T is the temperature, h is the Planck constant and k_{B} is the Boltzmann constant. The temperature is related to the kinetic energy of the molecule as $E_{kin} = \frac{3}{2} k_{\mathrm{B}} T$. Compared to room temperature, the De Broglie wavelength of a molecule at ultra-cold temperatures ($1 \sim \mu$K) is increased by many orders of magnitude ($\sim 4 - 5$). In this regime, the De Broglie wavelength becomes much larger than the typical range of the chemical interactions, and so a quantum mechanical description of the reaction process has to be taken into account. Classically, the Arrhenius equation gives the dependence of the rate constant of a chemical reaction as a function of the temperature

$$k = A \exp\left(\frac{-E_a}{RT}\right), \tag{1.2}$$

where k is the rate constant, T is the temperature in Kelvin, A is a pre-exponential factor, R is the universal gas constant and E_a is the activation energy for the reaction. From this relation, it is expected that the reaction rate at low temperatures tends to go to zero. However, certain types of gas-phase reactions for which there is no reaction barrier still do occur at these temperatures. These can include ion-molecule reactions, radical reactions and reactions of excited atoms or molecules [31]. Additionally, in reactions where there is a barrier, tunnelling of the nuclei of the collision partners through the barrier can occur and resonances in the collisional cross-sections can arise [32]. Another aspect of the ultra-cold regime is that long-range interactions start to exhibit an important role in ultra-cold collisions. This brings an important aspect in studying of these interactions: chemical interactions can be controlled by modifying the long-range interaction with external electric or magnetic fields [2, 29].

Originally, the field of cold and ultra-cold molecules grew out of cold atom research. Cold atom research saw rapid progress due to the developments in laser cooling and atom trapping techniques [33]. Owing to the more complex energy level structure, laser cooling of molecules has been achieved in only very few spe-

cific cases where closed cycling transitions could be established [34]. So far, laser cooling techniques have been achieved in SrF [35], CaF [36] and YO [37] diatomic molecules and SrOH [38], CaOH [39] and $CaOCH_3$ polyatomic molecules [40]. In parallel to the development of the laser-based cooling techniques, a whole range of other techniques has seen rapid development. These can more generally be classified into two groups: indirect cooling methods and direct cooling methods. Indirect cooling methods rely on direct cooling of atoms down to ultra-cold temperatures and merging cold atoms into molecules through a photo-association [41, 42] or magneto-association process [43, 44]. Additionally, a range of different cooling methods has been developed for the direct cooling of molecules. Some of these methods include collision-based approach such as buffer-gas cooling [45, 46], or kinematic collision technique employing inelastic [47] and reactive [48] collisional cooling in crossed molecular beams. Sympathetic cooling is another method for the production of cold molecules. In this approach, molecules are cooled through collisions with laser-cooled atomic species [7, 49]. Merged beam experiments have been developed for high-resolution studies of collisional interactions at low relative velocities between two species [50] relying on merging of one molecular beam guided in a magnetic quadrupole with a free-running supersonic beam with the possibility for tuning the collision energy between the two species. The velocity selection technique relies on the velocity selection from a thermal sample. In the sample of gas molecules at room temperature, the velocities of the molecules are distributed according to a Maxwell-Boltzmann distribution. A high-voltage electric quadrupole with a bend serves as a velocity selector, where polar molecules with velocities $v > v_{max}$ are ejected from the quadrupole, and molecules with velocities $v < v_{max}$ are guided through the quadropole bend [51]. Two methods that are most relevant to the experiments described in this thesis, namely Zeeman and Stark deceleration, rely on the interaction of dipolar molecules with external fields. Not all methods are mentioned here. For a more concise review on techniques developed for production of cold and ultra-cold molecules, the reader is referred to [3, 2, 5, 6, 52, 4].

1.2 Stark deceleration

In the Stark deceleration method, the forward velocity of a supersonic beam of polar molecules is reduced by exploiting the interaction of the electric dipole moment of the molecule with an inhomogeneous electric field. The interaction of the electric dipole with the electric field $\mathbf{E}$ is described by the Stark Hamiltonian

$$H_{\mathrm{S}} = -\boldsymbol{\mu}_{\mathbf{el}} \cdot \mathbf{E}, \tag{1.3}$$

where $\boldsymbol{\mu}$ is the electric dipole moment and $\mathbf{E}$ is the electric field. A first Stark decelerator was designed and implemented by Bethlem et al. in 1999 [53] by demonstrating the slowing of CO molecules from 225 m/s down to 98 m/s. A typical conventional Stark decelerator consists of a number of high-voltage electrode pairs which create large inhomogeneous electric field on the axis of expansion of the supersonic beam. A supersonic beam of molecules is expanded from a pulsed valve and coupled into the Stark decelerator. As molecules enter the Stark decelerator, they start to enter the region of high electric fields. The molecules which are in their low-field seeking states, that is the molecules which increase their potential energy with the increasing field, start to gain potential energy at the expense of their kinetic energy. Once the densest part of the molecular packet is at the maximum of the electric field, the electric field is switched off. The typical maximum electric field strength that is achieved is $\sim$200 kV/cm and typical potential energy that can be achieved is 1-2 orders of magnitude lower than the typical forward kinetic energies of molecules in supersonic beams. For this reason, Stark decelerators typically consist of many (>100) sets of electrodes. Molecules are flown to the next set of electrodes, and the procedure is repeated. In this way, a portion of the forward kinetic energy of the molecular beam is reduced at each stage, and over the course of a whole decelerator, a significant portion of the kinetic energy is removed. Schematic depiction of Stark deceleration is shown in Figure 1.1. A general property of all decelerators that rely on the deceleration of the species by manipulation with external fields is that they cannot increase the phase-space density of the sample. This fact comes from Liouville's theorem

which states that a 6D phase-space density of a system which is acted upon with conservative forces is constant. Ketterle et al. showed that this also holds true for systems which are acted upon by both adiabatic and sudden time-dependent potentials [54]. In the context of deceleration experiments, this means that the maximum phase-space density of molecules that can be achieved at the exit of the decelerator cannot be higher than that at the entrance of the decelerator, and so a special consideration has to be taken such that the molecular source with high phase-space density is selected.

Stark deceleration is best suited for molecules with low mass and high first-order Stark shifts. To date, a range of different species has been decelerated. Besides the already mentioned CO, these include OH [55, 56, 57, 58, 59], NH [60], NH_3 [61], ND_3 [62, 63], NO [64], CaF [65], YbF [66], H_2CO [67], SO_2 [68], SrF [69] and others. Slow molecules produced by Stark deceleration have found uses in a range of applications among which some are trapping of molecules in static magnetic fields [55, 62, 70], static and AC electric fields [63, 71], low-energy and tunable energy collision studies [72, 73, 74], high-resolution spectroscopy [12, 75], lifetime measurements [76, 77] and others. Additionally, highly excited Rydberg ($n = 10 - 100$) atoms and molecules exhibit large electric dipole moments which scale as $\sim n^2$ with the principal quantum number n. Electric dipole moments of molecules in Rydberg states can exceed by many orders of magnitude those in the ground state and thus these molecules are good candidates for deceleration experiments. First deceleration experiments of molecules in Rydberg states were reported in 2004, where H_2 molecules in the extreme low-field seeking and the extreme high-field seeking states were deflected, decelerated and accelerated in an inhomogenous electric field of a pair of cylindrical electrodes [78] and subsequently brought to rest from initial velocity of 500 m/s [79]. For a comprehensive review on manipulation of Rydberg atoms and molecules with electric fields, the reader is referred to [80].

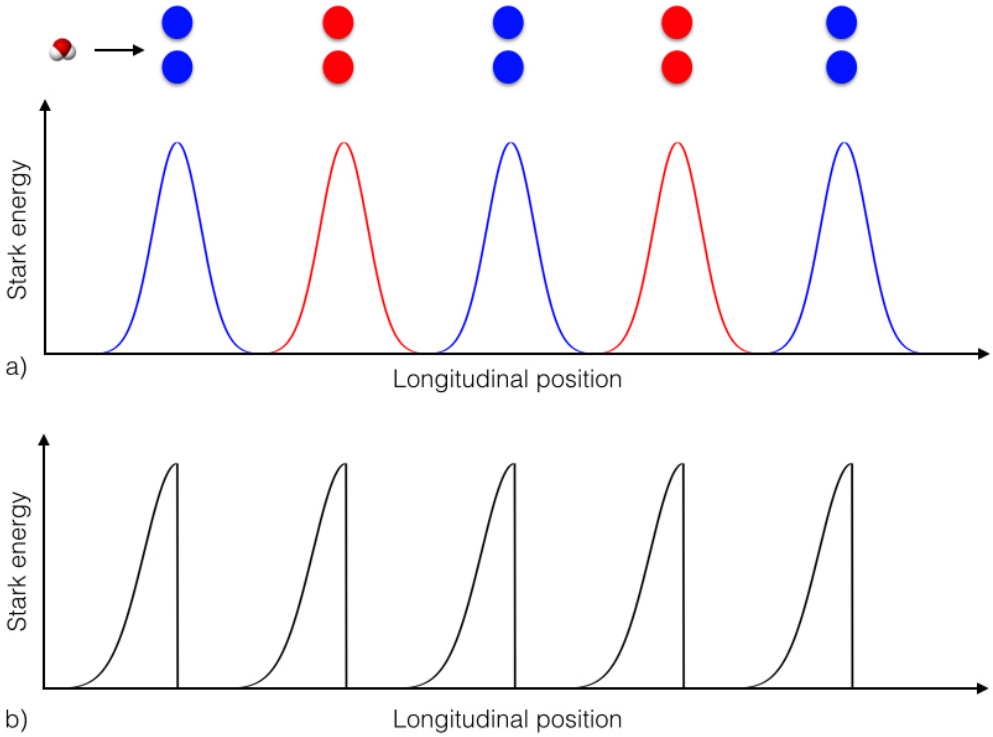

Figure 1.1: The potential energy on the beam axis of a Stark decelerator. Every second pair of electrodes is connected to the same electric potential. a) The potential energy of the low-field-seeking particle along the deceleration axis resulting from the electric potential applied to blue (red) electrodes. b) Stark energy of the synchronous particle (an idealized particle which is at the maximum of potential energy when electric fields are switched off) along the deceleration axis during the deceleration process.

1.3 Zeeman deceleration

Motivated by the demonstrated successes of first Stark deceleration experiments [81], a magnetic analogue was developed. Zeeman decelerators exploit the interaction of the magnetic dipole moment of an atom or a molecule with an inhomogeneous magnetic field. The interaction Hamiltonian of the magnetic dipole with a magnetic field is given by:

$$H_{\mathrm{Z}} = -\boldsymbol{\mu}_{mag} \cdot \mathbf{B}, \tag{1.4}$$

where $\boldsymbol{\mu}_{mag}$ is the magnetic dipole moment and $\mathbf{B}$ is the magnetic field. Zeeman deceleration experiments are particularly well suited for light atoms and

molecules with an unpaired electron. Similarly to the Stark decelerator, a typical conventional Zeeman decelerator consists of a series of solenoids placed on the axis of propagation of the supersonic beam. As molecules approach the entrance of the decelerator, a high current pulse ($\sim 10^2 - 10^3$ A) is passed through the first solenoid and consequently, a high inhomogeneous magnetic field is generated inside the solenoid. A synchronous particle in a low-field seeking state entering the decelerator starts to gain the potential energy with the increasing magnitude of the magnetic field at the expense of kinetic energy. When it reaches the maximum of the magnetic field, the current pulse is abruptly switched off, and the field is quenched. In this way, a portion of the kinetic energy is removed. Zeeman energy of a LFS particle during Zeeman deceleration is illustrated in Figure 1.2. A single OH molecule travelling with a forward velocity of 450 m/s has a kinetic energy of $E_k \approx 150$ cm^{-1}. In the $X^2\Pi_{3/2}(\nu = 0, m_J = 3/2)$ state OH, has an effective magnetic dipole moment $\mu_{eff} = 1.41\mu_{\mathrm{B}}$, where μ_{B} is Bohr magneton. Here, X denotes the electronic ground state, the orbital angular momentum of the molecule is denoted as Π, the projection of the total angular momentum on the intermolecular axis is $\Omega = 3/2$ and ν and m_J stand for the vibrational quantum number and the secondary total angular momentum quantum number, respectively. In order to completely remove the kinetic energy of the molecule in a single solenoid stage, it would be necessary to achieve and switch magnetic field magnitudes of ~ 230 T. For reference, the maximum magnetic field magnitudes achieved on the deceleration axis in the experiments described throughout this thesis are ~ 0.5 T. For that reason, the kinetic energy of the molecules is removed in multiple stages of a conventional Zeeman decelerator, just as in the case of the conventional Stark decelerator. Typical Zeeman decelerators consist of 100-200 solenoids. Species which are best suited for Zeeman deceleration are those which have a high ratio of effective magnetic dipole moment and mass, μ_{eff}/m.

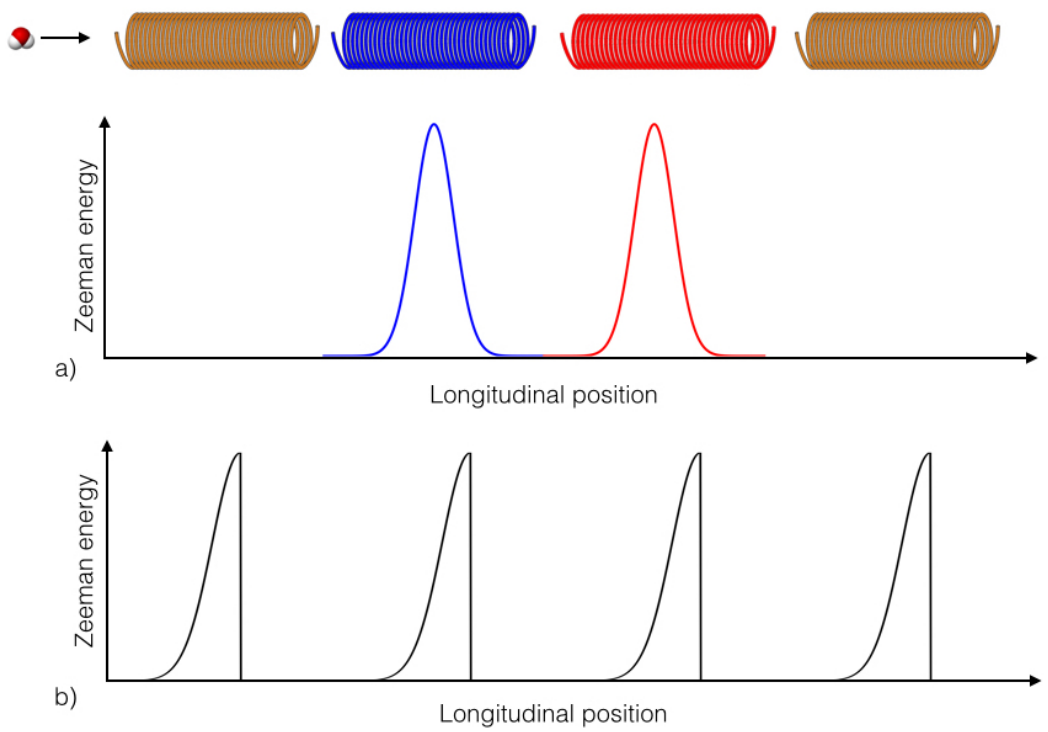

Figure 1.2: The potential energy on the beam axis of the Zeeman decelerator. a) The potential energy of the low-field-seeking particle along the deceleration axis resulting from a high current pulse applied to blue (red) coils which are switched at different times. b) Zeeman energy of the synchronous particle along the deceleration axis during the deceleration process.

1.3.1 Zeeman deceleration experiments

The first implementation of the Zeeman decelerator was demonstrated by Vanhaecke et al. in 2007. [82]. They reported on the deceleration of hydrogen atoms in their ground state from the initial forward velocity of 313 m/s down to 225 m/s. In the experiment, a pulsed supersonic beam of H atoms was produced by 193 nm photolysis of NH_3 seeded in Xe. A 140 A current pulse with 5 $\sim$ μs rise and fall time was pulsed through six 7.8 mm long solenoids, creating a $\sim$ 0.8 T maximum of the magnitude of the magnetic field. Subsequently, the enhanced version of the same decelerator was used by Hogan et al. to decelerate samples of H and D atoms [83] with 250 A current pulses and improved deceleration results. Additional improvements led to the deceleration of H atoms from 520 m/s forward velocity down to 100 m/s in a 12-stage Zeeman decelerator and subsequent trapping of H atoms in a magnetic quadrupole trap [84]. A range of atomic

and molecular species has been decelerated in the meantime by different groups. Among others, these include already mentioned H and D atoms, metastable He [85, 86], metastable $a^3\Sigma_u^+$ He_2 [87], metastable Ne [88, 89], metastable Ar [90], metastable N [91], O and O_2 [92, 93, 90], NH [94], NO [95] and CH_3 [96, 97]. Zeeman decelerated species have found use in a wide range of applications. Segev et al. have demonstrated trapping of O_2 and Li in a superconducting magnetic trap after Zeeman deceleration and studied O_2-O_2 collisions inside a trap [98]. Liu et al. have demonstrated magnetic trapping of cold methyl radicals after Zeeman deceleration [96]. Semeria et al. have used samples of Zeeman decelerated metastable He_2 molecules to perform precision measurements of the spin-rotation fine structure of the $a^3\Sigma_u^+$ state. Plomp et al. recently reported the first crossed-beam scattering experiments using Zeeman decelerated samples in combination with velocity map imaging for studies of molecular collisions [95]. Phase-space stability in conventional Zeeman decelerators was first studied by Wiederkehr et al. [99]. The model for the 1D phase-phase stability was proposed and compared to the results of 1D and 3D numerical trajectory simulations. It was revealed that the transverse effects lead to a considerable reduction of the phase-space acceptance at low values of the phase angle and to the enhancement at high values of the phase angle. An empty halo structure was shown to appear in the centre of the phase-space acceptance at low phase angles due to the lack of transverse focusing forces, thereby reducing significantly the phase-space acceptance of the decelerator. Dulitz et al. developed a model of the overall phase-space acceptance in a Zeeman decelerator which ascribed these effects to the coupling of the transverse and longitudinal dynamics [100]. Additional losses in the phase-space density were shown to arise from particles whose trajectory is close to the separatrix. Separatrix is a line in the phase-space diagram which marks the boundary between particles which have stable trajectories in the phase-space from ones which do not. Particles close to the separatrix experience strong focusing forces, get overfocused and are thereby ejected out of the phase-stable region. With an increasing phase angle, the acceptance of the decelerator decreases and the empty halo structure reduces in size and eventually disappears. Toscano et al. used an

evolutionary strategy for optimization of the current switching sequences in order to increase the output of the Zeeman decelerator [101, 102]. They have seen a 40% increase in the number of decelerated particles compared to when the decelerator was operated in a conventional way. Additionally, it was demonstrated that it was possible to remove up to 98% of the initial kinetic energy of the particles with an improved switching scheme, compared to 83% with a conventional switching scheme. In a conventional Zeeman decelerator, the 6D phase-space stability relies on the dynamical stabilization of the trajectories of particles during the deceleration process which leads to losses due to the coupling between the transverse and longitudinal motions, which becomes increasingly problematic at low velocities. One of the solutions to mitigate the problem is to trap the particles in a co-moving three-dimensional trap and then to decelerate the trap. This concept was first demonstrated by Meek at al. in a miniature chip trap for polar molecules in travelling potential wells [103] and later on by Osterwalder et al. in a first cylindrically symmetric travelling-wave Stark decelerator [104]. In the context of Zeeman deceleration, the idea was first proposed by Narevcius et al. [105] and the same concept was demonstrated by Lavert-Ofir et al. [89]. An effective moving magnetic quadrupole trap was created with a series of spatially overlapping traps, where each trap consisted of two coils in an anti-Helmholtz configuration. By gradually switching the currents in neighbouring traps, relative to each other, the minimum of the magnetic field was gradually moved from one trap to the other, and in that way, a moving magnetic trap was created on the deceleration axis. In a proof-of-principle experiment, they demonstrated deceleration of metastable neon from an initial forward velocity of 340 m/s down to a final velocity of 54 m/s. The same year, Trimiche et al. presented a different method for achieving a travelling magnetic wave. In their implementation, the decelerator consisted of two sets of flattened helical wire geometries each 138.2 mm long with 12 periods and an additional quadrupole guide [106] allowing for transverse confinement of particles. In a proof-of-principle experiment, they demonstrated trapping and guiding of metastable argon atoms at 464 m/s forward velocity. More recently, McArd et al. have presented a refined version of

the moving-trap Zeeman decelerator based on the design of Trimiche et al. In a proof-of-principle experiment, with the decelerator coil operated with a reduced current (100 A-200 A) a guiding of a metastable argon beam at 373 m/s and deceleration from 342 m/s down to 304 m/s was demonstrated [107]. In general travelling-wave decelerators offer higher phase-space acceptances relative to the conventional decelerators but at the same time due to increased complexity from an engineering perspective are more difficult to implement.

1.4 Thesis outline

This thesis describes the design and implementation of a novel travelling-wave Zeeman decelerator. The decelerator is based on a double-wire helix geometry which allows for full three-dimensional confinement of paramagnetic species throughout the whole deceleration process. The decelerator is capable of decelerating and accelerating species in a range of initial and final velocities, from 560 m/s to 30 m/s. The first proof-of-principle Zeeman deceleration results are described. The thesis is structured as follows: Chapter 2 gives the theoretical background for the understanding of the Zeeman effect. Zeeman diagrams and Zeeman energy splitting calculations are given for some of the species relevant in the context of the experiments described throughout this thesis. Chapter 3 gives a description of the experimental system excluding the decelerator itself. In Chapter 4 a mathematical foundation for the understanding of the emergence of the travelling wave from a double-helix coil geometry is given. The real-life implementation of the decelerator is described in detail. Various software programs that were developed for the operation of the experiment are described. Finally, numerical Monte-Carlo trajectory simulations are described in detail, including the genetic algorithm for optimization of initial parameters of the numerical trajectory simulation. Chapter 5 describes the design of the power electronics for production of arbitrary-waveform high-power current pulses. In Chapter 6 results of the deceleration experiments of OH radical in the $X^2\Pi_{3/2}$ state are given. The longitudinal and transverse phase-space stability of the decelerator is discussed.

Finally, in Chapter 7, the future prospects of the decelerator are given, including possible improvements on the decelerator itself.

Disclaimer: The work described in this thesis would not be possible without the efforts of many exceptional people who contributed to it. The Traveling-wave Zeeman decelerator project was first conceptualized under the supervision of Prof. Gerard Meijer. Dr. Nicolas Vanhaecke developed the concept behind the creation of the traveling wave. The decelerator and vacuum chambers were designed by Henrik Haak. Arbitrary-waveform current generators were designed by JeanPaul Cromiéres and improvements to it were made by Tomislav Damjanović. Embedded program for current generators was developed by JeanPaul Cromiéres, Dr. Nicolas Vanhaecke, Prof. Dongdong Zhang and Tomislav Damjanović. Decelerator modules were produced by FHI workshop and assembled by Prof. Dongdong Zhang. The Zeeman commander software was developed by Prof. Dongdong Zhang and Tomislav Damjanović, pressure monitoring software by Prof. Dongdong Zhang, power-supply and temperature measuring software by Tomislav Damjanović. Successful implementation of the traveling-wave Zeeman decelerator and all of the experiments described in this thesis were performed by Tomislav Damjanović. The work described in this thesis was supervised by Prof. Stefan Willitsch and Prof. Dongdong Zhang.

Chapter 2

Theoretical Background

2.1 Introduction

In 1896, the Dutch physicist Pieter Zeeman discovered what is now known as the Zeeman effect. He observed a clear widening of the sodium D-lines under the influence of a magnetic field [108]. The same year Hendrik Lorentz developed a theory which predicted that the observed widening was a splitting of the lines in three components when observed in a direction perpendicular to the field. In a direction parallel to the field, two lines, with opposite circular polarization would be visible [109, 110]. Both of these predictions were confirmed by Zeeman in 1897 [111, 112, 113]. Even to this day, Lorentz's classical model provides an intuitive way of understanding the emergence of the Zeeman effect. An atom in a magnetic field can be modelled as a simple harmonic oscillator where the equation of motion for the electron bound to the core and placed in a magnetic field $\mathbf{B}$ is given by [114]:

$$m\ddot{\mathbf{r}}(t) = -m\omega_0^2\mathbf{r}(t) - e\mathbf{v}(t) \times \mathbf{B}, \tag{2.1}$$

where m is the mass of the electron, e is the charge of the electron, $\mathbf{r}(t) = (x(t), y(t), z(t))$ is the position of the electron at time t and $\mathbf{v}(t)$ is the velocity of the electron at time t. An electron placed inside a magnetic field experiences a Lorentz force $\mathbf{F_L} = e\mathbf{v} \times \mathbf{B}$. Choosing the magnetic field to be pointing in the

z direction $\mathbf{B} = B\hat{z}$ gives:

$$\ddot{\mathbf{r}}(t) + 2\Omega_{\mathrm{L}}\dot{\mathbf{r}}(t) \times \hat{z} + \omega_0^2\mathbf{r}(t), \tag{2.2}$$

where Ω_L is the Larmor frequency:

$$\Omega_{\mathrm{L}} = \frac{eB}{2m}. \tag{2.3}$$

The solution of equation 2.2 is given by :

$$\mathbf{r}(t) = \begin{pmatrix} x \\ y \\ z \end{pmatrix} e^{-i\omega t}. \tag{2.4}$$

Inserting equation 2.4 into 2.2 gives:

$$\begin{pmatrix} \omega_0^2 - \omega^2 & -2i\omega\Omega_{\mathrm{L}} & 0 \\ 2i\omega\Omega_{\mathrm{L}} & \omega_0^2 & 0 \\ 0 & 0 & \omega_0^2 \end{pmatrix} \begin{pmatrix} x \\ y \\ z \end{pmatrix} = 0. \tag{2.5}$$

The eigenvalues ω^2 are calculated from the eigenvalue equation:

$$\Big(\omega^4 - (2\omega_0^2 + 4\Omega_{\mathrm{L}}^2)\omega^2 + \omega_0^4\Big)(\omega^2 - \omega_0^2) = 0, \tag{2.6}$$

giving the following eigenvalues: $\omega = \omega_0$ and $\omega \approx \omega \pm \Omega_L$, with $\Omega_L \ll \omega_0$. The eigenvectors corresponding to $\omega = \omega - \Omega_L, \omega_0$ and $\omega = \omega + \Omega_L$ are:

$$\mathbf{r} = \begin{pmatrix} \cos(\omega_0 - \Omega_{\mathrm{L}})t \\ -\sin(\omega - \Omega_{\mathrm{L}})t \\ 0 \end{pmatrix}, \begin{pmatrix} 0 \\ 0 \\ \cos\omega_0 t \end{pmatrix}, \begin{pmatrix} \cos(\omega_0 + \Omega_{\mathrm{L}})t \\ \sin(\omega + \Omega_{\mathrm{L}})t \\ 0 \end{pmatrix}. \tag{2.7}$$

From relation 2.7 follows that the motion of the electron along the z-axis is not affected by the magnetic field and angular frequency remains ω_0 in the z-axis. Off-diagonal elements $\pm 2i\omega\Omega_{\mathrm{L}}$ of the matrix in equation 2.5 cause the motion on the x-axis and the y-axis to be coupled together, induced by the introduction of the magnetic field. This results in two circular motions in the opposite direction in the x-y plane with two different angular frequencies. In other words, the

introduction of the magnetic field splits oscillations at a single angular frequency into oscillation with three different angular frequencies $\omega = \omega_0 - \Omega_L$, $\omega = \omega_0$ and $\omega = \omega_0 + \Omega_L$. Additionally, the classical model of the Zeeman effect also describes the polarization of the radiation produced by the oscillating electron. Classically, an electron that oscillates along z direction with angular frequency ω_0 radiates electromagnetic radiation with angular frequency ω_0. For the observer placed on the y-axis, the motion of the electron along the z-axis is seen as an up-down motion of the electron and the observed radiation has vertical linear polarization. This is the so-called π component. The motion of the electron oscillating with frequencies $\omega = \omega_0 \pm \Omega_L$ in the x-y plane is seen as the left-right motion of the electron and the observed radiation has horizontal linear polarization. These are the so-called σ-components. This effect is illustrated in Figure 2.1. Figure 2.1 a) illustrates the motion of the electron that the observer sees and splitting of spectral lines is illustrated in Figure 2.2 b).

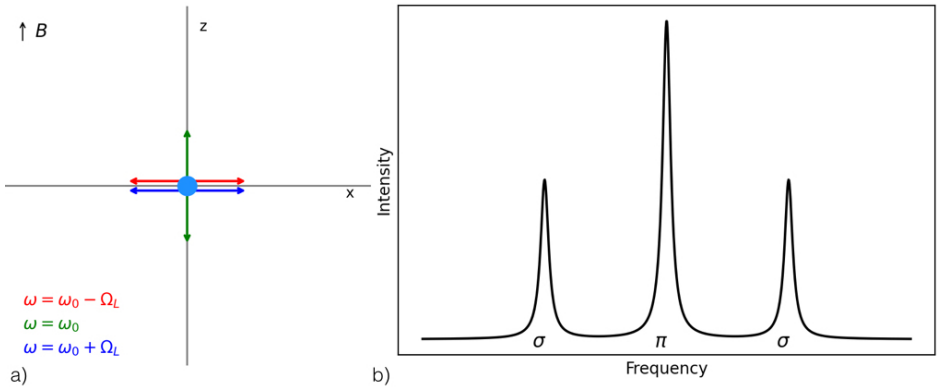

Figure 2.1: The normal Zeeman effect of a simple model of the atom. a) For the observer placed on the y-axis, the motion of the electron along the z-axis is seen as an up-down motion of the electron and the observed radiation has vertical linear polarization while the motion of the electron in the x-y plane is seen as the left-right motion of the electron and the observed radiation has horizontal linear polarization. b) Observed splitting of the spectral lines.

Similarly, if the observer is placed on the z-axis the motion of the electron along the z-axis can no longer be observed. The motion of the electron with angular frequencies $\omega = \omega_0 \pm \Omega_L$ is now seen as the circular motion in the x-y plane, and the emitted radiation has circular polarization. The circular motion in the clockwise direction is associated with the frequency $\omega_0 - \Omega_L$ and is referred

to as σ^--component, while motion in the anti-clockwise direction is associated with the frequency $\omega_0 + \Omega_\mathrm{L}$, and is referred to as σ^+-component. The motion of the electron from the observer's perspective is illustrated in Figure 2.2 a), and splitting of the spectral lines is shown in Figure 2.2 b).

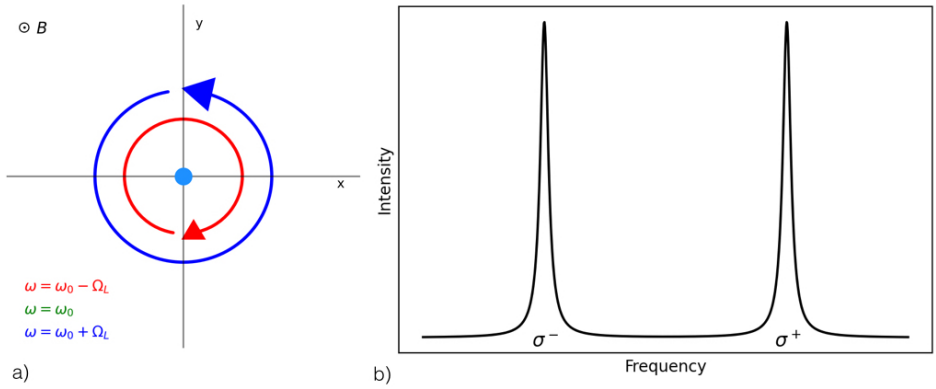

Figure 2.2: The normal Zeeman effect of a simple model of the atom. For the observer placed on the z-axis, the motion of the electron along the z-axis can no longer be observed. The motion of the electron with angular frequencies $\omega = \omega_0 \pm \Omega_\mathrm{L}$ is now seen as the circular motion in the x-y plane and the emitted radiation has circular polarization.

2.2 Atoms and molecules in a magnetic field

If an electron is orbiting a nucleus of an atom with an angular momentum $\boldsymbol{\ell}$, its behaviour can be described similar to that of a current loop with a magnetic moment $\mu_{\boldsymbol{\ell}}$, where the magnetic moment is given by:

$$\boldsymbol{\mu}_{\boldsymbol{\ell}} = -g_\ell \frac{\mu_\mathrm{B}}{\hbar} \boldsymbol{\ell}, \tag{2.8}$$

where $\mu_\mathrm{B} = e\hbar/2m_e$ is the Bohr magneton, m_e is the mass of the electron and e is the charge of the electron. The electron also has an intrinsic spin angular momentum $\mathbf{s}$ and an intrinsic magnetic moment:

$$\boldsymbol{\mu}_\mathbf{s} = -g_s \frac{\mu_\mathrm{B}}{\hbar} \mathbf{s}. \tag{2.9}$$

The total magnetic moment of the electron is then given by:

$$\boldsymbol{\mu}_\mathbf{e} = -\frac{\mu_\mathrm{B}}{\hbar}(g_\ell \boldsymbol{\ell} + g_s \mathbf{s}). \tag{2.10}$$

Here $g_\ell = 1$ and $g_s \approx 2.0023192$. For an an atom consisting of n electrons, the total magnetic moment is given by:

$$\boldsymbol{\mu} = -\frac{\mu_\mathrm{B}}{\hbar}\sum_{k=1}^{n}(g_\ell \boldsymbol{\ell}_k + g_s \mathbf{s}_k) = -\frac{\mu_\mathrm{B}}{\hbar}(g_\ell \mathbf{L} + g_s \mathbf{S}), \tag{2.11}$$

where $\mathbf{L} = \sum_{k=0}^{n} \boldsymbol{\ell}_k$ and $\mathbf{S} = \sum_{k=0}^{n} \mathbf{s}_k$.

The interaction of the magnetic moment $\boldsymbol{\mu}$ with a magnetic field $\mathbf{B}$ is governed by:

$$H_\mathrm{Z} = -\boldsymbol{\mu} \cdot \mathbf{B} = -\frac{\mu_\mathrm{B}}{\hbar}(g_\ell \mathbf{L} + g_s \mathbf{S}) \cdot \mathbf{B}. \tag{2.12}$$

If the magnetic field is pointing along the z-axis, $\mathbf{B} = B\hat{z}$ the interaction Hamiltonian becomes:

$$H_\mathrm{Z} = -\mu_z B = -\frac{\mu_\mathrm{B}}{\hbar}\hbar(g_\ell L_z + g_s S_z)B \tag{2.13}$$

Provided that the spin-orbit interaction dominates over the Zeeman interaction, Zeeman interaction can be treated as a perturbation to the fine structure. The expectation value of the Zeeman Hamiltonian can be calculated in the basis of $|LSJM_J\rangle$, where L is the angular momentum quantum number, S is the spin quantum number, J is the total angular momentum quantum number and M_J is the secondary total angular momentum quantum number. $\mathbf{L}$ and $\mathbf{S}$ are not separately conserved, but the total angular momentum $\mathbf{J} = \mathbf{L} + \mathbf{S}$ is conserved. In the angular momentum vector model, the orbital angular momentum and spin angular momentum are precessing rapidly about the total angular momentum $\mathbf{J}$, and $\mathbf{J}$ is precessing slowly about the z-axis. Projection of the orbital angular momentum and the spin angular momentum on $\mathbf{J}$ gives:

$$H_\mathrm{Z} = -\frac{\langle LSJM_J|\, \boldsymbol{\mu} \cdot \mathbf{J}\, |LSJM_J\rangle}{J(J+1)}\mathbf{J} \cdot \mathbf{B} \tag{2.14}$$

$$= \frac{\langle LSJM_J|\, \mathbf{L} \cdot \mathbf{J}\, |LSJM_J\rangle + g_s \langle LSJM_J|\, \mathbf{S} \cdot \mathbf{J}\, |LSJM_J\rangle}{J(J+1)}\mu_\mathrm{B} B J_z, \tag{2.15}$$

$\mathbf{L} \cdot \mathbf{J}$ and $\mathbf{S} \cdot \mathbf{J}$ are given by:

$$\mathbf{L} \cdot \mathbf{J} = \frac{1}{2}(\mathbf{J}^2 - \mathbf{L}^2 + \mathbf{S}^2), \tag{2.16}$$

$$\mathbf{S} \cdot \mathbf{J} = \frac{1}{2}(\mathbf{J}^2 + \mathbf{L}^2 - \mathbf{S}^2), \tag{2.17}$$

and

$$\mathbf{L}\cdot\mathbf{J}\,|LSJM_J\rangle = \frac{\hbar}{2}\Big((J(J+1)-L(L+1)+S(S+1)\Big), \tag{2.18}$$

$$\mathbf{S}\cdot\mathbf{J}\,|LSJM_J\rangle = \frac{\hbar}{2}\Big((J(J+1)+L(L+1)-S(S+1)\Big). \tag{2.19}$$

Applying this to the Hamiltonian 2.15 and taking into account $J_z\,|LSJM_J\rangle = \hbar M_J$ gives the Zeeman splitting:

$$\Delta E_{\mathrm{Z}} = \Big(\frac{J(J+1)+L(L+1)-S(S+1)}{2J(J+1)}+g_s\frac{J(J+1)-L(L+1)+S(S+1)}{2J(J+1)}\Big)\mu_{\mathrm{B}}M_J. \tag{2.20}$$

Projection of the magnetic dipole moment $\boldsymbol{\mu}$ onto the total angular momentum $\mathbf{J}$ gives:

$$\boldsymbol{\mu}_{eff} = \frac{\langle LSJM_J|\,\boldsymbol{\mu}\cdot\mathbf{J}\,|LSJM_J\rangle}{J(J+1)}\mathbf{J} = -g_J\mu_{\mathrm{B}}\mathbf{J}, \tag{2.21}$$

and the Zeeman energy shift is given by:

$$\Delta E_{\mathrm{Z}} = \langle LSJM_J|\,g_J\mu_{\mathrm{B}}BJ_z\,|LSJM_J\rangle = g_J\mu_{\mathrm{B}}BM_J \tag{2.22}$$

Comparing equations 2.20 and 2.22 gives:

$$g_J = \frac{J(J+1)+L(L+1)-S(S+1)}{2J(J+1)}+g_s\frac{J(J+1)-L(L+1)+S(S+1)}{2J(J+1)}. \tag{2.23}$$

g_J is the so-called Lande g-factor. So far, in our considerations effects arising from the nucleus of the atom have been disregarded. A nucleus with a nuclear spin angular momentum $\mathbf{I}$ has a magnetic moment given by:

$$\boldsymbol{\mu}_I = g_I\frac{\mu_{\mathrm{N}}}{\hbar}\mathbf{I}, \tag{2.24}$$

where $g_I = 5.585694713$, and $\mu_N = e\hbar/2m_p$ is the nuclear magneton. Since $\mu_{\mathrm{N}}/\mu_{\mathrm{B}} \approx 1/1836$ the contribution of the nuclear spin magnetic moment to the total magnetic moment can be neglected for most applications and the Hamiltonian for the Zeeman interaction is given by:

$$H_{\mathrm{Z}} = g_J\mu_{\mathrm{B}}\mathbf{J}\cdot\mathbf{B} \tag{2.25}$$

The hyperfine interaction is coupling the total angular momentum of the electron

J and the nuclear angular momentum **I** to form the total angular momentum of the atom $\mathbf{F} = \mathbf{J} + \mathbf{I}$. If the Zeeman interaction is weaker than the hyperfine interaction $A\mathbf{I} \cdot \mathbf{J}$, in the angular momentum vector model, the total angular momentum of the electron **J** and nuclear angular momentum **I** are rapidly precessing around the total angular momentum of the atom **F**, and the total angular momentum of the atom is slowly precessing around the $z-$axis. The eigenstates are now given by $|IJFM_F\rangle$. The projection of **J** onto **F** gives the effective Hamiltonian:

$$H_{\mathrm{Z}} = g_J \frac{\mu_{\mathrm{B}}}{\hbar} \frac{\langle IJFM_F | \, \mathbf{J} \cdot \mathbf{F} \, | IJFM_F \rangle}{F(F+1)} \mathbf{F} \cdot \mathbf{B} = g_F \mu_{\mathrm{B}} B F_z, \tag{2.26}$$

where

$$g_F = \frac{F(F+1) + J(J+1) - I(I+1)}{2F(F+1)}, \tag{2.27}$$

and the Zeeman splitting is then given by

$$\Delta E_{\mathrm{Z}} = g_F \mu_{\mathrm{B}} B M_F. \tag{2.28}$$

When the Zeeman interaction is dominating over the hyperfine interaction, F is not a good quantum number anymore and the effect of the hyperfine interaction can be calculated as the perturbation on the $|IM_IJM_J\rangle$ eigenstates. The Zeeman splitting is then given by:

$$\Delta E_{\mathrm{Z}} = g_J \mu_{\mathrm{B}} B M_J + \langle IM_IJM_J | \, A\mathbf{I} \cdot \mathbf{J} \, | IM_IJM_J \rangle \, . \tag{2.29}$$

In the relation $\mathbf{I} \cdot \mathbf{J} = I_x J_x + I_y J_y + I_z J_z$, the terms $\langle I_x J_x \rangle = \langle I_y J_y \rangle = 0$ due to the precession about the z-axis. In the strong field regime, the Zeeman splitting is then given by

$$\Delta E_{\mathrm{Z}} = g_J \mu_B B M_J + A M_I M_J, \tag{2.30}$$

where A is the hyperfine splitting constant.

Zeeman effect in the $1\ ^2S_{1/2}$ ground state of H

The ground state of the hydrogen atom is characterized with an orbital angular momentum quantum number $L = 0$, a spin angular momentum quantum number $S = 1/2$ and nuclear spin angular momentum quantum number $I = 1/2$. The

Zeeman Hamiltonian including the hyperfine interaction is then written as:

$$\begin{aligned} H &= H_Z + H_{hf} \\ &= -\frac{g_s \mu_\mathrm{B}}{\hbar} B S_z + A\mathbf{I}\cdot\mathbf{S}. \end{aligned} \tag{2.31}$$

The hyperfine structure constant for the hydrogen atom in the $1\ ^2S_{1/2}$ state has a value of $A \approx 0.05\ \mathrm{cm}^{-1}$.

As a basis for the calculation, the coupled representation is chosen. The relationship between the coupled basis $|Fm_F\rangle \equiv |F, m_F, S, I\rangle$ and uncoupled basis $|m_s m_I\rangle \equiv |Sm_S, Im_I\rangle$ is given by Glebsch-Gordan coefficients $\langle F, m_F | Sm_S, Im_I\rangle$ [115, 116] giving rise to the following relations:

$$|1,1\rangle = \left|\frac{1}{2}\frac{1}{2}\right\rangle, \tag{2.32}$$

$$|1,0\rangle = \frac{1}{\sqrt{2}}\left(\left|\frac{1}{2}-\frac{1}{2}\right\rangle + \left|-\frac{1}{2}\frac{1}{2}\right\rangle\right), \tag{2.33}$$

$$|1,-1\rangle = \left|-\frac{1}{2}-\frac{1}{2}\right\rangle, \tag{2.34}$$

$$|0,0\rangle = \frac{1}{\sqrt{(2)}}\left(\left|\frac{1}{2}-\frac{1}{2}\right\rangle + \left|-\frac{1}{2}\frac{1}{2}\right\rangle\right). \tag{2.35}$$

Ordering the states as $|1,1\rangle, |1,-1\rangle, |1,0\rangle, |0,0\rangle$ and calculating the matrix elements of the Hamiltonian H gives:

$$H = \begin{pmatrix} A/4+\mu_\mathrm{B}B & 0 & 0 & 0 \\ 0 & A/4-\mu_\mathrm{B}B & 0 & 0 \\ 0 & 0 & A/4 & \mu_\mathrm{B}B \\ 0 & 0 & \mu_\mathrm{B}B & -\frac{3A}{4} \end{pmatrix}. \tag{2.36}$$

The resultant energies of the Hamiltonian H as a function of the magnetic field are shown in Figure 2.3. In Figure 2.3 a), the low-field seeking states suitable for Zeeman deceleration are depicted in red. Figure 2.3 b) shows the Zeeman energy diagram for the $F = 0$ and $F = 1$ states. The Zeeman interaction splits the degeneracy of the $F = 1$ state into three components. When the Zeeman interaction becomes stronger than $A\mathbf{I}\cdot\mathbf{J}$, F is not a good quantum number anymore and $\mathbf{J}$ precesses about $\mathbf{B}$. This results in two states increasing linearly in energy

with increasing magnetic field and in two states decreasing linearly in energy with increasing magnetic field. This can be seen in Figure 2.3 a).

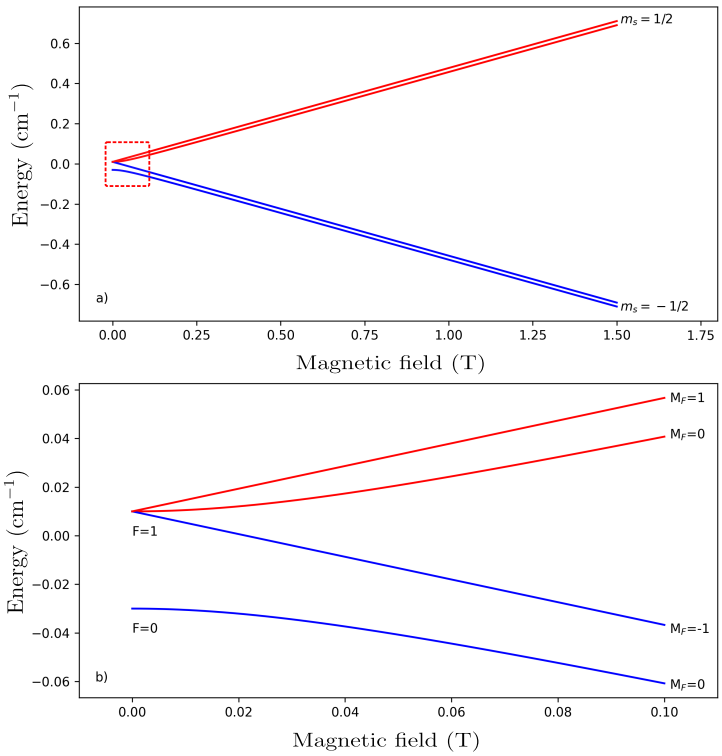

Figure 2.3: The Zeeman effect in the $1^2S_{1/2}$ state of the hydrogen atom. a) Introduction of the magnetic field splits the degeneracy of the level. Low-field seeking states suitable for Zeeman deceleration are depicted in red. b) Circled are of the upper panel. The state with total angular momentum quantum number $F = 1$ is split into three levels.

Zeeman effect in the n=2 state of H

To illustrate the Zeeman splitting in the $n = 2$ state of the hydrogen atom, the Hamiltonian is constructed from the contribution of the spin-orbit interaction and the Zeeman interaction.

$$H = H_{so} + H_Z = \frac{e}{2m^2c^2r^3}\hat{\mathbf{S}} \cdot \hat{\mathbf{L}} + \frac{g_\ell \mu_\mathrm{B}}{\hbar} B L_z. - \frac{g_s \mu_\mathrm{B}}{\hbar} B S_z \qquad (2.37)$$

The spin-orbit Hamiltonian is diagonal in the coupled basis $|nLJM_J\rangle$

$$H_{so}\,|2LJM_J\rangle = \gamma(3 - \frac{8}{J+1/2})\,|2LJM_J\rangle\,, \tag{2.38}$$

while the Zeeman Hamiltonian is diagonal in the uncoupled basis $|LM_L\rangle\,|SM_S\rangle$

$$H_Z\,|LM_L\rangle\,|SM_S\rangle = \beta(M_L + 2M_S)\,|LM_L\rangle\,|SM_S\rangle\,, \tag{2.39}$$

where $\gamma = \frac{(E_n^{(0)})^2}{2mc^2}$ and $\beta = \mu_{\mathrm{B}}B$. The relationship between the coupled and uncoupled basis is given with the help of the Clebsh-Gordan coefficients:

$$\left|20\frac{1}{2}\frac{1}{2}\right\rangle = |00\rangle\left|\frac{1}{2}\frac{1}{2},\right\rangle \tag{2.40}$$

$$\left|20\frac{1}{2}-\frac{1}{2}\right\rangle = |00\rangle\left|\frac{1}{2}-\frac{1}{2}\right\rangle, \tag{2.41}$$

$$\left|21\frac{3}{2}\frac{3}{2}\right\rangle = |11\rangle\left|\frac{1}{2}\frac{1}{2}\right\rangle, \tag{2.42}$$

$$\left|21\frac{3}{2}-\frac{3}{2}\right\rangle = |1-1\rangle\left|\frac{1}{2}-\frac{1}{2}\right\rangle, \tag{2.43}$$

$$\left|21\frac{3}{2}\frac{1}{2}\right\rangle = \sqrt{\frac{2}{3}}\,|10\rangle\left|\frac{1}{2}\frac{1}{2}\right\rangle + \sqrt{\frac{1}{3}}\,|11\rangle\left|\frac{1}{2}-\frac{1}{2}\right\rangle, \tag{2.44}$$

$$\left|21\frac{1}{2}\frac{1}{2}\right\rangle = -\sqrt{\frac{1}{3}}\,|10\rangle\left|\frac{1}{2}\frac{1}{2}\right\rangle + \sqrt{\frac{2}{3}}\,|11\rangle\left|\frac{1}{2}-\frac{1}{2}\right\rangle, \tag{2.45}$$

$$\left|21\frac{3}{2}-\frac{1}{2}\right\rangle = \sqrt{\frac{1}{3}}\,|1-1\rangle\left|\frac{1}{2}\frac{1}{2}\right\rangle + \sqrt{\frac{2}{3}}\,|10\rangle\left|\frac{1}{2}-\frac{1}{2}\right\rangle, \tag{2.46}$$

$$\left|21\frac{1}{2}-\frac{1}{2}\right\rangle = -\sqrt{\frac{2}{3}}\,|1-1\rangle\left|\frac{1}{2}\frac{1}{2}\right\rangle + \sqrt{\frac{1}{3}}\,|10\rangle\left|\frac{1}{2}-\frac{1}{2}\right\rangle. \tag{2.47}$$

Ordering the states as they are given in equations 2.40-2.47, the matrix of the Hamiltonian $H = H_{so} + H_Z$ can be calculated:

$$H = \begin{pmatrix}
\beta-5\gamma & 0 & 0 & 0 & 0 & 0 & 0 & 0 \\
0 & -\beta-5\gamma & 0 & 0 & 0 & 0 & 0 & 0 \\
0 & 0 & 2\beta-\gamma & 0 & 0 & 0 & 0 & 0 \\
0 & 0 & 0 & -2\beta-\gamma & 0 & 0 & 0 & 0 \\
0 & 0 & 0 & 0 & 2/3\beta-\gamma & -\sqrt{2}/3\beta & 0 & 0 \\
0 & 0 & 0 & 0 & -\sqrt{2}/3\beta & 1/3\beta-5\gamma & 0 & 0 \\
0 & 0 & 0 & 0 & 0 & 0 & -2/3\beta-\gamma & -\sqrt{2}/3\beta \\
0 & 0 & 0 & 0 & 0 & 0 & -\sqrt{2}/3\beta & -1/3\beta-5\gamma
\end{pmatrix} \tag{2.48}$$

The resultant energies of the Hamiltonian 2.48 as a function of the magnitude of the magnetic field are plotted in Figure 2.4. The splitting between the $^2P_{1/2}$ and $^2P_{3/2}$ states is due to the spin-orbit interaction. The resultant energies of the

$^2S_{1/2}$ and $^2P_{1/2}$ states calculated from 2.48 are degenerate, but in reality, they split by a so-called Lamb shift. This splitting has been included in the Zeeman diagram. The splitting of the $^2S_{1/2}$ level is shown in blue, $^2P_{1/2}$ in red and $^2P_{3/2}$ in green. Due to the rule that states with the same M never cross [117], the resultant Zeeman diagram exhibits repulsion between the states with the same M, as illustrated in Figure 2.4. For the states with $M_J = \pm 3/2$, there is no repulsion since the $^2P_{1/2}$ state does not have $M_J = \pm 3/2$ components. For that reason, these two states show linear dependence for all values of the magnetic field.

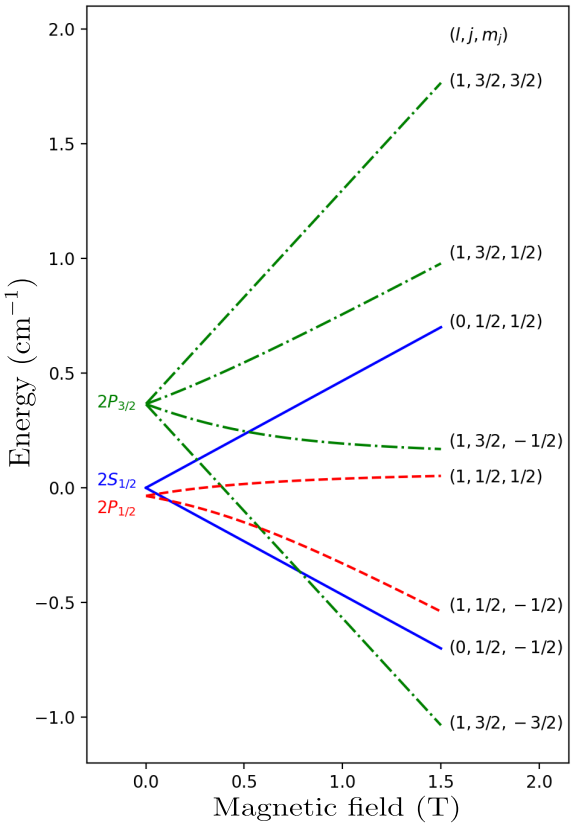

Figure 2.4: The Zeeman effect in the first excited state $n = 2$ of the hydrogen atom. The splitting of the $^2S_{1/2}$ state is shown in blue, for $^2P_{1/2}$ in red and for $^2P_{3/2}$ in green for magnetic fields up to 1.5 T.

Zeeman effect in the $X^2\Pi_{3/2}$ state of OH

The full Zeeman Hamiltonian for OH in the $X^2\Pi_{3/2}$ state is given by [118, 119, 120] :

$$
\begin{aligned}
H_{\mathrm{Z}} = \quad & g'_L \mu_B B_Z T^1_{p=0}(\mathbf{L}) && (2.49)\\
& + g_S \mu_B B_Z T^1_{p=0}(\mathbf{S}) && (2.50)\\
& - g_r \mu_B B_Z T^1_{p=0}(\mathbf{J}-\mathbf{L}-\mathbf{S}) && (2.51)\\
& - g_N \mu_N B_Z T^1_{p=0}(\mathbf{I}) && (2.52)\\
& + g_\ell \mu_B B_Z \sum_{q=\pm1} \mathscr{D}^{(1)*}_{0,q}(\omega) T^1_q(\mathbf{S}) && (2.53)\\
& + g'_\ell \mu_B B_Z \sum_{q=\pm1} \mathrm{e}^{-2\mathrm{i}q\phi}\, \mathscr{D}^{(1)*}_{0,-q}(\omega) T^1_q(\mathbf{S}) && (2.54)\\
& - g_r^{e'} \mu_B B_Z \sum_{q=\pm1} \sum_{p=0,\pm1} \mathrm{e}^{-2\mathrm{i}q\phi}\, (-1)^p\, \mathscr{D}^{(1)*}_{-p,-q}(\omega) T^1_p(\mathbf{J}-\mathbf{S}) \mathscr{D}^{(1)*}_{0,-q}(\omega). && (2.55)
\end{aligned}
$$

Here, $\mathscr{D}^{(j)}_{m',m}$ is the Wigner D-matrix and T^q_k is the spherical tensor operator. The seven terms in the expression are: the orbital Zeeman effect, the electron spin isotropic contribution, the rotational contribution, the nuclear-spin Zeeman effect, the anisotropic contribution to the electron spin Zeeman effect and two parity-dependent terms. The g-factors for the $X^2\Pi$ state are given in Table 2.1.

Table 2.1: g-factors for OH in the $X^2\Pi$ state

g'_L = 1.00107
g_S = 2.00152
g_r = -0.633 $\times 10^{-3}$
g_ℓ = 4.00 $\times 10^{-3}$
g'_ℓ = 6.386 $\times 10^{-3}$
$g_r^{e'}$ = 20.446 $\times 10^{-3}$

Matrix elements of each component of the Zeeman Hamiltonian expressed in the Hund's case (a) basis $|L\Lambda, S\Sigma, J\Omega M_J\rangle$ can be found in appendix A. As presented in Table 2.1, the Zeeman effect is dominated by the contributions from the orbital Zeeman effect and electronic-spin contribution. The diagonal matrix elements of the Zeeman Hamiltonian consisting of orbital Zeeman effect and

electronic spin contribution to the Zeeman effect are given by:

$$
\begin{aligned}
&\langle L\Lambda, S\Sigma, J\Omega M_J|\, H_Z \,|L\Lambda, S\Sigma, J\Omega M_J\rangle \qquad (2.56)\\
&= \langle L\Lambda, S\Sigma, J\Omega M_J|\, g'_L\mu_B B_Z T^1_{p=0}(\mathbf{L}) + g_S\mu_B B_Z T^1_{p=0}(\mathbf{S}) \,|L\Lambda, S\Sigma, J\Omega M_J\rangle\\
&= (2J+1)(-1)^{M_J-\Omega}\begin{pmatrix} J & 1 & J\\ -\Omega & 0 & \Omega\end{pmatrix}\begin{pmatrix} J & 1 & J\\ -M_J & 0 & M_J\end{pmatrix}\mu_{\mathrm{B}} B_Z(\Lambda + g_S\Sigma)\\
&= (2J+1)(-1)^{M_J-\Omega}\begin{pmatrix} J & J & 1\\ \Omega & -\Omega & 0\end{pmatrix}\begin{pmatrix} J & J & 1\\ M_J & M_J & 0\end{pmatrix}\mu_{\mathrm{B}} B_Z(\Lambda + g_S\Sigma)\\
&= (2J+1)(-1)^{MJ-\Omega}(-1)^{J-\Omega}(-1)^{J-M_J}\frac{4M_J\Omega}{(2J+2)(2J+1)2J}\mu_{\mathrm{B}} B_Z(\Lambda + g_s\Sigma)\\
&= \frac{\mu_{\mathrm{B}} B_Z M_J(\Lambda + g_S\Sigma)}{J(J+1)}.
\end{aligned}
$$

In the parity conserved basis of the $^2\Pi_{3/2}$ state

$$
\begin{aligned}
&|L, S; J, |\Omega|, M_J; \epsilon\rangle \qquad (2.57)\\
&= \frac{1}{\sqrt{2}}\Big(\,|L, |\Lambda|\rangle\,|S, |\Sigma|\rangle\,|J, |\Omega|, M_J\rangle + \epsilon\,|L, -|\Lambda|\rangle\,|S, -|\Sigma|\rangle\,|J, -|\Omega|, M_J\rangle\,\Big),
\end{aligned}
$$

the Zeeman Hamiltonian becomes:

$$
\begin{aligned}
&\langle L, S; J, |\Omega|, M_J; \epsilon'|\, g'_L\mu_B B_Z T^1_{p=0}(\mathbf{L}) + g_S\mu_B B_Z T^1_{p=0}(\mathbf{S}) \,|L, S; J, |\Omega|, M_J; \epsilon\rangle \qquad (2.58)\\
&= \mu_{\mathrm{B}} B_Z(|\Lambda| + g_S|\Sigma|)\frac{|\Omega| M_J}{J(J+1)}\Big(\frac{1+\epsilon\epsilon'}{2}\Big),
\end{aligned}
$$

where $\epsilon = \pm 1$. It is interesting to note that the Zeeman Hamiltonian does not couple states with different parity, and the upper and lower Λ-doublet has the same Zeeman shift. The Λ doublet splitting is $\Delta\Lambda = 0.056$ cm^{-1}. The Λ doubling arises from the $\Delta\Lambda = \pm 1$ terms in the spin-orbit and rotational Hamiltonians in which the $X^2\Pi$ ground state is mixed with the excited $A^2\Sigma$ state [118]. The Zeeman shift for OH in the $X^2\Pi_{3/2}$ state is illustrated in Figure 2.5. The low-field seeking states best suited for the deceleration experiments are depicted with red traces.

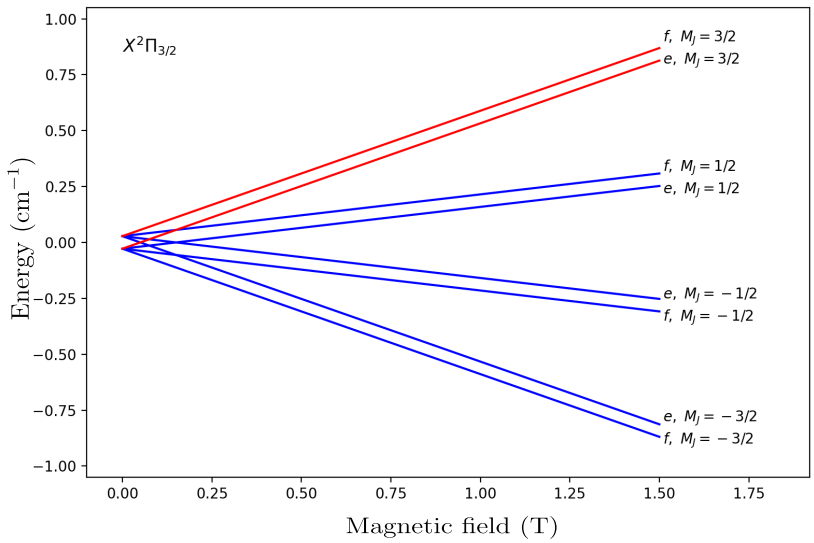

Figure 2.5: The Zeeman effect in the $X^2\Pi_{3/2}(\nu = 0, J = 3/2)$ ground state of OH. The low-field seeking states best suited for the Zeeman deceleration experiments are highlighted in red. The upper and the lower Λ-doublet display the same Zeeman shift.

Zeeman effect in the $A^2\Sigma^+$ state of OH

The first excited state of OH is best described by Hund's case (b). In order to show relative Zeeman shifts in the $A^2\Sigma^+$ state, it is enough to take into account only the spin-rotation coupling contribution and contributions from the Zeeman effect. The Hamiltonian is then written as:

$$H = H_{SN} + H_Z. \tag{2.59}$$

Expressed in the Hund's case (b) basis $|\Lambda N S J m_j\rangle$, the matrix elements of the spin-rotation Hamiltonian H_{SN} are given by:

$$\begin{aligned} H_{SN} &= \langle \Lambda N S J m_j | \, \gamma_v T_0^1(\mathbf{N}) T_0^1(\mathbf{S}) \, | \Lambda N S J' m_j' \rangle \qquad (2.60) \\ &= \gamma_v (-1)^{J+N+S} \sqrt{S(S+1)(2S+1)N(N+1)(2N+1)} \begin{Bmatrix} S & N & J \\ N & S & 1 \end{Bmatrix}, \end{aligned}$$

and of the Zeeman Hamiltonian H_Z by [121]:

$$H_z = \langle \Lambda N S J m_j | \, g_S \mu_B T_0^1(\mathbf{S}) \, | \Lambda N S J' m_j' \rangle \tag{2.61}$$
$$g_S u_B B (-1)^{J-m_j+J'+N+S+1} \sqrt{S(S+1)(2S+1)(2J'+1)(2J+1)}$$
$$\times \begin{pmatrix} J & 1 & J' \\ -m_j & 0 & m_j' \end{pmatrix} \begin{Bmatrix} S & J' & N \\ J & S & 1 \end{Bmatrix}.$$

Here, the spin-rotation coupling constant of the vibrational ground state of OH in $A^2\Sigma^+$ state is $\gamma_v = 0.226$ cm^{-1} [122, 123, 124]. In the $A^2\Sigma^+$ state, for each rotational level there are two degenerate energy levels corresponding to $\Omega = 1/2$ and $\Omega = -1/2$. The coupling between the electronic spin $\mathbf{S}$ and rotation $\mathbf{N}$ lifts the degeneracy. Matrix elements of the Hamiltonian H in the Hund's case (b) basis can be calculated from the relations 2.60 and 2.61. Eigenvalues of the Hamiltonian as a function of the magnetic field are plotted in Figure 2.6. The Hamiltonian matrix was constructed taking into account the $N = 0$ and $N = 1$ rotational levels of the vibrational ground state. Figure 2.6 a) shows the Zeeman splitting of the $A^2\Sigma^+(\nu = 0, N = 0)$ level and Figure 2.6 b) shows the Zeeman splitting of the $A^2\Sigma^+(\nu = 0, N = 1)$ level. The splitting between the $J = 1/2$ and $J = 3/2$ states is due to the spin-rotation coupling.

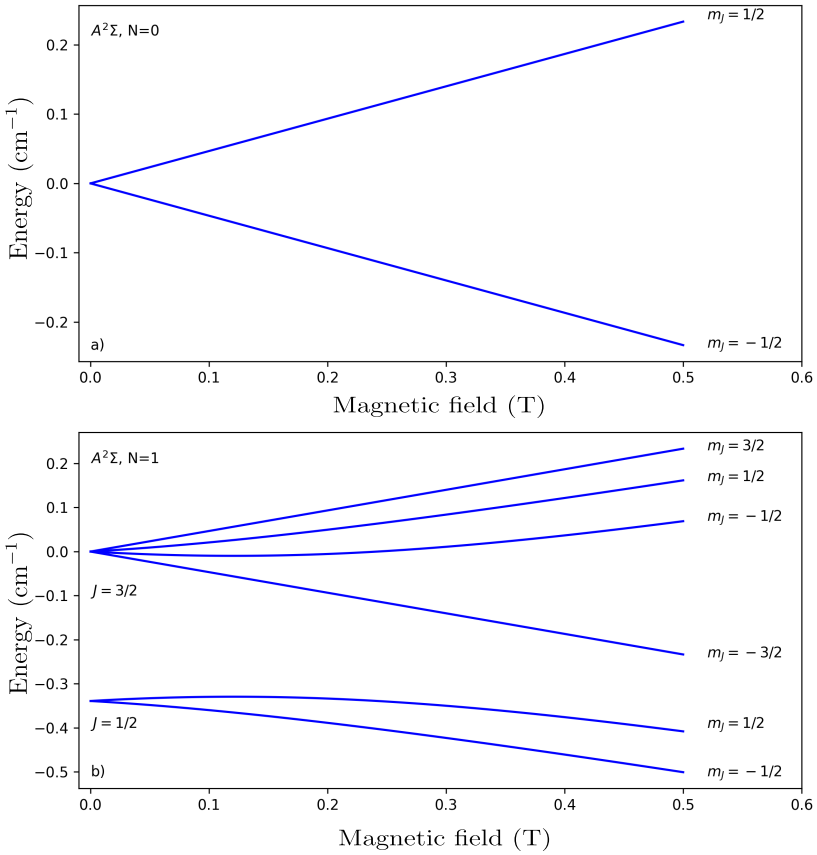

Figure 2.6: The Zeeman effect in the $A^2\Sigma^+(\nu = 0)$ excited state of OH. a) The Zeeman effect in the N=0 rotational state and b) in the $N = 1$ rotational state. The splitting between the $J = 1/2$ and $J = 3/2$ states is due to the spin-rotation coupling.

2.3 Energy level structure of OH

The hydroxyl radical is a simple but fascinating diatomic molecule with importance to the various fields of science. In the field of cold and ultra-cold physics, its importance stems from the fact that it is a polar molecule. Due to its electric and magnetic dipole moment in the ground state it is possible to manipulate its external degrees of freedom. This has lead to the ability to decelerate, cool, and trap OH radicals down to 10-100 mK temperatures [55, 70, 125]. In chemistry, it was the first free radical to be investigated in molecular beams [126] and it was

also the first short-lived molecule to be studied by microwave spectroscopy and by gas-phase electron paramagnetic resonance [127, 128]. In astronomy, the OH radical was the first interstellar molecule observed in the radio frequency range [129, 130]. OH masers were the first masers to be discovered in space and have been observed in more environments than any other type of maser [131]. It was first discovered in 1934 by Haber and Weiss in what is known today as the Fenton reaction [132, 133]. The OH radical consists of a hydrogen atom bonded to an oxygen atom which makes it reactive by allowing the abstraction of hydrogen atoms from other molecules to form water molecules. In the following section, a short review of the hydroxyl radical, including its energy structure in the electronic ground and first excited state is given. Different couplings that determine the energy level structure are discussed.

The hydroxyl molecule consists of one oxygen nucleus, one hydrogen nucleus, and 9 electrons. We start by writing the Hamiltonian of the whole system $\hat{H} = \hat{T} + \hat{V}$, where $\hat{H}$ is the Hamiltonian operator of the system, $\hat{T}$ is the kinetic the energy operator and $\hat{V}$ is the potential energy operator. The kinetic energy operator is written in the following [134]:

$$\hat{T} = -\frac{\nabla_H^2}{2m_H} - \frac{\nabla_O^2}{2m_O} - \sum_{n=1}^{9} \frac{\nabla_n^2}{2m_e}, \tag{2.62}$$

m_H, m_O and m_e are masses of the hydrogen nucleus, oxygen nucleus and electron, respectively and $\hbar = 1$. The gradient operators are to be operated on the coordinates of the relevant particles. The kinetic energy operator can be rewritten by setting the origin of the coordinate system at the center-of-mass of the whole system:

$$\hat{T} = -\frac{\nabla_M^2}{2M} - \frac{\nabla_r^2}{2m} - \sum_{n=1}^{9} \frac{\nabla_n'^2}{2m_e} - \sum_{n,k=1}^{9} \frac{\nabla_n' \cdot \nabla_k'}{2M_O + 2M_H}, \tag{2.63}$$

where $M = M_H + M_O + 9m_e$ is the total mass of the system, and $m = M_O M_H / M_O + MH$ is the reduced mass and center-of-mass coordinate $\mathbf{r_M} = (M_O \mathbf{r_O} + M_H \mathbf{r_H} + \sum_{n,k=1}^{9} m_e \mathbf{r_i})/M$. Casting equation 2.63 in spherical coordinates gives:

$$\hat{T} = -\frac{\nabla_M^2}{2M} - \frac{1}{2mr^2}\frac{\partial}{\partial r}(r^2\frac{\partial}{\partial r}) + \frac{1}{2mr^2}\hat{\mathbf{R}}^{\mathbf{2}} - \sum_{n=1}^{9}\frac{\nabla_n'^2}{m_e} - \sum_{n,k=1}^{9}\frac{\nabla_n' \cdot \nabla_k'}{2M_O + 2M_H}, \quad (2.64)$$

where the square of the rotational angular momentum operator is given by:

$$\hat{\mathbf{R}}^{\mathbf{2}} = -\frac{1}{\sin\theta}\frac{\partial}{\partial\theta}(\sin\theta\frac{\partial}{\partial\theta}) - \frac{1}{\sin^2\theta}\frac{\partial^2}{\partial\phi^2}. \quad (2.65)$$

In equation (2.64), the first term describes the translational motion of the molecule and can be discarded for current considerations. The second term relates to the radial motion while the third term relates to the angular motion of the two nuclei. The fourth term refers to the motion of the electrons while the fifth term is the so-called mass polarization term [135].

As a consequence of the Bohr-Oppenheimer approximation, the motion of the nuclei can be decoupled from the motion of the electrons and the Hamiltonian of the system can be separated into the electronic, vibrational and rotational contribution $\hat{H} = \hat{H}_{el} + \hat{H}_{vib} + \hat{H}_{rot}$. Taking into account the Coulomb interaction, electronic Hamiltonian can be written in the following form:

$$\hat{H}_{el} = -\sum_{n=1}^{9}\frac{\nabla_n'^2}{2m_e} + \frac{e^2}{4\pi\epsilon_0}(\sum_{n<k}\frac{1}{r_{nk}} - \sum_{n=1}^{9}(\frac{z_O}{r_{On}} + \frac{z_H}{r_{Hn}})), \quad (2.66)$$

here e is the electric charge of the electron, $z_O e$ and $z_H e$ are the electric charges of each nuclei, ϵ_0 is the permittivity of the vacuum, r_{nk} is the distance between each of the electrons, r_{On} and r_{Hn} is the distance between the i-th electron and each nucleus. The complete wavefunction of the system can be written as a composite of each contribution:

$$\Psi \approx \psi_{el}\psi_{vib}\psi_{rot} \quad (2.67)$$

and the total energy of the system as $E = E_{el} + E_{vib} + E_{rot}$.

Similarly as in atomic spectroscopy, electronic states of the diatomic molecules are classified by their orbital angular momentum and spin. The molecular term

symbol for the diatomic molecule has the following form:

$$^{2S+1}\Lambda^{(+/-)}_{\Omega,(g/u)}, \tag{2.68}$$

where S is the total spin angular momentum quantum number, Λ is the quantum number of the projection of the orbital angular momentum along the internuclear axis, Ω is the projection quanutm number of the total angular momentum along the internuclear axis, g/u is the electronic parity and $+/-$ is the reflection symmetry along an arbitrary plane containing the internuclear axis. Λ can take on values $\Lambda = 0, 1, 2, 3, ...$ and is labelled by capital Greek letters Σ, Π, Δ,.. Electronic states are labelled with capital letters, whereby the ground state is labelled as X and higher excited states as A, B, C. States with a spin multiplicity that differs from that of the ground state are labelled with lower case letters $a, b, c, ...$

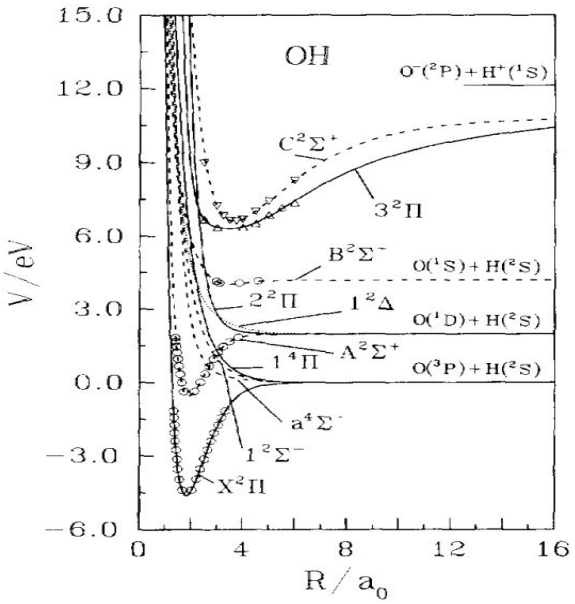

Figure 2.7: Potential energy curves for the first ten electronic states of OH. Reproduced from [136].

2.3.1 Hund's coupling cases a) and b)

Before discussing specifics of the Hund's a) and b) cases, let us first review relevant angular momenta of diatomic molecules. These are the electronic angular

momentum **L**, the spin angular momentum **S**, the nuclear spin angular momentum **I**, the total angular momentum **J**, the total angular momentum excluding spin **N** and the rotational angular momentum **R**. A summary of the different angular momenta and their properties is given in table 2.2. In a similar way, as is the case in atoms, the spin-orbit interaction between **L** and **S** can result in significant energy splittings. Moreover, the electronic degrees of freedom can couple with the rotational degrees of freedom. The presence of the coupling of different angular momenta introduces mixing terms into the Hamiltonian and destroys the validity of quantum numbers. However in some cases in which one interaction is dominant over another, 'almost' good quantum numbers are defined. These are the so-called Hund's cases. In the instance of the hydroxyl radical, Hund's case a) and b) apply.

Table 2.2: Angular momenta in diatomic molecules

Angular momentum	Quantum number	Description
L	L	electronic orbital angular momentum
S	S	spin angular momentum
J	J	total angular momentum excluding nuclear spin $\mathbf{J} = \mathbf{L} + \mathbf{S} + \mathbf{R}$
I	I	nuclear spin angular momentum
N	N	total angular momentum excluding spin $\mathbf{N} = \mathbf{R} + \mathbf{L} = \mathbf{J} - \mathbf{S}$
R	R	rotational angular momentum $\mathbf{R} = \mathbf{N} - \mathbf{L}$
$\mathbf{\Sigma}$	Σ	projection of **S** onto the intermolecular axis
$\mathbf{\Lambda}$	Λ	projection of **L** onto the intermolecular axis
$\mathbf{\Omega}$	Ω	projection of **J** onto the intermolecular axis

In Hund's case a) the orbital angular momentum **L** is coupled to the internuclear axis by the electrostatic forces, the spin **S** is coupled to the orbital angular momentum **L** by the spin-orbit interaction which in turn effectively couples it to the internuclear axis. The projections of **L** and **S** onto the internuclear axis are well defined and the projection of **S** onto the internuclear axis is denoted by Σ and takes values $S, S-1, ... -S$, while the projection of L onto the internuclear axis is denoted by Λ and takes values $\Lambda = 0, 1, 2, ...$ $\mathbf{\Omega}$ is a vector pointing along the internuclear axis with magnitude given by the projection of total angular momentum **J** on the internuclear axis, $\Omega = \Lambda + \Sigma$. $\mathbf{\Omega}$ couples with the rota-

tional angular momentum of the nuclei **R** to form the total angular momentum $\mathbf{J} = \mathbf{\Omega} + \mathbf{R}$. The good quantum numbers in case (a) are Λ , S, Σ , J and Ω. The dipole selection rules for optical transitions in Hund's case a) are: $\Delta\Lambda = 0, \pm 1$, $\Delta S = 0$, $\Delta\Sigma = 0$, $\Delta\Omega = 0, \pm 1$, and $\Delta J = 0, \pm 1$. A schematic representation of the Hund's coupling case a) is shown in Figure 2.8.

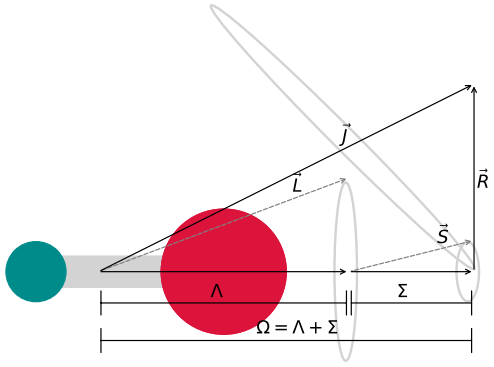

Figure 2.8: Angular momentum coupling diagram in Hund's case a): The orbital angular momentum **L** is coupled to the internuclear axis by electrostatic forces, the spin **S** is coupled to the orbital angular momentum **L** by the spin-orbit interaction which in turn effectively couples it to the internuclear axis. $\mathbf{\Omega}$ couples with the rotational angular momentum of the nuclei **R** to form the total angular momentum $\mathbf{J} = \mathbf{\Omega} + \mathbf{R}$. The good quantum numbers in case (a) are Λ , S, Σ , J and Ω.

In Hund's case b), the spin-orbit interaction is weak and the total spin angular momentum **S** is no longer coupled to the internuclear axis while the electronic orbital angular momentum **L** is still coupled to the internuclear axis. Ω ceases to be a good quantum number, while Λ remains a good quantum number. In this case, the spin angular momentum **S** couples to the total angular momentum excluding spin **N** by the so-called spin-rotation coupling. **N** and **S** couple then to form the total angular momentum **J**. The good quantum numbers in Hund's case (b) are Λ, N, S, and J. For Hund's case b), the optical selection rules are: $\Delta\Lambda = 0, \pm 1$, $\Delta S = 0$, $\Delta\Sigma = 0$, $\Delta\Omega = 0, \pm 1$, and $\Delta N = 0, \pm 1$. Cases a) and b) are the most common with most diatomic molecules falling somewhere in between. Additionally, many more Hund's cases exist but are not discussed here.

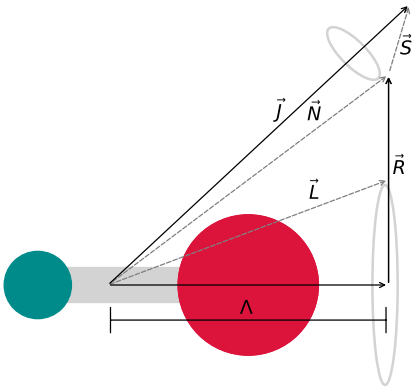

Figure 2.9: Angular momenta coupling diagram in Hund's case b): The orbital angular momentum **L** couples to the rotational angular momentum of the nuclei **R** to form **N**, the spin angular momentum **S** couples to **N** and **N** and **S** then couple together to from the total angular momentum **J**. The good quantum numbers in Hund's case (b) are Λ, N, S, and J.

2.3.2 The electronic ground state of OH

The orbitals of a diatomic molecule are typically described by the method of the linear combination of atomic orbitals (LCAO). In the united-atom picture, the configuration of the molecular orbitals in the electronic ground state $X^2\Pi$ of OH is:

$$X^2\Pi : (1s)^2(2s\sigma)^2(2p\sigma)^2(2p\pi)^3. \tag{2.69}$$

The partial filling of the $(2\pi p)$ orbital leads to OH having non-vanishing total electronic orbital **L** and spin angular momentum **S**. The magnitudes of the angular momenta **L**, **S** and **I** are $L = 1$, $S = 1/2$ and $I = 1/2$, while the rotational angular momentum number R takes non-negative integer values. For low rotational angular momentum quantum numbers, the OH molecule in the ground state is best described by the Hund's case a) scheme. Field free Hamiltonian of the OH molecule in the $X^2\Pi(v = 0)$ state, where v denotes vibrational quantum number, is given by [120]:

$$\hat{H} = \hat{H}_{\mathrm{SO}} + \hat{H}_{\mathrm{R}} + \hat{H}_{\mathrm{SR}} + \hat{H}_{\Lambda} + \hat{H}_{\mathrm{HF}}, \tag{2.70}$$

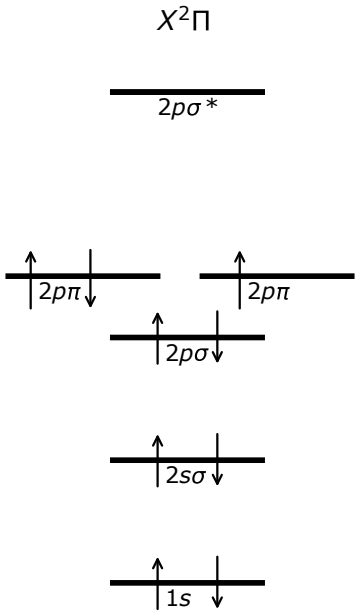

Figure 2.10: Molecular orbital (MO) diagram of OH in the $X^2\Pi$ state.

where $\hat{H}_{\rm SO}$ is the spin-orbit interaction Hamiltonian

$$\hat{H}_{\rm SO} = A_{\rm SO} T^1_{q=0}(\mathbf{L}) T^1_{q=0}(\mathbf{S}), \tag{2.71}$$

$\hat{H}_{\rm R}$ is the rotational Hamiltonian of the molecule

$$\hat{H}_{\rm R} = B_{\rm N}(\mathbf{J} - \mathbf{L} - \mathbf{S})^2, \tag{2.72}$$

$\hat{H}_{\rm SR}$ is the spin-rotation coupling Hamiltonian

$$\hat{H}_{\rm SR} = \gamma T^1(\mathbf{J} - \mathbf{S}) \cdot T^1(\mathbf{S}), \tag{2.73}$$

$\hat{H}_{\Lambda}$ represents the Λ-doubling terms, and

$$\hat{H}_{\Lambda} = \sum_{q=\pm 1} e^{-2iq\phi}[-Q T^2_{2q}(\mathbf{J}, \mathbf{J}) + (P + 2Q) T^2_{2q}(\mathbf{J}, \mathbf{S})], \tag{2.74}$$

$\hat{H}_{HF}$ is the hyperfine interaction Hamiltonian

$$\hat{H}_{HF} = aT^1_{q=0}(\mathbf{I})T^1_{q=0}(\mathbf{L}) + b_{\mathrm{F}}T^1(\mathbf{I})\cdot T^1(\mathbf{S}) + \sqrt{2/3}cT^2_{q=0}(\mathbf{I},\mathbf{S}) + d\sum_{q=\pm1} e^{-2iq\phi}T^2_{2q} + \\ + c_{\mathrm{I}}T^1(\mathbf{I})\cdot T^1(\mathbf{J}-\mathbf{S}) + c_{\mathrm{I}}^{'}\sum_{q=\pm1} e^{-2iq\phi}1/2[T^2_{2q}(\mathbf{I},\mathbf{J}-\mathbf{S}) + T^2_{2q}(\mathbf{J}-\mathbf{S},\mathbf{I})]. \tag{2.75}$$

The different parameters are given in Table 2.3 and the energy scales of different contributions to the total Hamiltonian are shown in Figure 2.11.

Table 2.3: Parameters for OH in $X^2\Pi(v=0)$ state [120]

Parameters	Strength [MHz]
A_{SO}	-4168639.13
B_{N}	555660.97
γ	-3574.88
Q	-1159.991650
P	7053.09846
a	86.1116
b_{F}	-73.2537
c	130.641
d	56.6838
c_{I}	-0.09971
$c_{\mathrm{I}}^{'}$	0.00643

Parameters in the table correspond to coupling strengths of various interactions. A_{SO} is the spin-orbit coupling constant, B_{N} is the rotational coupling constant, γ is the spin-rotation coupling constant, P and Q determine the Λ doubling and constants a, b_{F}, d, c_{I} and $c_{\mathrm{I}}^{\prime}$ determine the strength of hyperfine splitting.

For OH in the ground state L=1, $\Lambda = \pm1$, $S = 1/2$, $\Sigma = \pm1/2$, $J \geq 1/2$, $\Omega = \Lambda + \Sigma$, $-J \leq M_J \leq J$, I =1/2 and $M_I = \pm 1/2$. The $^2\Pi$ ground state of OH can be classified into two cases: one with $|\Lambda + \Sigma| = 3/2$ and one with $|\Lambda+\Sigma|$=1/2 splitting it into two manifolds, namely $^2\Pi_{3/2}$ and $^2\Pi_{1/2}$. In the $^2\Pi_{3/2}$ manifold, the molecular-axis projections $\mathbf{\Lambda}$ and $\mathbf{\Sigma}$ point in the same direction, and the total angular momentum quantum number start from J=3/2 and increases by an integer value for each higher rotational quantum number. In the $^2\Pi_{1/2}$ manifold, $\mathbf{\Lambda}$ and $\mathbf{\Sigma}$ point in opposite directions and the total angular momentum

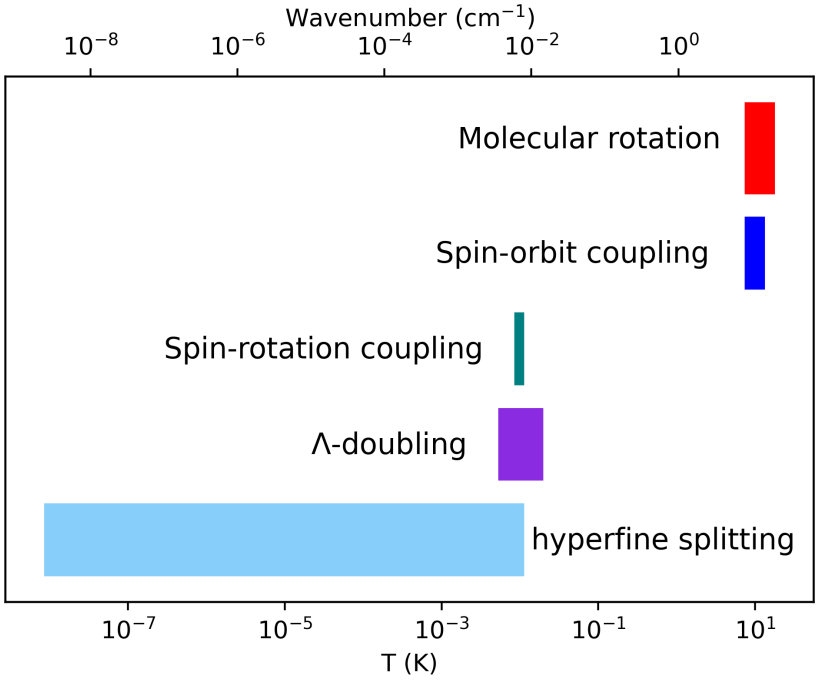

Figure 2.11: Energy scales of different contributions to the total Hamiltonian for the OH molecule in $X^2\Pi$ state [120]

quantum number starts from J=1/2. More generally, the molecular eigenstates should have well-defined parity. Hund's case a) and b) basis functions are defined in terms of quantities defined in the molecule-fixed frame, and for that reason, they do not have well-defined parities in the space-fixed frame. For that reason, it is more convenient to switch to the parity-adapted basis [137]

$$|J,\Omega,M_J,\epsilon\rangle = \frac{1}{\sqrt{2}}(|J,\Omega,M_J\rangle + \epsilon\,|J,-\Omega,M_J\rangle), \tag{2.76}$$

with $\epsilon = \pm 1$. The parity of the wavefunction is given by:

$$p = \epsilon(-1)^{J-S}. \tag{2.77}$$

$^2\Pi$ states with $\epsilon = 1$ are labelled as e and states with $\epsilon = -1$ are labelled as f. Taking into account the spin-orbit and the rotational contribution, the Hamiltonian matrix can be written in the parity basis $\left|^2\Pi^{\pm}_{1/2}\right\rangle, \left|^2\Pi^{\pm}_{3/2}\right\rangle$ [124]:

$$H = \begin{pmatrix} A_{SO}/2 + B_N(J(J+1) - 7/4) & -B_N((J+3/2)(J-1/2))^{1/2} \\ -B_N((J+3/2)(J-1/2))^{1/2} & -A_{SO}/2 + B_N(J(J+1) + 1/4) \end{pmatrix}, \tag{2.78}$$

with eigenvalues given by

$$E(^2\Pi_{3/2}, JM_J, \epsilon) = B_N((J-1/2)(J+3/2) - 1/2X), \tag{2.79}$$

$$E(^2\Pi_{1/2}, JM_J, \epsilon) = B_N((J-1/2)(J+3/2) + 1/2X), \tag{2.80}$$

where $X = (4(J+1/2)^2 + Y(Y-4))^{1/2}$ and $Y = A_{SO}/B_N$. The corresponding eigenvectors are given by:

$$\left|^2\Pi_{3/2}, JM_J\epsilon\right\rangle = a_1 \left|J, \Omega = 1/2, M_J\epsilon\right\rangle + a_2 \left|J, \Omega = 3/2, M_J\epsilon\right\rangle, \tag{2.81}$$

$$\left|^2\Pi_{1/2}, JM_J\epsilon\right\rangle = -a_2 \left|J, \Omega = 1/2, M_J\epsilon\right\rangle + a_1 \left|J, \Omega = 3/2, M_J\epsilon\right\rangle, \tag{2.82}$$

where a_1 and a_2 are

$$a_1 = \sqrt{\frac{X+Y-2}{2X}}, \tag{2.83}$$

$$a_2 = \sqrt{\frac{X-Y+2}{2X}}. \tag{2.84}$$

The eigenvalues $E(^2\Pi_{3/2}, JM_J, \epsilon)$ are labelled F_1 and $E(^2\Pi_{1/2}, JM_J, \epsilon)$ are labelled F_2. From equation 2.78, off-diagonal elements increase with increasing rotational quantum number leading to mixing of states with $|\Omega|$=1/2 and $|\Omega|$=3/2. For that reason, the Hund's case a) coupling is valid only for low values of the rotational quantum number. Energy levels from equation 2.79 and 2.80 depend on the value of $|\Omega| = 1/2, 3/2$ but not on the sign of $|\Omega|$. The degeneracy is broken if a higher-order Λ-doubling interaction is included, with effective Hamiltonian given by:

$$\hat{H} = \hat{H}_{\mathrm{R}} + \hat{H}_{\mathrm{S}} + \hat{H}_{\Lambda}, \tag{2.85}$$

where $\hat{H}_{\Lambda}$ is given by equation 2.74. Including the Λ-doubling term, the eigenvalues are given by

$$E(^2\Pi_{3/2}, JM_J, \epsilon) = B_N((J-1/2)(J+3/2) - 1/2X) \pm \Delta/2, \tag{2.86}$$

$$E(^2\Pi_{1/2}, JM_J, \epsilon) = B_N((J-1/2)(J+3/2) + 1/2X) \pm \Delta/2. \tag{2.87}$$

Here $+$ and $-$ signs correspond to e and f parity states in the F_1 manifold and to f and e states in the F_2 manifold. The Λ splitting is very small ($\Delta = 0.05\mathrm{cm}^{-1}$)

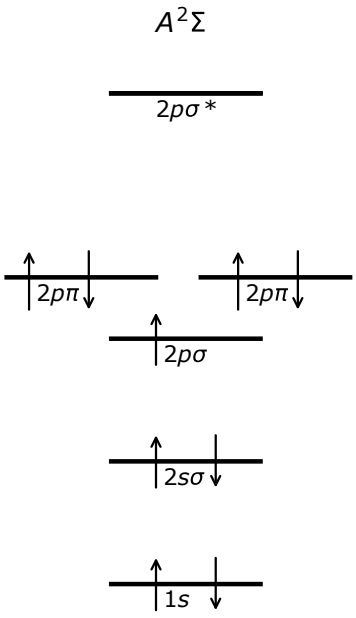

Figure 2.12: Molecular orbital (MO) diagram of OH in the $A^2\Sigma^+$ state.

compared to the rotational spacing [138].

2.3.3 The first electronic excited state of OH

In the first excited state of OH, $2p\sigma$ electron is promoted to the $2p\pi$ state and the electron configuration is given by:

$$A^2\Sigma^+ : (1s)^2(2s\sigma)^2(2p\sigma)^1(2p\pi)^4. \tag{2.88}$$

In this state, $L = 0$ and the projection onto the intermolecular axis $\Lambda = 0$. This state is best described by Hund's case b). The Hamiltonian which includes rotational and spin-rotation interaction is [139]:

$$\hat{H} = \hat{H}_R + \hat{H}_{SR} = B_N \mathbf{N}^2 + \frac{\gamma}{2}(\mathbf{J^2} - \mathbf{N^2} - \mathbf{S^2}). \tag{2.89}$$

With S=1/2 and $J = N \pm 1/2$, the eigenvalues are given by:

$$E(N+1/2) = B_N N(N+1) + \frac{\gamma}{2}N, \tag{2.90}$$

$$E(N-1/2) = B_N N(N+1) + \frac{\gamma}{2}(N+1). \tag{2.91}$$

States with $J = N+1/2$ are labelled F_1 and states with $J = N-1/2$ are labelled F_2, and the parity of the states is:

$$p(-1)^N. \tag{2.92}$$

2.3.4 A←X transition in OH

The detection of OH radicals performed in the experiments described in this thesis is carried out by Laser-Induced Fluorescence (LIF) on the $A^2\Sigma^+ \leftarrow X^2\Pi$ transition. OH molecules are excited from the ground electronic state $X^2\Pi$, $v = 0$ to the first electronically excited state $A^2\Sigma^+$, $v = 1$ which has a lifetime of 720 ns [140] after which it fluoresces down to the $X^2\Pi$, $v = 1$ state. Fluorescence is recorded onto the photo-multiplier tube detector. The selection rules for the electric dipole allowed transitions are:

$$\Delta J = 0, \pm 1, \tag{2.93}$$

and

$$\Delta N = 0, \pm 1, \pm 2, \tag{2.94}$$

and only transition that change parity are allowed. Transitions with $\Delta N = -2, -1, 0, 1, 2$ are labelled as O, P, QR and S.

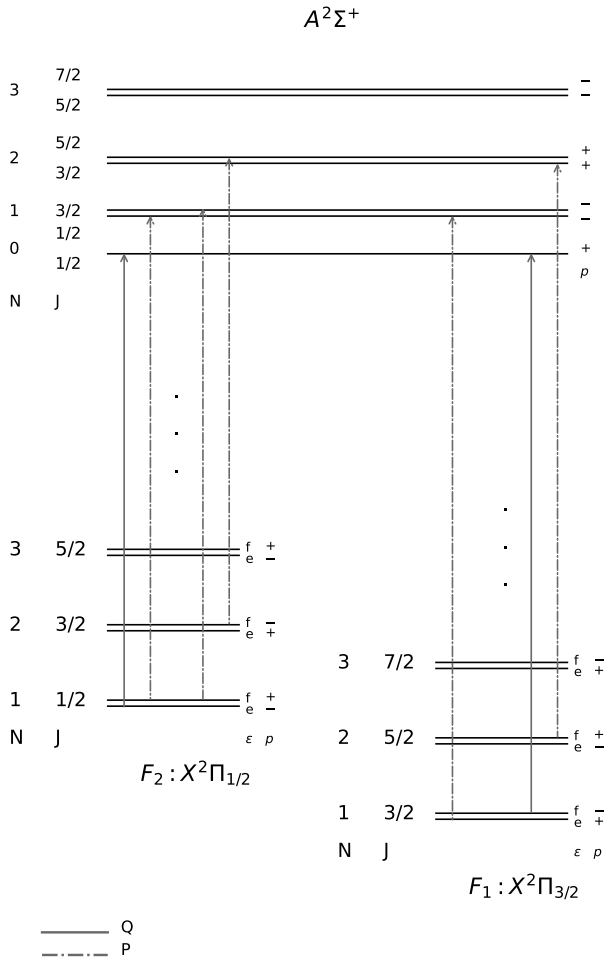

Figure 2.13: Schematic energy level diagram of the electronic ground state $X^2\Pi$ and first electronic excited state $A^2\Sigma^+$ of OH. In the ground state, the $\Pi_{3/2}$ branch is labelled as F_1 and the $\Pi_{1/2}$ branch is labelled as F_2. Λ-doubling splittings in the ground state and ρ-doubling splittings in the excited state are overemphasized for clarity. Some electronic transitions are shown, with Q and P branch transitions denoted with full and broken arrow style, respectively.

2.4 Conclusions

In this chapter, the description of the Zeeman effect was given both in the frameworks of classical and quantum mechanics. Calculations of the Zeeman effect were given for the species relevant to the experiments described in this thesis. The Zeeman energy structure was calculated for H atoms both in the ground $1^2S_{1/2}$ state and first excited $2^2S_{1/2}, 2^2P_{1/2}$, and $2^2S_{3/2}$ states. Zeeman energy structure was illustrated for OH radical in the ground $X^2\Pi_{3/2}(\nu = 0)$ state and the first excited $A^2\Sigma^+(\nu = 0)$ state.

Chapter 3

Experimental setup

3.1 Introduction

This chapter introduces the description of the experimental setup excluding the details for the design of the travelling-wave Zeeman decelerator which will be given in the next chapter. First, the details concerning the laser-based detection methods that are employed in the experiments described throughout this thesis are presented. Details on the 282 nm laser setup for Laser-Induced Fluorescence (LIF) [141, 142, 143, 144] and 243 nm laser for Resonance-Enhanced Multiphoton Ionization (REMPI) [145, 146, 147, 148] setup are given. The details on the molecular beams are given with a short discussion on the theory of the formation of supersonic beams. The details on the design of Nijmegen pulsed valve (NPV) and pinhole discharge mechanism are given in short, and most important measurements of the properties of the supersonic radical beams generated by the NPV are presented. Finally, the design of the time-of-flight mass spectrometer (TOF-MS) is described. First, the operational principle of the micro-channel plate (MCP) detector is given and measurements of the metastable species on the MCP detector are illustrated. Operation of the TOF-MS is briefly outlined and the design of the homemade Wiley-McLaren [149] type TOF-MS is described. Resolution of the spectrometer is optimized relative to the ratio of the applied electric potential differences on the TOF-MS electrodes.

3.2 Pulsed dye laser setup for the production of 243 nm and 282 nm laser light

In the experiments described throughout this thesis two types of laser-based methods were implemented for particle state detection, namely: Laser-Induced-Fluorescence (LIF) which was adopted to measure the OH radicals in their $X^2\Pi_{3/2}$ state, and 2+1 Resonance-Enhanced-Multiphoton-Ionization (REMPI) for the detection of H atoms in the $1^2S_{1/2}$ state. The detection of OH molecules was executed by simultaneously inducing the transition in the $Q_{21}(1): X^2\Pi_{3/2}(J''=3/2, N''=1, \nu''=0) \rightarrow A^2\Sigma^+(J'=1/2, N'=1, \nu'=1)$ branch and in the $Q_1(1): X^2\Pi_{3/2}(J''=3/2, N''=1, \nu''=0) \rightarrow A^2\Sigma^+(J'=1/2, N'=1, \nu'=1)$ branch with laser light centred around 282 nm. The OH molecules in the $A^2\Sigma^+$ state spontaneously fluoresce mainly to the $X^2\Pi_{3/2}(J''=3/2, N''=1, \nu''=1)$ state with a radiative lifetime of $\tau = 717 \pm 18$ ns [150]. A schematic energy level diagram illustrating the transitions involved in the LIF detection is depicted in Figure 3.1 a). The Nd: YAG laser (Continuum Surelight, model: SLII-20) operated in a pulsed mode with a repetition rate of 10 Hz and generated pulses of laser light at around 532 nm (second-harmonic) with a pulse duration of $\sim$ 10 ns, and energy of $\sim$ 120 mJ/pulse ($\sim$1.2 W). The laser light was used to pump a dye laser (Lambda Physik, model: ScanMate 2E) prepared with Rhodamine 6G (Sirah Lasertechnik) dye dissolved in ethanol. Laser light generated by the dye laser, centred at 564 nm and an energy of $\sim$11.5 mJ/pulse was sent through a BBO second-harmonic generation crystal where it was frequency doubled. The 282 nm laser light with an energy of $\sim$1.5 mJ/pulse was then sent through a Pellin-Broca prism where it was separated from the undoubled light. The experimental setup was arranged in such a way that the LIF detection with a 282 nm laser light could be performed either in the first vacuum chamber in front of the NPV, or in the last vacuum chamber, 36 mm after the decelerator exit. The procedure for generation of laser light at 282 nm is schematically depicted in Figure 3.2 a).

The REMPI detection method utilizes a high photon density source to excite

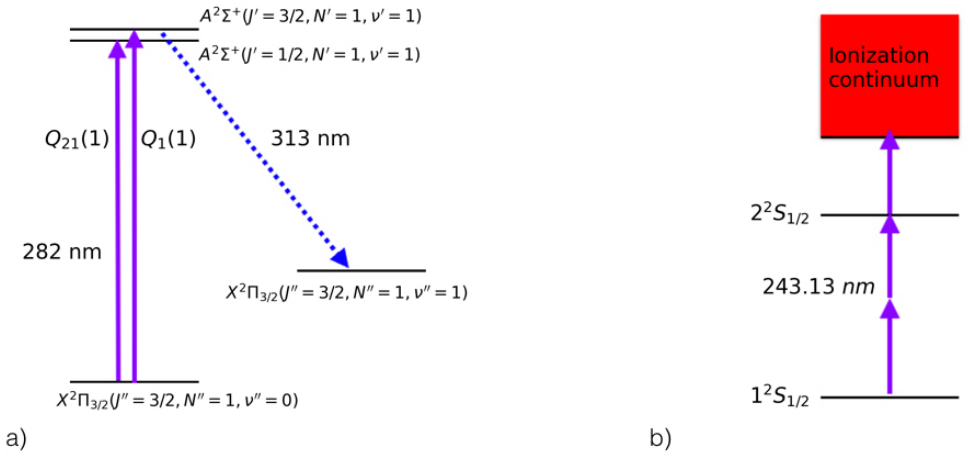

Figure 3.1: Schematic diagram of laser excitation and energy transfer processes of the a) LIF detection of OH in the $X^2\Pi_{3/2}$ state and b) 2+1 REMPI process of the ground state of the hydrogen atom.

a sample of atoms or molecules into the excited state followed by ionization of the sample. This is a stepwise process requiring at least 2 photons to ionize the atom or a molecule. It usually involves a resonant single or multiple photon absorption to an electronically excited intermediate state followed by one or more photons which ionize the atom or the molecule. Each REMPI process is characterized by $n + m'$ photons utilized in the ionization process where n identical photons are used to drive a resonant multiphoton transition to an intermediate state and additional m' photons to ionize the atom or the molecule from the intermediate state, with the prime indicating that the photons exciting the atom or the molecule to the intermediate state are different wavelength than the ionization photons. Created ions are typically detected by a time-of-flight mass spectrometer. In the context of our experiment, a 2+1 REMPI scheme was developed for detection of the hydrogen atoms. Hydrogen atoms in the $1^2S_{1/2}$ state are excited by two photons at 243.13 nm to the $2^2S_{1/2}$ state. From there hydrogen atom is ionized by absorption of a third photon at the same wavelength. Energy diagram of the process is depicted in Figure 3.1 b).

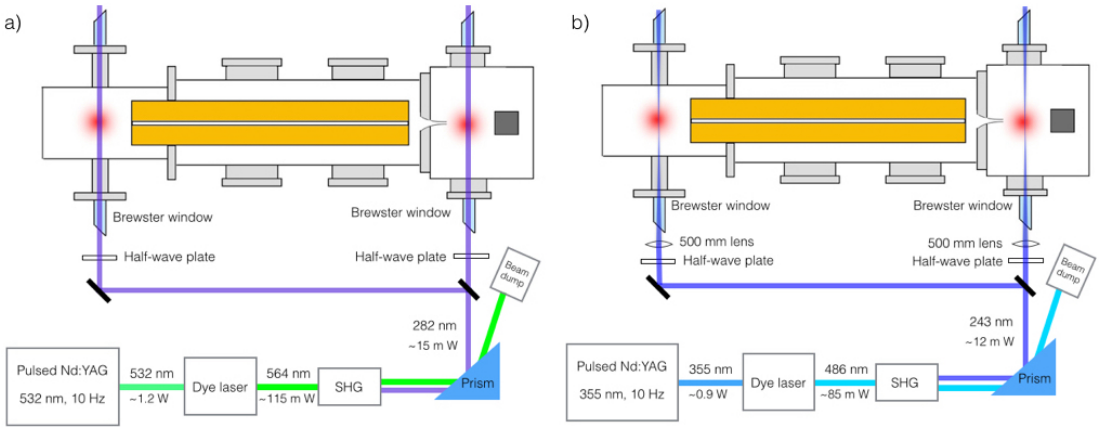

Figure 3.2: Experimental setup for production of the a) 282 nm laser radiation and b) 243 nm laser radiation. a) A Nd: YAG laser generated pulses of laser light at 532 nm which pump a dye laser prepared with Rhodamine 6G dye. Laser light generated by the dye laser centred at 564 nm was sent through a BBO second-harmonic generation crystal where it was frequency-doubled and sent to the experimental setup. b) The Nd:YAG laser generated a third-harmonic laser pulse at 355 nm which then pumped the dye laser prepared with Coumarin 102 dye. Laser light generated by the dye laser centred at 486 nm was frequency doubled by a BBO crystal to 243.13 nm and focused into the detection region.

Laser radiation at 243.13 nm was produced in the similar way as described in a case of 282 nm laser radiation. Here, the Nd: YAG laser generated a third-harmonic laser pulse at 355 nm with an energy of ∼90 mJ/pulse which was then used to pump the dye laser prepared with Coumarin 102 dye (Sirah Lasertechnik) dissolved in ethanol. The laser light generated by the dye laser was centred at 486 nm with an energy of ∼8.5 mJ/pulse which was then frequency-doubled through a BBO crystal to 243.13 nm with an energy of ∼1.2 mJ/pulse. The 243.13 nm laser light was then sent to the experimental apparatus and focused through a $f = 500$ mm spherical UV lens into the detection region creating a beam size of ∼100 μm in the region where it intersects the molecular beam. The procedure for generation of laser light at 243.13 nm is schematically depicted in Figure 3.2 b).

3.3 The molecular beam source [1]

Atomic or molecular beams are produced by expanding the sample from a high-pressure reservoir at a temperature T_0 and a pressure p_0 to a low-pressure region at a pressure p_b through a narrow orifice with a diameter of the orifice larger than the free mean path of the gas particles in the high-pressure reservoir. As the gas is expanded through the orifice, it is accelerated by the pressure difference $p_0 - p_b$. With the increased mean velocity of the gas, the enthalpy of the gas is decreased, leading to the cooling of the internal and external degrees of freedom of the expanding gas. The particles forming a beam are moving at approximately similar forward velocities, with very few collisions between the particles. Atoms or molecules forming the beams are internally cold (∼1 K) with the forward velocity of several hundred meters per seconds in the laboratory frame and narrow velocity spread in the direction of propagation [151, 152].

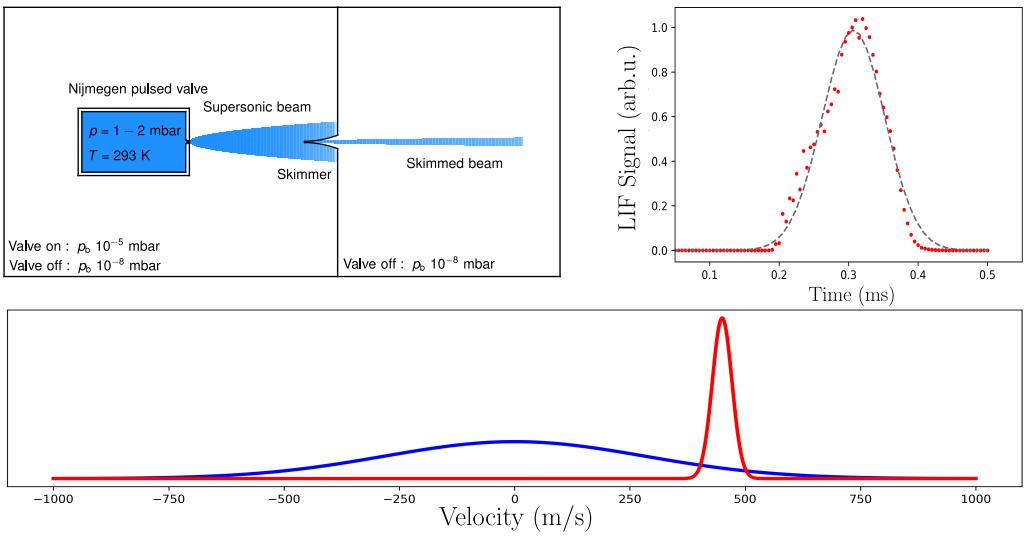

Figure 3.3: A supersonic beam. a) Supersonic beams are produced by expanding the gas from a high-pressure reservoir at a temperature T_0 and a pressure p_0 to a low-pressure reservoir at a pressure p_b through a narrow orifice. b) A measured time-of-flight profile of the supersonic beam in the present experiment. c) Velocity distribution of particles in the reservoir and in the supersonic beam.

Conservation of energy before and after the adiabatic expansion process can

be written in terms of the molar enthalpy:

$$h_0 = h + \frac{1}{2}mv^2, \tag{3.1}$$

where h_0 is a stagnation molar enthalpy of the gas reservoir, h is the rest internal enthalpy of the gas in the reference frame moving with the velocity v and $\frac{1}{2}mv^2$ is the kinetic energy of the gas. From equation 3.1, it follows that the difference in the specific enthalpy before and after the expansion results in the increase of the kinetic energy of the expanding gas. Taking into the account relation for the enthalpy at a constant pressure $dH = C_p dT$, equation 3.1 can be rearranged:

$$v = \sqrt{2C_p(T_0 - T)}. \tag{3.2}$$

The maximum (terminal) velocity that can be reached ($T \approx 0$) is :

$$v_{max} = \sqrt{2C_P T_0} = \sqrt{\frac{2k_{\mathrm{B}}T_0}{m}\frac{\gamma}{\gamma - 1}}, \tag{3.3}$$

where $C_p = \frac{k_{\mathrm{B}}}{m}\frac{\gamma}{\gamma-1}$ and k_{B} is the Boltzmann constant and $\gamma = C_p/C_v$ is the specific heat ratio. The specific heat ratio $\gamma = 3/5$ applies for the monoatomic gases and $\gamma = 7/5$ applies for the diatomic gases in the vibrational ground state [153]. The maximum velocity calculated from equation 3.3 for different noble gases at three different temperatures is illustrated in Table 3.1.

Table 3.1: Terminal velocity of noble gases in a molecular beam at $T_0 = 293\ K$ and $T_0 = 77\ K$

Species	$v_{max}(T_0 = 293\ K)$	$v_{max}(T_0 = 77\ K)$
^4He	1744 m/s	894 m/s
^{20}Ne	776 m/s	398 m/s
^{40}Ar	552 m/s	-
^{84}Kr	381 m/s	-
^{131}Xe	304 m/s	-

The terminal velocities of the noble gasses at $T_0 = 293$ K are illustrated in Figure 3.4. More details on the theoretical aspects of the production of supersonic atomic and molecular beams can be found in [154, 155, 156].

For the experiments described in this thesis, a pulsed molecular beam source

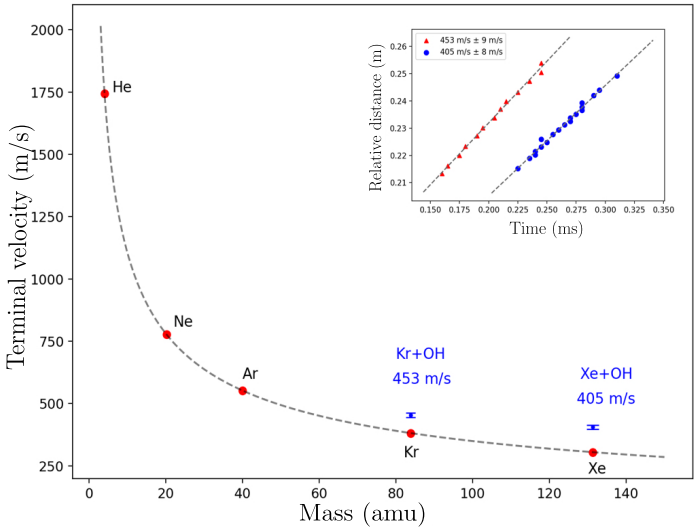

Figure 3.4: The terminal velocities of the noble gasses at $T_0 = 293$ K are shown (red dots). The grey dashed line represents the terminal velocity as a function of the mass given by equation 3.3. For reference, measured velocities of the OH radical seeded in Kr and Xe generated by the Nijmegen pulsed valve are shown in blue. Velocities are measured by moving the valve relative to the detection region. The mean arrival time of each package and relative position of the valve are recorded for each setting. A linear fit is performed on the recorded data and the velocity is extracted from each fit. The recorded data together with the fit and extracted velocities are shown in the inset.

was required. The advantages of the pulsed sources compared to the continuous sources is that they require lower pumping capacity of the system, they have higher peak particle densities inside the beam with internally colder beams and narrow velocity spreads [157, 158]. Currently, there are a few available options on the market for pulsed molecular beam sources [159, 160, 161, 162]. The production of molecular beams in the experiments described throughout this thesis was performed with the use of a home-built Nijmegen Pulsed Valve (NPV) [1]. The opening mechanism of the valve operates by supplying a short (20 μs - 60 μs) and intense (400 A - 1000 A) current pulse through an aluminium spring (length l= 6 mm and thickness l_t= 0.2 mm) which is placed inside a magnetic field ($\sim$ 1.4 T) generated by NdFeB permanent magnets. In the centre of the spring, a spherical poppet (diameter d = 1.5 mm) is attached, which is then placed on the Viton O-ring centred onto the nozzle (diameter 0.5 mm), making a boundary between the interior and the exterior of the valve body. The interior of the valve body is closed in such a way that the pressurized gas ($p \sim 4-5$ bar) is confined inside the interior of the valve, and no gas is able to escape through the nozzle. When the high-current pulse is passed through the aluminium spring, the Lorentz force $\mathbf{F} = l \cdot \mathbf{I} \times \mathbf{B}$, typically $\sim 4-7$ N, pulls the spring in the opposite direction of the nozzle, and in that way opens the nozzle channel. After the current pulse ends, the spring is pulled back to its original position by the spring force thereby rendering the interior of the valve body leak-tight. The spring is locked between two electrodes over which the current from the valve driver is passed. The gas is supplied to the interior of the valve through the gas inlet which is connected to the gas lines over 1/4″ Swagelok connectors. The optimal backing pressure of the gas during the operation of the valve was found to be $p_{\text{backing}} = 1-2$ bar. The current pulse is supplied by a low-voltage current pulse driver. The current driver consists of a 10000 μF capacitor bank which is charged by an adjustable 0-20 V power supply, a switch and two potentiometers. An internal or external TTL pulse opens the switch which consists of four parallelized MOSFETs (IRLU9743) which in turn are directly connecting the capacitor bank to the NPV electrodes and the current is supplied through the NPV spring. Once the TTL pulsed

is completed, the switch is closed and the current is not supplied to the NPV anymore. The current pulse duration and the capacitor charging voltage, which determines the amplitude of the current pulse, are adjusted externally through potentiometers. The NPV is typically operated at 10 Hz repetition rate, with the possibility to increase the repetition rate up to 30Hz. Yan et al. [1] found that the peak number of particles in a single pulse produced by the NPV was $5 \cdot 10^{13} - 9 \cdot 10^{13}$ depending on the backing pressure and measured with 0.1% NO seeded in He. Additionally, they measured peak beam densities of $2.8 \cdot 10^{15}$ particles cm^{-3} for 0.1 % NO seeded in Helium and $1.2 \cdot 10^{15}$ particles cm^{-3} for 0.5% NO seeded in Argon.

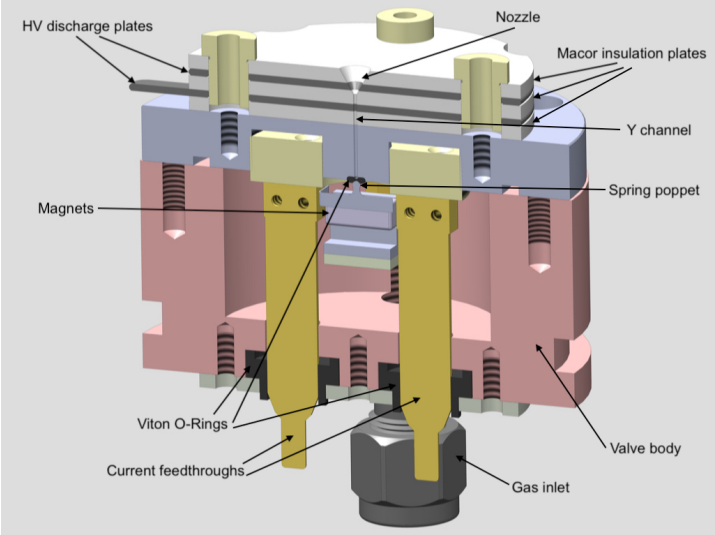

Figure 3.5: Schematic cut through the Nijmegen pulsed valve and the pinhole discharge mechanism.

On the front side of the NPV, a pinhole-discharge assembly, based on the design developed by Lewandowski et al. [163], was installed. The pinhole-discharge assembly consised of two stainless steel disk electrodes (0.7 mm thickness) sandwiched between three disk insulators made from Macor ceramic (2.3 mm thickness). Through the centre of the stacked disks, a 0.5 mm hole was machined, extending the nozzle of the valve. From the middle of the second insulator, a 60° cone was machined forming a Y-shaped discharge nozzle. Even et al. have found that conically shaped nozzles produce beam densities that are one order of magnitude larger than the ones produced by a simple pinhole nozzle [164, 165].

Experiments with different discharge-nozzle geometries were performed within our group, and it was found that Y-shaped nozzle is superior for production of radical sources compared to other discharge nozzle geometries [139, 166]. Radical species were created by applying a DC voltage between the first and the second electrode generating discharge throughout the gas inside the nozzle. The electric discharge occurus when the electric current starts to flow through the gas due to the ionization of the gas. With an increasing voltage difference, the free electrons carrying the current gain enough energy to cause further ionization thereby causing an "avalanche". Details on the discharge processes and different discharge regimes in gases can be found in [167, 168, 169, 170, 171, 172]. The NPV was operated typically in the glow discharge mode, which in the case of the NPV, with the described geometry of the pinhole discharge assembly, occured between V = -600 V and -1000 V. The voltage was applied in such way that the electrode closer to the valve body was grounded and the electrode which is further away was negatively biased. The voltage applied to the discharge electrodes was pulsed in time and the initial timing of the pulses was related to the opening of the valve. The typical duration of the pulses was 10 μs - 200 μs. The pulsing of the high-voltage was performed via high-voltage switching electronics. Details on the design of the NPV valve and the pinhole discharge as well as the electronics necessary for the operation both of the NPV and the pinhole discharge are described in [139]. Ploenes et al. measured radical densities 5 cm downstream from the nozzle. OH radicals were produced by generating a discharge through H_2O seeded in Ar, Kr or Xe, with a resulting radical densities of $3.0 \pm 0.6 \cdot 10^{11}$ cm^{-1} for Ar, $3.0 \pm 0.6 \cdot 10^{11}$ cm^{-1} for Kr and $0.9 \pm 0.2 \cdot 10^{11}$ cm^{-1} for Xe.

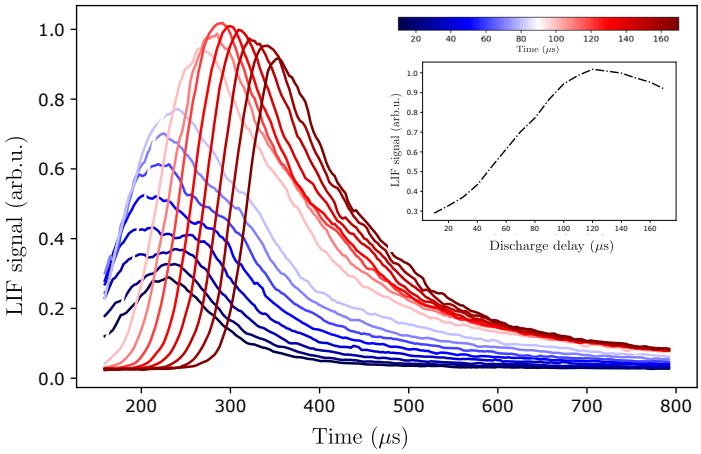

Figure 3.6: LIF measurements of the time-of-flight profiles of OH radicals generated by the NPV with a range of discharge pulse offsets relative to the opening of the NPV. The discharge duration is kept constant at $t_{\text{duration}} = 70$ μs and discharge delays are scanned relative to the NPV opening time from $t_{\text{delay}} = 10$ μs up to $t_{\text{delay}} = 170$ μs in 10 μs steps. A normalized total OH yield as a function of the discharge delay is shown in the inset.

For successful Zeeman deceleration experiments, it is necessary to have a high phase-space density of particles at the entrance of the decelerator. For that reason, a set of experiments that maximize the yield of OH radicals produced by the NPV was conducted . Measurements of the time-of-flight profiles of OH radicals generated by the NPV both with a range of discharge pulse offsets relative to the opening of the NPV and a range of discharge pulse durations were conducted. Results of these measurements can be seen in figure 3.6 and 3.7. In the first set of measurements, the discharge duration was kept constant at $t_{\text{duration}} = 70$ μs and discharge delay is scanned relative to the NPV opening time from $t_{\text{delay}} = 10$ μs up to $t_{\text{delay}} = 170$ μs in 10 μs steps. The experiments were conducted with -760 V voltage difference applied between two electrodes of the pinhole discharge. Results of these measurements are shown in Figure 3.6. From the figure, it can be seen that the overall radical yield is low at low discharge delays and it increases with increasing discharge delay up to a maximum value, after which it starts to decrease again. At low discharge delay, the molecular beam does not have enough time to fully expand through the nozzle due to limits by the mechanics of the valve opening mechanism. As the density of the molecules increases inside the nozzle, so does the radical yield. At higher values of discharge delay, the density

of molecules inside the nozzle channel is again decreased due to the mismatch of temporal overlap between the discharge and the molecular beam. The measured time-of-flight traces are depicted in Figure 3.6. The time-of-flight profiles are colour-coded with the color bar illustrating the discharge delay at which each trace was recorded. In the inset, the normalized total OH yield as a function of the discharge delay is shown.

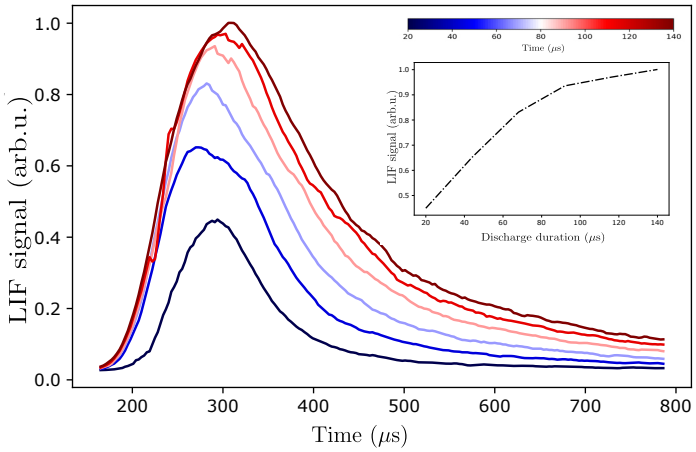

Figure 3.7: LIF measurements of the time-of-flight profiles of OH radicals generated by the NPV for the range of discharge durations between $t_{\text{duration}} = 20$ μs and $t_{\text{duration}} = 140$ μs with 20 μs steps between each measurement and constant discharge delay of $t_{\text{delay}} = 140$ μs throughout the measurements. In the inset, a normalized total OH yield as a function of the discharge duration is shown.

Figure 3.7 illustrates measurements of the time-of-flight profiles of OH radicals generated by the NPV for the range of discharge durations between $t_{\text{duration}} = 20$ μs and $t_{\text{duration}} = 140$ μs and 20 μs steps between each measurement. The discharge delay was kept constant at $t_{\text{delay}} = 140$ μs throughout the measurement. From the figure, it can be seen that the radical yield is low for low discharge durations, and it starts to increase with the increasing discharge duration. At low discharge duration, the high-voltage pulse is short and the discharge process inside the nozzle is not efficient. With increasing discharge duration, the overall radical yield also increases. At long discharge durations the radical yield is limited by the duration of the gas pulse. The time-of-flight profiles in Figure 3.7 are colour-coded with the color bar illustrating the discharge duration at which each profile was recorded. In the inset, a normalized total OH yield as a function of

the discharge duration is shown.

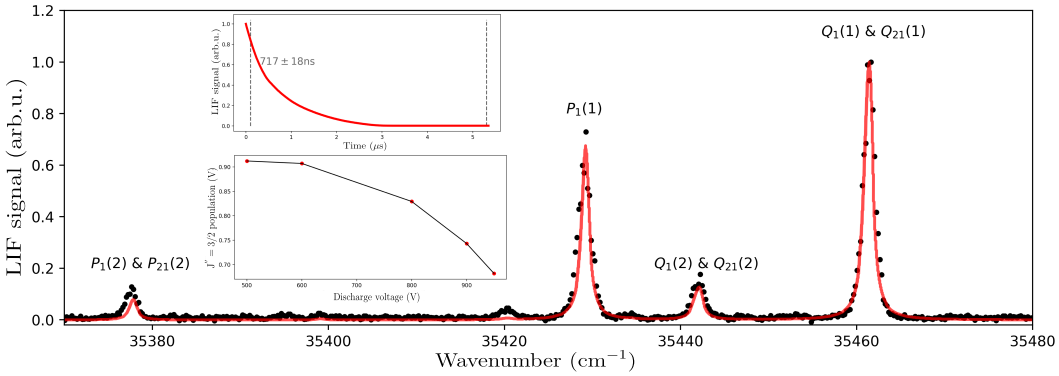

Figure 3.8: LIF spectrum of the beam of OH molecules generated by the pulsed discharge of H_2O. Black dots illustrate data points acquired by integrating the recorded LIF signal, while the red line depicts data simulated with the LIFBASE software [173]. In the upper inset, a LIF signal corresponding to a single data point (red) and the signal range (dashed lines) are shown. Ratios of rotational state populations in the rotational ground state as a function of discharge voltage are illustrated in the lower inset.

As described, the measurements of the OH radical are executed by implementing LIF measurements on the $Q_{21}(1)$ and $Q_1(1)$ transitions. For that reason, it was important that the 282 nm laser was on resonance with the transitions. In order to find the resonances, a laser wavelength scan was performed. The laser wavelength was scanned between 35350 cm^{-1} and 35500 cm^{-1} in steps of 0.1 cm^{-1}. Each data point was created by first measuring the fluorescence signal at 313 nm generated by OH and measured on the photo-multiplier tube, and then the fluorescence signal was integrated over a predefined time period, typically 4-5 μs. A typical fluorescence signal is illustrated with a red line in the upper inset of Figure 3.8. The integration limits of the signal are depicted with grey broken lines. Each data point on the wavelength scan is an average of 20 shots of fluorescence measurement. The results of the laser wavelength scan are illustrated in Figure 3.8. The black dots represent the measured data, while the red line depicts data simulated with the LIFBASE software [173]. The wavenumbers of the measured spectrum are corrected by 5 cm^{-1} with respect to the simulation, accounting for the offset in the calibration of the laser. Four distinct peaks can be distinguished, resulting from excitations from different initial states in the

electronic ground state to final states of the first excited electronic state. The $Q_2(1)$, $Q_{21}(1)$ and $P_1(1)$ are transitions arising from the rotational ground state $J'' = 3/2$ of the electronic ground state while the transitions $P_1(2)$, $Q_1(2)$ and $Q_{21}(2)$ are arising from the first rationally excited state $J'' = 5/2$ of the electronic ground state. All of the transitions were resolved except the $Q_1(1)$ and $Q_{21}(1)$ and $Q_1(2)$ and $Q_{21}(2)$. From the recorded spectra, we can infer the ratio of the populations in the rotational ground state relative to the first excited rotational state by numerically calculating the total area under the peaks arising from populations in the rotational ground state and dividing them by the total area under the peaks arising from populations in the first excited state. Relative populations in the rotational ground state increase with decreasing voltage of the discharge pulse with the highest population ratio of ~92% at -500 V of discharge voltage applied, at the expense of lower OH yield at lower discharge voltage. The spectrum in Figure 3.8 was recorded with $t_{\text{delay}} = 130$ μs discharge pulse delay and $t_{\text{duration}} = 80$ μs discharge pulse duration. The measured ratios of rotational state populations in the rotational ground state as a function of discharge voltage are shown in the lower inset of Figure 3.8.

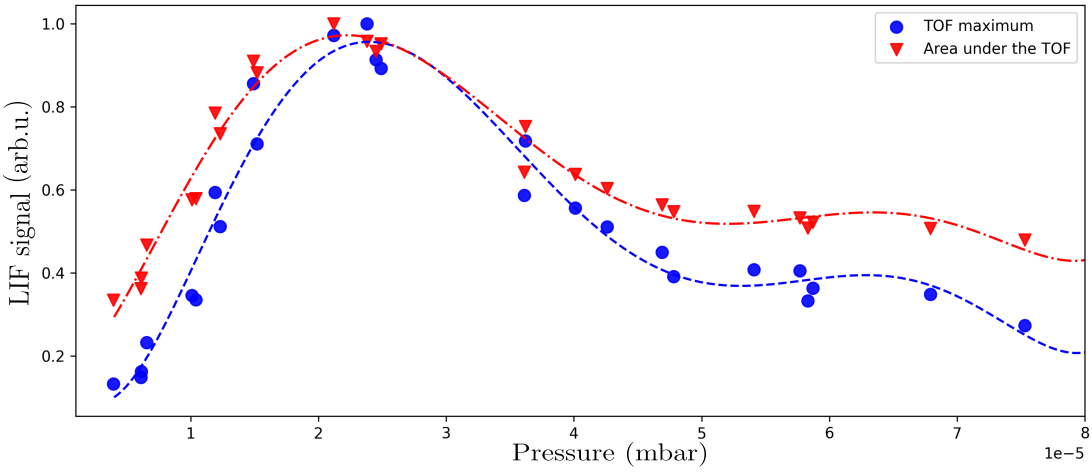

Figure 3.9: Normalized OH yield generated by the NPV as a function of the recorded pressure inside the vacuum chamber. OH yield was extracted in two ways: from each time-of-flight profile a relative total number of radicals was extracted by integrating the area under the profile (red triangles) and a relative maximum peak density of radicals was extracted by finding the maximum of the time-of-flight profile (blue dots). The fit through the data is shown to guide the eye.

The operation of the NPV valve is controlled by two potentiometers. One potentiometer adjusts the voltage, which determines the output current to the spring mechanism, and the second potentiometer determines the duration of the current pulse. An optimization which maximizes the OH yield with respect to these two parameters was performed. For each setting of the NPV current pulse duration and current pulse amplitude, the pressure in the vacuum chamber was collected and time-of-flight profile was recorded. The pressure inside the vacuum chamber when the valve is running at 10 Hz repetition rate was in the range $1 \cdot 10^{-5}$-$1 \cdot 10^{-4}$ mbar. With increasing current pulse duration and amplitude through the spring mechanism, the poppet is pulled further away from the nozzle of the NPV, and the nozzle stays open for a longer period of time. For that reason, the recorded pressure inside the vacuum chamber is increasing with the increasing current pulse duration and amplitude. From each time-of-flight profile, a relative number of radicals was extracted by integrating the area under the profile and a relative maximum peak density of radicals was extracted by finding the maximum of the time-of-flight profile. The normalized data points are plotted as a function of pressure in Figure 3.8. From the figure, it can be seen that the maximum radical yield is achieved at the recorded pressure in the vacuum chamber of $\sim 2 \cdot 10^{-5}$ mbar. One possible explanation is the following: if the nozzle is opened for a very short amount of time there is not enough time to fill the nozzle with the gas completely and the production of radicals in the discharge is inefficient. As the nozzle is opened for longer periods of time, the pressure inside the nozzle increases and with it the radical production. If the pressure inside the nozzle further increases the electron drift velocity goes down and with it also the production of radicals.

3.4 Time-of-flight mass spectrometer

3.4.1 Time-resolved detection with MCP detectors

Within the scope of this thesis the detection of ions and metastable atoms was conducted with the use of a micro-channel plate (MCP) detector. The MCP

detector described here consists of multiple channels with 10 μm pore size, 12° bias angle, 25 mm in diameter of the active area and 60:1 length-to-diameter ratio. MCPs are typically fabricated from lead glass in such a way that the production of the secondary electrons is maximized. The channel walls are semiconducting and as such allow charge replenishment from an external voltage source. By applying an electric field across the MCP, each channel acts as a particle multiplier. A photon or a particle that enters the channel pore collides with the channel walls. The collision starts an avalanche of electrons that propagates through the channel and in that way the signal from a single particle is amplified into an electric signal by several orders of magnitude. The electrons exit on the opposite side of the channel where they can be detected. The MCP detector used throughout experiments described in the thesis consists of two MCPs assembled in Chevron configuration. In this configuration, the channels are rotated by 180° to each other. In this way electrons that exit the first plate start a cascade in the second plate. Typical resistance across the MCP is on the order of $\sim 10^9$ Ω. MCPs assembled in this configuration typically allow for electron multiplication by a factor in the range $10^4 - 10^7$. A schematic of a single micro-channel plate is depicted in Figure 3.10 a) and typical electron multiplication factor of a one-stage, a two-stage and a three-stage MCP is depicted in Figure 3.10 b).

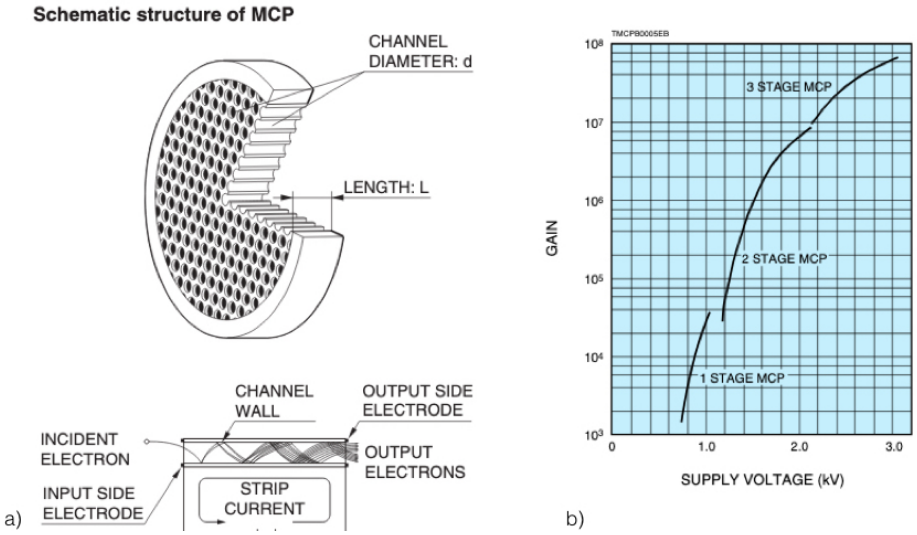

Figure 3.10: MCP structure and gain characteristics. a) A schematic illustration of the MCP plate and operating principle. b) Gain characteristics of a typical MCP detector shown for the different number of stages. Figures reproduced from [174]

.

The model of the MCP detector used in the experiments described in this thesis is Photonis APD 2 MA, PS31373. The external electrical connections to the MCP detector are arranged in a way that the MCP detector is set up for detection of positive ions. The electrical schematic scheme is depicted in Figure 3.11 a). A negative high voltage difference, up to -2400 V, is applied across the two microchannel plates and a voltage difference typically ~ -100 V is applied between the end of the second microchannel plate and the anode. The voltage difference across the microchannel plates determines the electron multiplication across the microchannel plates and voltage difference between second microchannel plate and anode ensures that the created electrical signal is transported from the microchannel plates across to the anode. The signal from the anode is then coupled to the 1:10 amplification preamplifier and from there the signal is directed to the digital-signal acquisition system. The preamplifier serves two purposes: first, it amplifies the signal generated on the anode and second, in the case of malfunction of the MCP detector, the preamplifier serves as a safety element for the data acquisition system.

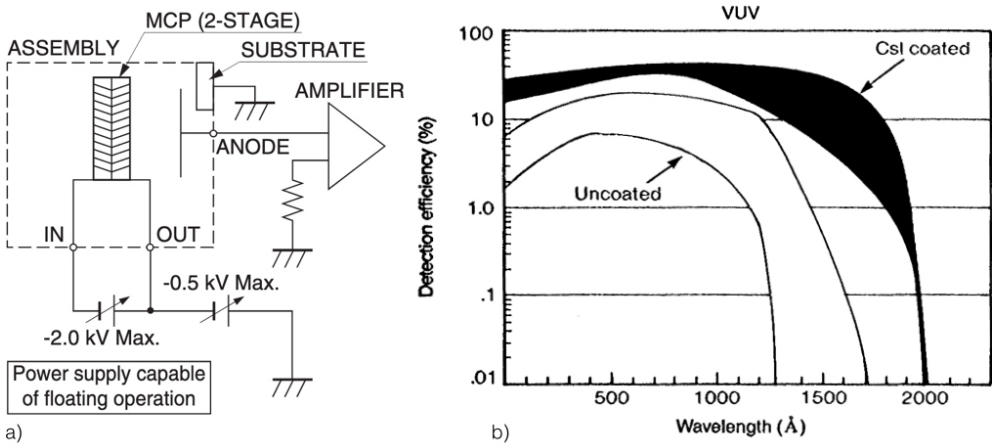

Figure 3.11: Schematic of the electric connections for the measurement of positive ions on the MCP (a) and the detection efficiency as a function photon wavelength of the MCP detector used in the experiments described throughout this thesis (b). [174]

The MCP detectors are sensitive to various high energy particles, from high-energy electrons to high energy positive ions, UV photons, X-rays and neutrons. Table 3.2 outlines sensitivity of a typical MCP detector to various high-energy particles. The detection efficiency as a function of the photon wavelength of the MCP detector used in the experiments described throughout this thesis is shown in Figure 3.11 b).

Table 3.2: Detection efficiency of a typical MCP detector [174]

Types of radiation	Energy or Wavelength	Detection efficiency (%)
Electron	0.2 keV - 2 keV	50 - 85
	2 keV - 50 keV	10-60
Ion (H^+, He^+,AR^+)	0.5 keV - 2 keV	5 - 58
	2 keV - 50 keV	60 - 85
	50 keV-200 keV	4 - 60
UV	300 Å - 1100 Å	5 - 15
	1100 Å - 1500 Å	1 -5
Soft X-ray	2 Å - 50 Å	5 - 15
Hard X-ray	0.12 Å - 0.2 Å	<1
High energy particles	1 GeV - 10 GeV	<95
Neutron	2.5 MeV - 14 MeV	0.14 - 0.64

Time-of-flight measurements of metastable particles impinging onto the MCP detector surface have been conducted. The mechanism behind the detection of

metastable particles on the MCP detector is twofold: in the first mechanism, a metastable particle after a collision with the microchannel walls creates an electron avalanche only if the internal excess energy of the particle is higher than the photoelectric work function of the MCP material. In the second mechanism, when a metastable particle enters a microchannel pore, the electric field inside the pore is very high and there is a probability that the particle gets ionized and accelerated by the electric field towards the channel walls. Time-of-flight experiments have been conducted in the following way: A beam of metastable species was produced by applying a high-voltage discharge pulse across discharge electrodes of the NPV. The beam was then skimmed with a 2 mm diameter skimmer and coupled into the 4 mm diameter decelerator tube. The decelerator is kept switched off at this time. After a field-free expansion, metastable particles were detected on the MCP detector. The total flight distance of the beam is 1069 mm. Measurements were conducted for H_2, Kr, Xe and Kr + 10% H_2 beams. Results of the time-of-flight experiments are shown in Figure 3.12. When an incoming beam of metastable particles impinges onto the MCP detector, each metastable particle starts a production of secondary electrons. For that reason, the whole time-of-flight profile of the beam can be recorded in a single shot. Each time-of-flight profile is shown in Figure 3.12 is an average of 900 shots with a 10 point running average over the data points. In the figure, the time-of-flight profile for H_2^* (and H^* produced in the discharge) is shown in green, Kr^* in blue and Xe^* in red. In the inset, the time-of-flight profiles of the pure Kr^* beam and beam consisting of the mixture of Kr^* + 10 % H_2^* are shown.

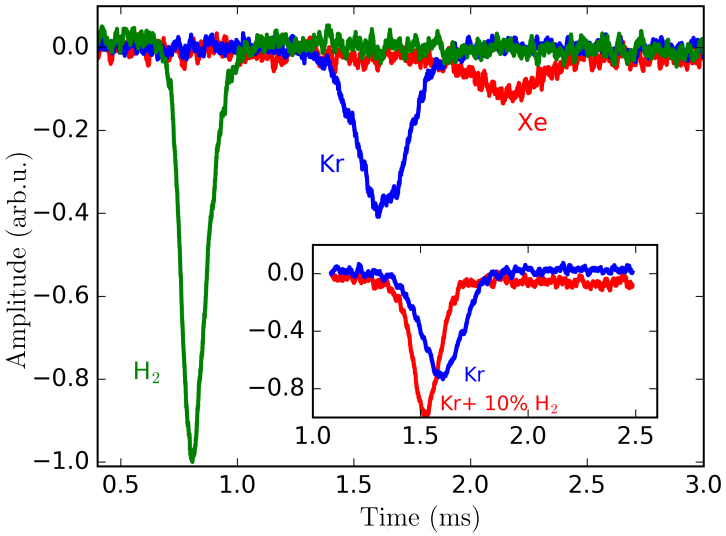

Figure 3.12: Time-of-flight profiles of different metastable species detected on the MCP detector. The time-of-flight profile for H_2^* is shown in green, Kr^* in blue and Xe^* in red. In the inset, the time-of-flight profiles of the pure Kr^* beam and beam consisting of the mixture of Kr^* + 10 % H_2^* are shown.

3.4.2 Design of the time-of-flight mass spectrometer

In order to be efficiently detected on the MCP detector, ions need to have kinetic energies on the order few keV. After the deceleration process and REMPI ionization, the generated ions have much lower kinetic energies than is necessary for successful detection. For that reason, a time-of-flight mass spectrometer (TOF-MS) [175, 176, 177, 178, 179] based on the design of Wiley and McLaren [149] was designed and constructed. A schematic representation of the TOF-MS is shown in Figure 3.13. The TOF-MS consists of three regions. In the first region, atoms or molecules are ionized. 200 ns - 500 ns after ionization a voltage difference $\Delta U_1 = U_0 - U_1$ is applied between the repeller and extractor electrode and ions are accelerated in the electric field towards the extractor electrode. Ions which are created further away from the extractor electrode will be accelerated in this region to higher velocities since they experience a higher electric potential, while ions which are created closer to the extractor will be accelerated to lower velocities since they experience lower electric potential. In this way, a spread in time in which ions arrive at the detector is reduced and the resolution of the device is increased. Once ions reach the extractor electrode they enter a region of space

where they are further accelerated in the electric field created by a voltage difference $\Delta U_2 = U_1$ applied between the extractor electrode and a third grounded electrode. Upon exiting the acceleration region, ions enter a field-free region of space in which they freely propagate towards the detector. Since all ions that are created at the same distance from the extractor electrode have the same kinetic energy, ions with different mass-to-charge ratios will have different final velocities, and in this way, ions can be separated according to their mass-to-charge ratio. The electric potential as a function of distance is shown in the bottom figure.

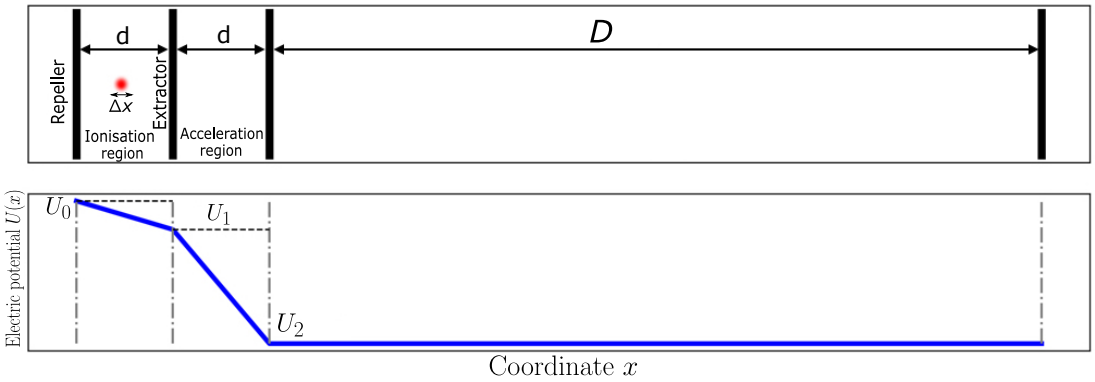

Figure 3.13: Principle of operation of the Wiley-McLarey type TOF-MS. A schematic of the TOF-MS is shown in the upper panel. A voltage difference of $\Delta U_1 = U_0 - U_1$ is applied between the repeller and the extractor electrode and ions are accelerated in the electric field towards the extractor electrode. The ions are further accelerated in an electric field created by a voltage difference $\Delta U_2 = U_1 - U_2$ applied between the extractor electrode and a grounded electrode after which the ions enter a field-free region of space in which they freely fly towards the detector. The electric potential as a function of x coordinate is shown in the bottom panel.

Assuming that an ion with mass m and a charge ze is created in the centre of the ionization region and that the electric potential difference between the centre of the ionization region and the last electrode is ΔU, the potential energy of the ion in the electric field is $E_p = ze\Delta U$, where z is the charge number and e is the charge of electron. At the start of the field-free expansion all of the potential energy of the ions is converted into kinetic energy:

$$ez\Delta U = \frac{1}{2}mv^2. \tag{3.4}$$

The time necessary for the ion to travel the field free region is:

$$t = \frac{D}{\sqrt{2\Delta U}}\sqrt{\frac{m}{ze}}. \tag{3.5}$$

Here, m is the ion mass and D is the distance from the ground electrode to the MCP detector. From the time-of-flight mass-to-charge ratio can be calculated:

$$m/z = \frac{2e\Delta U}{D^2}t^2. \tag{3.6}$$

In other words, given a time-dependent spectrum of the ions measured on the detector, their corresponding mass-to-charge ratios can be determined. The resolution of the linear TOF mass spectrometer is given by:

$$R = \frac{m}{\Delta m} = \frac{t}{2\Delta t}. \tag{3.7}$$

Assuming a more general case in which particles are ionized at a position x inside the ionization region and an electric potential difference $\Delta U_1 = U_0 - U_1$ is applied between the first and second electrode of the TOF-MS and an electric potential difference $\Delta U_2 = U_1$ is applied between the second and third electrode of the TOF-MS, the total time-of-flight of the ion to the detector is $t = t_1 + t_2 + t_3$ where t_1 is the time necessary for the ion to traverse the ionization region, t_2 is the time necessary to traverse the acceleration region and t_3 the time necessary to traverse the field-free region, where t_1, t_2 and t_3 are given by:

$$t_1 = \frac{\sqrt{2a_1(d-x) + v_0^2} - v_0}{a_1}, \tag{3.8}$$

$$t_2 = \frac{\sqrt{2a_1(d-x) + 2a_2d + v_0^2} - \sqrt{2a_1(d-x) + v_0^2}}{a_2}, \tag{3.9}$$

$$t_3 = \frac{D}{\sqrt{2a_1(d-x) + 2a_2d + v_0^2}}, \tag{3.10}$$

and d is the distance between the repeller and the extractor electrode and also the distance between the extractor and the ground electrode (in our design these two distances are the same), v_0 is the initial velocity of the ions,

$$a_1 = \frac{ze}{m}\frac{(U_0 - U_1)}{d} \tag{3.11}$$

is the acceleration of the ion in the ionization region and

$$a_2 = \frac{ze}{m}\frac{U_1}{d} \tag{3.12}$$

is the acceleration of the ion in the acceleration region. With the use of equations 3.8-3.12, the time-of-flight spectrum was simulated for species of particles typically found air. Particles are created inside an ionization region with spatial spread $\Delta x = 500$ μm, mean forward velocity of $v_0 = 450$ m/s and a longitudinal velocity spread of $\Delta v_0 = 90$ m/s. The electric potentials applied to each electrode is $U_1 = 5000$ V, $U_2 = 4300$ V and $U_3 = 0$ V, and TOF-MS distances $d = 12$ mm and $D = 412$ mm. Results of the time-of-flight simulations are shown in Figure 3.14. The upper trace shows the time-of-flight spectrum while the bottom trace shows time-of-flight spectrum converted to a mass-over-charge spectrum. Masses-to-charge ratios belonging to different species can clearly be resolved.

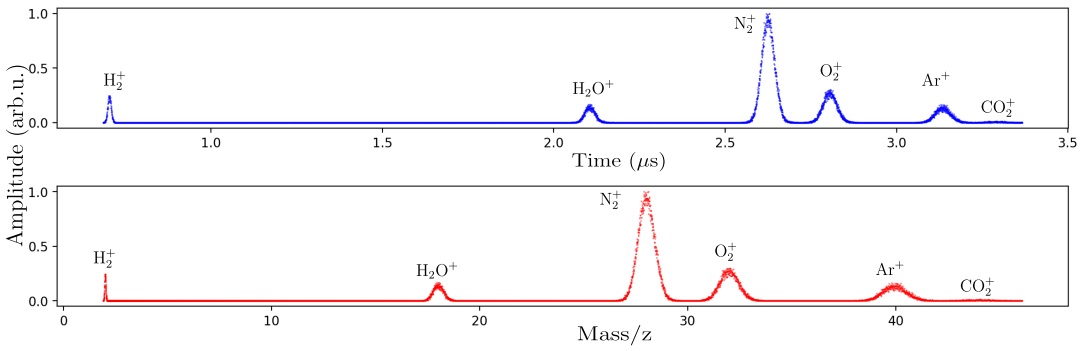

Figure 3.14: Simulated time-of-flight spectrum. Particles are created inside an ionization region with spatial spread $\Delta x = 500$ μm, mean forward velocity of 450 m/s and a longitudinal velocity spread of 90 m/s. The electric potential applied to each electrode is $U_1 = 5000$ V, $U_2 = 4300$ V and $U_3 = 0$ V, and TOF-MS distances $d = 12$ mm and $D = 412$ mm. The upper trace shows the time-of-flight spectrum while the bottom trace shows the time-of-flight spectrum converted to a mass-over-charge spectrum. Masses belonging to different species can clearly be resolved.

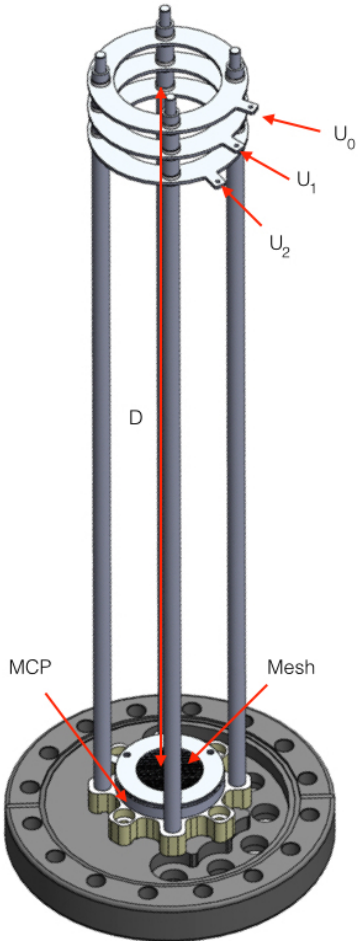

Figure 3.15: A schematic depiction of the design of the TOF-MS. The TOF-MS consists of a PEEK base mounted onto a CF-100 flange, an MCP detector with a mesh, and three high-voltage electrodes mounted on stainless steel rods. Electrodes are insulated from the rods by Macor ceramic elements.

The design of the TOF-MS is shown in Figure 3.15. The TOF-MS was designed as a standalone unit mounted onto a CF-100 flange. On the flange, a 60 mm diameter polyether ether ketone (PEEK) base was mounted and on the base, the MCP detector was placed. In front of the MCP detector, a grounded mesh was installed such that a field-free region is created between the mesh and the ground electrode of the TOF-MS. Three disc electrodes with a 60 mm diameter were mounted on four stainless steel rods which were anchored into the PEEK base. The distance between the neighbouring electrodes was d = 12 mm and the distance between the ground electrode and the MCP detector was D = 412 mm. Over each electrode, a stainless steel mesh (100 μm pore size) was spanned. This ensures a uniform electric field in the region between two electrodes. Each elec-

trode was insulated from the rods by a Macor ceramic element. Voltages necessary for the operation of the MCP detector were applied through ultra-high vacuum and high-voltage compatible feedthroughs located on the flange. $U_0 = 5000$ V, $U_1 = 4300$ V and $U_2 = 0$ V were voltages typically applied to the TOF-MS electrodes. In order to minimize the stray electric field inside the field-free region of the TOF-MS setup, the voltages U_0, U_1 and U_2 were supplied through the feedthroughs which were perpendicular to the TOF-MS extraction axis. The design of the TOF-MS is depicted in Figure 3.15. The TOF-MS is placed on the deceleration axis. Atoms or molecules exiting the decelerator entered the region between repeller and extractor electrode of the TOF-MS where they were ionized by the REMPI laser. The distance between the decelerator and ionization region was 36 mm. 200 ns - 500 ns after the ionization, voltages U_0, U_1, U_2 were applied to the three electrodes of the TOF-MS, and ions were accelerated in the electric field towards the MCP detector. The signal from the MCP detector was output to the data-acquisition system where it was recorded. The experimental setup including the TOF-MS setup and REMPI laser is illustrated in Figure 3.16. Details on the decelerator design are given in the next chapter.

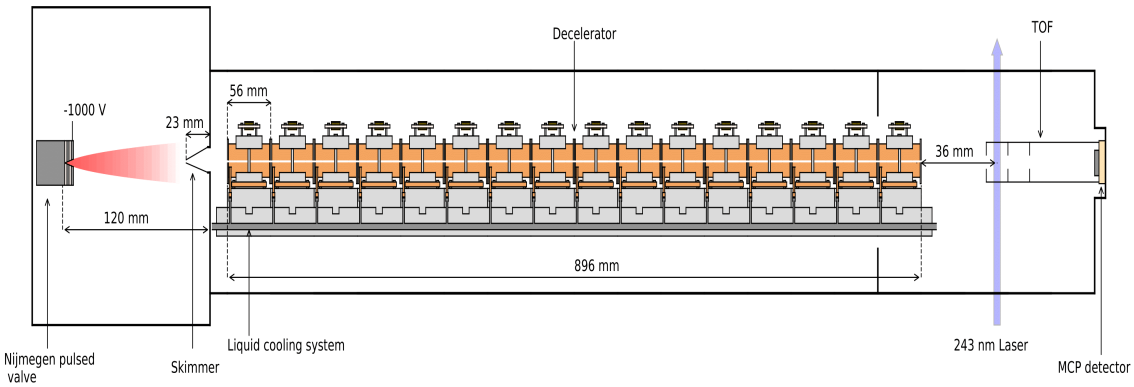

Figure 3.16: Experimental setup for the TOF-MS experiments. The experimental setup consists of NPV, skimmer, travelling-wave Zeeman decelerator, REMPI ionization laser and a TOF-MS setup. The TOF-MS is placed in parallel to the deceleration axis such that metastable atoms or molecules exiting the decelerator can be directly detected on the MCP.

The time-of-flight mass spectrum was calibrated by collecting flight times of H^+ ions generated by the 2+1 photon ionization in the detection region and accelerated by varying electric potential between 0-1100 V on the first two electrodes. The data has been fitted to the formula $V = \frac{k}{(t-t_0)^2}$, where k and t_0 are fitting parameters. A calibrated time-of-flight mass spectrum is shown in Figure 3.17 a). Figure 3.17 b) shows the calibration curve of the TOF-MS. Recorded data are shown in red and the fitting function in black. The wavelength dependence of the measured 2+1 REMPI resonance on the hydrogen atom is shown in Figure 3.17 c). The vertical red line corresponds to the literature value of the 1S-2S transition in hydrogen [180], corresponding to $4 \times 20564.73\ \mathrm{cm}^{-1} = 82258.95\ \mathrm{cm}^{-1}$. Linewidth of the transition of $\approx 1\ \mathrm{cm}^{-1}$ is due to the natural linewdith of the dye laser.

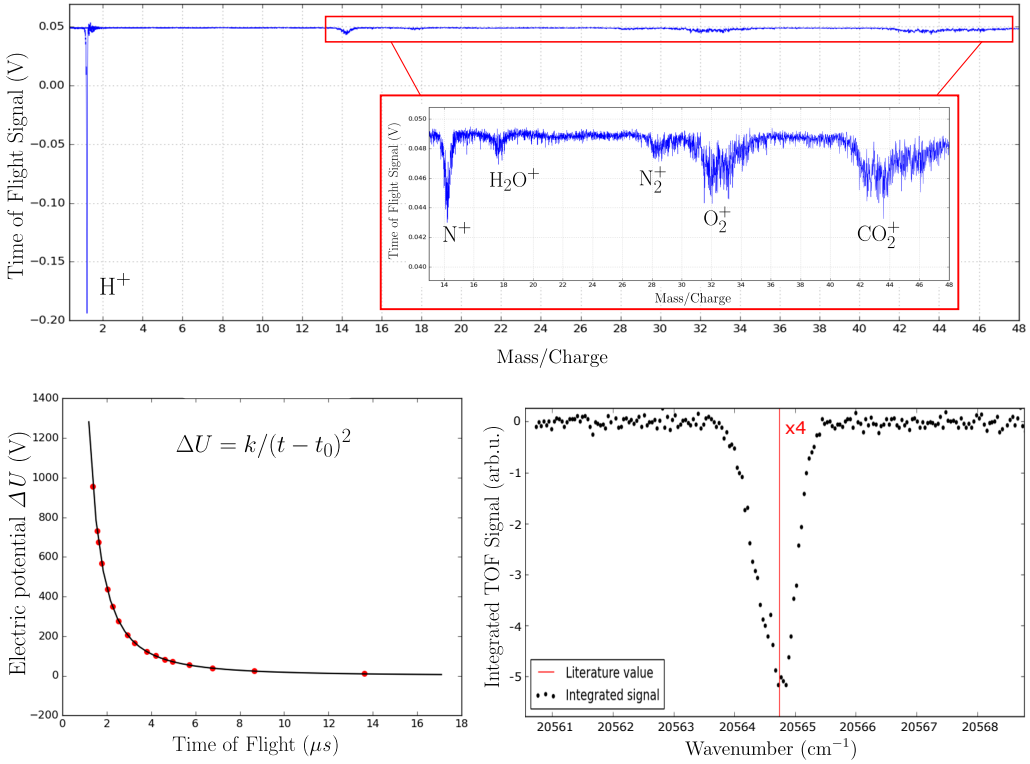

Figure 3.17: Calibration of the Time-of-flight mass spectrum. a) Calibrated time-of-flight mass spectrum. b) Calibration curve of the TOF-MS. c) Wavelength dependence of the measured 2+1 REMPI resonance on the hydrogen atom.

One of the biggest drawbacks of the first TOF analysers was the low mass resolution. The mass resolution of the TOF analyser depends on many factors

among which are, e.g., the size of the ionization region, the duration of the ionization pulse, the kinetic energy spread of the ions and the physical limitation of the detection systems. Additionally, the resolution of the TOF-MS depends on the voltages that are applied to the TOF-MS electrodes. In the experimental realization of time-of-flight analysers it is desirable to have maximum mass resolution. Assuming that the voltages applied to the TOF-MS electrodes are U_0, $U_1 = \beta U_0$ and $U_2 = 0$ V it is of interest at which value of the parameter β does the TOF-MS achieve the highest resolution. The accelerations that a single ion experiences in two regions can be written as :

$$a_1 = \frac{ze}{m}\frac{(1-\beta)U_0}{d}, \tag{3.13}$$

$$a_2 = \frac{ze}{m}\frac{\beta U_0}{d}. \tag{3.14}$$

In the experiments $U_0 = 5$ kV. The total time-of-flight for the ion created in the centre of the ionization region is then given by:

$$t(d/2,\beta) = \frac{D}{\sqrt{a_1 d + 2a_2 d + v_0^2}} + \frac{\sqrt{a_1 d + v_0^2} - v_0}{a_1} + \frac{\sqrt{a_1 d + 2a_2 d + v_0^2} - \sqrt{a_1 d + v_0^2}}{a_2}, \tag{3.15}$$

where $t(x,\beta)$ is the total flight time of the ion created at the position x with the electric potential difference applied to extractor electrode $U_1 = \beta U_2$. If the ion cloud has the size Δx, the total time-of-flights for the particles located at the positions $d/2 - \Delta x/2$ and $d/2 + \Delta x/2$ are given by:

$$t(d/2-\Delta x/2,\beta) = \frac{D}{\sqrt{a_1(d+\Delta \mathrm{x}) + 2a_2 d + v_0^2}} + \frac{\sqrt{a_1(d+\Delta \mathrm{x}) + v_0^2} - v_0}{a_1} + \\ + \frac{\sqrt{a_1(d+\Delta \mathrm{x}) + 2a_2 d + v_0^2} - \sqrt{a_1(d+\Delta \mathrm{x}) + v_0^2}}{a_2}, \tag{3.16}$$

$$t(d/2+\Delta x/2,\beta) = \frac{D}{\sqrt{a_1(d-\Delta \mathrm{x}) + 2a_2 d + v_0^2}} + \frac{\sqrt{a_1(d-\Delta \mathrm{x}) + v_0^2} - v_0}{a_1} + \\ + \frac{\sqrt{a_1(d-\Delta \mathrm{x}) + 2a_2 d + v_0^2} - \sqrt{a_1(d-\Delta \mathrm{x}) + v_0^2}}{a_2}. \tag{3.17}$$

The resolution of the TOF-MS is maximal when:

$$\frac{dR}{d\beta} = \frac{d}{d\beta} \frac{t(d/2, \beta)}{2\Big(t(d/2 - \Delta x/2, \beta) - t(d/2 + \Delta x/2, \beta)\Big)} = 0 \tag{3.18}$$

When $t(d/2 - \Delta x/2, \beta) - t(d/2 + \Delta x/2, \beta) \to 0$ the two particles are arriving at the same time to the detector and the resolution $R \to \infty$. This is only valid for the three-particle system, and in the realistic system resolution never goes to infinity. Equation 3.17 was numerically solved and parameter β for which the resolution of the TOF-MS is maximal was found. The results were confirmed with the help of the numerical trajectory calculations. In the simulation, a cloud consisting of 20000 atomic hydrogen ions with a spatial distribution with a full width at half maximum (FWHM) of $\Delta x_{\mathrm{FWHM}} = 100$ μm was created at $t = 0$ and propagated through the TOF-MS to the detector. Mean arrival of the cloud t_{mean} and a FWHM of the distribution of the arrival times Δt_{FWHM} were extracted from the simulation and resolution $R = t_{\mathrm{mean}}/2\Delta t_{\mathrm{FWHM}}$ was calculated. Calculations were repeated for values of β in range β = 0-1. The MCP detector used in our experiments has a time resolution of 250 ps which was taken into account when calculations of the TOF-MS were performed. Results of the calculations are shown in Figure 3.18. Figure 3.18 a) shows a time-of-flight distribution of hydrogen ions arriving at the detector from which t_{mean} and Δt_{FWHM} were extracted. In Figure 3.18 b), the resolution of the TOF-MS as a function of the size of the initial ion cloud Δx_{FWHM} is illustrated. The resolution increases with decreasing size of the ionization region until it starts to saturate at around $\Delta x_{\mathrm{FWHM}} \approx 700$ μm. The saturation effect comes due to the fact that the MCP had finite time resolution. Figure 3.18 c) shows resolution of the TOF-MS as a function of the parameter β. The thick red line depicts the resolution of the TOF-MS as a function of the parameter β with the time resolution of the MCP taken into account while the dashed red line depicts the same resolution but without the time resolution of the MCP taken into account. The dashed blue line is a result of the numerical calculation of the parameter β which maximizes the resolution from equation 3.18. The maximum resolution $R \approx 1800$ is achieved

for β_{max} ≈0.86. The resolution for the hydrogen atoms is again saturated around β_{max} limited by the time resolution of the MCP. The grey line represents Δt_{FWHM} as a function of β. The horizontal grey line shows the limiting time resolution of the MCP.

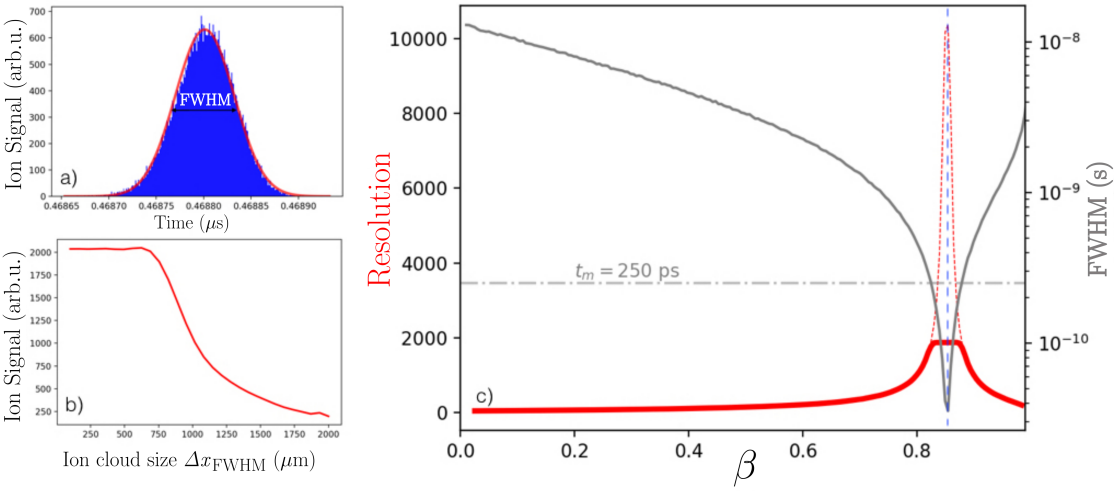

Figure 3.18: Optimization of the resolution of the TOF-MS. a) An example of a simulated time-of-flight distribution of hydrogen ions arriving at the detector from which t_{mean} and Δt_{FWHM} are extracted. b) Resolution of the TOF-MS as a function of the size of the initial ion cloud Δx_{FWHM}. c) Resolution of the TOF-MS as a function of the parameter β with the time resolution of the MCP taken into account (red line) and resolution without the time resolution of the MCP taken into the account (red dashed line). The grey line illustrates Δt_{FWHM} as a function of β and the horizontal grey line shows the limiting time resolution of the MCP. The maximum resolution $R \approx 1800$ is achieved for β_{max} ≈0.86.

3.5 Conclusions

For successful travelling-wave Zeeman deceleration experiments many, different aspects of the experimental procedures have to come together in a straightforward way. In this chapter, we described some of the necessary experimental procedures excluding the details on the design of the decelerator itself, which will be given in the next chapter. Details on the production of the laser radiation necessary for the LIF detection of OH and 2+1 REMPI detection of hydrogen ions were given. A short discussion on supersonic beams was presented, and a brief description of the Nijmegen pulsed valve and a pinhole discharge mechanism was introduced. The

most important characteristics of the properties of the radical beams generated by the NPV have been described. For more details on the NPV itself and properties of the beams generated by the NPV, the reader is referred to [1, 140, 139]. Finally, the description of the design of the TOF-MS system was given.

Chapter 4

A travelling-wave Zeeman decelerator

4.1 Introduction

To the best of our knowledge, there have been three different implementations of a travelling-wave Zeeman decelerator so far. The first implementation was by Trimiche et al.[106] in 2011. They presented the trapping of a supersonic beam of metastable argon inside a travelling magnetic wave at selected, constant velocities. The decelerator was based on a geometry consisting of two sets of planar helical coils. In the same year, Lavert-Ofir et al. [89] demonstrated deceleration of metastable neon from an initial velocity of 429 m/s down to 53.8 m/s with a two orders of magnitude improved phase-space volume compared to previous works. In their case, a travelling three-dimensional magnetic confinement was obtained by switching a series of spatially overlapping quadrupole traps. In 2018., McArd et al.[107] demonstrated an improved version of a travelling-wave decelerator based on the design of Trimiche et al., by decelerating metastable argon from 373 m/s to 342 m/s.

Here, a novel method for the production of the travelling-wave Zeeman deceleration technique is presented. Implementation of the method in a real-life decelerator design is described together with the descriptions of the module design

and the design of the experimental setup which was used for the deceleration experiments of the OH radical. Details on the accompanying software for control and monitoring of the decelerator operation is illustrated. Accompanying Monte-Carlo numerical trajectory simulations and numerical calculations of the magnetic fields are described in detail. Finally, the evolutionary algorithm for optimization of initial parameters of the molecular beam together with respective results is discussed.

4.2 Principles of operation of the travelling-wave Zeeman decelerator

4.2.1 Mathematical description of our implementation of the travelling wave Zeeman decelerator

In this section, mathematical description of the production of the travelling magnetic wave is given. Consider a single right-hand oriented current-carrying helix. The magnetic field inside a helix can be calculated by applying the Biot-Savart law:

$$\mathbf{B}(\mathbf{r}) = \frac{\mu_0}{4\pi}\int_C \frac{Id\mathbf{l}\times\mathbf{r}'}{|r'|^3}. \tag{4.1}$$

Parameterizing the right-hand helix in cylindrical coordinates (see Figure 4.1):

$$\mathbf{l}(\theta) = (R\cos\theta,\ R\sin\theta,\ \frac{\lambda\theta}{2\pi}), \tag{4.2}$$

and substituting it into the Biot-Savart law gives the expressions for the components of the magnetic field inside a single helix as:

$$B_{\mathrm{x}} = \frac{\mu_0 I}{4\pi}\int \frac{\lambda R\sin\theta + R\cos\theta(2\pi z-\theta\lambda) - \lambda y}{2\pi\left((x-R\cos\theta)^2+(y-R\sin\theta)^2+\left(z-\frac{\theta\lambda}{2\pi}\right)^2\right)^{3/2}}d\theta, \tag{4.3}$$

$$B_{\mathrm{y}} = \frac{\mu_0 I}{4\pi}\int \frac{-\lambda R\cos\theta + R\sin\theta(2\pi z-\theta\lambda) + \lambda x}{2\pi\left((x-R\cos\theta)^2+(y-R\sin\theta)^2+\left(z-\frac{\theta\lambda}{2\pi}\right)^2\right)^{3/2}}d\theta, \tag{4.4}$$

$$B_{\mathrm{z}} = \frac{\mu_0 I}{4\pi}\int \frac{R(R-x\cos\theta-y\sin\theta)}{\left((x-R\cos\theta)^2+(y-R\sin\theta)^2+\left(z-\frac{\theta\lambda}{2\pi}\right)^2\right)^{3/2}}d\theta, \tag{4.5}$$

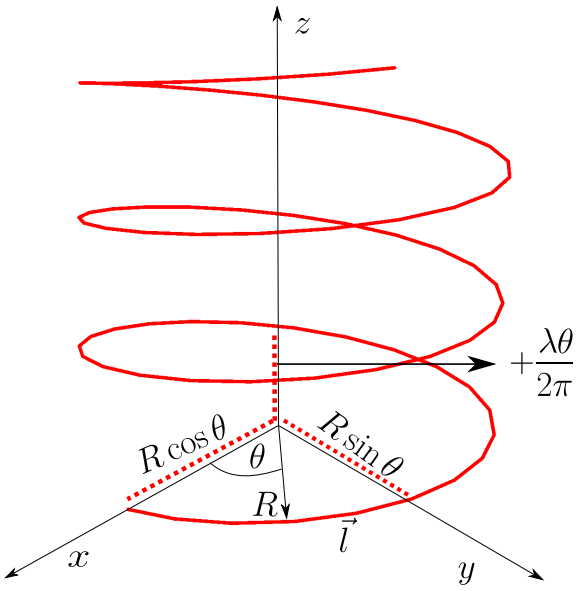

Figure 4.1: Parametrization of a right-hand oriented helix in cylindrical coordinates.

where θ is the parameterized angle in cylindrical coordinates, R is the radius of the helix, λ is the periodicity of the helix and I is the current supplied to the helix. Unfortunately, integrals in 4.3-4.5 cannot be calculated analytically and numerical approach has to be used. Numerical calculations of the full magnetic field are discussed later in the text. From equations 4.3-4.5 on-axis magnetic field components along z axis can be calculated. Taking $x = 0$ and $y = 0$, equations 4.3-4.5 reduce to:

$$B_x = \frac{\mu_0 I}{4\pi} \int \frac{\lambda R \sin\theta + R\cos\theta(2\pi z - \theta\lambda)}{2\pi\left(R^2 + \left(z - \frac{\theta\lambda}{2\pi}\right)^2\right)^{3/2}} d\theta, \tag{4.6}$$

$$B_y = \frac{\mu_0 I}{4\pi} \int \frac{-\lambda R \cos\theta + R\sin\theta(2\pi z - \theta\lambda)}{2\pi\left(R^2 + \left(z - \frac{\theta\lambda}{2\pi}\right)^2\right)^{3/2}} d\theta, \tag{4.7}$$

$$B_z = \frac{\mu_0 I}{4\pi} \int \frac{R^2}{\left(R^2 + \left(z - \frac{\theta\lambda}{2\pi}\right)^2\right)^{3/2}} d\theta. \tag{4.8}$$

With the use of the following integral identities:

$$\int_{-\infty}^{\infty} \frac{\sin\left(\alpha(\xi - \eta)\right)}{(r^2 + \eta^2)^{3/2}} d\eta = \frac{2\alpha}{r} K_1(\alpha r)\sin(\alpha\xi), \tag{4.9}$$

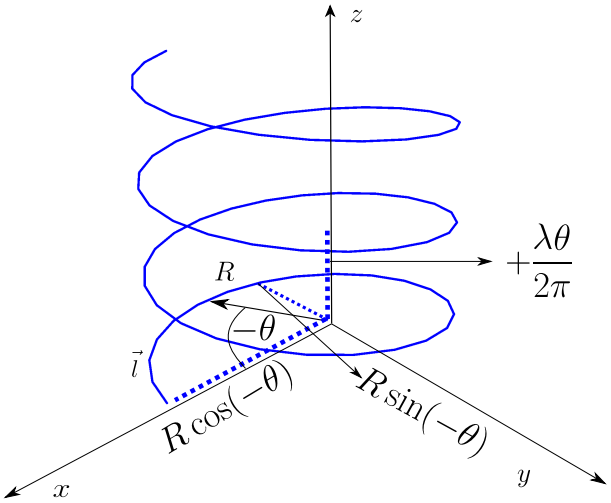

Figure 4.2

$$\int_{-\infty}^{\infty} \frac{\cos\big(\alpha(\xi-\eta)\big)}{(r^2+\eta^2)^{3/2}} d\eta = \frac{2\alpha}{r} K_1(\alpha r)\cos(\alpha\xi), \tag{4.10}$$

$$\int_{-\infty}^{\infty} \frac{\eta\sin\big(\alpha(\xi-\eta)\big)}{(r^2+\eta^2)^{3/2}} d\eta = -2\alpha K_0(\alpha r)\cos(\alpha\xi), \tag{4.11}$$

$$\int_{-\infty}^{\infty} \frac{\eta\cos\big(\alpha(\xi-\eta)\big)}{(r^2+\eta^2)^{3/2}} d\eta = 2\alpha K_0(\alpha r)\sin(\alpha\xi), \tag{4.12}$$

$$\int_{-\infty}^{\infty} \frac{1}{(r^2+\eta^2)^{3/2}} d\eta = \frac{2}{r^2} \tag{4.13}$$

and setting $r = R$, $\alpha = \frac{2\pi}{\lambda}$, $\xi = z$, the on-axis magnetic field components evaluate to:

$$B_x = \frac{\mu_0 I}{\lambda}\Big[K_1(\frac{2\pi R}{\lambda}) + \frac{2\pi R}{\lambda}K_0(\frac{2\pi R}{\lambda})\Big]\sin\left(\frac{2\pi}{\lambda}z\right), \tag{4.14}$$

$$B_y = \frac{\mu_0 I}{\lambda}\Big[K_1(\frac{2\pi R}{\lambda}) + \frac{2\pi R}{\lambda}K_0(\frac{2\pi R}{\lambda})\Big]\cos\left(\frac{2\pi}{\lambda}z\right), \tag{4.15}$$

$$B_z = \frac{\mu_0 I}{\lambda} \tag{4.16}$$

where $K_n(x)$ is the modified Bessel function of the second kind.

In similar fashion, taking into account the parametrization of the left-hand oriented helix (see Figure 4.2), from Biot-Savart law the expressions for the magnetic field inside the left-hand oriented helix can be derived:

$$B_{\mathrm{x}} = -\frac{\mu_0 I}{4\pi}\int \frac{\lambda R\sin\theta + R\cos\theta(2\pi z - \theta\lambda) + \lambda y}{2\pi\left((x - R\cos\theta)^2 + (y + R\sin\theta)^2 + \left(z - \frac{\theta\lambda}{2\pi}\right)^2\right)^{3/2}}d\theta, \tag{4.17}$$

$$B_{\mathrm{y}} = \frac{\mu_0 I}{4\pi}\int \frac{-\lambda R\cos\theta + R\sin\theta(2\pi z - \theta\lambda) + \lambda x}{2\pi\left((x - R\cos\theta)^2 + (y + R\sin\theta)^2 + \left(z - \frac{\theta\lambda}{2\pi}\right)^2\right)^{3/2}}d\theta, \tag{4.18}$$

$$B_{\mathrm{z}} = -\frac{\mu_0 I}{4\pi}\int \frac{R(R - x\cos\theta + y\sin\theta)}{\left((x - R\cos\theta)^2 + (y + R\sin\theta)^2 + \left(z - \frac{\theta\lambda}{2\pi}\right)^2\right)^{3/2}}d\theta, \tag{4.19}$$

Taking $x = 0$ and $y = 0$ reduces to:

$$B_x = -\frac{\mu_0 I}{4\pi}\int \frac{\lambda R\sin\theta + R\cos\theta(2\pi z - \theta\lambda)}{2\pi\left(R^2 + \left(z - \frac{\theta\lambda}{2\pi}\right)^2\right)^{3/2}}d\theta, \tag{4.20}$$

$$B_y = \frac{\mu_0 I}{4\pi}\int \frac{-\lambda R\cos\theta + R\sin\theta(2\pi z - \theta\lambda)}{2\pi\left(R^2 + \left(z - \frac{\theta\lambda}{2\pi}\right)^2\right)^{3/2}}d\theta, \tag{4.21}$$

$$B_z = -\frac{\mu_0 I}{4\pi}\int \frac{R^2}{\left(R^2 + \left(z - \frac{\theta\lambda}{2\pi}\right)^2\right)^{3/2}}d\theta. \tag{4.22}$$

Taking into account the integral identities 4.9-4.13 and setting $r = R$, $\alpha = \frac{2\pi}{\lambda}$, $\xi = z$, the on-axis magnetic field components of the left-hand helix evaluate to:

$$B_x = -\frac{\mu_0 I}{\lambda}\left[K_1(\frac{2\pi R}{\lambda}) + \frac{2\pi R}{\lambda}K_0(\frac{2\pi R}{\lambda})\right]\sin\left(\frac{2\pi}{\lambda}z\right), \tag{4.23}$$

$$B_y = \frac{\mu_0 I}{\lambda}\left[K_1(\frac{2\pi R}{\lambda}) + \frac{2\pi R}{\lambda}K_0(\frac{2\pi R}{\lambda})\right]\cos\left(\frac{2\pi}{\lambda}z\right), \tag{4.24}$$

$$B_z = -\frac{\mu_0 I}{\lambda}. \tag{4.25}$$

In the calculation of magnetic field components the approximation of infinite helix was used.

Next, consider a double helix wire geometry consisting of two helices with a helix periodicity $\lambda = 14$ mm: a right-hand oriented helix and a left-hand oriented helix. If the current $I_{RH}(t)$ and $I_{LH}(t)$ is produced through the right-hand and left-hand helix, respectively, the magnetic field components inside of each helix

on the z axis are given by the following equations:

$$\begin{pmatrix} B^0_{\mathrm{RH,x}} \\ B^0_{\mathrm{RH,y}} \\ B^0_{\mathrm{RH,z}} \end{pmatrix} = \begin{pmatrix} a_{\mathrm{RH}} I_{\mathrm{RH}}(t) \sin(kz) \\ a_{\mathrm{RH}} I_{\mathrm{RH}}(t) \cos(kz) \\ a_{\mathrm{RH,z0}} I_{\mathrm{RH}}(t) \end{pmatrix} \tag{4.26}$$

for the right-handed helix, and by:

$$\begin{pmatrix} B^0_{\mathrm{LH,x}} \\ B^0_{\mathrm{LH,y}} \\ B^0_{\mathrm{LH,z}} \end{pmatrix} = \begin{pmatrix} -a_{\mathrm{LH}} I_{\mathrm{LH}}(t) \sin(kz) \\ a_{\mathrm{LH}} I_{\mathrm{LH}}(t) \cos(kz) \\ a_{\mathrm{LH,z0}} I_{\mathrm{LH}}(t) \end{pmatrix} \tag{4.27}$$

for the left-hand helix, where $k = \frac{2\pi}{\lambda}$. Constant factors a_{RH}, a_{LH}, $a_{\mathrm{RH,z0}}$, $a_{\mathrm{LH,z0}}$ can be read out from 4.14-4.25:

$$a_{\mathrm{RH}} = \frac{\mu_0 I}{\lambda}\Big[K_1(\frac{2\pi R_1}{\lambda}) + \frac{2\pi R_1}{\lambda} K_0(\frac{2\pi R_1}{\lambda})\Big] \tag{4.28}$$

$$a_{\mathrm{LH}} = \frac{\mu_0 I}{\lambda}\Big[K_1(\frac{2\pi R_2}{\lambda}) + \frac{2\pi R_2}{\lambda} K_0(\frac{2\pi R_2}{\lambda})\Big] \tag{4.29}$$

$$a_{\mathrm{RH,z0}} = \frac{\mu_0 I}{\lambda} \tag{4.30}$$

$$a_{\mathrm{LH,z0}} = -\frac{\mu_0 I}{\lambda} \tag{4.31}$$

The two helices with helix periodicity λ are illustrated in Figure 4.3 a), where the right-hand helix is depicted with a thick blue line and the left-hand helix with a thick red line. Right-hand oriented helix has a radius of $R_1 = 2$ mm, and left-hand oriented helix has radius of $R_2 = 2.4$ mm. Numerically calculated components of the magnetic field of both helices, with a constant current of $I =$ 300 A supplied through each helix is shown in Figure 4.3 b), with correspondingly coloured lines. The numerically calculated fields are well described by equations 4.26 and 4.27. This illustrates the on-axis magnetic field of the geometry consisting of one right-handed helix and one left-handed helix.

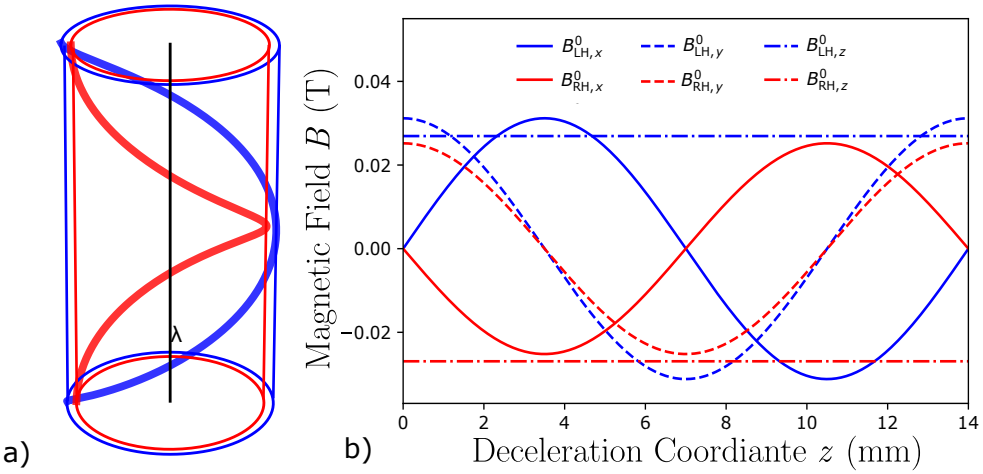

Figure 4.3: The magnetic field of a double-helix coil structure. a) Double-helix structure consisting of one right-hand (blue) and one left-hand (red) helix with periodicity $\lambda = 14$ mm. The radius of the right (left) hand helix is 2.0 mm (2.4 mm). b) Calculated on-axis magnetic field $\mathbf{B}(x = 0, y = 0, z)$ generated by constant current $I = +300$ A. Blue (red) traces correspond to the components of the magnetic field generated in right (left) hand oriented helix.

Let us consider now a geometry consisting of 16 right-hand oriented helices, and on top of it another layer consisting of 16 left-hand oriented helices with an initial starting position of the helices distributed around the circle, with the angular offset between neighbouring helices $\Delta = \pi/8$. The depiction of the wire geometry is given in Figure 4.4. The magnetic field components for the n-th helix, n=0, 1, ..., 15, both in the right-hand oriented and left-hand oriented layer, can be derived by applying rotation symmetry in x-y plane on the magnetic field components expressed by equations 4.26 and 4.27, respectively. The equations for the magnetic fields of the n-th helix are given as:

$$\begin{pmatrix} B^n_{\mathrm{RH,x}} \\ B^n_{\mathrm{RH,y}} \\ B^n_{\mathrm{RH,z}} \end{pmatrix} = R(n\Delta) \cdot \begin{pmatrix} B^0_{\mathrm{RH,x}} \\ B^0_{\mathrm{RH,y}} \\ B^0_{\mathrm{RH,z}} \end{pmatrix} = \begin{pmatrix} a_{\mathrm{RH}} I_{\mathrm{RH}}(t) \sin(kz - n\Delta) \\ a_{\mathrm{RH}} I_{\mathrm{RH}}(t) \cos(kz - n\Delta) \\ a_{\mathrm{RH,z0}} I_{\mathrm{RH}}(t) \end{pmatrix}, \tag{4.32}$$

$$\begin{pmatrix} B^n_{\mathrm{LH,x}} \\ B^n_{\mathrm{LH,y}} \\ B^n_{\mathrm{LH,z}} \end{pmatrix} = R(n\Delta) \cdot \begin{pmatrix} B^0_{\mathrm{LH,x}} \\ B^0_{\mathrm{LH,y}} \\ B^0_{\mathrm{LH,z}} \end{pmatrix} = \begin{pmatrix} -a_{\mathrm{LH}} I_{\mathrm{LH}}(t) \sin\left(kz + n\Delta\right) \\ a_{\mathrm{LH}} I_{\mathrm{LH}}(t) \cos\left(kz + n\Delta\right) \\ a_{\mathrm{LH,z0}} I_{\mathrm{LH}}(t) \end{pmatrix}, \tag{4.33}$$

where $R(\theta)$ is the rotation matrix in x-y plane, by an angle θ:

$$R(\theta) = \begin{pmatrix} \cos\theta & -\sin\theta & 0 \\ \sin\theta & \cos\theta & 0 \\ 0 & 0 & 1 \end{pmatrix}. \tag{4.34}$$

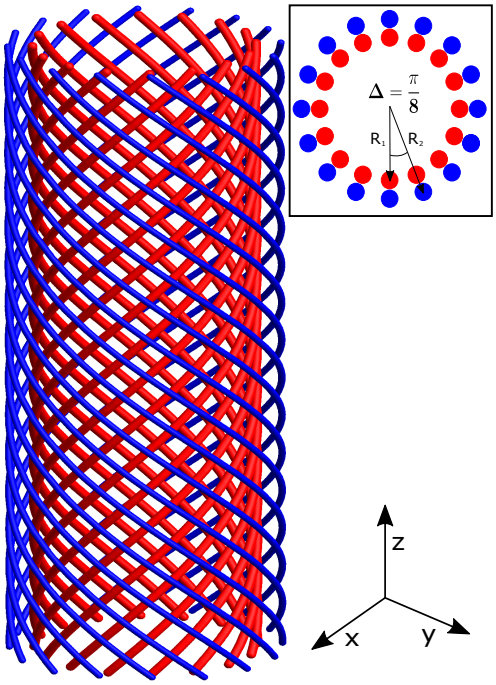

Figure 4.4: Double-layer helix geometry consisting of 16 right-hand oriented helices in the first (blue) layer, and 16 left-hand oriented helices in the second (red) layer. Neighboring helices are offset by $\Delta = \frac{\pi}{8}$ (inset).

The following time dependence of the currents that are supplied to the n-th helix in each layer is assumed:

$$I^{\mathrm{n}}_{\mathrm{RH}}(t) = I_{\mathrm{RH}} \sin(\phi_{\mathrm{RH}}(t) + n\Delta), \tag{4.35}$$

$$I^{\mathrm{n}}_{\mathrm{LH}}(t) = I_{\mathrm{LH}} \sin(\phi_{\mathrm{LH}}(t) + n\Delta), \tag{4.36}$$

where $\phi_{\mathrm{RH,LH}}$ is the time-dependent phase of the current supplied to the right(left)-hand oriented layer, and $I_{\mathrm{RH,LH}}$ is the amplitude of the current supplied to the respective layers. The additional phase offset $n\Delta$ added to the current supplied to the n-th helix in each layer serves as compensation to the geometric offset of the n-th helix. Summing up contributions from all helices in both layers gives the components of the total magnetic field on the axis of the helix geometry:

$$\begin{aligned} B_{\mathrm{x}} = \sum_{n=0}^{15} \big\{ & I_{\mathrm{RH}} a_{\mathrm{RH}} \sin\left(\phi_{\mathrm{RH}}(t) + n\Delta\right) \sin(kz - n\Delta) \\ & - I_{\mathrm{LH}} a_{\mathrm{LH}} \sin\left(\phi_{\mathrm{LH}}(t) + n\Delta\right) \sin(kz + n\Delta) \big\} \end{aligned} \tag{4.37}$$

$$\begin{aligned} B_{\mathrm{y}} = \sum_{n=0}^{15} \big\{ & I_{\mathrm{RH}} a_{\mathrm{RH}} \sin\left(\phi_{\mathrm{RH}}(t) + n\Delta\right) \cos(kz - n\Delta) \\ & + I_{\mathrm{LH}} a_{\mathrm{LH}} \sin\left(\phi_{\mathrm{LH}}(t) + n\Delta\right) \cos(kz + n\Delta) \big\} \end{aligned} \tag{4.38}$$

$$B_{\mathrm{z}} = \sum_{n=0}^{15} \big\{ I_{\mathrm{RH}} a_{\mathrm{RH,z0}} \sin\left(\phi_{\mathrm{RH}}(t) + n\Delta\right) + I_{\mathrm{LH}} a_{\mathrm{LH,z0}} \sin\left(\phi_{\mathrm{LH}}(t) + n\Delta\right) \big\} \tag{4.39}$$

It doesn't follow immediately from the equations 4.37-4.39 that a travelling magnetic wave can be produced. It can be shown that this is indeed the case. Let us look at the contributions of the components of the magnetic field for the right-hand oriented and the left-hand oriented layers separately. Using the following trigonometric relations:

$$\sin(\alpha \pm \beta) = \sin\alpha\cos\beta \pm \cos\alpha\sin\beta, \tag{4.40}$$

$$cos(\alpha \pm \beta) = \cos\alpha\cos\beta \mp \sin\alpha\sin\beta, \tag{4.41}$$

$$2\sin\alpha\sin\beta = \cos(\alpha - \beta) - \cos\left(\alpha + \beta\right), \tag{4.42}$$

$$2\sin\alpha\cos\beta = \sin(\alpha + \beta) + \sin\left(\alpha - \beta\right), \tag{4.43}$$

the total magnetic field components in the right-hand oriented layer can be expressed in the following form:

$$\begin{pmatrix} B_{\mathrm{RH,x}} \\ B_{\mathrm{RH,y}} \\ B_{\mathrm{RH,z}} \end{pmatrix} = \sum_{n=0}^{15} \begin{pmatrix} \frac{1}{2} I_{\mathrm{RH}} a_{\mathrm{RH}} \big[-\cos(kz + \phi_{\mathrm{RH}}(t)) + \cos(kz - \phi_{\mathrm{RH}}(t) - 2n\Delta) \big] \\ \frac{1}{2} I_{\mathrm{RH}} a_{\mathrm{RH}} \big[-\sin(kz - \phi_{\mathrm{RH}}(t) - 2n\Delta) + \sin(kz + \phi_{\mathrm{RH}}(t)) \big] \\ I_{\mathrm{RH,z0}} a_{\mathrm{RH,z0}} sin(\phi_{\mathrm{RH}}(t) + n\Delta) \end{pmatrix}, \tag{4.44}$$

and in the left-hand oriented layer in the following form:

$$\begin{pmatrix} B_{\mathrm{LH,x}} \\ B_{\mathrm{LH,y}} \\ B_{\mathrm{LH,z}} \end{pmatrix} = \sum_{n=0}^{15} \begin{pmatrix} \frac{1}{2} I_{\mathrm{LH}} a_{\mathrm{LH}} \big[-\cos(kz - \phi_{\mathrm{LH}}(t)) + \cos(kz + \phi_{\mathrm{LH}}(t) + 2n\Delta) \big] \\ \frac{1}{2} I_{\mathrm{LH}} a_{\mathrm{LH}} \big[\sin(kz + \phi_{\mathrm{LH}}(t) + 2n\Delta) - \sin(kz - \phi_{\mathrm{LH}}(t)) \big] \\ I_{\mathrm{LH,z0}} a_{\mathrm{LH,z0}} sin(\phi_{\mathrm{LH}}(t) + n\Delta) \end{pmatrix}. \tag{4.45}$$

These expressions can be simplified with the use of the following relation:

$$\sum_{n=0}^{N-1} \sin(\phi_{\mathrm{RH}}(t) + n\Delta) = Im[\sum_{n=0}^{N-1} e^{i\phi_{\mathrm{RH}}(t) + in\Delta}] = Im[e^{i\phi_{\mathrm{RH}}(t)} \frac{1 - e^{iN\Delta}}{1 - e^{i\Delta}}] = 0, \tag{4.46}$$

taking into account that $N\Delta = 2\pi$. The simplified expression for the magnetic field components generated from the right-hand oriented layer is given by:

$$\begin{pmatrix} B_{\mathrm{RH,x}} \\ B_{\mathrm{RH,y}} \\ B_{\mathrm{RH,z}} \end{pmatrix} = \frac{1}{2} I_{\mathrm{RH}} a_{\mathrm{RH}} \sum_{n=0}^{15} \begin{pmatrix} -\cos(kz - \phi_{\mathrm{RH}}(t)) \\ -\sin(kz - \phi_{\mathrm{RH}}(t)) \\ 0 \end{pmatrix} = \frac{N}{2} I_{\mathrm{RH}} a_{\mathrm{RH}} \begin{pmatrix} -\cos(kz - \phi_{\mathrm{RH}}(t)) \\ -\sin(kz - \phi_{\mathrm{RH}}(t)) \\ 0 \end{pmatrix}, \tag{4.47}$$

and from the left-hand layer is given by:

$$\begin{pmatrix} B_{\mathrm{LH,x}} \\ B_{\mathrm{LH,y}} \\ B_{\mathrm{LH,z}} \end{pmatrix} = \frac{1}{2} I_{\mathrm{LH}} a_{\mathrm{LH}} \sum_{n=0}^{15} \begin{pmatrix} -\cos(kz + \phi_{\mathrm{LH}}(t)) \\ \sin(kz + \phi_{\mathrm{LH}}(t)) \\ 0 \end{pmatrix} = \frac{N}{2} I_{\mathrm{LH}} a_{\mathrm{LH}} \begin{pmatrix} -\cos(kz + \phi_{\mathrm{LH}}(t)) \\ \sin(kz + \phi_{\mathrm{LH}}(t)) \\ 0 \end{pmatrix}. \tag{4.48}$$

Taking into the account the following substitutions:

$$A_{\mathrm{RH}} = I_{\mathrm{RH}} a_{\mathrm{RH}}, \tag{4.49}$$

$$A_{\mathrm{LH}} = I_{\mathrm{LH}} a_{\mathrm{LH}}, \tag{4.50}$$

and :

$$A_{\mathrm{RH}} = A_{\mathrm{Avg}} + \frac{\Delta A}{2}, \tag{4.51}$$

$$A_{\mathrm{LH}} = A_{\mathrm{Avg}} - \frac{\Delta A}{2}, \tag{4.52}$$

$$\phi_{\mathrm{RH}}(t) = \phi_{\mathrm{Avg}}(t) + \frac{\Delta\phi(t)}{2}, \tag{4.53}$$

$$\phi_{\mathrm{LH}}(t) = \phi_{\mathrm{Avg}}(t) - \frac{\Delta\phi(t)}{2}, \tag{4.54}$$

the components of the total magnetic field can then be expressed as:

$$B_{\mathrm{x}} = -NA_{Avg}\cos\phi_{Avg}(t)\cos\left(kz - \frac{\Delta\phi(t)}{2}\right) + N\frac{\Delta A}{2}\sin\phi_{Avg}(t)\sin\left(kz - \frac{\Delta\phi(t)}{2}\right), \tag{4.55}$$

$$B_{\mathrm{y}} = NA_{Avg}\sin\phi_{Avg}(t)\cos\left(kz - \frac{\Delta\phi(t)}{2}\right) + N\frac{\Delta A}{2}\cos\phi_{Avg}(t)\sin\left(kz - \frac{\Delta\phi(t)}{2}\right), \tag{4.56}$$

$$B_{\mathrm{z}} = 0. \tag{4.57}$$

Recasting these expressions into matrix form gives:

$$\begin{pmatrix} B_{\mathrm{x}} \\ B_{\mathrm{y}} \\ B_{\mathrm{z}} \end{pmatrix} = \begin{pmatrix} -\cos\phi_{\mathrm{Avg}}(t) & \sin\phi_{\mathrm{Avg}}(t) & 0 \\ \sin\phi_{\mathrm{Avg}}(t) & \cos\phi_{\mathrm{Avg}}(t) & 0 \\ 0 & 0 & 0 \end{pmatrix} \begin{pmatrix} NA_{\mathrm{Avg}}\cos\left(kz - \frac{\Delta\phi(t)}{2}\right) \\ N\frac{\Delta A}{2}\sin\left(kz - \frac{\Delta\phi(t)}{2}\right) \\ 0 \end{pmatrix}. \tag{4.58}$$

Parameters a_{RH} and a_{LH} depend on the radius of the helix, and typically the difference between them is $< 5\%$. If the current amplitudes supplied to both layers are the same $I_{\mathrm{RH}} = I_{\mathrm{LH}}$, then it follows $\Delta A = I_{\mathrm{RH}}a_{\mathrm{RH}} - I_{\mathrm{LH}}a_{\mathrm{LH}} \approx 0$. Equation 4.58 can then be expressed as:

$$\begin{pmatrix} B_{\mathrm{x}} \\ B_{\mathrm{y}} \\ B_{\mathrm{z}} \end{pmatrix} = \begin{pmatrix} -\cos\phi_{\mathrm{Avg}}(t) & \sin\phi_{\mathrm{Avg}}(t) & 0 \\ \sin\phi_{\mathrm{Avg}}(t) & \cos\phi_{\mathrm{Avg}}(t) & 0 \\ 0 & 0 & 0 \end{pmatrix} \begin{pmatrix} NA_{\mathrm{Avg}}\cos\left(kz - \frac{\Delta\phi(t)}{2}\right) \\ 0 \\ 0 \end{pmatrix}. \tag{4.59}$$

Inserting one final substitution:

$$\phi_{\mathrm{z}}(t) = \frac{\Delta\phi(t)}{2} - \frac{\pi}{2}, \tag{4.60}$$

$$\phi_\theta(t) = \phi_{\mathrm{Avg}}(t), \tag{4.61}$$

gives:

$$\begin{pmatrix} B_\mathrm{x} \\ B_\mathrm{y} \\ B_\mathrm{z} \end{pmatrix} = NA_{\mathrm{Avg}} \begin{pmatrix} -\cos\phi_{\theta(t)} & \sin\phi_\theta(t) & 0 \\ \sin\phi_\theta(t) & \cos\phi_\theta(t) & 0 \\ 0 & 0 & 0 \end{pmatrix} \begin{pmatrix} sin(kz - \phi_\mathrm{z}(t)) \\ 0 \\ 0 \end{pmatrix}. \tag{4.62}$$

From the equation 4.62 the total magnitude of the magnetic field generated on the axis of the double-helix geometry can be calculated:

$$|\mathbf{B}| = \sqrt{B_\mathrm{x}^2 + B_\mathrm{y}^2 + B_\mathrm{z}^2} = NA_{\mathrm{Avg}}|\sin(kz - \phi_\mathrm{z}(t))|. \tag{4.63}$$

Setting the time-dependent phase $\phi_\mathrm{z}(t)$ as:

$$\phi_\mathrm{z}(t) = p_2 t^2 + p_1 t + p_0, \tag{4.64}$$

leads to the travelling-wave equation of the magnitude of the magnetic field along the z axis:

$$|\mathbf{B}| = NA_{\mathrm{Avg}} \sin(kz - (p_2 t^2 + p_1 t + p_0)). \tag{4.65}$$

Positions of the minima and maxima of the magnitude of the magnetic field as a function of time are given by:

$$z_{\mathrm{Trap}}(t) = \frac{\phi_\mathrm{z}(t)}{k}. \tag{4.66}$$

Parameters p_2 and p_1 and p_0 are governing the acceleration of the travelling wave, the initial velocity of the travelling wave and the initial position of the travelling wave respectively:

$$p_2 = \frac{k}{2} a_{\mathrm{acc}} = \frac{k}{2} \frac{v_\mathrm{F}^2 - v_\mathrm{I}^2}{2L}, \tag{4.67}$$

$$p_1 = k v_\mathrm{I}, \tag{4.68}$$

$$p_0 = k z_0 = 0, \tag{4.69}$$

where v_I and v_F are the initial and final velocity of the travelling wave, respectively, a_{acc} is the acceleration (deceleration) of the travelling wave and L is the travelling distance of a single minimum (maximum). The magnitude of the

on-axis travelling magnetic field is governed by the time-dependent phase $\phi_z(t)$ (equation 4.63) and is independent of the time-dependent phase $\phi_\theta(t)$. Later in text it is shown that the phase $\phi_\theta(t) = 2\pi f_\theta t$ governs the radial dynamics of the magnitude of the magnetic field. Both $\phi_z(t)$ and $\phi_\theta(t)$ are experimentally controllable parameters. The travelling-wave aspect of the magnetic field is shown in Figure 4.5 by plotting the calculated magnitude of the on-axis magnetic field $|\mathbf{B}|$ at different times. Minima of the magnitude of the magnetic field can be seen to propagate in a $+z$ direction, with a corresponding velocity of 445 m/s. With an appropriate choice of parameters p_2 and p_1, the travelling magnetic wave can decelerate, accelerate or propagate with a constant velocity in both $+z$ and $-z$ directions.

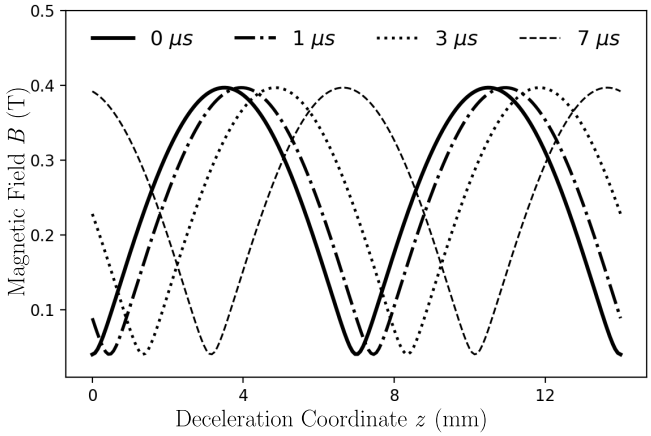

Figure 4.5: Time dependence of the magnitude of the magnetic field. Calculated magnitude of the magnetic field $|\mathbf{B}|$ on-axis of the decelerator at different times (0 μs, 1 μs, 3 μs and 7 μs) for a travelling wave with velocity 445 m/s.

Coming back to equations 4.35 and 4.36, currents that need to be supplied to the n-th helix in order to generate a travelling magnetic wave described by equation 4.63 are given by:

$$\begin{aligned} I_{\mathrm{RH}}^{\mathrm{n}} &= I_{\mathrm{RH}} \sin\Big(\phi_\theta(t) + (\phi_z(t) + n\Delta + \frac{\pi}{2})\Big) \\ &= I_{\mathrm{RH}} \sin\Big(2\pi f_\theta t + (p_2 t^2 + p_1 t + p_0 + n\Delta + \frac{\pi}{2})\Big) \end{aligned} \tag{4.70}$$

$$\begin{aligned} I_{\mathrm{LH}}^{\mathrm{n}} &= I_{\mathrm{LH}} \sin\Big(\phi_\theta(t) - (\phi_z(t) + n\Delta + \frac{\pi}{2})\Big) \\ &= I_{\mathrm{LH}} \sin\Big(2\pi f_\theta t - (p_2 t^2 + p_1 t + p_0 + n\Delta + \frac{\pi}{2})\Big) \end{aligned} \tag{4.71}$$

So far, only the on-axis magnetic field generated from the double-helix geometry was discussed. For a full picture, the description of the fields inside the whole double-helix geometry is needed.

4.3 Decelerator design

4.3.1 Design of the deceleration modules

First, the description of the design of a single deceleration module is given. Each module consisted of a 56 mm long, 4 mm diameter Vespel tube. Vespel was chosen for its favourable thermal and vacuum properties. Unlike most plastics, it does not produce significant outgassing even at high temperatures and thus it performs well in vacuum applications down to cryogenic temperatures [181]. However, Vespel tends to absorb a small amount of water, resulting in longer pump times. It can withstand repeated heating up to 300 °C without altering its thermal and mechanical properties. On the outer surface of the Vespel tube, grooves were machined for easier alignment of the wires. On top of the tube, a right-hand oriented layer of wires was mounted into the grooves, and on top of it, a left-hand oriented layer was mounted. Each layer consisted of 16 square wires (0.36 mm x 0.36 mm), mounted in a helical geometry, with helix periodicity $\lambda = 14$ mm. The Vespel tube (brown), together with a left-hand (yellow) and a right-hand (blue) oriented layer of wires, are shown in Figure 4.6. The starting position of each of the wires on the front face of each module is schematically depicted in Figure 4.12. $R_1 = 2.0$ mm and $R_2 = 2.4$ mm are radial distances from the center of the deceleration tube to the left and right-handed layer respectively.

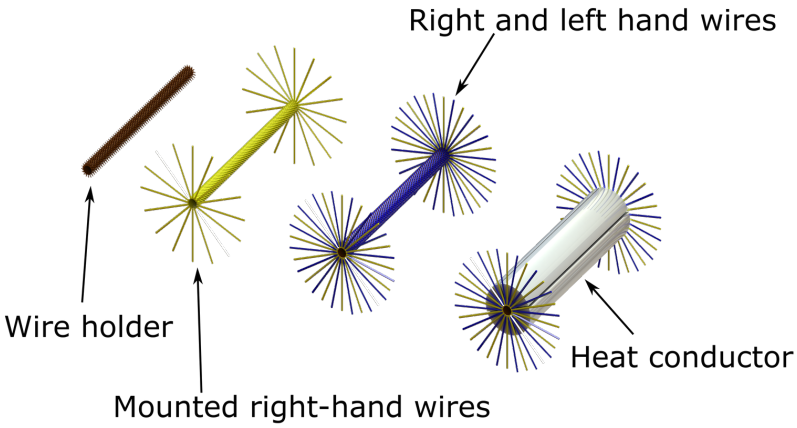

Figure 4.6: Schematic representation of the wire geometry used to create a travelling magnetic-wave. 16 right-hand oriented helical wires (yellow) were wound around a 4 mm diameter Vespel tube (brown) on top of which 16 left-hand oriented helical wires (blue) were wound. The decelerator coil unit was encased in four AlN pieces serving as heat conductors.

Four segments of 7 mm thick, precision-machined aluminium-nitride (AlN) elements were placed around the wire assembly. Aluminium nitride was chosen for its exquisite thermal conduction properties (285 W/mK) and low electric conductance (10^{-11}-$10^{-13}\Omega^{-1}\text{cm}^{-1}$). Remarkably, already at moderate temperatures ($>$ 200 °C) the thermal conductivity of AlN exceeds that of copper. Neighbouring AlN segments were separated by a 0.5 mm gap providing faster pumping of trapped gas between the different elements of the module. On top of each AlN segment, a 12.5 mm thick cooling unit made of copper was placed. The heat produced during the operation of the decelerator was dissipated into the AlN and copper cooling units. On the outer surface of the copper cooling unit, a 5 mm wide and 4 mm deep U-shaped groove was machined. Inside the groove, a 1.8 mm inner diameter and a 4.2 mm outer diameter copper tube was placed. A single copper tube was placed inside the grooves of all four cooling units and connected to the main liquid cooling system. To improve the heat transfer between a copper cooling unit and a cooling tube, a vacuum compatible heat conduction paste was applied, and tube was pressed against the cooling unit. An illustration of a cooling unit is given in Figure 4.7.

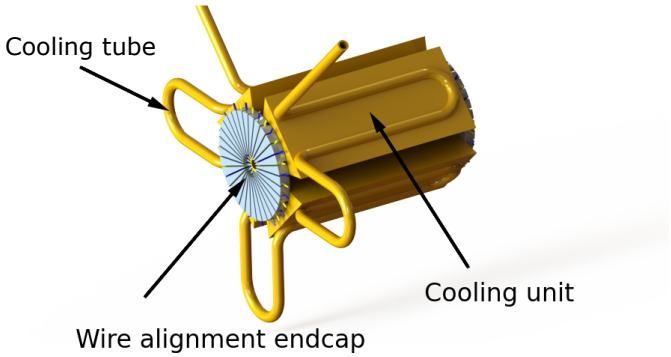

Figure 4.7: Wire cooling unit is depicted. The four aluminium nitride (not shown in the figure) and copper cooling units were placed around the wire assembly. The cooling units were efficiently cooled by a liquid-circulating cooling system. The position of each wire on the front and the rear side of each module was fixed by a wire alignment endcap.

On the front and the rear side of each module, wire alignment endcaps were placed. The disk-shaped endcaps were constructed out of polyether-ether-ketone (PEEK) thermoplastic with 33 mm outer diameter, 10 mm inner diameter, and 6 mm thickness. 32 equidistantly spaced slits around the endcap were used to position and guide individual wires (see Figure 4.7). The assembled segments were locked between two aluminium blocks (upper: 60 mm x 24 mm x 30 mm, lower: 60 mm x 24 mm x 30 mm) and mounted onto the copper base (60 mm x 43 mm x 6 mm) which in turn was mounted onto the aluminium base of the module (85 mm x 43 mm x 9 mm). Four fine alignment screws were placed on four corners of the copper base. Their purpose was to fine-adjust module-to-module alignment, both vertical offset and angle in the horizontal plane between the neighbouring modules. On top of each module a 16-pin wire female adapter was installed. Its purpose was to allow for easy connection between current supplying feedthroughs on the vacuum chamber and current supplying wires of the double-helix geometry. The fully assembled module is illustrated in Figure 4.8.

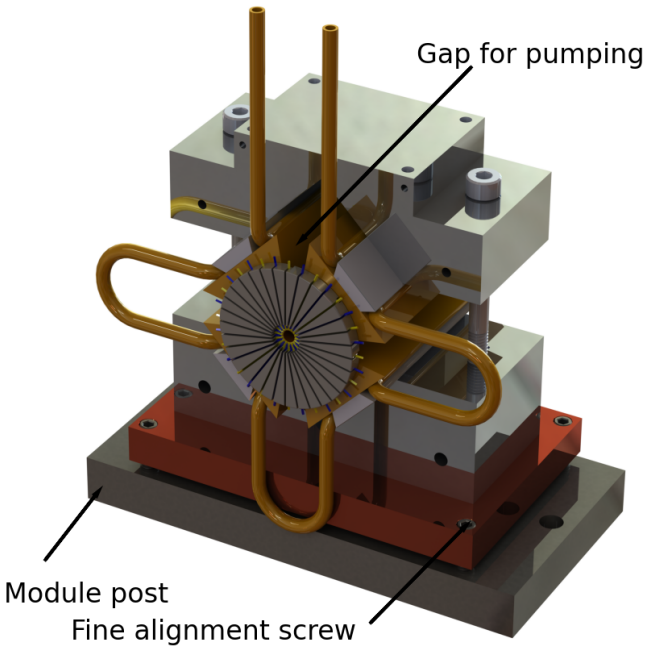

Figure 4.8: Schematic depiction of a fully assembled deceleration module. The relative alignment between neighbouring modules was adjusted by four fine alignment screws. The position of each module on the decelerator base plate was fixed by module alignment pins.

4.3.2 General decelerator design

The travelling-wave Zeeman decelerator is modular in design. It consisted of 16 individual modules, each module constructed as described in the previous section. Each module was placed on the main aluminium decelerator base plate (100 mm x 896 mm x 30 mm). The position of each module on the base plate was fixed by two pins placed at the bottom of each module (15 mm x 6 mm diameter, 40 mm separation). Module-to-module alignment was adjusted with the fine-alignment screws on each module. Once the assembly is mounted into the vacuum chamber, additional alignment was performed. The whole module assembly was aligned to the nozzle of the NPV and the skimmer with the use of a theodolite. This ensured that the molecular beam is efficiently coupled to the decelerator. Modules assembled onto the decelerator base plate and placed inside a vacuum chamber can be seen in Figure 4.9 a) and c). A parallel cooling system for efficient cooling of the module assembly was mounted on the sides of the base plate. The cooling system of all 16 modules was connected in parallel to a main in-vacuum cooling system.

The connection between the cooling system and each module was established over 4 mm Swagelok 316 fitting. In order to keep an adequate vacuum seal between the liquid cooling system and vacuum chamber, each fitting was coated with an epoxy EPO-TEK 353ND-T, mixed in 1:10 ratio. This is a two-component, high-temperature epoxy designed for semiconductor, hybrid, fiber optic, and medical applications, with low outgassing characteristics. The epoxy was cured at 150 °C for 3 hours. The cooling liquid, typically at 5 °C, is passed through the cooling system by a compact low-temperature thermostat (RCS 6 Lauda, 2.4 kW). The vacuum chamber was equipped with 16x8 electrical feedthroughs, grouped in 16 segments which supplied currents to 16 modules. Each segment was additionally split into two segments, one which supplied the currents to the right-hand oriented layer and one which supplied the currents into the left-hand oriented layer of wires. Inside the vacuum chamber, 2.2 mm diameter 30 cm long Kapton insulated wires were soldered onto each feedthrough with a vacuum compatible solder. Wires belonging to the same module were grouped together and soldered to the 16-pin male adapter. Each adapter was then connected to the female adapter on the corresponding deceleration module. Since there is a considerable number of wires that needed to be tracked, a wire addressing system both for wire adapters on each module and feedthrough segments was developed. The wire addressing system is described in the next section.

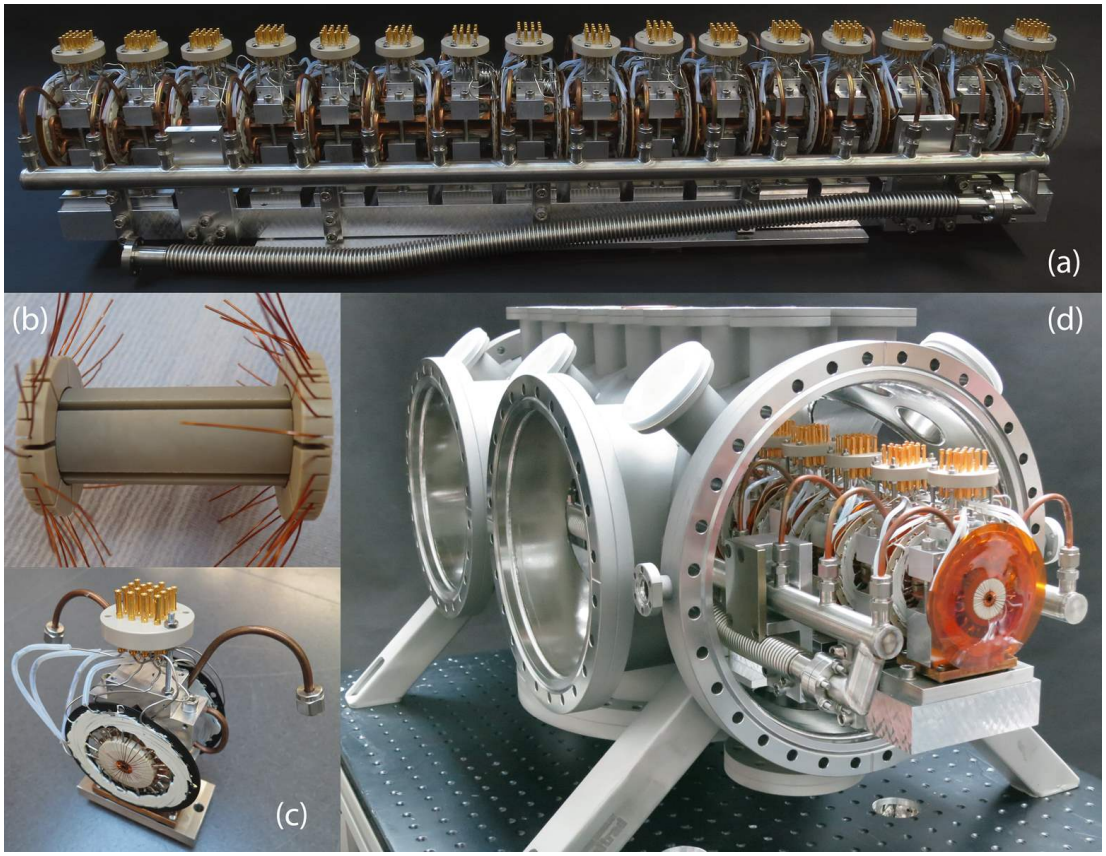

Figure 4.9: Photographs of the travelling-wave Zeeman decelerator. a) Decelerator assembly with a cooling system, b) a coil unit and c) a decelerator module unit are shown. d) The decelerator assembled inside the vacuum chamber.

The full experimental apparatus, which was used for deceleration experiments of OH molecules in the $X^2\Pi$ state described throughout this thesis, is depicted in Figure 4.11. The experimental apparatus consisted of the following parts: Nijmegen pulsed valve where the molecular source is produced, a molecular beam skimmer, 16 deceleration modules each 56 mm long giving a total length of the decelerator at 896 mm, and a detection system. The details on the Nijmegen pulsed valve are given in Chapter 3. The longitudinal distance of the valve in relation to the skimmer was tunable in a range of 80 mm - 200 mm through a precision linear translation stage. The skimmer was trumpet-shaped made out of nickel and produced by Beam Dynamics with 2 mm in diameter and 23 mm in length. Nickel is generally preferred for our application since it is a hard material and can be finely polished. There are two main factors which cause skimmer interference and limit the throughput of the skimmer: first, molecules

in the molecular beam can be scattered by molecules which are reflected from the exterior surface of the skimmer and second, molecules inside a molecular beam can be scattered by collisions with the gas that builds up inside the skimmer through collisions with the interior surface of the skimmer. The unique shape of the skimmer reduces interference from reflected molecules and minimizes excess gas buildup inside the skimmer.

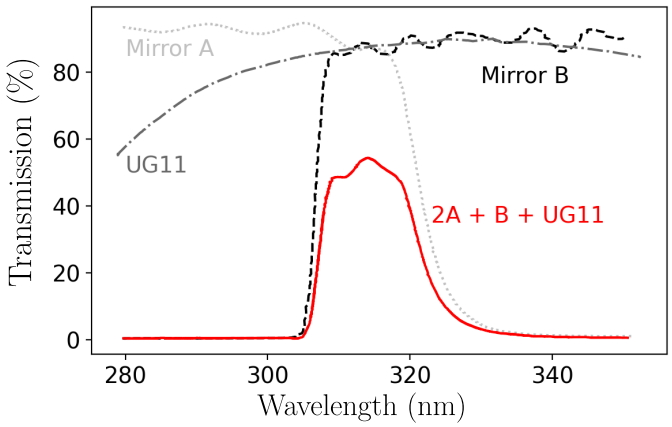

Figure 4.10: Optical filter- system consisting of four filters. Type A mirror: a 50 mm long-pass filter 305 Alp, Omega optics, 85% transimission @ 310 nm - 380 nm. Type B mirror: a 50 mm short-pass filter, Laser Optik, 92 % transmission @ 280 nm - 320 nm. 50 mm UG11 bandpass filter, Schott, 85% transmission @ 250 nm - 400 nm. Combination of UG11+2A+B produces $\sim$ 50% transmission centered at 315 nm with FWHM of $\sim$15 nm.

The detection system consisted of a 51 mm ET Enterprises, series 9831B photomultiplier tube, a 50 mm focal length UV lens, a filter stack consisting of four filters, laser radiation centered around 282 nm, four 4 mm inner diameter light baffles which limited the number of stray photons which impinged on the photomultiplier tube and pair of Brewster windows which only allowed a vertically polarized beam to enter the detection region. There was a possibility to achieve the detection of the molecules both directly in front of the source and after the decelerator. The photomultiplier tube is an extremely sensitive photon detector with $\sim$30% quantum efficiency @ 313 nm and a voltage gain of $\sim 10^8$ @ 2100 V. The filter stack consisted of two type A mirrors (a 50 mm long-pass filter 305 Alp, Omega optics, 85% transmission @ 310 nm - 380 nm), one type B mirror

(a 50 mm short-pass filter, Laser Optik, 92 % transmission @ 280 nm - 320 nm) and one 50 mm UG11 bandpass filter (Schott, 85% transmission @ 250 nm - 400 nm). The whole filter stack produces $\sim$ 50% transmission centered at 315 nm with FWHM of $\sim$15 nm. The transmission of each filter as well as of the entire filter system as a function of the photon wavelength is shown in Figure 4.10. A schematic illustration of the the experimental system is shown in Figure 4.11.

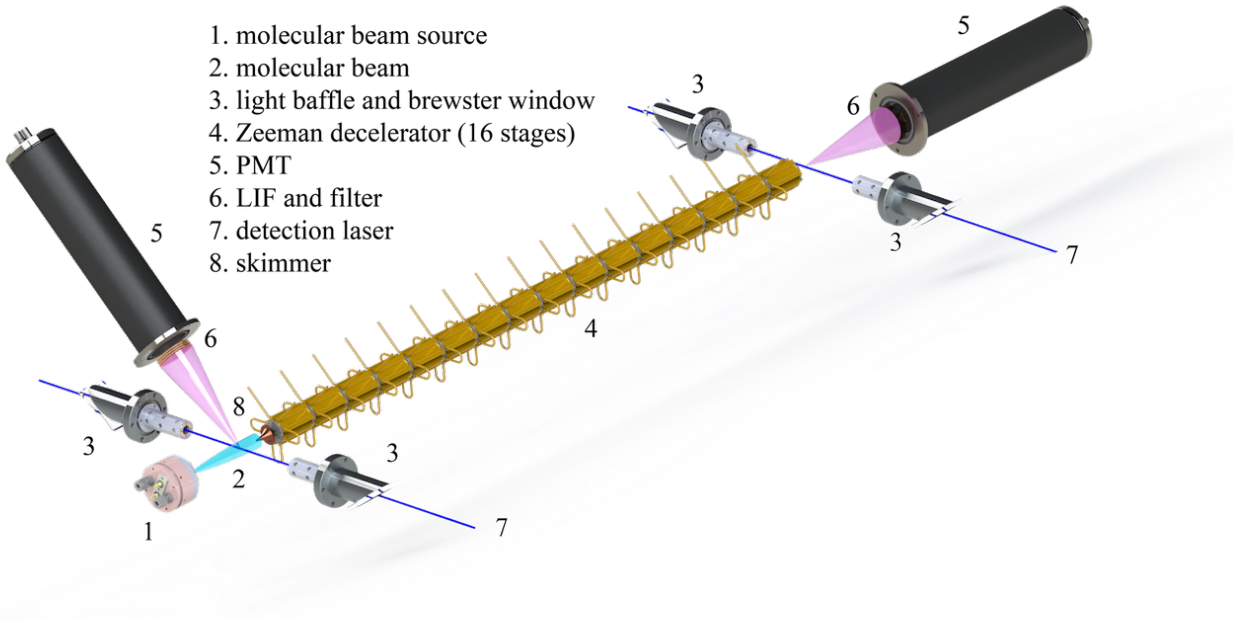

Figure 4.11: The complete experimental apparatus. A molecular beam of OH radicals was produced by pulsed gas nozzle. (1). After passing through a skimmer (8), molecules were coupled into the travelling-wave Zeeman decelerator (4), where they were decelerated from an initial velocity of 445 m/s down to 350 m/s. Following deceleration, molecules are detected by laser-induced fluorescence (LIF) collected using a photo-multiplier tube (PMT)(6).

4.3.3 Double-helix geometry

Here, the implementation in the real system of the mathematical model introduced at the beginning of the chapter is described. The mathematical model does not assume any physical limitations coming from the real system. The real-life implementation is limited by the inductance and the resistance that the

system would possess if the whole decelerator would be implemented as a single standalone unit. For that reason, in order to limit the inductances and resistances of the double-helix wire geometry, the decelerator was modular in design. The decelerator described in this thesis consisted of 16 deceleration modules where each module consisted of two layers of wire helices each consisting of 16 wires. Currents in each of the wires have to be separately addressed. Since the decelerator is modular in design, currents that are supplied to different modules are supplied at different times, depending on the position of the synchronous molecule inside a travelling wave. The calculations of the timings of individual currents in each module are given in the next chapter. The shape of the currents that are supplied to different helices in a single module and allow for the production of the travelling magnetic wave on the deceleration axis are given by equations 4.70 and 4.71. In order to address individual currents, we developed a current-generation system based on high-power arbitrary-waveform current generators. The current generators design is described in the next chapter.

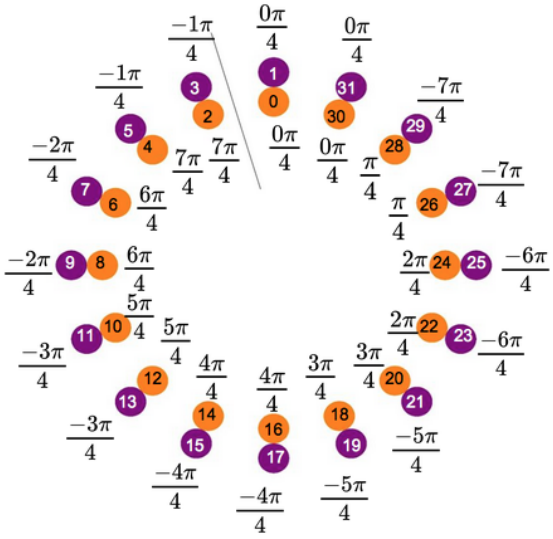

Figure 4.12: Schematic representation of the position of each helix on the front-face of a single module. The initial positions of the helices belonging to the right-hand oriented layer is depicted with orange circles and the initial positions of the helices belonging to the left-hand oriented layer is depicted with purple circles. Helices are labelled with numbers 0 - 31. The phase $\varphi = n\Delta$ of the current supplied to each helix is specified.

A schematic representation of the position of each helix on a front-face of a single module is given in Figure 4.12. The right-hand oriented layer is represented by orange circles and the left-hand oriented layer by purple circles. Neighbouring helices are offset by an angle $\Delta = \pi/8$. Individual helices are labelled by numbers 0-31, right-hand oriented helices with even numbers in a clockwise fashion, and left-hand oriented helices with odd numbers in a counterclockwise fashion. The phase $\varphi = n\Delta$ of the current that is supplied to each helix is specified. In order to limit the number of currents that have to be addressed to the individual module, groups of four helices are wound from a single wire. This reduces the number of individual currents that have to be addressed in each module from 32 down to 8. For the implemented wire geometry, it is imperative that it still follows the structure laid out in the mathematical model. Instead of the 16 individual currents that need to be supplied to each layer, there are now 4 individual currents that need to be supplied. Tables 4.1 and 4.2 illustrate the positions on the front-face and rear-face of each module pointing to which helices are supplied with the same current source. The helices on the front-face of a module are labelled in a fashion previously described, while helices on the rear-face of a module are labelled in a similar fashion but with underlined numbers.

Table 4.1: Right-hand layer: Initial position of the helices on the front-face and the rear-face of the module with the same supplied current.

Input	Wire connections	Output
$\overline{A}$	$\rightarrow \underline{31} \rightarrow 30 \rightarrow 14 \rightarrow \underline{15} \rightarrow \underline{1} \rightarrow 0 \rightarrow 16 \rightarrow \underline{17} \rightarrow$	$\overline{A'}$
$\overline{B}$	$\rightarrow \underline{3} \rightarrow 2 \rightarrow 18 \rightarrow \underline{19} \rightarrow \underline{5} \rightarrow 4 \rightarrow 20 \rightarrow \underline{21} \rightarrow$	$\overline{B'}$
$\overline{C}$	$\rightarrow \underline{7} \rightarrow 6 \rightarrow 22 \rightarrow \underline{23} \rightarrow \underline{9} \rightarrow 8 \rightarrow 24 \rightarrow \underline{25} \rightarrow$	$\overline{C'}$
$\overline{D}$	$\rightarrow \underline{11} \rightarrow 10 \rightarrow 26 \rightarrow \underline{27} \rightarrow \underline{13} \rightarrow 12 \rightarrow 28 \rightarrow \underline{29} \rightarrow$	$\overline{D'}$

Table 4.2: Left-hand layer: Initial position of the helices on the front-face and the rear-face of the module with the same supplied current.

Input	Wire connections	Output
A	$\rightarrow 31 \rightarrow \underline{0} \rightarrow \underline{16} \rightarrow 15 \rightarrow 1 \rightarrow \underline{2} \rightarrow \underline{18} \rightarrow 17 \rightarrow$	A'
B	$\rightarrow 3 \rightarrow \underline{4} \rightarrow \underline{20} \rightarrow 19 \rightarrow 5 \rightarrow \underline{6} \rightarrow \underline{22} \rightarrow 21 \rightarrow$	B'
C	$\rightarrow 7 \rightarrow \underline{8} \rightarrow \underline{24} \rightarrow 23 \rightarrow 9 \rightarrow \underline{10} \rightarrow \underline{26} \rightarrow 25 \rightarrow$	C'
D	$\rightarrow 11 \rightarrow \underline{12} \rightarrow \underline{28} \rightarrow 27 \rightarrow 13 \rightarrow \underline{14} \rightarrow \underline{30} \rightarrow 29 \rightarrow$	D'

A labelling system was implemented, designating different individual currents that are supplied to each module. Currents that were supplied to the left-hand oriented layer were labelled as A, B, C and D, and currents that were supplied to the right-hand oriented layer were labelled as $\overline{A}$, $\overline{B}$, $\overline{C}$ and $\overline{D}$. If a connection is an input of the current, it was labelled without an apostrophe, and if a connection is an output of the current, it was labelled with an apostrophe. The labels of the currents that are supplied to each of the helices are shown in Figures 4.13 a) for the front-face of the module and 4.14 a) for the rear-face of the module. Photographs of the front-face and the rear-face of the deceleration module are shown in Figures 4.13 b) and 4.14 b), respectively.

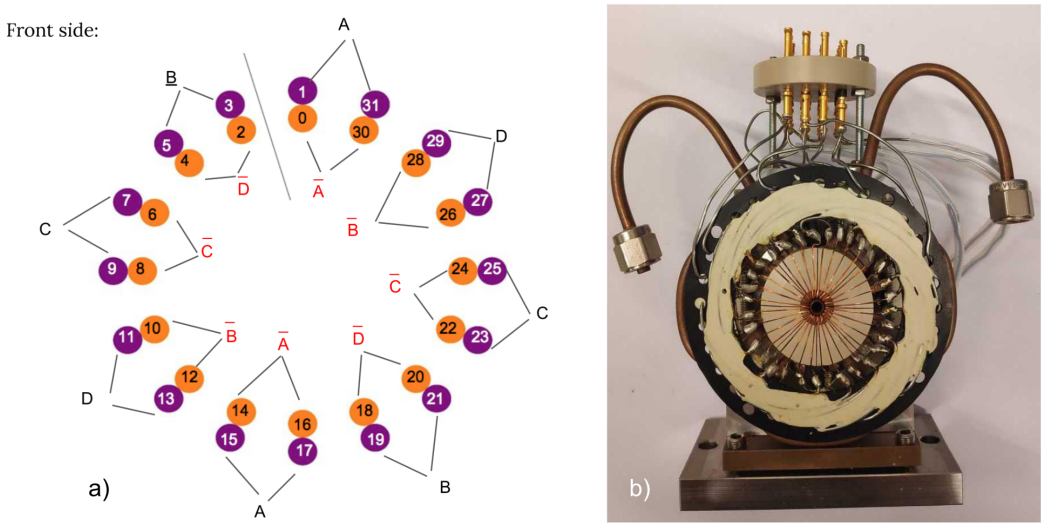

Figure 4.13: The front-face of a deceleration module. a) A schematic representation of the starting position of each helix on the front-face of each module numerically labelled. The four currents that are supplied to each layer together with their respective helix are illustrated. b) A photograph of the front-face of a deceleration module.

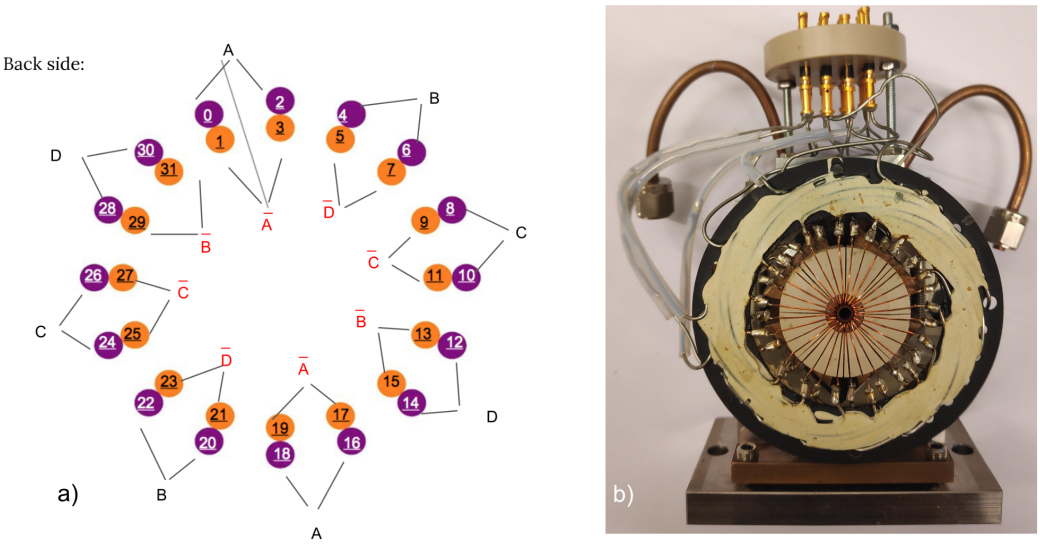

Figure 4.14: The rear-face of the deceleration module. a) A schematic representation of the starting position of each helix on the rear-face of each module numerically labelled. The four currents that are supplied to each layer together with their respective helix are illustrated. b) A photograph of the rear-face of a deceleration module.

As described, on top of each module a 16-pin female adapter was placed. Inputs and outputs of each double-helix layer were soldered onto the bottom side of each pin on the adapter, and currents to the module were distributed over the adapter. Each pin was labelled with the same labels that was used to label the four currents that were supplied to each layer. A schematic representation of the adapter together with the labels for each pin is shown in Figure 4.15 a). Current input and output pins were labelled as previously described. A photograph of the 16-pin adapter is shown in Figure 4.15 b). Currents were supplied to the modules over the current feedthroughs located on the outside of the vacuum chamber. Feedthroughs were grouped into 16 segments, each segment designated for supplying the currents to each module. Each segment is grouped into two additional segments, one supplying the current to the right-hand layer and another to the left-hand layer. In order to keep track of all the wire connections, a color code which helps determine the currents that need to be supplied through each of the feedthroughs was developed. The color coding of the feedthroughs is illustrated in Figure 4.15 c) for the right-hand oriented layer and in Figure 4.15 d) for the left-hand oriented layer. The position of

each feedthrough on the vacuum chamber flange is illustrated schematically and currents which need to be supplied through each feedthrough are labelled. A photograph of the wires connected to the feedthroughs with the color-coding for each feedthrough is shown in Figure 4.15 e).

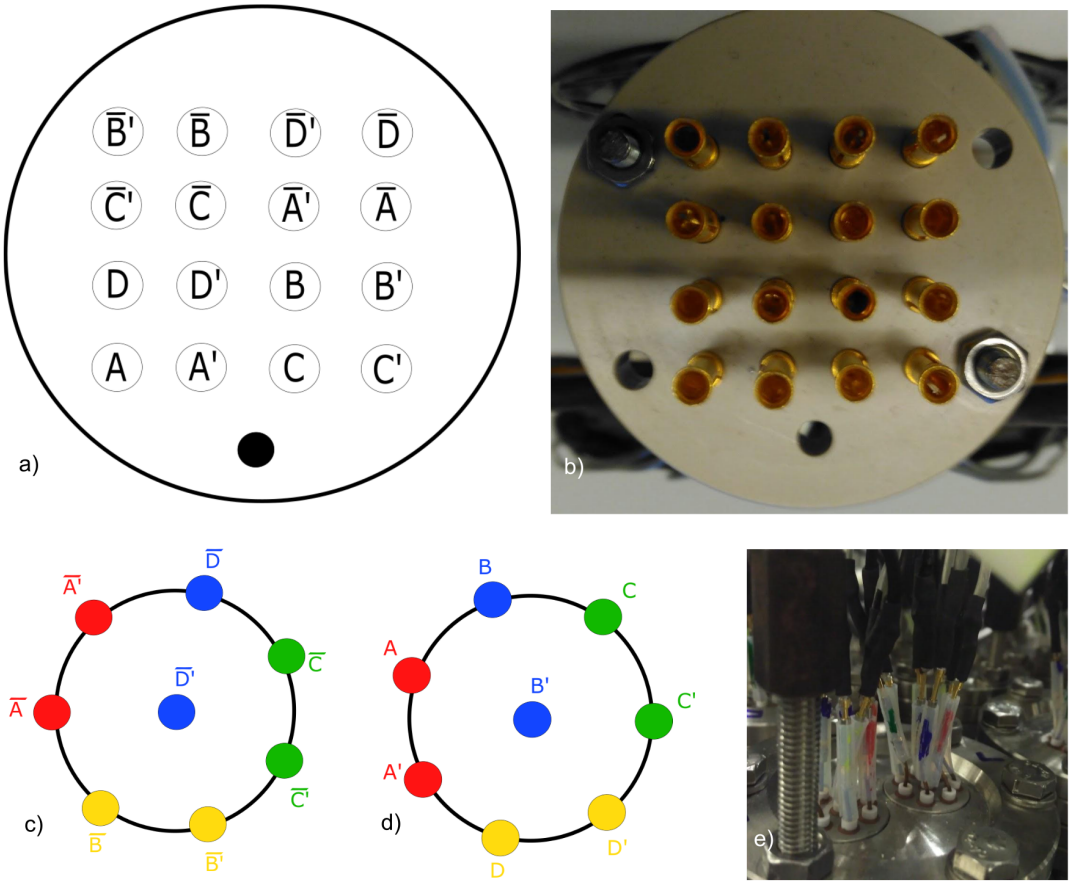

Figure 4.15: A 16-pin adapter. a) Schematic representation of the adapter together with the labels for each pin. b) Photograph of the 16-pin adapter. c) and d) Color-code illustrating schematically the position of each feedthrough on the vacuum chamber flange. Currents that are to be supplied through each of the feedthroughs are labelled. e) A photograph of the wires connected to the feedthroughs with the color-coding for each feedthrough.

4.3.4 Control and monitoring of the operation of the decelerator

For the successful operation of the travelling-wave Zeeman decelerator, it is important to have control of as many aspects of the experiment as possible. For that reason, various control and monitoring software was developed. Four separate

programs were developed: a program for control, monitoring and initialization of the current generating system and operation of the decelerator, a second program for control and monitoring of the power supply system purpose of which is to supply power to the capacitor bank from which the currents to the decelerator are generated, a third program which monitors the temperature of different components of the experiment, and fourth a pressure monitoring software monitoring the quality of the vacuum inside the vacuum chambers.

Travelling-wave Zeeman decelerator control software

The most crucial piece of software is the program which controls the current generation and monitors the operation of the decelerator. The program was developed in LabView [182], a system-design platform and development environment for a visual programming language from National Instruments. The graphical interface of the program is depicted in figure 4.16. In the program, the user defines the initial parameters of the travelling wave: the initial velocity, the final velocity, the rotational frequency of the trap, the delay between the initial pulse for the start and the execution of the current switching sequence and a parameter which increases the duration of the current pulses such that the synchronous molecule experiences adiabatic transfer from one module to another. These parameters are highlighted with a red line in the figure. After these parameters are initialized, the program calculates parameters p_0, p_1, p_2, ω_θ, t_{Delay}, highlighted with a green line in the figure. These parameters are then distributed over to the current generating system, highlighted with an orange line in the figure.

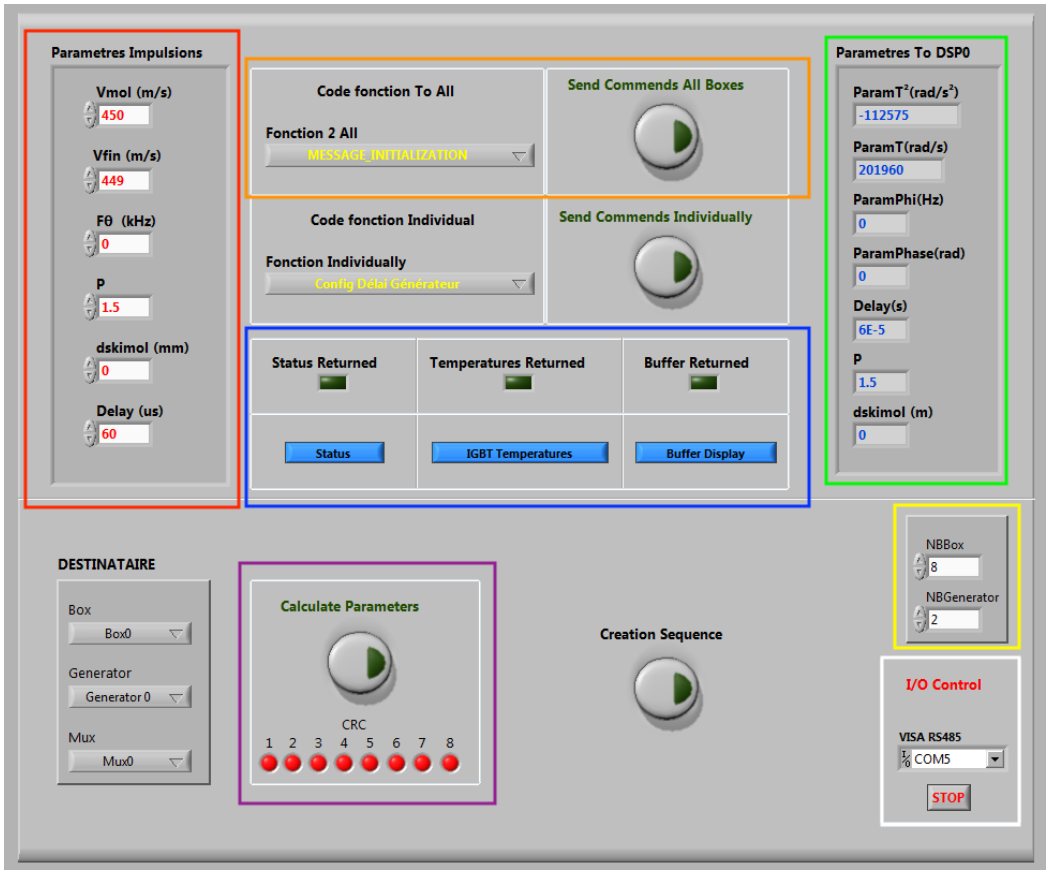

Figure 4.16: ZeemanCommander software. The program controls initialization of the currents that are to be generated and monitors the status of the operation of the travelling-wave Zeeman decelerator.

In the program, it is possible to specify the number of racks housing the current generators, and a number of generators inside each rack. This is highlighted with a yellow line in the figure. Monitoring of the operation of different aspects of the decelerator is performed via different functionalities of the program. The program has the ability to inquire about the status of each current generator in the current generating system. The status of the current generators are then shown graphically. This is illustrated in Figure 4.17 a). Due to the way in which the fast current switching is executed on the current generators, power losses on the current generators are unavoidable. For that reason, temperatures on four current switches on each current generator are monitored at all times. The program acquires the values of the temperatures from each generator and displays them on the graphical interface. This is illustrated in the figure 4.17 b). The software was developed by Nicolas Vanhaecke, Dongdong Zhang and

Tomislav Damjanović.

Figure 4.17: The status of the decelerator. a) The status of each current generator in the current generating system. b) Temperatures are read out on each current switch on each current generator.

Power supply control software

Another program for the control and monitoring of the power that is supplied to the capacitor bank from which the currents to the decelerator are generated was developed. The power to the capacitor bank is supplied over two power supplies (Soerensen SG) which have an option for remote control. The program was coded in Python [183] programming language with the help of the PyQt and PyQtGraph libraries. The graphical interface was developed in the QT4 graphical interface toolkit. The communication between the program and the power supply is established over the RS-232 protocol. [184]. In the program, the output voltage, maximum output current and voltage ramp-up and ramp-down times are defined by the user. The output current and the output voltage delivered by the power supply are measured every 100 ms, and measured values for both power supplies are displayed on the graphical interface in real-time. The last 1000 measured data points are plotted. This enables the user to detect if there are any abnormalities in the voltages and currents that are supplied from the power supply. Additional protection measures were implemented into the

program, e.g. for overvoltage (when the measured voltage on the power supply exceeds the predefined maximum allowed voltage, the power supplies immediately go into shutdown mode) and for reset (if abnormalities are observed, the power supply output voltage and current can be reset). The connection to the power supply and user-defined parameters can be verified and displayed at any time. The graphical user interface of the program is shown in Figure 4.18.

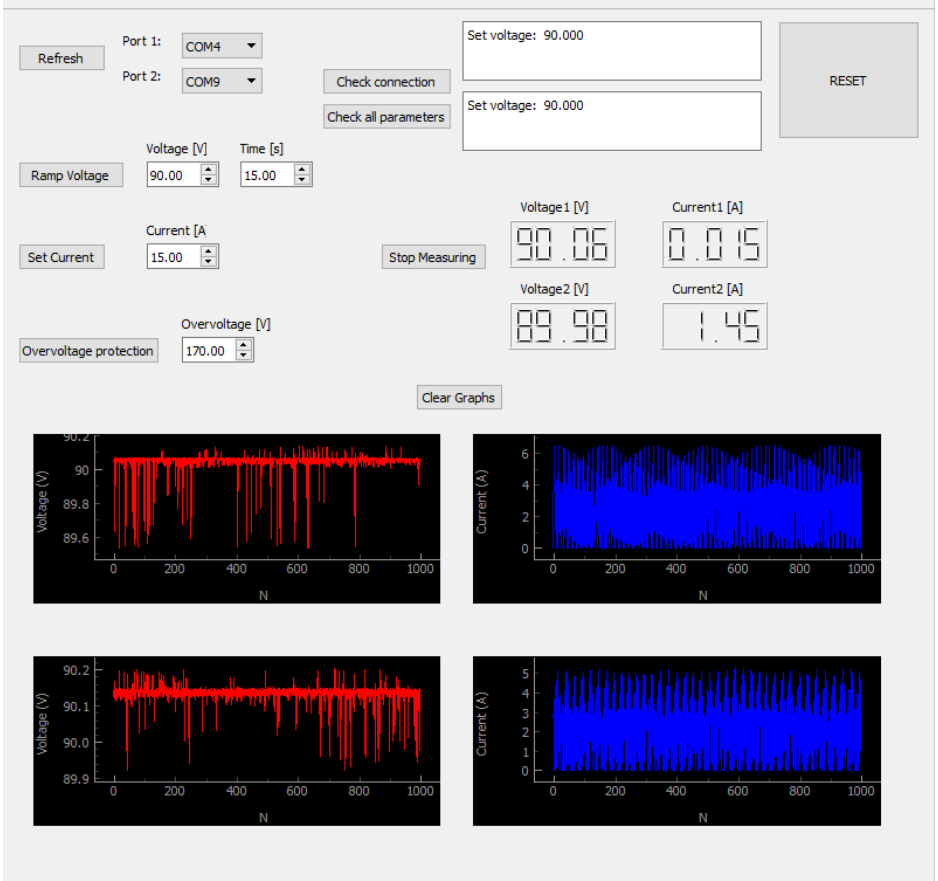

Figure 4.18: The graphical interface of the control and monitor software for the capacitor bank power supply. The voltages and the currents used to charge the capacitor bank are controlled through the software.

Temperature monitoring software

The temperature of the various elements of the experimental setup is another piece of information important for the smooth operation of the experiment. For that reason, a temperature sensing system consisting of seven temperature sensors placed on different elements of the experimental setup, an Arduino Nano microcontroller board and a temperature readout and display graphical interface were

developed. Two K-type thermocouples are placed inside the vacuum chamber on the last deceleration module of the decelerator. One thermocouple is placed close to the exit of the decelerator and another one is placed at the outer edge of the front face of the module. The other five temperature sensors are 9-bit to 12-bit temperature resolution programmable digital temperature sensors, model DS18B20. The sensors communicate over a 1-wire bus that requires only one data line for communication with a central microprocessor. Each DS18B20 has a unique 64-bit serial code, which allows multiple DS18B20s to be read out on the same bus. For that reason it is simple to use one microprocessor to control many distributed DS18B20s. Temperature from each sensor is read out every 1 ms, and the data is stored in the Arduino Nano memory. Similarily to the power supply control program, the graphical interface for the temperature monitoring program was developed using the Python programming language with the help of the PyQt and PyQtGraph libraries and QT4 graphical interface toolkit. The interface communicates with the Arduino Nano over the serial port. Temperatures are read out from the Arduino Nano memory and are shown in real-time on the graphical interface of the program. The last 20000 data points for each temperature sensor are stored and plotted in the graphical interface. The graphical interface of the temperature monitoring program is shown in Figure 4.19.

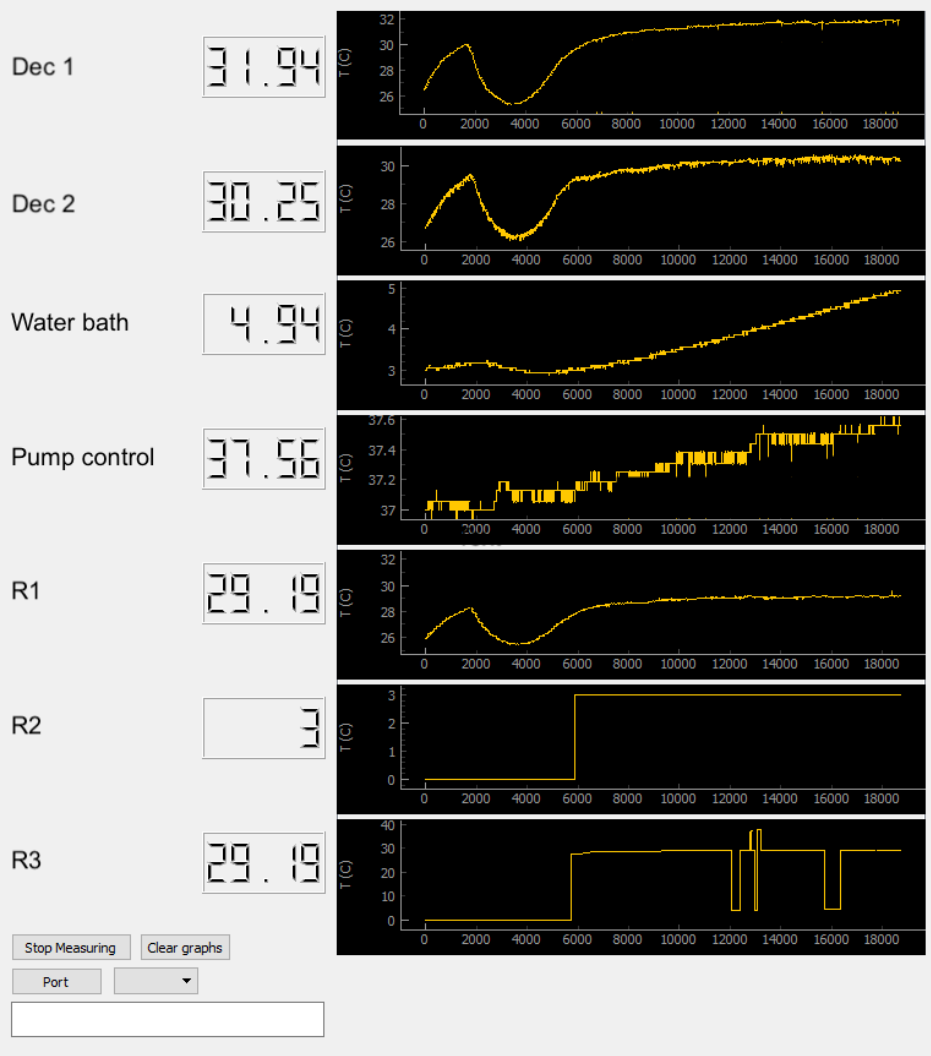

Figure 4.19: Temperature monitoring software. Temperatures are readout from 7 temperature sensors with the help of Arduino Nano microcontroller and plotted in the graphical interface.

Pressure monitoring software

A pressure measurement program is the last piece of software necessary for the smooth operation of the experiment. The program was developed in LabView. It connects over the serial port to the vacuum measurement and control unit, Pfeiffer MaxiGauge TPG 256. The MaxiGauge TPG 256 is a 6-port total pressure measurement and control unit for Pfeiffer Vacuum Compact Gauges. In our experiment, it records the pressure data from 6 pressure gauges: two PKR 261 compact cold-cathode gauges and one PKR 251 compact full-range gauge which measure the pressure inside the vacuum chambers and three TPR 281 Pirani

gauges which are measuring the pre-vacuum pressure. The data is stored in the MaxiGauge memory, and at request, data is communicated to the pressure monitoring software where it is then displayed in real-time and plotted for each pressure gauge. The pressure measurement software is shown in Figure 4.20. The software was developed by Dongdong Zhang.

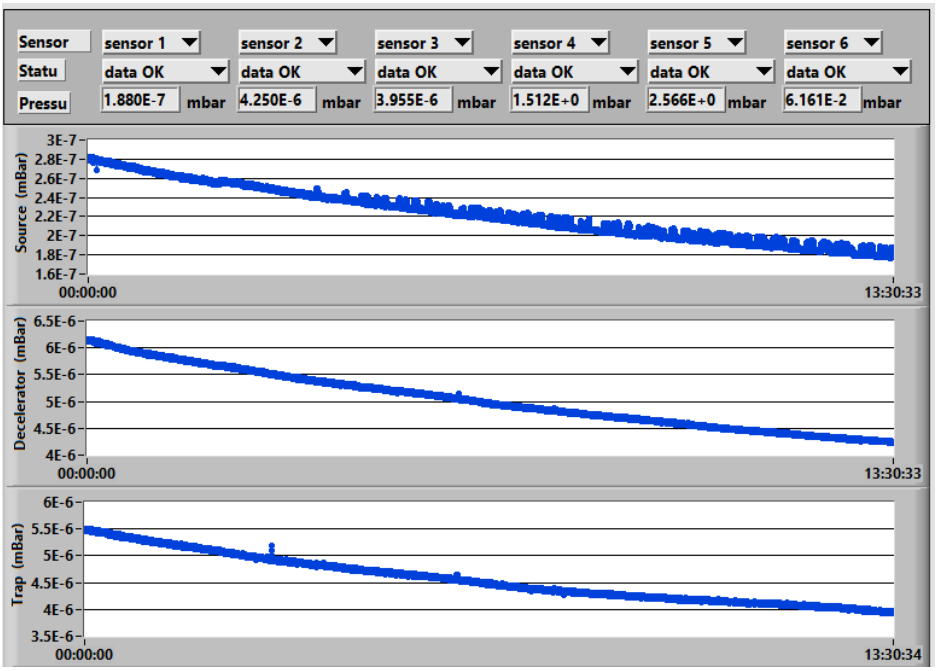

Figure 4.20: The pressure monitoring software. The pressure data is collected by the MaxiGauge TPG 256 and distributed to the pressure monitoring software where it is plotted and displayed in real-time.

4.4 Numerical trajectory simulations

4.4.1 Numerical calculations of time-dependant inhomogeneous magnetic fields

Previously, it was expressed that there is no analytic expression of the magnetic field components everywhere in space inside of a single helix geometry. This means that the numerical approach has to be adopted. In order to calculate the total magnetic field inside the double-helix geometry, the contributions to the total magnetic field from 32 helices has to be calculated. At the precision that is necessary for accurate numerical trajectory simulations, this would not be

possible due to time and computer memory requirements. A method which takes into account the rotational symmetry of the problem and reduces the computation time and computer memory requirements has to be adopted. Expressions for the magnetic field components of the right-hand oriented helix 4.3, 4.4 and 4.5 are numerically integrated between $\theta_1 = -6\pi$ and $\theta_2 = 6\pi$ at a plane $z = 0$. Expressions for the magnetic field components of the right-hand oriented helix are given by:

$$B^0_{\mathrm{RH,x}}(x,y,z=0) = \frac{\mu_0 I_{\mathrm{RH}}}{4\pi}\int_{\theta_1}^{\theta_2} \frac{\lambda(R_{\mathrm{RH}}\sin(\theta)+\theta R_{\mathrm{RH}}\cos(\theta)-y)}{2\pi\left(\frac{\theta^2\lambda^2}{4\pi^2}+(x-R_{\mathrm{RH}}\cos(\theta))^2+(y-R_{\mathrm{RH}}\sin(\theta))^2\right)^{3/2}}d\theta, \tag{4.72}$$

$$B^0_{\mathrm{RH,y}}(x,y,z=0) = \frac{\mu_0 I_{\mathrm{RH}}}{4\pi}\int_{\theta_1}^{\theta_2} \frac{\lambda(\theta R_{\mathrm{RH}}\sin(\theta)-R_{\mathrm{RH}}\cos(\theta)+x)}{2\pi\left(\frac{\theta^2\lambda^2}{4\pi^2}+(x-R_{\mathrm{RH}}\cos(\theta))^2+(y-R_{\mathrm{RH}}\sin(\theta))^2\right)^{3/2}}d\theta, \tag{4.73}$$

$$B^0_{\mathrm{RH,z}}(x,y,z=0) = \frac{\mu_0 I_{\mathrm{RH}}}{4\pi}\int_{\theta_1}^{\theta_2} \frac{R_{\mathrm{RH}}(R_{\mathrm{RH}}-x\cos(\theta)-y\sin(\theta))}{\left(\frac{\theta^2\lambda^2}{4\pi^2}+(x-R_{\mathrm{RH}}\cos(\theta))^2+(y-R_{\mathrm{RH}}\sin(\theta))^2\right)^{3/2}}d\theta, \tag{4.74}$$

and similarly for the left-hand oriented helix:

$$B^0_{\mathrm{LH,x}}(x,y,z=0) = \frac{\mu_0 I_{\mathrm{LH}}}{4\pi}\int_{\theta_1}^{\theta_2} \frac{\lambda(R_{\mathrm{LH}}\sin(\theta)+\theta R_{\mathrm{LH}}\cos(\theta)+y)}{\left(\frac{\theta^2\lambda^2}{4\pi^2}+(x-R_{\mathrm{LH}}\cos(\theta))^2+(y+R_{\mathrm{LH}}\sin(\theta))^2\right)^{3/2}}d\theta, \tag{4.75}$$

$$B^0_{\mathrm{LH,x}}(x,y,z=0) = \frac{\mu_0 I_{\mathrm{LH}}}{4\pi}\int_{\theta_1}^{\theta_2} \frac{\lambda(\theta R_{\mathrm{LH}}\sin(\theta)-R_{\mathrm{LH}}\cos(\theta)+x)}{\left(\frac{\theta^2\lambda^2}{4\pi^2}+(x-R_{\mathrm{LH}}\cos(\theta))^2+(y+R_{\mathrm{LH}}\sin(\theta))^2\right)^{3/2}}d\theta, \tag{4.76}$$

$$B^0_{\mathrm{LH,x}}(x,y,z=0) = \frac{\mu_0 I_{\mathrm{LH}}}{4\pi}\int_{\theta_1}^{\theta_2} \frac{R_{\mathrm{LH}}(R_{\mathrm{LH}}-x\cos(\theta)+y\sin(\theta))}{\left(\frac{\theta^2\lambda^2}{4\pi^2}+(x-R_{\mathrm{LH}}\cos(\theta))^2+(y+R_{\mathrm{LH}}\sin(\theta))^2\right)^{3/2}}d\theta, \tag{4.77}$$

where $R_{\mathrm{RH}} = 2.0$ mm and $R_{\mathrm{LH}} = 2.4$ mm are radii of the right-hand oriented and left-hand oriented helix, respectively. Magnetic field components at $z = 0$ are then calculated everywhere inside each helix on a 0.02 mm grid separation, and values are stored in memory. This gives the magnetic field components in the x-y plane at z = 0, in order to calculate fields everywhere in space the following symmetry relations are used:

$$\mathbf{B^0_{RH}}(x,y,z) = \mathbf{R}^{\mathrm{3D}}_{\mathrm{kz}} \cdot \mathbf{B^0_{RH}}\Big(\mathbf{R}^{\mathrm{2D}}_{-\mathrm{kz}} \cdot \{x,y\}, 0\Big) \tag{4.78}$$

for the right-hand oriented helix, and:

$$\mathbf{B}^{\mathbf{0}}_{\mathrm{LH}}(x,y,z) = \mathbf{R}^{\mathrm{3D}}_{-\mathrm{kz}} \cdot \mathbf{B}^{\mathbf{0}}_{\mathrm{LH}}\Big(\mathbf{R}^{\mathrm{2D}}_{\mathrm{kz}} \cdot \{x,y\}, 0\Big) \tag{4.79}$$

for the left-hand oriented helix. $\mathbf{R}^{\mathrm{2D}}_{\alpha}$ and $\mathbf{R}^{\mathrm{3D}}_{\alpha}$ are 2D and 3D rotation matrices :

$$\mathbf{R}^{\mathrm{2D}}_{\alpha} = \begin{pmatrix} \cos\alpha & -\sin\alpha \\ \sin\alpha & \cos\alpha \end{pmatrix}, \tag{4.80}$$

$$\mathbf{R}^{\mathrm{3D}}_{\alpha} = \begin{pmatrix} \cos\alpha & -\sin\alpha & 0 \\ \sin\alpha & \cos\alpha & 0 \\ 0 & 0 & 1 \end{pmatrix}. \tag{4.81}$$

Similarly, with the symmetry relations we can obtain the magnetic fields for the n-th helix in each layer:

$$\mathbf{B}^{\mathbf{0}}_{\mathrm{RH}}(x,y,z) = \mathbf{R}^{\mathrm{3D}}_{\mathbf{n\Delta}} \cdot \mathbf{B}^{\mathbf{0}}_{\mathrm{RH}}\Big(\mathbf{R}^{\mathrm{2D}}_{\mathbf{-n\Delta}} \cdot \{x,y\}, z\Big), \tag{4.82}$$

$$\mathbf{B}^{\mathbf{0}}_{\mathrm{LH}}(x,y,z) = \mathbf{R}^{\mathrm{3D}}_{\mathbf{-n\Delta}} \cdot \mathbf{B}^{\mathbf{0}}_{\mathrm{LH}}\Big(\mathbf{R}^{\mathrm{2D}}_{\mathbf{n\Delta}} \cdot \{x,y\}, z\Big), \tag{4.83}$$

The total magnetic field inside the double-helix geometry is then given by:

$$\begin{aligned} \mathbf{B}(x,y,z) = \sum_{n=0}^{15} \Bigg(& \mathbf{R}^{\mathrm{3D}}_{\mathbf{n\Delta}} \cdot \mathbf{R}^{\mathrm{3D}}_{\mathrm{kz}} \cdot \mathbf{B}^{\mathbf{0}}_{\mathrm{RH}}\Big(\mathbf{R}^{\mathrm{2D}}_{\mathbf{-n\Delta}} \cdot \mathbf{R}^{\mathrm{2D}}_{-\mathrm{kz}} \cdot \{x,y\}, 0\Big) + \\ & + \mathbf{R}^{\mathrm{3D}}_{\mathbf{-n\Delta}} \mathbf{R}^{\mathrm{3D}}_{-\mathrm{kz}} \cdot \mathbf{B}^{\mathbf{0}}_{\mathrm{LH}}\Big(\mathbf{R}^{\mathrm{2D}}_{\mathbf{n\Delta}} \cdot \mathbf{R}^{\mathrm{2D}}_{\mathrm{kz}} \cdot \{x,y\}, 0\Big) \Bigg). \end{aligned} \tag{4.84}$$

Taking into the account the time dependence of the currents $I_{\mathrm{RH}}(t)$ and $I_{LH}(t)$:

$$\begin{aligned} \mathbf{B}(x,y,z,t) = \sum_{n=0}^{15} \Bigg[& \mathbf{R}^{\mathrm{3D}}_{\mathbf{n\Delta}} \cdot \mathbf{R}^{\mathrm{3D}}_{\mathrm{kz}} \cdot \mathbf{B}^{\mathbf{0}}_{\mathrm{RH}}(\mathbf{R}^{\mathrm{2D}}_{\mathbf{-n\Delta}} \cdot \mathbf{R}^{\mathrm{2D}}_{-\mathrm{kz}} \cdot \{x,y\}, 0) \\ & \times \sin\Big(\phi_\theta(t) + (\phi_{\mathrm{z}}(t) + \frac{\pi}{2} + n\Delta)\Big) \\ & + \mathbf{R}^{\mathrm{3D}}_{\mathbf{-n\Delta}} \cdot \mathbf{R}^{\mathrm{3D}}_{-\mathrm{kz}} \cdot \mathbf{B}^{\mathbf{0}}_{\mathrm{LH}}(\mathbf{R}^{\mathrm{2D}}_{\mathbf{n\Delta}} \cdot \mathbf{R}^{\mathrm{2D}}_{\mathrm{kz}} \cdot \{x,y\}, 0) \\ & \times \sin\Big(\phi_\theta(t) - (\phi_{\mathrm{z}}(t) + \frac{\pi}{2} + n\Delta)\Big) \Bigg], \end{aligned} \tag{4.85}$$

gives the overall magnetic field generated by the time-dependent currents inside the double-helix geometry.

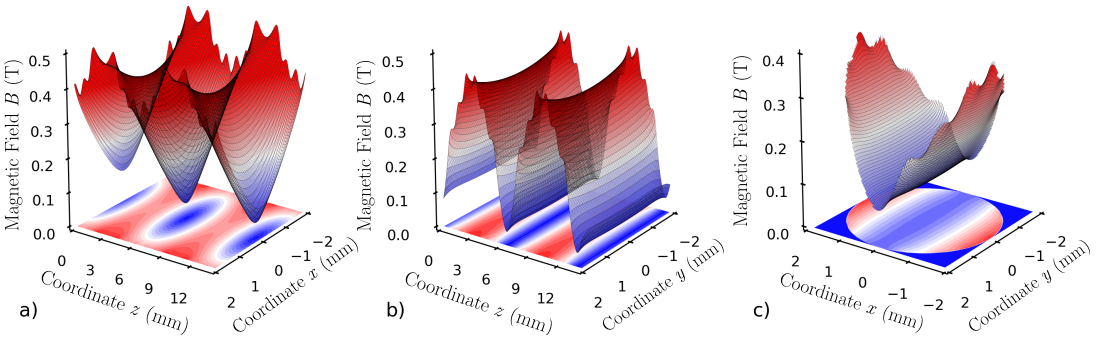

Figure 4.21: The magnitude of the magnetic field generated by a double-helix geometry. a) - c) Calculated magnitude of the magnetic field $|\mathbf{B}(x,0,z,0)|$, $|\mathbf{B}(0,y,z,0)|$, $|\mathbf{B}(x,y,0,0)|$ at $t = 0$ s, generated by currents $I^{\mathrm{n}}_{\mathrm{RH}}(t) = I_{\mathrm{RH}}\sin(\phi_{\mathrm{RH}}(t) + n\Delta)$ and $I^{\mathrm{n}}_{\mathrm{LH}}(t) = I_{\mathrm{LH}}\sin(\phi_{\mathrm{LH}}(t) + n\Delta)$ supplied to the n-th helix. $I_{RH} = I_{LH} = +300$ A.

The magnetic field $|\mathbf{B}(x,0,z,0)|$, $|\mathbf{B}(0,y,z,0)|$ and $|\mathbf{B}(x,y,0,0)|$ are calculated for a full double-helix geometry at a time $t = 0$ s from the equation 4.85 and shown in Figure 4.21 a), b) and c) respectively. The magnetic field is calculated with I_{RH} and I_{LH} set to $I_{\mathrm{RH}} = I_{\mathrm{LH}} = +300$ A. As can be seen from the Figure 4.21, magnetic field allows full confinement of particles in low-field-seeking states along the x and z coordinates, but almost no confinement along the y coordinate. This problem can be mitigated by introducing a nonzero rotational frequency f_θ on which the phase $\phi_\theta(t) = \omega_\theta t = 2\pi f_\theta t$ depends. Previously, by examining equations 4.62 and 4.63 it was concluded that the dynamics of the travelling magnetic wave in the longitudinal direction does not depend on $\phi_\theta(t)$. However, what does depend is the travelling-wave dynamics in the transverse direction.

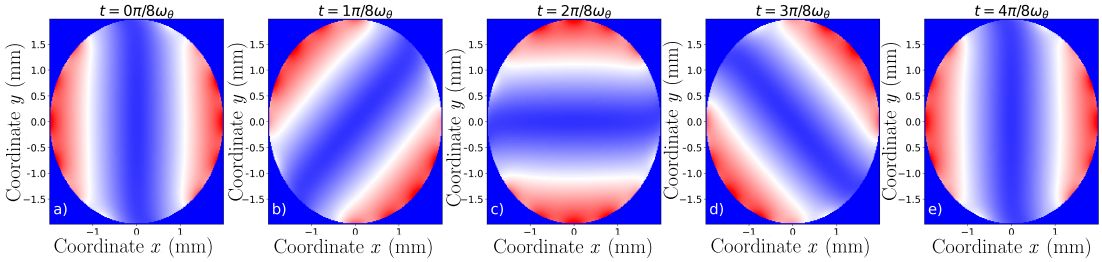

Figure 4.22: The magnitude of the magnetic field $|\mathbf{B}(x,y,0,t)|$ is calculated at the following times: a) $\frac{0\pi}{8\omega_\theta}$, b) $\frac{1\pi}{8\omega_\theta}$, c) $\frac{2\pi}{8\omega_\theta}$, d) $\frac{3\pi}{8\omega_\theta}$ and e) $\frac{4\pi}{8\omega_\theta}$, where $\omega_\theta = 2\pi \cdot 10$ kHz. The magnitude of the overall magnetic field rotates with an angular frequency ω_θ.

Change in phase ϕ_θ leads to change of orientation of the trap in transverse direction. This effect can be understood by following reasoning: assuming the stationary on-axis magnetic wave $\big(\phi_z(t) = 0\big)$, the magnetic field in transverse direction (at $z = 0$) generated by the n-th right- and left-hand oriented helix is given by:

$$\begin{aligned}\mathbf{B}_n(x, y, 0, t) =& \mathbf{B}^n_{\mathrm{RH}}(x, y, 0)\sin(\phi_\theta(t) + n\Delta) \\ &+ \mathbf{B}^n_{\mathrm{LH}}(x, y, 0)\sin(\phi_\theta(t) + n\Delta),\end{aligned} \tag{4.86}$$

where $\mathbf{B}^n_{\mathrm{RH/LH}}(x, y, 0)$ is the magnetic field in the x-y plane ($z = 0$) generated by the n-th right (left)-hand helix. Right and left hand oriented n-th helix are maximally contributing to the overall magnetic field when $\phi_\theta + n\Delta = \frac{k\pi}{2}, k = 0, 1, 2, ...$ If the phase $\Delta\phi_\theta(t)$ changes with time as $\phi_\theta = \omega_\theta t$, where ω_θ is the angular frequency, the time at which the n-th helices in both layers are maximally contributing is given by $t_n = \frac{k\pi - n\Delta}{2\omega_\theta}$. At the time $t_{n+1} = t_n + \frac{\Delta}{2\omega_\theta}$ maximal contribution comes from $(n + 1)$-th helices and the transverse field has been rotated by an angle Δ. In this way the transverse field can be rotated in time with an angular frequency ω_θ. The two phases $\phi_z(t)$ and $\phi_\theta(t)$ are independent from each other, leading to decoupling of the longitudinal and transverse motion of the trap. This feature prevents the significant losses due to the motional coupling which are characteristic in the conventional Stark and Zeeman decelerators [185]. Both phases are experimentally independently controllable parameters through the time dependent phases of the supplied currents $\phi_{\mathrm{RH}}(t)$ and $\phi_{\mathrm{LH}}(t)$.

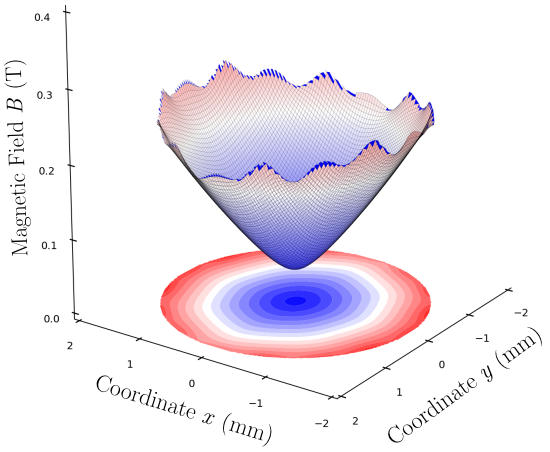

Figure 4.23: The overall magnitude of the magnetic field averaged over one rotation period.

The magnitude of the magnetic field $|\mathbf{B}(x, y, 0, t)|$ is calculated at the following times: $\frac{0\pi}{8\omega_\theta}$, $\frac{1\pi}{8\omega_\theta}$, $\frac{2\pi}{8\omega_\theta}$, $\frac{3\pi}{8\omega_\theta}$ and $\frac{4\pi}{8\omega_\theta}$, where $\omega_\theta = 2\pi \cdot 10$ kHz, see Figure 4.22 a) - e). The magnitude of the overall magnetic field can be seen to rotate with an angular frequency ω_θ. The parameter f_θ is a fully experimentally controllable parameter in the range f_θ = 0-10 kHz. By applying a non-zero rotational frequency f_θ a particle in a low-field-seeking state will experience confinement along all three coordinates. The overall magnitude of the magnetic field averaged over one rotation period is shown in Figure 4.23.

Additionally, it is possible to reduce the computational cost of calculating the overall magnetic field inside the double-helix geometry by calculating first the magnetic field contribution of all 16 helices from both layers in the x-y plane at $z = 0$. Let us consider the substitutions:

$$k_{\mathrm{RH}}(t) = \phi_\theta(t) + (\phi_{\mathrm{z}}(t) + \frac{\pi}{2}), \tag{4.87}$$

$$k_{\mathrm{LH}}(t) = \phi_\theta(t) - (\phi_{\mathrm{z}}(t) + \frac{\pi}{2}). \tag{4.88}$$

Then, from the equation 4.85 at $z = 0$ follows:

$$\begin{aligned}\mathbf{B}(x,y,0,t) = \sum_{n=0}^{15}\Bigg[&\mathbf{R}^{\mathrm{3D}}_{\mathbf{n\Delta}} \cdot \mathbf{B}^{\mathbf{0}}_{\mathrm{RH}}(\mathbf{R}^{\mathrm{2D}}_{\mathbf{-n\Delta}} \cdot \{x,y\},0)\sin\Big(k_{\mathrm{RH}(t)} + n\Delta\Big) + \\ &+ \mathbf{R}^{\mathrm{3D}}_{\mathbf{-n\Delta}} \cdot \mathbf{B}^{\mathbf{0}}_{\mathrm{LH}}(\mathbf{R}^{\mathrm{2D}}_{\mathbf{n\Delta}} \cdot \{x,y\},0)\sin\Big(k_{\mathrm{LH}(t)} - n\Delta\Big)\Bigg].\end{aligned} \tag{4.89}$$

Applying the trigonometric relation 4.40 gives:

$$\begin{aligned}\mathbf{B}(\mathbf{x},\mathbf{y},\mathbf{0},\mathbf{t}) = &\sin(k_{\mathrm{RH}}(t))\sum_{n=0}^{15}\mathbf{R}^{\mathrm{3D}}_{\mathbf{n\Delta}} \cdot \mathbf{B}^{\mathbf{0}}_{\mathrm{RH}}(\mathbf{R}^{\mathrm{2D}}_{\mathbf{-n\Delta}} \cdot \{x,y\},0)\cos(n\Delta) + \\ &+ \cos(k_{\mathrm{RH}}(t))\sum_{n=0}^{15}\mathbf{R}^{\mathrm{3D}}_{\mathbf{n\Delta}} \cdot \mathbf{B}^{\mathbf{0}}_{\mathrm{RH}}(\mathbf{R}^{\mathrm{2D}}_{\mathbf{-n\Delta}} \cdot \{x,y\},0)\sin(n\Delta) - \\ &- \sin(k_{\mathrm{LH}}(t))\sum_{n=0}^{15}\mathbf{R}^{\mathrm{3D}}_{\mathbf{n\Delta}} \cdot \mathbf{B}^{\mathbf{0}}_{\mathrm{LH}}(\mathbf{R}^{\mathrm{2D}}_{\mathbf{-n\Delta}} \cdot \{x,y\},0)\cos(n\Delta) + \\ &+ \cos(k_{\mathrm{LH}}(t))\sum_{n=0}^{15}\mathbf{R}^{\mathrm{3D}}_{\mathbf{n\Delta}} \cdot \mathbf{B}^{\mathbf{0}}_{\mathrm{LH}}(\mathbf{R}^{\mathrm{2D}}_{\mathbf{-n\Delta}} \cdot \{x,y\},0)\sin(n\Delta).\end{aligned} \tag{4.90}$$

It can be noted that in the equation 4.90 time dependence has been successfully decoupled from individual helices. Setting

$$\mathbf{H}^{\mathbf{1}}_{\mathrm{RH}}(x,y,0) = \sum_{n=0}^{15}\mathbf{R}^{\mathrm{3D}}_{\mathbf{n\Delta}} \cdot \mathbf{B}^{\mathbf{0}}_{\mathrm{RH}}(\mathbf{R}^{\mathrm{2D}}_{\mathbf{-n\Delta}} \cdot \{x,y\},0)\cos(n\Delta), \tag{4.91}$$

$$\mathbf{H}^{\mathbf{2}}_{\mathrm{RH}}(x,y,0) = \sum_{n=0}^{15}\mathbf{R}^{\mathrm{3D}}_{\mathbf{n\Delta}} \cdot \mathbf{B}^{\mathbf{0}}_{\mathrm{RH}}(\mathbf{R}^{\mathrm{2D}}_{\mathbf{-n\Delta}} \cdot \{x,y\},0)\sin(n\Delta), \tag{4.92}$$

$$\mathbf{H}^{\mathbf{1}}_{\mathrm{LH}}(x,y,0) = \sum_{n=0}^{15}\mathbf{R}^{\mathrm{3D}}_{\mathbf{n\Delta}} \cdot \mathbf{B}^{\mathbf{0}}_{\mathrm{LH}}(\mathbf{R}^{\mathrm{2D}}_{\mathbf{-n\Delta}} \cdot \{x,y\},0)\cos(n\Delta), \tag{4.93}$$

$$\mathbf{H}^{\mathbf{2}}_{\mathrm{LH}}(x,y,0) = \sum_{n=0}^{15}\mathbf{R}^{\mathrm{3D}}_{\mathbf{n\Delta}} \cdot \mathbf{B}^{\mathbf{0}}_{\mathrm{LH}}(\mathbf{R}^{\mathrm{2D}}_{\mathbf{-n\Delta}} \cdot \{x,y\},0)\sin(n\Delta), \tag{4.94}$$

equation 4.90 becomes

$$\begin{aligned}\mathbf{B}(\mathbf{x},\mathbf{y},\mathbf{0},\mathbf{t}) = &\sin(k_{\mathrm{RH}}(t))\mathbf{H}^{\mathbf{1}}_{\mathrm{RH}}(x,y,0) + \cos(k_{\mathrm{RH}}(t))\mathbf{H}^{\mathbf{2}}_{\mathrm{RH}}(x,y,0) - \\ &- \sin(k_{\mathrm{LH}}(t))\mathbf{H}^{\mathbf{1}}_{\mathrm{LH}}(x,y,0) + \cos(k_{\mathrm{LH}}(t))\mathbf{H}^{\mathbf{2}}_{\mathrm{LH}}(x,y,0).\end{aligned} \tag{4.95}$$

$\mathbf{H}^{\mathbf{1}}_{\mathrm{RH}}(x,y,0)$, $\mathbf{H}^{\mathbf{2}}_{\mathrm{RH}}(x,y,0)$, $\mathbf{H}^{\mathbf{1}}_{\mathrm{LH}}(x,y,0)$ and $\mathbf{H}^{\mathbf{2}}_{\mathrm{LH}}(x,y,0)$ are time-independent, which will prove useful in the context of the numerical trajectory simulations,

since they can be calculated a priori and stored in the computer memory. Finally, the overall magnetic field everywhere inside the double-helix geometry is then given by:

$$\begin{aligned}\mathbf{B}(x,y,z,t) = \; & \sin(k_{\mathrm{RH}}(t))\mathbf{R}^{\mathrm{3D}}_{\mathrm{kz}} \cdot \mathbf{H}^{\mathbf{1}}_{\mathrm{RH}}(\mathbf{R}^{\mathrm{2D}}_{-\mathrm{kz}} \cdot \{x,y\},0) + \\ & + \cos(k_{\mathrm{RH}}(t))\mathbf{R}^{\mathrm{3D}}_{\mathrm{kz}} \cdot \mathbf{H}^{\mathbf{2}}_{\mathrm{RH}}(\mathbf{R}^{\mathrm{2D}}_{-\mathrm{kz}} \cdot \{x,y\},0) - \\ & - \sin(k_{\mathrm{LH}}(t))\mathbf{R}^{\mathrm{3D}}_{-\mathrm{kz}} \cdot \mathbf{H}^{\mathbf{1}}_{\mathrm{LH}}(\mathbf{R}^{\mathrm{2D}}_{\mathrm{kz}} \cdot \{x,y\},0) + \\ & + \cos(k_{\mathrm{LH}}(t))\mathbf{R}^{\mathrm{3D}}_{-\mathrm{kz}} \cdot \mathbf{H}^{\mathbf{2}}_{\mathrm{LH}}(\mathbf{R}^{\mathrm{2D}}_{\mathrm{kz}} \cdot \{x,y\},0).\end{aligned} \tag{4.96}$$

One of the added hurdles in the process of Zeeman deceleration is the existence of the Majorana transitions [186, 83]. Particles confined in a magnetic field can escape by making spin-flip Majorana transitions due to a breakdown of the adiabatic approximation close to zero field. Our travelling-wave Zeeman deceleration method provides a way to mitigate the problem by applying a slightly different amplitude of currents in each layer. With decreasing the ratio $I_{\mathrm{RH}}/I_{\mathrm{LH}}$ the minimum of the magnitude of the magnetic field is increased away from the zero point. In this way, Majorana spin-flip transitions can be avoided during the deceleration process. The ratio should still be $I_{\mathrm{RH}}/I_{\mathrm{LH}} \approx 1$, since lower ratios lead to lower trapping depths. The magnitudes of the magnetic field along the deceleration axis for different $I_{\mathrm{RH}}/I_{\mathrm{LH}}$ ratios is illustrated in Figure 4.24.

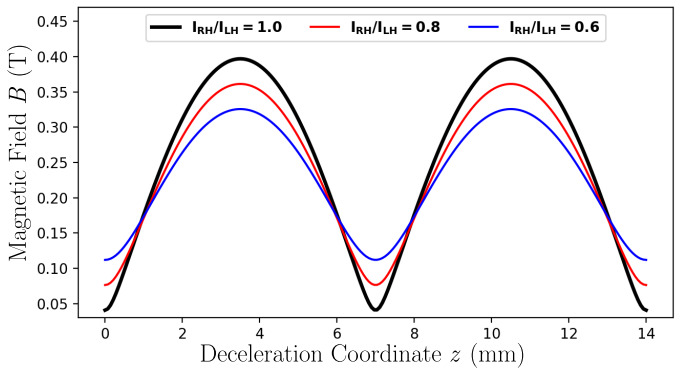

Figure 4.24: The magnitudes of the magnetic field along the deceleration axis for different $I_{\mathrm{RH}}/I_{\mathrm{LH}}$ ratios.

4.4.2 Numerical particle trajectory simulation program

Design and operation of the travelling-wave Zeeman decelerator heavily rely on accurate numerical trajectory simulations. Not only do they provide verification of the experimentally obtained results, but also give insight into which results are to be expected from a given system. For that reason, a three-dimensional numerical particle trajectory Monte-Carlo simulation code for the travelling-wave Zeeman decelerator was developed. The concrete numerical implementation was developed in Python programming language [183]. In the simulation, each particle's initial position and velocity are drawn from distributions defined by equations 4.97 and 4.98 after which the particle is propagated through the decelerator according to the initial conditions. The velocity distribution of a pulsed supersonic molecular beam just at the nozzle of a pulsed valve is typically modelled by an ellipsoidal drifting Maxwellian function [187, 188]:

$$f(\mathbf{v}) = \sqrt{\frac{m}{2\pi k_{\mathrm{B}} T_{||}}} \frac{m}{2\pi k_{\mathrm{B}} T_{\perp}} \exp\left\{ -\frac{m}{2k_{\mathrm{B}} T_{||}} (v_{||} - \bar{v})^2 - \frac{m}{2k_{\mathrm{B}} T_{\perp}} v_{\perp}^2) \right\} \tag{4.97}$$

where m is the mass of the particle, $k_{\mathrm{B}} = 1.3806 \cdot 10^{23}\ JK^{-1}$ is the Boltzmann constant and $v_{||}$ and $v_{\perp}$ are velocity components parallel and perpendicular to the deceleration axis. $T_{||}$ and $T_{\perp}$ correspond to the parallel and perpendicular temperature of the molecular beam, respectively, and $\bar{v}$ corresponds to the mean forward velocity. Spatial distribution of the particles is defined in the following way:

$$f(\mathbf{x}) = \frac{1}{\sqrt{2\pi\sigma_{||}}} \frac{1}{2\pi\sigma_{\perp}} \exp\left\{ -(\frac{x_{||}}{2\sigma_{||}})^2 - (\frac{x_{\perp}}{2\sigma_{\perp}})^2 \right\} \tag{4.98}$$

where $x_{||}$ and $x_{\perp}$ are components of the position parallel and perpendicular to deceleration axis, respectively. $\sigma_{||}$ and $\sigma_{\perp}$ are the parallel and perpendicular positional spread of the molecular beam. Generally, during the operation of the experiment, parameters $\bar{v}$, $T_{||}, T_{\perp}$, $\sigma_{||}$ and $\sigma_{\perp}$ are not fully known. Particles with a magnetic dipole moment μ_{eff} interact with an inhomogeneous magnetic field via the Zeeman interaction. As a result, the magnetic field exerts the following

force onto a particle:

$$\mathbf{F}(\mathbf{r},t) = m\mathbf{a}(\mathbf{r},t) = -\nabla \cdot \big(- \mu_{\mathbf{eff}} \cdot \mathbf{B}(\mathbf{r},t)\big), \tag{4.99}$$

where m is the mass of the particle and $\mathbf{a}(\mathbf{r},t)$ is the acceleration that the particle experiences at a position $\mathbf{r}$ and time t. Upon reaching the decelerator, particles enter into the inhomogeneous magnetic field. For each position of the particle $\mathbf{r}$ at a given time t, the overall magnetic field components are calculated using equation 4.96. Due to the time-dependence of the magnetic fields, they cannot be precalculated and stored in the computer memory, but have to be calculated on the fly for each particle at each time-step. Values of $\mathbf{H}_{\alpha}^{\beta}(x,y,0)$ are time-independent, and thus can be stored in the computer memory, which significantly reduces the computational cost of the simulation. Here $\beta = (1,2)$ and $\alpha = (\mathrm{RH},\ \mathrm{LH})$. Values of $\mathbf{H}_{\alpha}^{\beta}(x,y,0)$ are calculated on a 0.02 mm spaced grid. In the trajectory simulation, bilinear 2D interpolation is used to calculate the values of $\mathbf{H}_{\alpha}^{\beta}(x,y,0)$ in-between the grid points. The following interpolation technique is used: Let us assume that the position of the particle in the x-y plane is given by the coordinates $\{x,y\}$ which falls between the gridpoints $\{x_n,y_n\}$, $\{x_{n+1},y_n\}$, $\{x_n,y_{n+1}\}$ and $\{x_{n+1},y_{n+1}\}$, then $\mathbf{H}_{\alpha}^{\beta}(x,y,0)$ can be calculated from the following relation:

$$\begin{aligned}\mathbf{H}_{\alpha}^{\beta}(x,y,0) =& \frac{1}{(x_{n+1}-x_n)(y_{n+1}-y_n)} \begin{pmatrix} x_{n+1}-x \\ x-x_n \end{pmatrix} \times \\ & \times \begin{pmatrix} \mathbf{H}_{\alpha}^{\beta}(x_n,y_n,0) & \mathbf{H}_{\alpha}^{\beta}(x_n,y_{n+1},0) \\ \mathbf{H}_{\alpha}^{\beta}(x_{n+1},y_n,0) & \mathbf{H}_{\alpha}^{\beta}(x_{n+1},y_{n+1},0) \end{pmatrix} \begin{pmatrix} y_{n+1}-y \\ y-y_n \end{pmatrix}.\end{aligned} \tag{4.100}$$

the overall magnetic field at coordinates (x,y,z) and time t is then calculated by applying equation 4.96. The dynamics of the particle is calculated from equation 4.99. Rearranging equation 4.99 produces a set of second-order differential equations describing the motion of the particle along each coordinate:

$$\ddot{x}(t) + \frac{\mu_{eff}}{m}\frac{\partial}{\partial x}|\mathbf{B}(x,y,z,t)| = 0, \tag{4.101}$$

$$\ddot{y}(t) + \frac{\mu_{eff}}{m}\frac{\partial}{\partial y}\mathbf{B}(x,y,z,t)| = 0, \tag{4.102}$$

$$\ddot{z}(t) + \frac{\mu_{eff}}{m}\frac{\partial}{\partial z}\mathbf{B}(x,y,z,t)| = 0. \tag{4.103}$$

Partial derivatives $\frac{\partial}{\partial x_i}\mathbf{B}(x,y,z,t)|$, $x_i = x, y, z$ are calculated using the following approximation:

$$\frac{\partial}{\partial x}|\mathbf{B}(x,y,z,t)| \approx \frac{|\mathbf{B}(x+h,y,z,t)| - |\mathbf{B}(x,y,z,t)|}{h}, \tag{4.104}$$

$$\frac{\partial}{\partial y}|\mathbf{B}(x,y,z,t)| \approx \frac{|\mathbf{B}(x,y+h,z,t)| - |\mathbf{B}(x,y,z,t)|}{h}, \tag{4.105}$$

$$\frac{\partial}{\partial z}|\mathbf{B}(x,y,z,t)| \approx \frac{|\mathbf{B}(x,y,z+h,t)| - |\mathbf{B}(x,y,z,t)|}{h}, \tag{4.106}$$

where h is set to the spacing of the grid. The numerical integration of the equations 4.101-4.103 is carried out using the Velocity Verlet algorithm [189, 190]. The algorithm provides good numerical stability, time reversibility and preservation of the symplectic form of phase space at no additional cost compared to the Euler method [189]. The error of the algorithm at each time-step is $O(\Delta t^4)$ in position and $O(\Delta t^2)$ in velocity. If a particle is given at position $\mathbf{r}(t)$ and velocity $\mathbf{v}(t)$ at a time t, then the position $\mathbf{r}(t+\Delta t)$ and velocity $\mathbf{v}(t+\Delta t)$ of a particle at a time $t+\Delta t$ can be calculated with the Velocity Verlet algorithm in the following way:

$$\mathbf{r}(t+\Delta t) = \mathbf{x}(t) + \mathbf{v}(t)\Delta t + \frac{1}{2}\mathbf{a}(t)\Delta t^2 + O(\Delta t^4), \tag{4.107}$$

$$\mathbf{v}(t+\Delta t) = \mathbf{v}(t) + \frac{\mathbf{a}(t) + \mathbf{a}(t+\Delta t)}{2}\Delta t + O(\Delta t^2), \tag{4.108}$$

where Δt is the step size. In this way, the position and the velocity of the particle are updated n times from the initially defined values, where $n = int(T/\Delta t)$, $int()$ is a function which returns an integer value and T is the total time for which the simulation is run.

At this point, the numerical trajectory simulation still has a high computational cost since the calculation of the magnitude of the magnetic field has to be performed at each time-step for each particle. In order to improve the simulation time, the trajectory simulation was parallelized for computation on a graphics processing unit (GPU). The parallelization was executed with the use of Numba and Numba CUDA Python libraries [191]. Numba is a library that translates a

subset of Python and NumPy code into fast machine code. Algorithms compiled in Numba can approach speeds comparable to that of C or FORTRAN. Numba CUDA supports CUDA GPU programming by directly compiling a restricted subset of Python code into CUDA kernels and device functions. To illustrate the mathematical model of the decelerator described in this chapter, the following example is given. In the simulation, 10^5 OH molecules in the $X^2\Pi_{3/2}$ state are created at the entrance of the travelling magnetic wave. For the purpose of the simulation, only molecules in $M_J = 3/2$ states are created. Molecules are created within a cylinder ($r = 2$ mm, $h = 11$ mm) with a velocity spread of 45 m/s transversally and 90 m/s longitudinally, and 450 m/s mean forward velocity filling a 6-dimensional phase-space volume of 0.5×10^8 mm^3[m/s]^3. In the simulation, the decelerator is 1.792 m long followed by a 15 mm of the free-flight region after which molecules are detected. Results of the time-of-flight trajectory simulations can be seen in Figure 4.25. Molecules are decelerated for nine different final velocities, in the range of 449 m/s - 50 m/s, corresponding to deceleration values 0.25 km/s^2 - 55.8 km/s^2. Depending on the final velocity, it takes between 4.1 ms and 8.2 ms to traverse the deceleration distance. Owing to the multiple-trap geometry of the travelling wave, depending on the initial longitudinal phase-space volume of created molecules, many moving traps can be filled and successfully decelerated. This can be seen on the time-of-flight traces in Figure 4.25, especially at lower finally velocities where neighbouring traps are more separated in time.

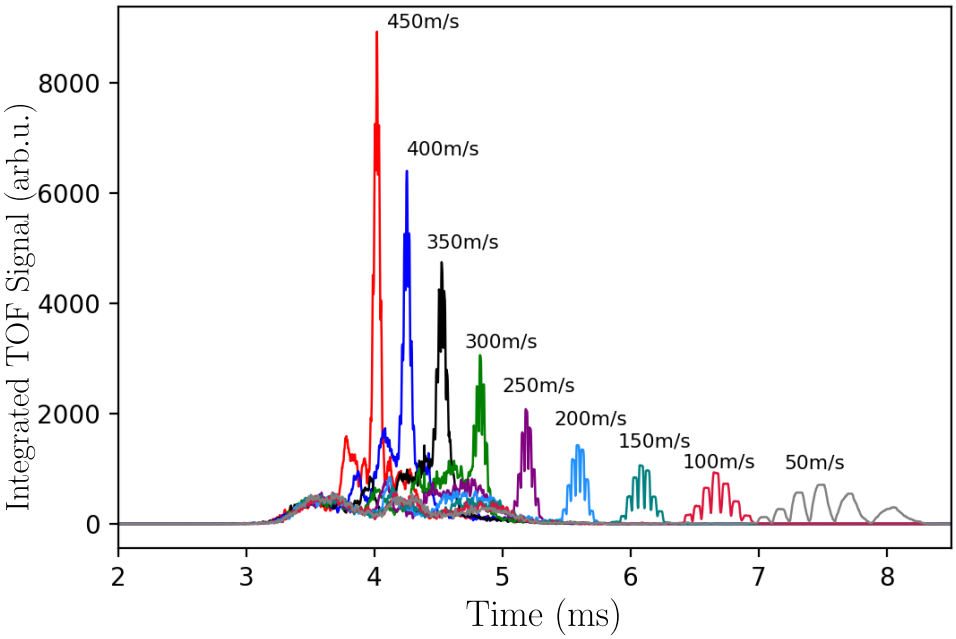

Figure 4.25: Time-of-flight traces of OH molecules in the $X^2\Pi_{3/2}(m_J = 3/2)$ state produced by the classical numerical particle trajectory simulations. Molecules are decelerated from 450 m/s mean forward velocity down to 400 m/s, 350 m/s, 300 m/s, 250 m/s, 200 m/s, 150 m/s, 100 m/s and 50 m/s.

4.4.3 Evolutionary algorithm for optimization of numerical trajectory simulations

Evolutionary algorithms are a class of stochastic optimization algorithms designed to find an optimal set of parameters with respect to a fitness function. In order to optimize conditions and better understand the experimental results, we developed a simple evolutionary algorithm that finds optimal values for the parameters of the molecular beam, $\mathbf{P} = \{T_{||}, T_{\perp}, \sigma_{||}, \sigma_{\perp}, \bar{v}\}$. The algorithm aims to minimize the discrepancy between the experimentally measured time-of-flight measurements and numerically calculated time-of-flight measurements.

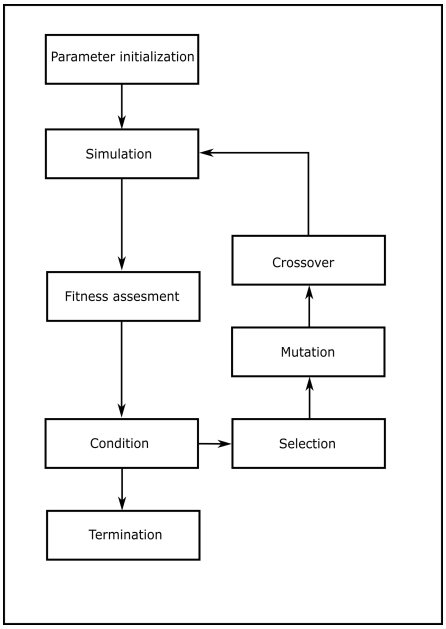

Figure 4.26: Flowchart of the algorithm. The population of N candidate solutions is initialized. Numerical particle trajectory simulations are run for each member of the population and the fittest members of the population are selected. The population in the next generation is created by applying mutation and crossover operators on the fittest members from the previous population. Numerical particle trajectory simulations are run for the new generation and its fitness is assessed. The procedure is repeated until the termination condition is met.

First, the optimization problem is addressed by defining an objective function that expresses the fitness of any potential solution. The chi-squared function:

$$\chi^2 = \sum_{k=1}^{K} \left(\frac{y_k - f(t_k; \mathbf{P})}{\sigma_k} \right)^2 \tag{4.109}$$

is used for fitness assessment. Here, y_k represents K measured data points in the time-of-flight measurement, with Gaussian error σ_k for each data point, and $f(t_k; \mathbf{P})$ K data points resulting from numerically calculated time-of-flight measurements, with initial parameters of the molecular beam defined by $\mathbf{P}$. Next, a population of N candidate solutions $\mathbf{P}_i^0$ is created, where each member of the population consists of l parameters $\mathbf{P_i^0} = \{p_{i,1}^0, ..., p_{i,l}^0\}$, and the superscript denotes the generation number. Typically in our optimization algorithm $N = 30$ and $l = 5$.

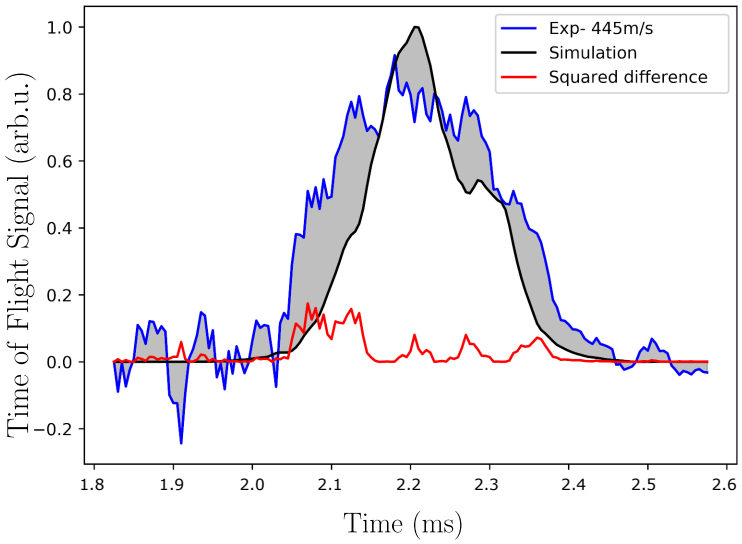

Figure 4.27: Illustration of the objective fitness function. The experimental time-of-flight profile is compared to one generated from the numerical trajectory simulations. The squared difference between the two profiles is plotted in red. The objective fitness function is calculated from equation 4.109.

Values for each parameter set are drawn from a normal distribution, $p_{i,j} = \mathcal{N}(p_{0,j}, \sigma_j)$, where $p_{0,j}$ and σ_j represent initial guesses for the mean and the standard deviation. Numerical particle trajectory simulations are then run for each member of the population and χ^2 is calculated for each member. Only $n_1 = 5$ members of the population for which χ^2 is minimal are kept and others are discarded, and overall χ^2_{tot} of n_1 members is calculated, $\chi^2_{tot} = \frac{1}{n_1}\sum_{i=1}^{i=n_1}\chi^2_i$. In the next generation, new N members in the population are created. The fittest n_1 members from the previous generation are kept the same, next $n_2 = 20$ new members in the population are created by first applying a mutation operator and then a crossover operator on the n_1 fittest members from the previous generation. The mutation operator picks a random member from n_1, $\mathbf{P^m_i} = \{p^m_{i,0}, ..., p^m_{i,l}\}$, and from this member one or more parameters $p^m_{i,j}$ are randomly drawn from a normal distribution, $p^{m+1}_{i,j} = \mathcal{N}(p^m_{i,j}, \sigma_j)$, where m and $m+1$ denote the previous and next generation, respectively. Crossover operator picks at random two parent members from n_1, $\mathbf{P^m_{i_1}} = \{p^m_{i_1,0}, ..., p^m_{i_1,l}\}$ and $\mathbf{P^m_{i_2}} = \{p^m_{i_2,0}, ..., p^m_{i_2,l}\}$. A new member is created by crossing-over one or more parameters from one parent to the other, $p^{m+1}_{i_{k_1},j} = p^m_{i_{k_1},j} \leftrightarrow p^m_{i_{k_2},j} = p^m_{i_{k_2},j}$. Finally, $n_3 = 5$ members are created by drawing

parameter values from initially defined normal distributions, $p_{i,j}^{m+1} = \mathcal{N}(p_{0,j}, \sigma_j)$. This step tries to minimize the chance that the algorithm gets stuck in local minima. Numerical trajectory simulations are run for the newly created population, χ^2 is calculated for each member of the population, n_1 fittest members are chosen again and χ^2_{tot} is calculated. Next, the exit condition for the algorithm is checked. If χ^2_{tot} does not improve from one generation to the other by at least some predefined minimum value (in our case this is set to 0.5%), the optimization is considered to have converged and the algorithm is terminated, otherwise the whole process is repeated. A flowchart of the algorithm is presented in Figure 4.26.

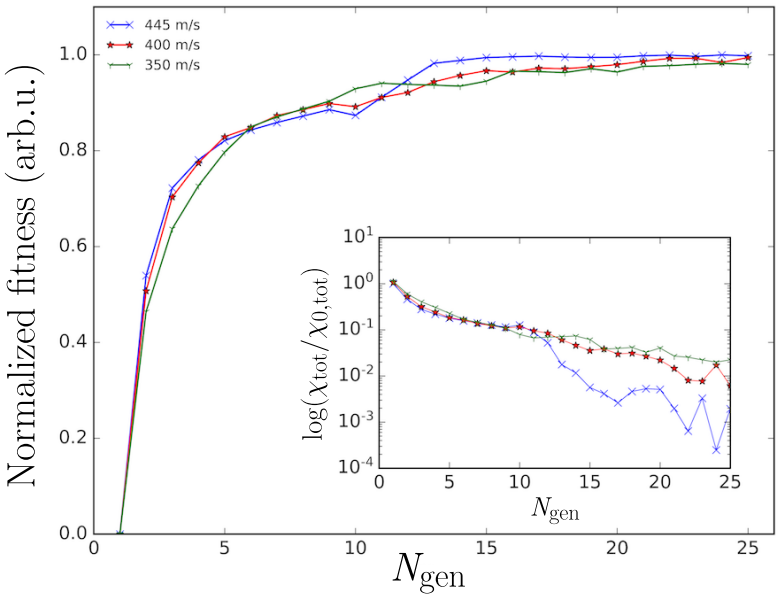

Figure 4.28: Results of the optimization procedure employed on the experimental time-of-flight measurements. The overall fitness is plotted versus generation number. Optimal parameters are reached in less than 20 generations. Inset: $\log(\chi_{tot}/\chi_{0,tot})$ versus generation number is shown.

Figure 4.28 shows results of the optimization procedure employed on the experimental time-of-flight measurements presented in Chapter 6 corresponding to 445 m/s, 400 m/s and 350 m/s final velocity. The normalized fitness defined as: $\mathcal{F}_n = 1 - \frac{\chi^2_{n,tot}}{\chi^2_{0,tot}}$ is plotted against the generation number. The algorithm converges close to an optimal set of parameters in less than 20 genera-

tions. A general trend of the improvement of the fitness follows a trend that is typical for evolutionary algorithm optimizers [192, 193, 194]. In the inset, $\log(\chi_{tot}/\chi_{0,tot})$ versus generation number is plotted. Somewhat better optimization is achieved for the guiding mode of the decelerator ($v = 445$ m/s). This is attributed to the differences arising from the real-life implementation of the travelling-wave Zeeman decelerator and numerical trajectory simulations. The optimized parameters that are produced by the algorithm agree reasonably to the values that are expected from a pulsed supersonic valve. Typical optimized values are: $\bar{v} = 447$ m/s (445 m/s), $T_{||} = 2.1$ K (1.9 K), $T_{\perp} = 2.6$ K, $\sigma_{||} = 83$ mm (105 mm), $\sigma_{\perp} = 0.5$ mm (0.5 mm). The values in parenthesis are the estimated experimental values. The algorithm reaches optimal values in less than 20 generations and produces time-of-flight simulations that agree well with time-of-flight experiments.

4.5 Conclusions

A novel design of a travelling-wave Zeeman decelerator was presented. The method relies on a double-helix wire geometry and time-dependent sinusoidal currents supplied to the geometry. The decelerator offers full confinement of the particles in low-field seeking Zeeman states during the whole deceleration process. The decelerator is capable to accelerate, decelerate or guide particles at their initial velocity along the deceleration axis. The implementation of the decelerator was described. Accompanying Monte-Carlo numerical trajectory simulations were described in detail together with an evolutionary algorithm for the optimization of the initial parameters of the simulation.

Chapter 5

Power electronics

5.1 Introduction

This chapter describes the current generation system that was developed for the travelling-wave Zeeman deceleration experiments conducted in our lab. In the previous chapter, the mathematical description of our implementation of a travelling wave Zeeman decelerator and the current profiles that are necessary for the creation of the travelling magnetic wave were described. Here, the way in which the generation of these currents has been implemented in the real experiment and technological choices which were considered and made during the design and implementation of the power electronics are described. The design considerations of the system are introduced, and functionalities of the parts of the system and the system as a whole is presented. Additionally, control strategies for producing high-power high-frequency current pulses are discussed.

5.2 General considerations in the design of the high-power arbitrary-waveform current generators

Here, the general principle of operation of the current generators developed for the Travelling-wave Zeeman decelerator is described. Deceleration of paramagnetic neutral atoms or molecules by Zeeman deceleration requires changes in the magnetic field of several Tesla over distances of a few millimeters. In addition, these magnetic fields are time-dependant, typically involving frequencies on the order of tens of kHz. For this purpose, we developed a high-power current generator, which produces bipolar currents up to 300 A amplitude, with frequencies ranging from 0-40 kHz. A representative waveform of the current is schematically depicted in Figure 5.1. Bursts of sinusoidal currents I_{L} of variable instantaneous frequency are generated with a repetition rate of $1/t_r$, typically 2Hz.

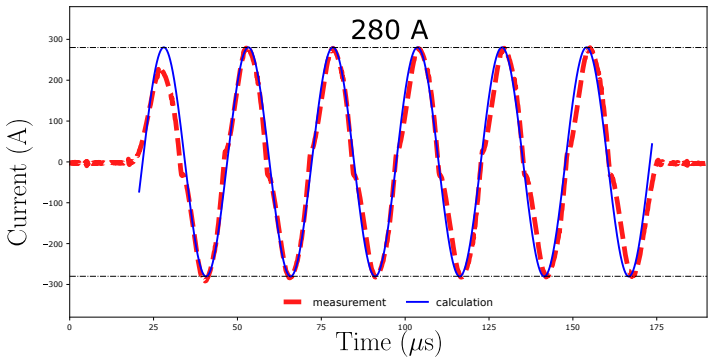

Figure 5.1: The sinusoidal current pulse (red) with an amplitude of 280 A and duration of ∼150 μs, generated by an arbitrary-waveform high-power current generator. The measured profile is compared to the expected profile (blue).

The desired current waveform is generated by a full H-bridge inverter [195] followed by a low-pass filter and the load itself (see Figure 5.2). The H-bridge inverter consists of four switches Q_1-Q_4 operating the bridge itself, and two switches Q_a-Q_b used to control the power supplied to the bridge. A low-pass filter is used to remove high-frequency components. Before the very first pulse, switches Q_1-Q_4

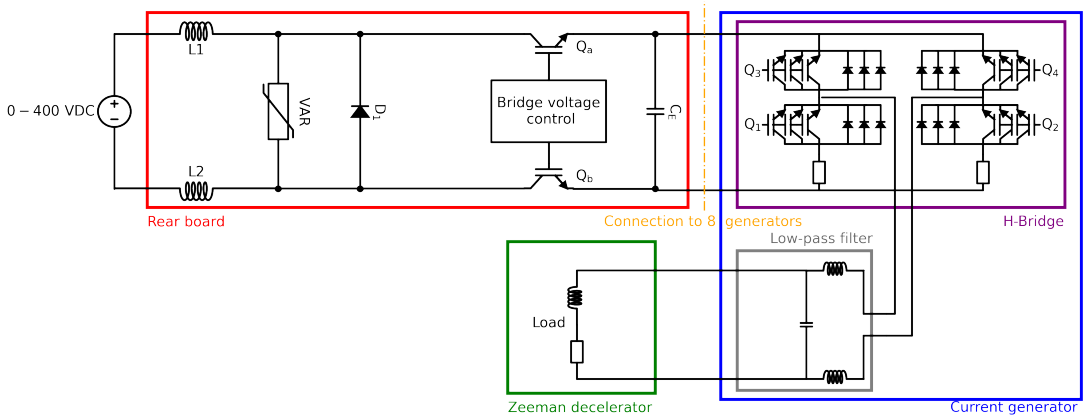

Figure 5.2: Simplified electric circuit diagram of the arbitrary-waveform current generator. A DC power supply loads the capacitor C_E on the rear circuit board. Switches Q_1-Q_4 in the H-bridge configuration on each current generator are alternately operated converting the DC voltage V_H across the bridge into the AC current. Higher harmonics of the resulting current are filtered by a low-pass filter before the current is supplied to the Zeeman decelerator modules.

are open, while switches Q_a-Q_b are closed, allowing the DC power supply to load the capacitor C_E (C_E = 1000 μF). The DC power supply is smoothly ramped up to avoid current peaks and voltage drops. At the beginning of the pulse, switches Q_a and Q_b are opened which isolates the DC power supply from the bridge. This allows use of a single power supply to operate up to eight current generators. Switches Q_1-Q_4 are alternately operated, in order to convert the DC voltage V_C of the capacitor C_E into an AC voltage V_H across the low-pass filter. The low-pass filter reduces the amplitude of the higher frequency components of V_H to only a few percent of the main frequency component. After each pulse, switches Q_1-Q_4 are maintained open, while Q_a and Q_b are closed again and capacitor C_E is recharged.

Two control strategies have been applied to the present generator: A three-level modified square wave control (MSW) and a pulse width modulation (PWM), see Figure 5.3. The MSW control consists of generating a modified square signal of three discrete values (-E, 0, +E) across the load at the effective frequency. The ratio between the main frequency component h1 and the odd harmonics (h3, h5, h7, ...) is tuned via the angle β defined as $\beta = \frac{\pi \Delta t}{T}$, where Δt is the time duration

of the zero level and T is duration of one period [196]. When $\beta = \pi/3$, h3 vanishes and the first undesired harmonic becomes h5, which amounts to 14 dB less than the fundamental component and is easily filtered out since its frequency is five times that of the fundamental. In addition, the peak of the current can slightly be tuned through the angle β at the cost of increased harmonic distortion of the signal. The MSW control implies limited power losses in the switches since switching occurs at the frequency ν of the desired current I_{L}. The MSW control is especially well adapted to the generation of high-frequency currents (20-40 kHz). The harmonics h5 and h7 lie far outside the bandwidth of the low-pass filter (cutoff at 40 kHz) and are therefore easily eliminated. The generation of low-frequency currents (0-20 kHz) requires a different control strategy because higher harmonics fall into the bandwidth of the low-pass filter. PWM consists of applying a square wave to the load, at a fixed frequency ν_{PWM}, which is chosen much higher than the frequency ν of the target current I_{L} [197]. The duty cycle of the square wave is modulated at the frequency ν. The voltage $\mathrm{V_H}$ across the bridge exhibits a fundamental frequency component at ν, and the strongest unwanted frequency components at ν_{PWM}-2ν and ν_{PWM}. Unwanted frequency components always lie around ν_{PWM}, and are then easily pushed outside the bandwidth of the low-pass filter. This control strategy can in principle be adapted to the generation of all frequencies in the range 0-40 kHz, as long as ν_{PWM} is chosen high enough. The downside is that the PWM produces more losses in the switches than the MSW method as more switching is required. As a consequence, the PWM control strategy is used for generating current pulses with a frequency lower than 20 kHz.

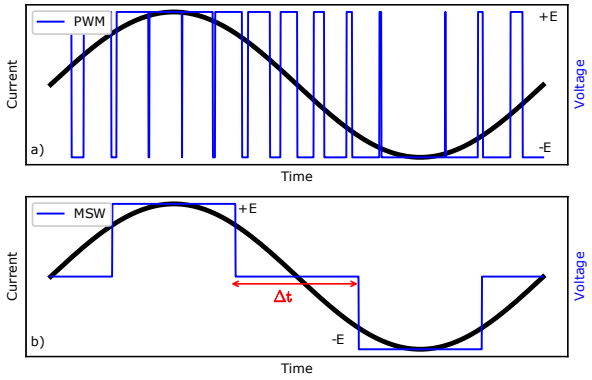

Figure 5.3: Two procedures in producing a lower frequency and a higher frequency current pulses. a) Pulse-width modulation (PWM): Square wave at a frequency $\nu_{\mathrm{PWM}} > \nu$ is applied to the load and modulated at frequency ν when $\nu < 20$ kHz. b) A three-level modified square wave (MSW): A modified square wave pulse consisting of three levels (+E, 0, -E) realized at frequency ν is applied to the load when 20 kHz $\leq \nu \leq$ 40 kHz. Voltage dependence across the H-bridge as a function of time is shown in blue, and the expected current in the load after applying the filtering is shown in black.

The goal of the low-pass filter is to reduce unwanted frequency components to less than 1% of the fundamental component. A third-order Butterworth filter, whose frequency response is given by $G(s) = 1/\sqrt{1+s^6}$, where s is the reduced angular frequency [198] was chosen. In the MSW control strategy, the filter reduces the h5 harmonic by 42 dB, thereby reducing the ratio h1/h5 from 20% to 0.16%. In the PWM control strategy, the minimum acceptable PWM frequency ν_{PWM} is set by the frequency component ν_{PWM}-2ν and the attenuation requirement. In order to generate frequencies up to 20 kHz, we have set $\nu_{\mathrm{PWM}} = 120$ kHz. The relative weights of ν_{PWM} and ν_{PWM}-2ν components with the respect to the fundamental are 0.4% and 0.2%, respectively. The schematic power-spectrum of the time-dependent voltage V_H across the H-bridge is shown in Figure 5.4.

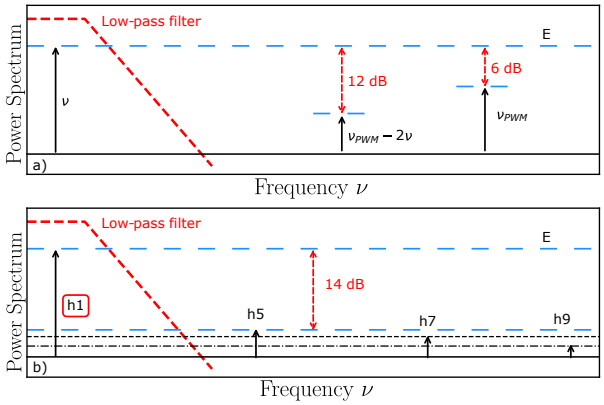

Figure 5.4: The schematic power-spectrum of the time-dependent voltage V_H across the bridge. a) Pulse-width modulation approach and b) modified square wave control approach. The attenuation function of the low-pass filter is shown schematically. Higher frequency components are exaggerated for reasons of clarity. The low-pass filter is chosen such that unwanted frequency components are efficiently filtered out.

Our application requires high peak currents, high frequencies and fast current changes. Therefore, electrical connections need to be treated with the utmost care. The capacitor C_E is mounted on a motherboard with a biplanar connection to the H-bridge. In order to minimize the voltage overshoots due to the connection inductance, this biplanar connection is realized through a very-low-impedance printed circuit board which exhibits a linear induction lower than 1 nH/m. For the same reason, the low pass filter is located as close as possible to the load and consists of only three components: two inductors and one capacitor. Due to the high currents flowing in the low-pass-filter, the internal magnetic field in the conductors is quite high, so low inductances of 1.2 μH and air-core inductors have been preferred in order to prevent significant core losses. Finally, the connection from the H-bridge to the load is about 1 m long and consists of a 50 Ω coaxial cable. This cable introduces a small additional inductance of 250 nH/m, which has been taken into account in the design of the low-pass filter.

5.3 Implementation of the power electronics in our travelling-wave Zeeman decelerator

So far, only the implementation of a single arbitrary-waveform current generator for the production of the single current pulse has been described. As previously expressed, the travelling-wave Zeeman decelerator described in this thesis consists of 16 individual modules. Each module consists of 32 individual wires. In order to produce the desired travelling magnetic wave, currents that are pulsed through the wires of each of the modules need to be generated with a (chirped) frequency specific to each module, the phase of which is specific to each wire within the module as is the initial timing of the pulse and the pulse duration. The details on these specifics can be found in Chapter 4. This means that in order to produce a travelling magnetic wave, it is necessary to have full control over the current pulses that are supplied into the deceleration modules. For that purpose, an arbitrary-waveform current generator system that is able to produce 8x32x8 individual current pulses was developed. The generator system consists of eight 19" racks that can house up to eight current generators and each current generator is able to produce eight individual current pulses addressed to different deceleration modules.

Let us start with the description of an implementation of the arbitrary-waveform current generator for the travelling-wave Zeeman decelerator. Previously, the principles of the design of the current generator were described. Next, the physical properties of the current generators and the technological choices that went into their design are described. Each current generator transforms a voltage V_H across the H-Bridge into the AC current by alternately operating switches Q_1-Q_4. After a careful look into the switching technologies available on the market, we settled on insulated gate bipolar transistors (IGBT) as our main choice. The IGBTs are appropriate for the range of different applications in power electronics e.g. switch-mode power supplies (SMPS), AC and DC motor drives, uninterruptible power

supplies (UPS), traction motor control, pulse-width modulation control, etc. The IGBTs are voltage control devices which require a relatively small voltage applied to the gate to stay in the conduction state. They can only switch the current in the forward direction, from collector to the emitter. Metal–oxide–semiconductor field-effect transistors (MOSFET) were another switching element that was considered for our purposes. The main advantages of the IGBTs over the MOSFETs is that they have a very low on-state voltage drop. This allows for a more compact design and lowers the cost of production making it economically more affordable. The IGBTs have high current conduction capabilities with low conduction losses. MOSFETs are known to exhibit faster switching than IGBTs, but are more subject to self-triggering. In order to limit the size of the single generator and make it more compact, IGBTs in a TO3-PN configuration rather than IGBTS with integrated heat dissipation pads were chosen. For our applications, the IGBT of choice was a Fairchild Semiconductors SGH80N60UFD model. Electrical characteristics of this IGBT are given in the Table 5.1. Features of this specific model include high-speed switching, low saturation voltage V_{CE} = 2.1 V @ I_C = 40 A and high input impedance. In order to maximize the current switching capacity of the current generators, each switch on the H-Bridge contains three IGBTs connected in parallel. For the purpose of avoiding overheating of the IGBTs during the operation, each IGBT is enclosed inside a heat dissipation unit, which is actively cooled during the operation. The temperature of each switch on the H-Bridge is monitored during the operation of the generator ensuring that the IGBTs are operating within the specified temperature range. Figure 5.5 a) depicts a schematic of the TO3-PN type of IGBT, while Figure 5.5 b) shows a representation of the IGBT in electrical circuit diagrams. G, C and E refer to G - gate, C - collector and E - emitter pin, respectively.

For our high-power current switching applications, thermal effects and thermal losses have to be carefully taken into account. In the most extreme mode of operation of the current generators, using the PWM control procedure with ν_{PWM}= 120 kHz, ν = 20 kHz and 0-peak current amplitude I = 300 A in the load, the losses amount to 230 W per switch. The losses can be decomposed into

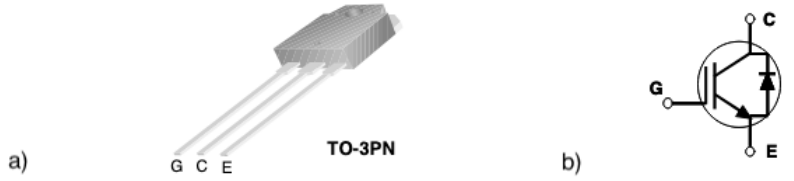

Figure 5.5: a) Drawing of the insulated gate bipolar transistor, model: SGH80N60UFD. b) Representation of the IGBT for electrical circuit diagrams. G - gate, C - collector, E - emitter.

three contributions: 40 W loss due to the conduction in the diodes, 60 W loss due to the conduction in the IGBT and 130 W loss during switching of the IGBT. To limit further losses, the low-pass filter is placed as close as possible to the H-bridge. The low-pass filter itself consists of two inductors (1.2 μH) and three capacitors (2.2 μF) connected in parallel. The electric circuit diagram of the low-pass filter is highlighted with a grey box in Figure 5.2, where three parallel capacitors are replaced with a single equivalent capacitor. After filtering, current pulses need to be supplied to the load. Since our decelerator is constituted of 16 separate modules, not all modules need to be supplied with current at all times. Switching times are calculated for each module according to the position of the synchronous molecule. For that reason, we developed the capability for each current generator to supply current to eight different channels, allowing for deployment of current pulses to eight individual modules at different instances of time. Each channel consists of two additional switches constituted of three parallelized SGH80N60UFD IGBTs and a high voltage, high-speed power MOSFET and IGBT driver, model: IR2127. The purpose of the IGBT driver is to drive the state of the IGBTs on each channel according to the input logic state supplied to it. The On/Off state of each channel is programmatically determined. For that purpose, each current generator is equipped with two digital-signal processing units (DSP). An embedded software was developed for each DSP with specific functionalities. The functionalities of each of the DSPs are described later in the text. In short, among other responsibilities DSP 1 is responsible for the calculation and storing of the current switching times for each current output channel, while DSP 2 is responsible for sending the switch On/Off logic states to

Table 5.1: Absoulute maximum ratings for the SGH80N60UFD

Symbol	Description	Value
V_{CES}	Collector-Emitter Voltage	600 V
V_{GES}	Gate-Emitter Voltage	±20 V
I_C	Collector Current @25 °C	80 A
I_C	Collector Current @100 °C	40 A
I_{CM}	Pulsed Collector Current	220 A
I_F	Diode Continuous Forward Current @100 °C	25 A
I_{FM}	Diode Maximum Forward Current	280 A
P_D	Maximum Power Dissipation @25 °C	195 W
P_D	Maximum Power Dissipation @100 °C	78 W
T_J	Operating Junction Temperature	-55 to + 150 °C
T_{stg}	Storage Temperature	-55 to + 150 °C
T_L	Maximum Lead Temp. for Soldering	300 °C

the IGBT driver on each of the output channels. For our applications, the DSP model dsPIC33FJ256GP510A from Microchip was chosen for both DSP 1 and DSP 2. Among other functionalities, it features a 16-bit dsPIC33F CPU with $40 \cdot 10^6$ instructions per second, independent watchdog timer, low-power management mode, two analog-to-digital converter modules, up to nine 16-bit timers and two Universal asynchronous receiver-transmitter (UART) modules. In our implementation a serial communication protocol RS-485 [199] was implemented over the UART modules between DSP 1 and DSP 2 and a central control unit (DSP 0). This describes the main features of a single arbitrary-waveform current generator. In order to keep the size of each generator as small as possible, they were designed on a compact Eurosize 100 mm x 160 mm printed circuit board (PCB). A photograph of an arbitrary-waveform current generator is shown in Figures 5.7 a) and b) and Figure 5.6 a). Figure 5.7 a) shows the front side of the generator, while the 5.7 b) shows the back side. In Fig 5.6 a), various elements of the current generator are outlined. A 280 A amplitude sinusoidal current pulse generated on a single current generator on all eight channels consecutively is measured with a current probe and shown in Figure 5.6 b).

As stated, the full system consists of eight 19" racks that can house up to eight current generators. Each rack additionally contains one main current generator control unit, an interconnection board and a rear board with the H-Bridge drive

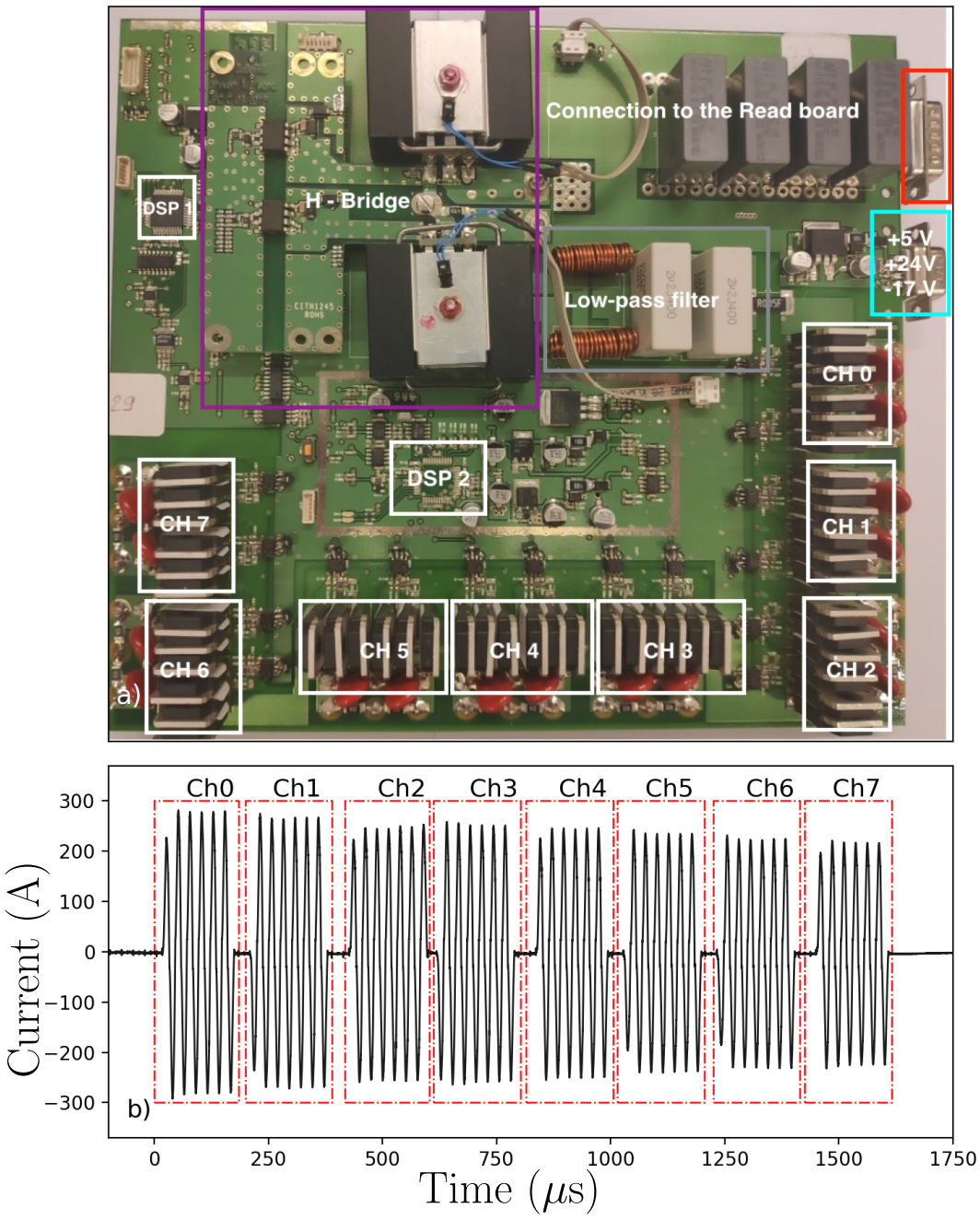

Figure 5.6: a) A single arbitrary-waveform current generator is shown. H-Bridge, low-pass filter and 8 current supply channels are highlighted. Each current generator is able to deliver the current to 8 different channels at a different instance of time. Channels are opened or closed programmatically thorough a multiplexer. b) Measurement of time-dependent current delivered to the decelerator module measured simultaneously at 8 channels of a single current generator.

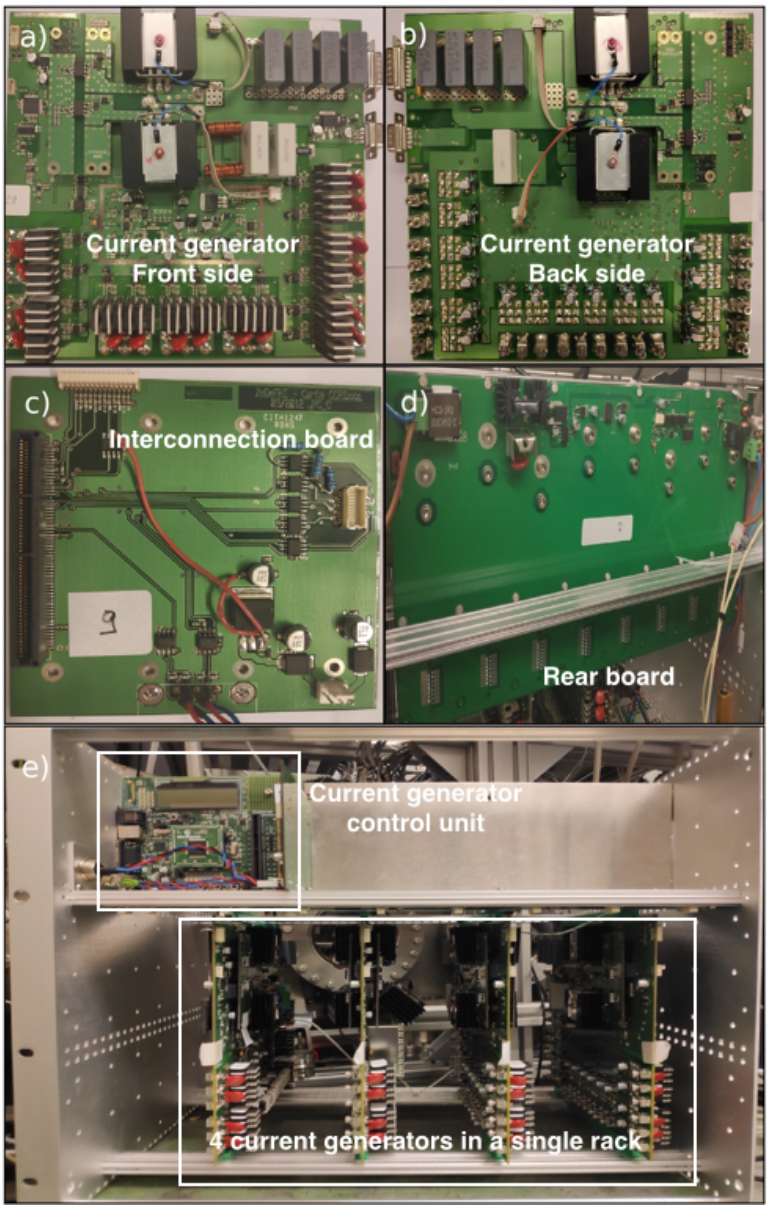

Figure 5.7: Implementation of the current generators for our travelling-wave Zeeman decelerator. a) and b) A compact 100 mm x 160 mm arbitrary-waveform current generator developed on a printed circuit board. a) Front side of the generator, b) back side. c) Interconnection board which acts as a communication intermediary between the PC, the main control unit, the rear board and different current generators. d) Rear board: part of the setup which is responsible for the control of charging the capacitor C_E. e) A single rack housing 4 current generators (with a possibility for up to eight). The main control unit ensures the operation of the whole system according to the appropriate specifications.

capacitors. The main current generator control unit is the part of the system that is responsible for the distribution of commands to the current generators

contained in the single rack and it is in charge of their synchronous operation, among other functionalities. It is based on a Explorer 16 development board from Microchip. The Explorer 16 development board is a flexible development system for Microchip's 16-bit PIC microcontrollers and supports devices from the PIC24 and PIC32 MCU and dsPIC families. Moreover, it includes an alpha-numerical 16x2 LCD display, interfaces to MPLAB ICD 3 in-circuit debugger, and RS-232 communication protocol and an TC1047A high-accuracy analog-output temperature sensor. In label classification used so far it is labelled as DSP 0. DSP 0 in each rack directly communicates with the control PC. For this purpose, we developed a LabView [182] software termed 'ZeemanCommander'. Depending on the initial parameters of the synchronous molecule and additional predefined parameters, the Labview software calculates parameters necessary for the creation of the travelling magnetic wave. These parameters are sent over the RS-485 protocol to the DSP 0 in each of the eight racks. DSP 0 in each rack then forwards these parameters to DSP 1 on each of the generators in their respective rack, where the current switching times are calculated and stored. A simplified schematic of the current distribution system is shown in Figure 5.8.

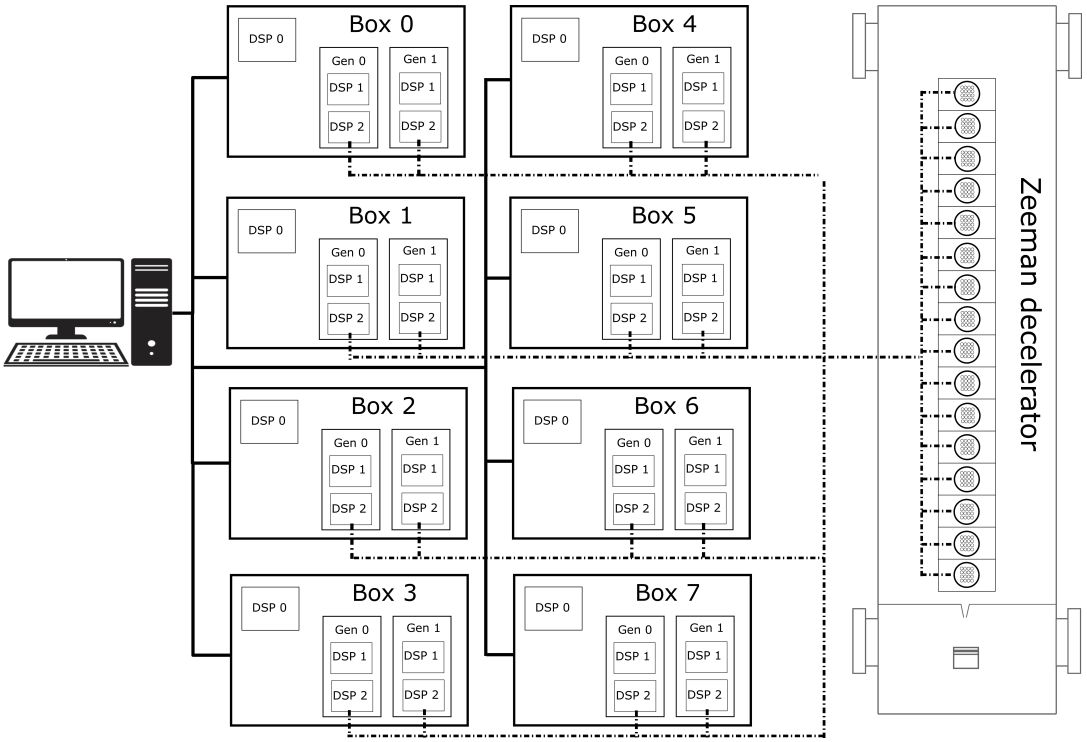

Figure 5.8: A simplified schematic of the current distribution system. The system consists of a control PC, 8 racks each housing up to eight current generators. Currents produced by the generators are distributed to the Zeeman deceleration modules.

Another important component of the current generation system that was developed is the rear board. The rear board houses the capacitors in which the energy for the current generation is stored. The rear board is connected to the 0-400 V DC power supply (Soerensen SG). Two MOSFET switches (IXYS, IXFK140N30P) are regulating the connection to the power supply. After every current pulse sequence, a trigger is emitted from DSP 0 to the switch driver (Broadcom, HCPL-3180) on the rear board at the repetition rate of the experiment, which opens the connection between the power supply and the capacitors and charges the capacitors. The opening time is preprogrammed as typically $\sim$70 ms. During the operation of the experiment, the voltage and current that is output from the power supply is directly measured on the power supply output and is plotted in the control software. Moreover, the voltage supplied to the capacitors which in turn defines the maximum current amplitude of the pulse is also programmatically controlled. More details on the voltage supply control

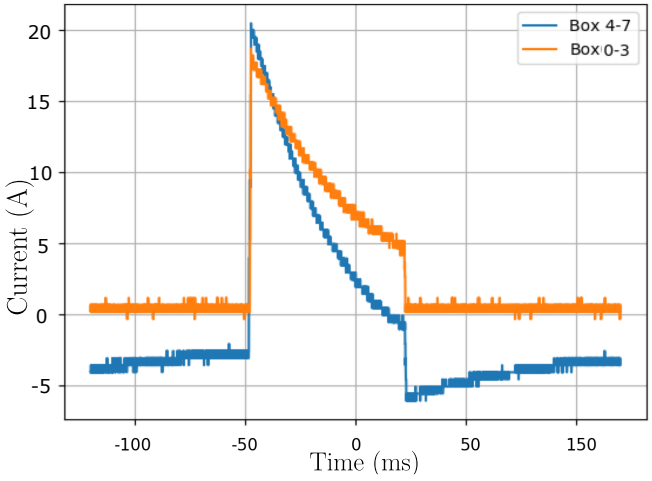

Figure 5.9: Current measured directly on the external DC power supply during the operation of the current generating system. A single pulse of current that is supplied from the external power supply to the capacitors of the four racks. The duration of the capacitors charging pulse is 70 ms.

software can be found in Chapter 4. Fig 5.9 displays the current and voltage that is supplied from the power supply to the capacitors C_E located on the rear board. Figure 5.9 a) shows a single pulse of current that is supplied from the external power supply to the capacitors measured with a current probe. As expected, the pulse displays an exponential decrease of the current as the capacitors recharge.

5.3.1 Generation of current switching sequences

Every rack, every current generator in each rack and every channel on each current generator is assigned an address, which is unique for every current output channel that is supplying current to the decelerator. Addresses are given as an 8-bit binary number: *mmmmmdcc*. The first three bits define $2^3 = 8$ addresses of the channels on the current generator, the fourth and fifth bit define the $2^2 = 4$ addresses of the generators in a single rack for the case when there are four current generators in a single rack. If there would be eight current generators in a single rack, an additional bit to define a unique address would be required. Moreover, the first five bits *mmmmmm* also define a unique address for each module. The last

three bits define the 2^3 addresses of each individual rack. The d bit determines if the produced current is to be fed to the left or right-hand oriented layer in the deceleration module, and the last two cc bits define $2^2 = 4$ addresses which determine the phase offset that the current pulses have relative to each other. The address assignment scheme is illustrated in Figure 5.10.

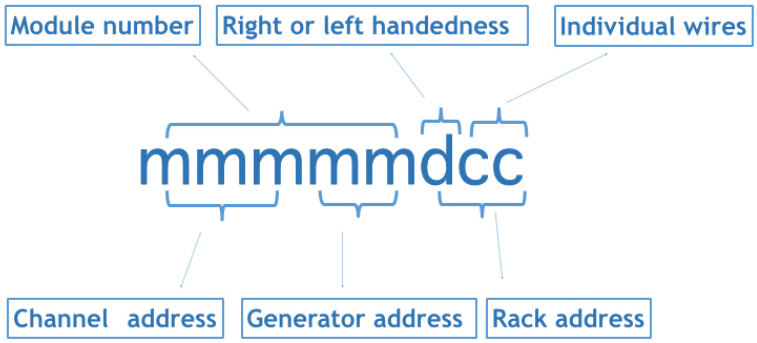

Figure 5.10: A 8-bit address scheme for assigning unique addresses to each current that is output to the decelerator. The first five bits ($mmmmm$) assign the deceleration module address, while the first three bits (mmm) also assign the channel address on a single current generator, and the last two bits (mm) the address of the current generator inside one rack. The last three bits (dcc) assign the address of each rack. The d bit determines if the produced current is to be fed to the left or right-handed oriented layer, and the last two bits (cc) determine the phase offset that the current pulse will have.

The addresses for both DSP 0 and DSP 1 are assigned during the programming of each device. Each DSP 1 calculates current switching times depending both on the DSP 0 address and DSP 1 address. The whole sequence from the first initialization of the parameters of the travelling magnetic wave down to the calculation of the current switching times is described next. In the ZeemanCommander program, the initial parameters v_I, v_F, N_{Stages}, P, t_{Delay}, f_θ of the travelling wave are input. Here, v_I is the initial velocity of the travelling wave, v_F is the final velocity of the travelling wave, N_{Stages} is the number of deceleration modules contained in the decelerator, P is a parameter which increases the duration of the current pulse such that the synchronous molecule experiences adiabatic transfer from one module to another, t_{Delay} is the time delay between the initial trigger for the start of the current switching sequence and the actual starting time of the

switching sequence, and f_θ is a parameter that defines the rotational frequency of the radial trapping field of the travelling magnetic wave. From these parameters, the new parameters p_1 and p_2 are calculated:

$$p_1 = kv_I, \tag{5.1}$$

$$p_2 = \frac{(v_F^2 - v_I^2)k}{16N_{Stages}\lambda}. \tag{5.2}$$

Here $k = \frac{2\pi}{\lambda}$, and $\lambda = 14$ mm is the helix periodicity. As previously introduced in Chapter 4, parameters p_1 and p_2 determine the initial velocity and deceleration of a travelling wave, respectively. The parameters p_1, p_2, $\omega_\theta = 2\pi f_\theta$ and t_{Delay} are then forwarded to the 8 current generator control units (DSP 0), which distributes the parameters to their respective current generators (DSP 1). Current switching time tables and current polarity tables are then calculated by each DSP 1 for each channel according to their addresses. First, the timings t_{min} and t_{max} for each channel are calculated:

$$t_{min} = \frac{-p_1 + \sqrt{\Delta_0}}{2p_2}, \tag{5.3}$$

$$t_{max} = \frac{-p_1 + \sqrt{\Delta_1}}{2p_2}, \tag{5.4}$$

where Δ_0 and Δ_1 are given by:

$$\Delta_0 = p_1^2 - 4p_2(\phi_0 - k(4(mmmmm)\lambda + P\lambda), \tag{5.5}$$

$$\Delta_1 = p_1^2 - 4p_2(\phi_0 - k(4(mmmmm + 1)\lambda + P\lambda), \tag{5.6}$$

Here, $mmmmm$ is the unique binary-converted-to-decimal address of each channel in each generator in a single rack as previously described, and ϕ_0 is a predefined phase offset of the travelling wave, typically set to 0. With t_{min} and t_{max} calculated, the time-dependent amplitude of the current is calculated:

$$A(t) = \sin\left(\omega_\theta t + (-1)^{Q_{dcc}}((p_2 t^2 + p_1 t + \phi_0) + \pi/2) + \frac{\pi}{4}\gamma_{dcc}\right). \tag{5.7}$$

Here $Q_{dcc} = f_{\text{ceil}}(\frac{dcc}{4})$ where f_{ceil} is the ceiling function, and γ_{dcc} is the remainder of division $\frac{dcc}{4}$, where dcc is the binary-converted-to-decimal address of each rack.

From the calculated time-dependent amplitude $A(t)$, switching timing tables and current polarity tables are calculated by applying either a pulse-width modulation control sequence or a modified-square-wave control sequence, depending on the frequency of $A(t)$, as previously described. Current switching sequences are then executed according to the timing tables and the current polarity tables for each channel on each generator. The current switching is initiated with an external TTL trigger pulse transmitted to each of the generator control units (DSP 0), from where the command to start the current switching procedure is then distributed to all the respective current generators (DSP 1). Examples of the current pulses measured with a current probe from the generators and channels with the address $mmmmm = 00000$ and different dcc address are given in Figure 5.11. Figure 5.11 a) shows current pulses that are to be supplied into the right-handed layer and Figure 5.11 b) currents that are to be fed into the left-handed layer.

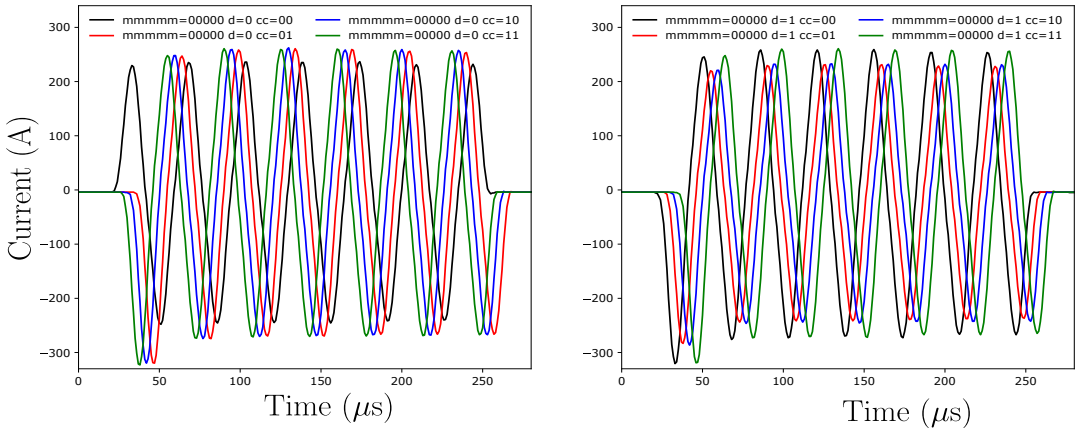

Figure 5.11: Measured current profiles produced in each rack by a channel with an address $mmmmmm = 00000$ of a single current generator. a) Currents supplied to the right-handed layer of wires and b) Currents supplied to the left-handed layer. Switching times and polarities of the currents are determined from the equations 5.3-5.7 and by applying either a PWM or MSW control scheme.

5.3.2 The power distribution system

The power distribution system was developed for the supply of electrical power to the whole current generating system. A schematic diagram showing the voltage distribution to different parts of the system is shown in Figure 5.12 a), and the

photograph of the power distribution system is shown in Figure 5.12 b). In total there are 5 different power supplies that power the whole system. Three different units (+24 V, +17 V and +5 V) supply the power directly to the different parts of each current generator boards. -15 V and +7 V are distributed over the interconnection board both as power source to the DSP 0 board and to power the DSP 1 circuitry on each generator. Additionally, -15 V are supplied to elements on the rear board. Each of these voltages is down-converted with various voltage regulators to the values that are necessary for the error-free functioning of the various elements to which the voltage is supplied.

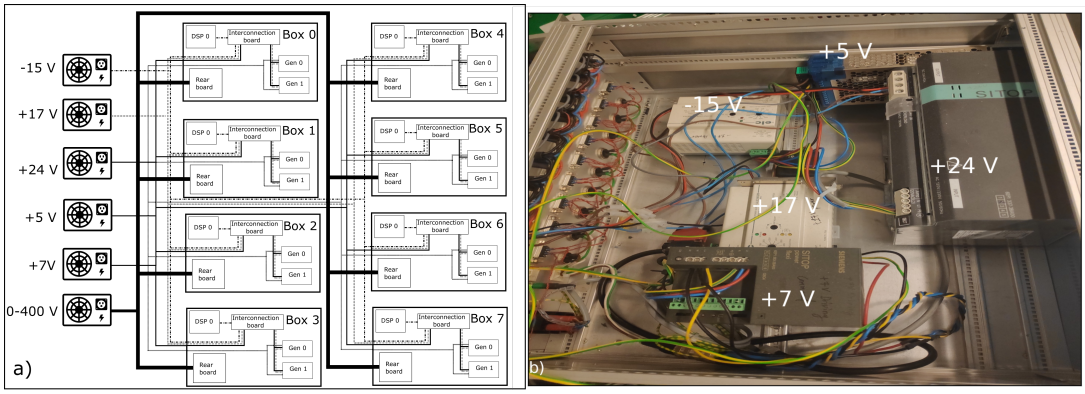

Figure 5.12: Different power sources responsible for supplying electrical power to the current generation system. a) Schematic diagram illustrating which parts of the current generating system are powered by which power supplies. b) A photograph of the power supply arrangement.

5.4 The embedded software for controlling the production of arbitrary current waveforms

In the previous section, some of the functionalities that were developed for the current generation system were described. In order to produce these functionalities, an embedded software system [200, 201] had to be developed. There are in total three distinct digital-signal processing units (DSP 0, DSP 1 and DSP 2) each with its own specialized functionalities. Here, in more detail some of the more important functionalities that have been implemented are described. When

developing programs for the embedded system, it is of outmost importance to pay attention to the specific architecture of the microcontroller that is to be programmed. As previously detailed, in our electronics design two different types of microcontrollers were used, namely dsPIC33FJ256GP710a for the DSP 0 boards and dsPIC33FJ256GP510A for the DSP 1 and DSP 2 boards. Although belonging to the same family of microcontrollers, there are differences in their architecture, e.g. DSP 0 being a 100-pin microcontroller and DSP 1 and DSP 2 being a 40-pin microcontroller. Programs for the microcontrollers were developed in MPLAB [202], which is a proprietary freeware integrated development environment for the development of embedded applications on PIC and dsPIC microcontrollers based on the C programming language. Programming of each microcontroller is carried out through the MPLAB ICD 3 in-circuit debugger and programmer. It connects to the PC via USB and to the device through the ICSP [203]. Each program first loads the working state at the power-on of each device. The clock frequency is configured, which in our case for each microcontroller is set to 40 Mhz, then functionalities on the microcontroller pinout are set up and analog-to-digital and digital-to-analog conversion functionalities are initialized. In the end, the RS-485 communication protocol is established between different microcontrollers. DSP 0 is the center of the communication protocol. It receives messages from the control PC and passes instructions to DSP 1. It also indirectly communicates with DSP 2, where messages to DSP 2 are transferred over DSP 1. The communication is established over a universal asynchronous receiver-transmitter (UART) device, with a data transmission baud rate of $5 \cdot 10^5$ baud. It is not unusual that there are at times spurious errors in the raw data that is emitted over the communication protocol. In order to deal with unwanted errors, a cyclic redundancy check (CRC) was implemented into the communication protocol. This is an error-detecting code commonly used in digital networks to detect accidental changes to raw data. There exist different implementations of the CRC protocol. For our purposes, protocol CRC-32 was chosen. Details on the protocol itself and the implementation of the protocol can be found in [204, 205, 206]. After the power on and initialization of each microcontroller, the main loop of the program

is executed. It consists of two modes of operation: 1. a normal mode which executes if everything is running according to the defined specifications, and 2. an error mode which engages if a predefined error has occured. There are a few different sources of errors that if unchecked could potentially lead to permanent damage to the current generators or a whole current generation system. Errors are generated through interrupt signals on specific pins on each microcontroller. Some of the errors are:

- **Shortcut halfbridge:** This error comes up when the current that is extracted from the capacitor bank on the rear board exceeds a predefined limitation
- **Overvoltage HV:** This error happens when the voltage across the capacitor bank exceeds the limitation
- **Error Sequence:** Before current switching times are calculated on each current generator, it is necessary to check that the switching times are within the switching capabilities of the current generator. If this is not the case, calculation of the switching times is stopped.
- **Unload capas:** If there is a problem detected on the capacitors, this error handler will request the capacitors to be unloaded.
- **Gene missing:** This error will be generated every time the communication between the DSP 0 and any of the DSP 1 boards in a single rack is broken.
- **Reset box:** This is not an error per se, but a functionality that if an error occurs the device can be restarted.

Next, a short list of the most important functionalities developed for each of the DSPs is given. A schematic diagram of some of the processes is given in Figure 5.13. The diagram shows where each process originates, and how it is communicated to other DSP units. The most important functionalities are:

- **RS-485 protocol:** This protocol was implemented for communication between different DSPs. DSP 0 is the main control unit which passes messages and requests between the PC, DSP 1 and DSP 2. Some of these messages or requests are: an update of the full status of the current generators or the status of individual current output channels on each generator, testing the presence of each current generator, testing the status of the current sequence on each generator, status of the measured temperatures on the H-Bridge, reset of the generators, request for the content of the DMA buffer.

- **LCD screen display:** Each DSP 0 comes with an integrated 16x2 LCD display which is programmed for displaying the status of the device during operation. In the normal mode of operation, the decimal *dcc* address of each rack is shown. Once an error occurs, the source of the error is displayed on the screen.

- **Temperature measurement:** The current switching on the H-Bridge is the main source of power losses in the system. Losses in the switches are manifested as a temperature increase on the switches. For that reason, the temperature on all four switches on each current generator is monitored during operation. This process is controlled by DSP 2. Requests from the ZeemanCommander software can be sent to the whole system, and the temperatures of every switch on the H-Bridges of each generator will be recorded and transmitted to the software where they can be read out. If the temperature of the switches reaches $T > 70$ °C, current switching is suspended.

- **Fan control:** Since the power losses in the switches can lead to the overheating, every H-Bridge is additionally equipped with a cooling fan. If the measured temperature on the current switches reaches $T > 30$ °C, the fans are switched on.

- **DMA buffer:** For the decelerator described in this thesis, it is necessary to individually control 128 current pulses. It is not always possible to

know that each current pulse, due to some fault, is operating within specified parameters at all times. For that reason, the current generators have integrated current measurement capabilities. By request from the Zeeman-Commander software, current profiles for each generator and every channel on the generator can be recorded into a DMA buffer, and the data can be transmitted to the software where it is plotted.

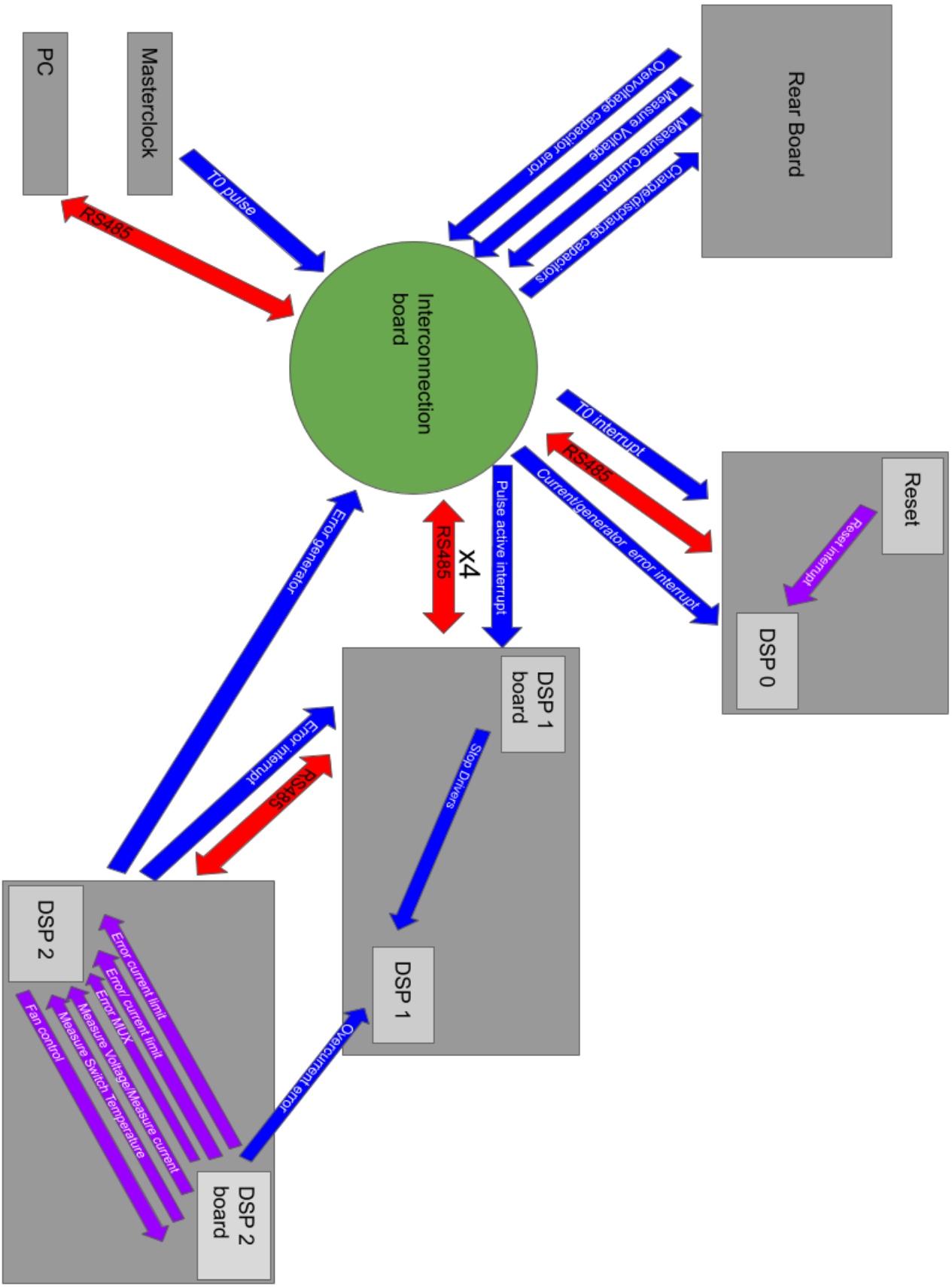

Figure 5.13: Schematic diagram of some of the processes developed for the current generation system.

5.5 Conclusions

A current generation system developed for the travelling-wave Zeeman deceleration experiments has been described. The system consists of a control PC, eight subsystems for the current generation where each subsystem can house up to eight current generator boards, an external power supply, and an external triggering system. Programmable arbitrary-waveform current generators were developed with the capability of generating arbitrary current pulses with current amplitudes up to 300 A with frequencies of the pulses in the 0-40 kHz range. Two control strategies for current generation were implemented, a pulse-width modulation and a three-level modified square wave strategy. An extensive embedded software was developed for the three digital-signal processing units in order to ensure the reliable and controllable generation of the current pulses.

Chapter 6

Guiding and deceleration of OH radicals

6.1 Introduction

In order to demonstrate the operation of the travelling-wave Zeeman decelerator, a series of experiments were conducted in which we either guided or decelerated supersonic beams of OH molecules in their ground state. The OH molecules were decelerated from an initial forward velocity of 445 m/s down to a range of velocities spanning from 444 m/s to 349 m/s. The experimental results were interpreted by numerical trajectory simulations. In addition, the phase-space behaviour during the deceleration process was analyzed. Longitudinal and transverse motion of particles during the deceleration process was examined, and 2D phase-space acceptance in each direction was quantified. Furthermore, 6D phase-space acceptance of the decelerator was characterized.

6.2 Characterization of the phase-space stability of decelerated OH radicals

For the purpose of the following discussion, the traveling wave decelerator mechanism developed in Chapter 4 is briefly summarized. By applying time-dependant

currents of the following form to the double-helix coil geometry:

$$I_{\mathrm{RH},n}(t) = I_{\mathrm{RH}} \sin(\phi_{\mathrm{RH}}(t) + n\Delta) \tag{6.1}$$

$$I_{\mathrm{LH},n}(t) = I_{\mathrm{LH}} \sin(\phi_{\mathrm{LH}}(t) + n\Delta) \tag{6.2}$$

to the n-th wire (n=0,...,15) in each layer, an on-axis magnetic field magnitude of the form of a traveling wave is obtained:

$$|\mathbf{B}(x = 0, y = 0, z, t)| = |B_0 \sin(kz - \phi_z(t))|. \tag{6.3}$$

$I_{RH} = I_{LH} = +300\ A$ denote the amplitude of the current in the right and left handed layers, respectively. $\phi_{RH}(t)$ and $\phi_{LH}(t)$ are the time-dependant phases of the currents fed into the right-handed and left-handed layer, $\phi_{RH}(t)$ and $\phi_{LH}(t)$ are related to $\phi_z(t)$ and $\phi_\theta(t)$ in the following way:

$$\phi_{RH}(t) = \phi_z(t) + \phi_\theta(t) \tag{6.4}$$

$$\phi_{LH}(t) = \phi_z(t) - \phi_\theta(t). \tag{6.5}$$

Here $\phi_z(t) = p_2 t^2 + p_1 t + p_0$ defines the time-dependent position of the minima of the magnetic field, and $\phi_\theta(t) = \omega_\theta t = 2\pi f_\theta t$ the orientation of the magnetic field in the $x - y$ plane at a given instance of time t, where f_θ is an experimentally controllable parameter. The parameters a/k and b/k denote the deceleration (or acceleration) and the initial velocity of the traveling wave. $k = 2\pi/\lambda$, where $\lambda = 14$ mm is the periodicity of the helices. c is a free parameter, corresponding to an arbitrary phase shift of the traveling wave at t=0 s. With an appropriate choice of parameters a and b, the travelling magnetic wave can decelerate, accelerate or propagate with a constant velocity in both $+z$ and $-z$ directions. Setting parameter $f_\theta = 0$ kHz keeps the orientation of the magnitude of the magnetic field stationary in the x-y plane, while setting the parameter $f_\theta > 0$ rotates the field with an angular frequency $\omega_\theta = 2\pi f_\theta$.

Particle dynamics inside the traveling magnetic wave are discussed on the example

of OH molecule in the $X^2\Pi_{3/2}$ state. The potential energy that the OH molecule experience both in the longitudinal and the transverse directions is shown in Figure 6.1. In Figure 6.1 a), the potential energy that molecules experience along the deceleration axis is plotted, both for particles in $m_J = 1/2$ and $m_J = 3/2$ states. The potential energy is plotted at time $t = 0$ s along the deceleration coordinate for the length of the single module. As illustrated, eight individual traps are formed along the distance of the module for the static traps. Once the travelling wave is implemented, for each trap that reaches the end of the module a new trap will be created at the beginning of the module. Depending on the switching time duration, many additional traps can be created extending the possible longitudinal phase-space volume that can be accepted by the decelerator. The maximum of the trapping potential along the deceleration axis for OH in the $m_J = 3/2$ state is ≈ 0.25 cm^{-1}. In Figure 6.1 b) and c) the transverse trapping potentials are plotted for the $m_J = 3/2$ and $m_J = 1/2$ states, respectively. The full black line represents the calculated potential plotted along the x-axis, the broken black line the calculated potential along the y-axis. This corresponds to the stationary transverse trapping potential, where $f_\theta = 0$ kHz. The red trace corresponds to the average trapping potential in both radial directions when a rotation to the transverse trapping potential is applied, $f_\theta > 0$, where typically $f_\theta = 10$ kHz. Details on how stationary and rotational transverse traps are produced can be found in Chapter 4.

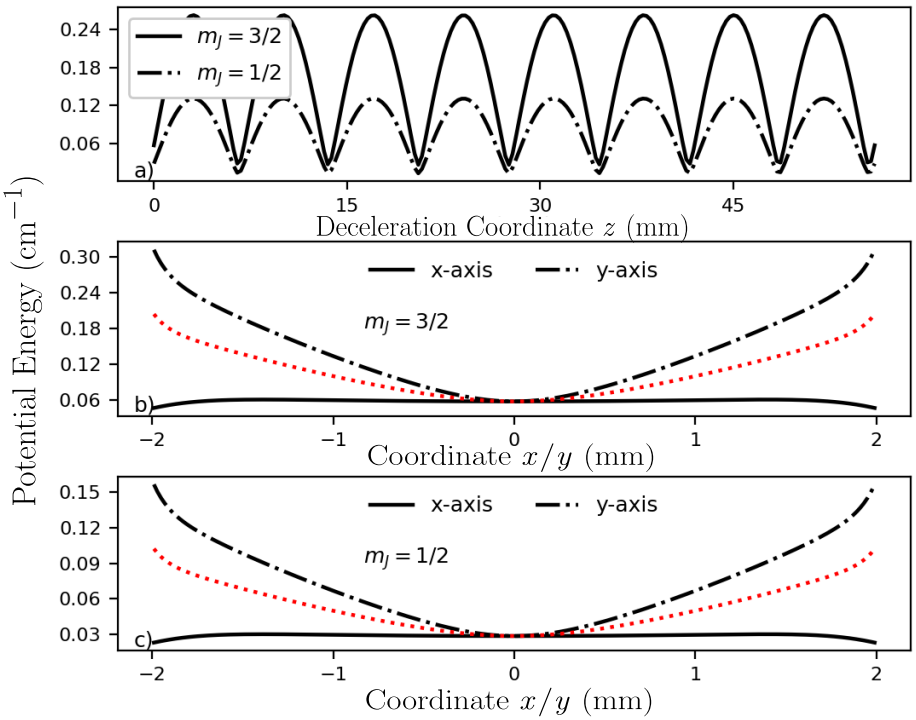

Figure 6.1: The calculated potential experienced by an OH molecule in the $X^2\Pi_{3/2}$ state inside the travelling-wave Zeeman decelerator. The potential energy is calculated for the low-field seeking states $m_J = 3/2$ and m_J=1/2. a) Potential at t=0 s is plotted on-axis for a single deceleration module for both low-field seeking states $m_J = 1/2$ and 3/2. b) and c) Calculated potential energy along transverse directions. Potential energy of the stationary ($f_\theta = 0$ kHz) transverse trap is shown in black, an average potential energy of the rotating ($f_\theta > 0$) trap is shown in red.

An important aspect of every decelerator is the phase-space stability during the deceleration process and the maximum phase-space acceptance of the decelerator. Here the phase-space characteristics of the travelling wave Zeeman decelerator are discussed in more detail. Discussion is separated into two parts: in the first part, the on-axis motion of the particles in the traveling wave and in the second part the transverse motion is discussed. The phase-space acceptance in each of the directions is characterized and the full 6D phase-space acceptance of the decelerator is calculated. Calculations are compared to the results of the numerical trajectory simulations.

6.2.1 Longitudinal motion in the trap and 2-dimensional phase-space stability

The aim of the decelerator is to produce samples of atoms or molecules at low kinetic energies with the maximum phase-space density. Since the phase-space density cannot be increased with conservative forces [207], the aim of every decelerator is to achieve the maximum phase-space acceptance for highest deceleration and in that way maximizing the fraction of the initial molecular package that is to be decelerated. First, the longitudinal 2D phase-space stability of the Traveling-wave Zeeman decelerator is characterized. By definition, a synchronous molecule is a molecule that is traveling with the same velocity as the traveling wave and is located at the center of the trap. In the frame of reference of the traveling wave, the synchronous molecule is stationary at the bottom of the potential well and by definition it is not affected by the potential. Contrary to the synchronous molecule, the non-synchronous molecule is non-stationary in the frame of reference of the traveling wave. Depending on its total energy $E = E_{kin} + V(z_0)$, it either oscillating inside the trapping potential if $E < E_{max}$ or flies out of the trapping potential if $E > E_{max}$. E_{max} is the maximum energy a particle can have in order for it to be confined by the trapping potential. The potential energy that a non-synchronous OH molecule in the $X^2\Pi_{3/2}(m_J = 3/2)$ state experiences in the longitudinal direction in the frame of the traveling wave is illustrated in Figure 6.2 a). A synchronous molecule is illustrated with a red dot, while a non-synchronous molecule is illustrated with a black dot. Once traveling wave is decelerated, in the frame of reference of the traveling wave, particles experience a fictitious force $F_{fict} = ma$ which leads to the deformation of the trapping potential. This effect can be seen in Figure 6.2 b). The trap becomes more asymmetric for higher deceleration, limiting the maximum energy E_{max} that particles need to have in order to stay trapped within the trapping potential, and consequently limiting the number of molecules that can be efficiently decelerated. The trapping potential is shown for the following accelerations: 0.25 km/s^2, 22.51 km/s^2, 39.20 km/s^2, 50.30 km/s^2 and 55.83 km/s^2. Positive values denote deceleration

in the $+z$ direction.

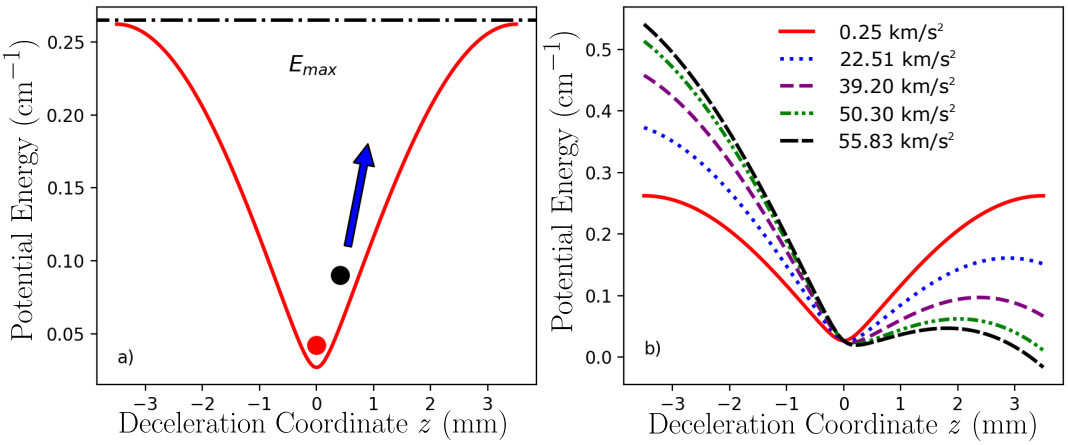

Figure 6.2: The potential energy experienced by a synchronous and a non-synchronous molecule in the frame of reference of the traveling magnetic wave calculated for OH in $X^2\Pi_{3/2}(m_J = 3/2)$ state. a) Synchronous (red) and non-synchronous (black) molecules in the potential of the traveling magnetic wave traveling at a constant velocity. b) The potential energy that molecules experience due to the fictitious force when deceleration is applied to the traveling magnetic wave.

The total energy of the molecule in the traveling magnetic wave in the frame of reference of the traveling wave is given by:

$$E = \frac{mv^2}{2} + \mu_{eff}\mu_B B(z) + maz, \tag{6.6}$$

where m is the mass of the molecule, v is the instantaneous velocity of the molecule in the traveling-wave frame of reference, μ_{eff} is the effective magnetic-dipole moment, μ_B is the Bohr magneton, $B(z)$ is the applied magnetic field at position z and a is the acceleration (deceleration) of the traveling wave. Phase-space stability diagrams are obtained from equation 6.6 by exploring v-z space for constant values of energy. The phase-space stability diagrams are illustrated in Figure 6.3. Phase-space stability diagrams are calculated for OH in $X^2\Pi_{3/2}(m_J = 3/2)$ state and for the following decelerations: a) 0.25 km/s^2, b) 22.51 km/s^2, c) 39.20 km/s^2, d) 50.30 km/s^2, e) 55.83 km/s^2 and f) - 27.59 km/s^2. The diagrams are shown for two consecutive traveling traps. In Figure 6.3, isoenergetic lines are shown in black. Isoenergetic lines for which molecules will have stable trajectories

over the whole deceleration process are the lines that close unto itself, while the open lines represent molecules that have energies higher than the maximum allowed energy E_{max} for each of the deceleration values of the traveling wave, and their trajectories are unstable. A separatrix is a line which marks a boundary in a phase-space diagram between the stable and the unstable trajectories and is indicated with a red line in Figure6.3. The area inside the separatrix gives the maximum area of phase space that is amenable for a phase-space stable deceleration for a given value of the deceleration and is referred to as the phase-space acceptance. The main goal of every decelerator is to maximize the phase-space acceptance, and it is especially important to achieve high longitudinal 2D phase-space acceptance at high deceleration values.

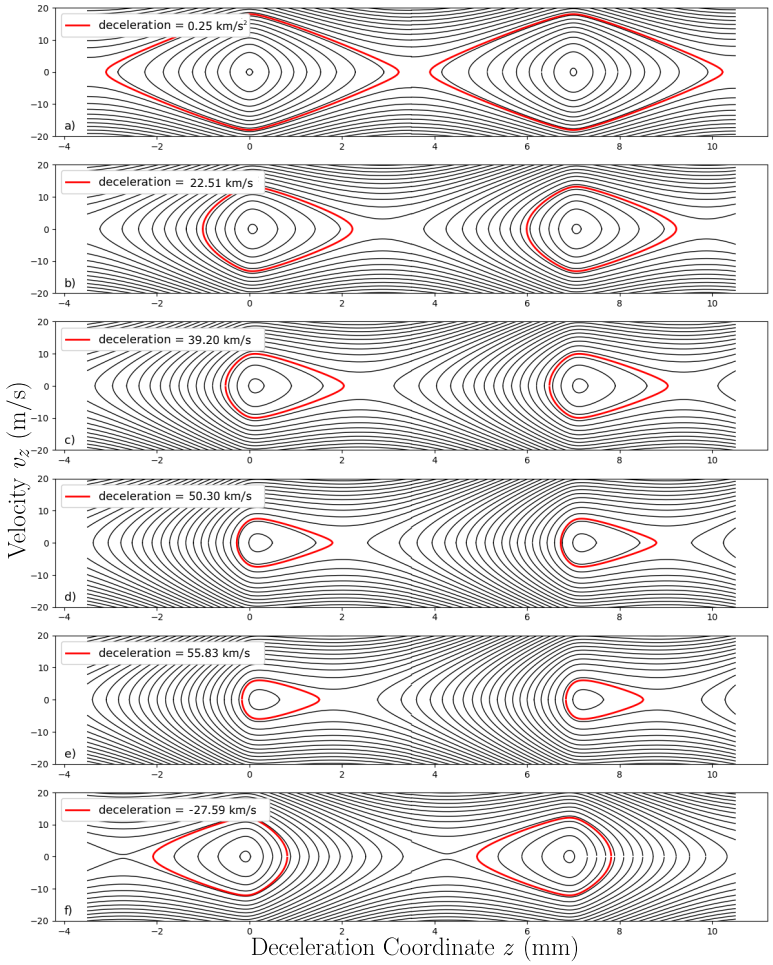

Figure 6.3: Longitudinal phase-space stability diagrams for OH in the $X^2\Pi_{3/2}(m_J = 3/2)$ state for two consecutive traveling traps. Stability diagrams are shown for various values of the deceleration of the trap. The phase-space region that remains stable throughout the deceleration process is highlighted by the separatrix in red.

In order to explore the longitudinal 2D phase-space acceptance of our deceleration method in more detail, we ran further numerical trajectory simulations. In the simulations, 10^5 OH molecules in $X^2\Pi_{3/2}$ state were created at the entrance of the traveling magnetic wave. For the purpose of the simulation, only molecules in $M_J = 3/2$ states were considered. Molecules were initialized within a cylinder (r = 2 mm, h = 11 mm) with a transverse velocity spread of 45 m/s in the transverse direction and 90 m/s in the longitudinal direction and 450 m/s mean forward velocity filling a 6-dimensional phase-space volume of 0.5×10^8 mm^3[m/s]^3. In the simulation, the decelerator was 1.792 m long followed by 15 mm of field-free re-

gion after which molecules were detected. Molecules were decelerated in a range of 449 m/s - 50 m/s final velocities and in a single case accelerated to final velocity of 550 m/s, corresponding to decelerations in range of 0.25 km/s^2 to 55.83 km/s^2 and in a case of acceleration to -27.59 km/s^2. Depending on the final velocity, it takes between 4.1 ms and 8.2 ms to traverse the decelerator. Owing to the multiple-trap geometry of the traveling wave and depending on the initial longitudinal phase-space volume of molecules, many moving traps can be filled and successfully decelerated as shown in Figure 6.16. The 2D phase-space particle density at the end of the decelerator for a single trap is depicted in Figure 6.4 for each of the simulations. Particles are shown in blue, while the calculated separatrix is indicated with a black line.

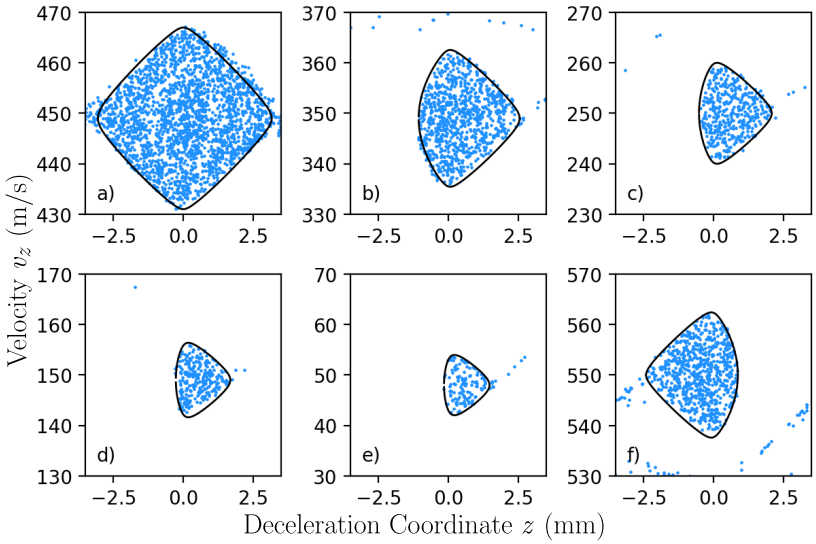

Figure 6.4: 2D longitudinal phase-space distribution of molecules generated from the numerical trajectory simulations at the end of the decelerator and calculated maximum phase-space acceptance (black). Phase-space distributions are plotted for following accelerations: a) 0.25 km/s^2, b) 22.51 km/s^2, c) 39.20 km/s^2, d) 50.30 km/s^2, e) 55.83 km/s^2 and f) -27.59 km/s^2

From the particle trajectory simulations the phase-space evolution of molecules during the deceleration can be extracted. This is shown in Figure 6.5. The phase-space evolution is illustrated for a package of OH molecules decelerated from an initial forward velocity of 450 m/s down to 50 m/s. Starting at $t = 0$ ms, every 1 ms a snapshot is taken up to 8 ms in total. It can be seen that initially a

cloud of OH molecules is centered around $z = 0$ m in position and 450 m/s in velocity. The initial phase-space distribution becomes more tilted towards one side with increasing time. This corresponds to molecules which are outside of the phase-space stable area that are not being efficiently decelerated. The phase-space distribution becomes tilted because molecules that have higher velocity can traverse a greater distance in the same amount of time and thereby spatially separate from the molecules with lower velocity. Figure 6.5 shows that a small patch of molecules in the phase-space becomes detached from the main package. These molecules represent the portion of the initial package that falls withing the phase-space acceptance region of the decelerator and thereby is efficiently decelerated. The black trace in the figure represents the calculated velocity and position of the synchronous molecule for every time step of the deceleration process.

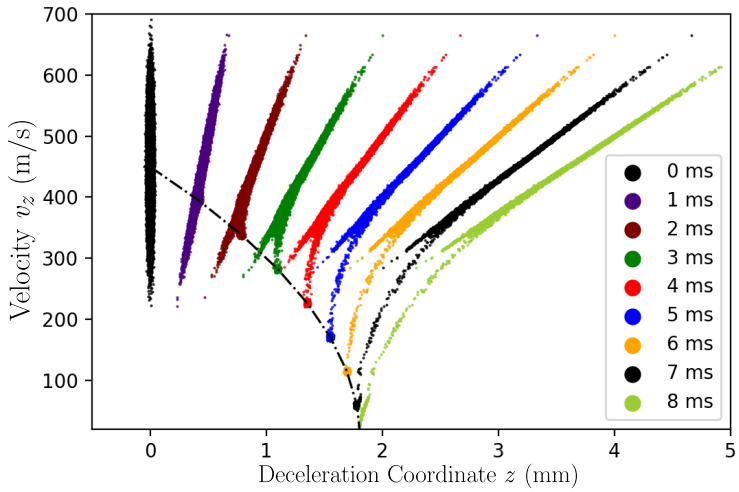

Figure 6.5: Phase-space evolution of the package of OH molecules in the $X^2\Pi_{3/2}(m_J = 3/2)$ state and 450 m/s mean forward velocity decelerated down to 50 m/s. With increasing time, the phase-space accepted fraction of the molecular package is separated from the rest of the package and is efficiently decelerated. The calculated velocity and position of the synchronous molecule during the deceleration process are illustrated with the black trace.

In Figure 6.6, the phase-space distribution of OH molecules in the $X^2\Pi_{3/2}(m_J = 3/2)$ state 8.6 ms after the initialization of the numerical simulation is shown. Molecules are decelerated up to the end of the deceleration region, after which

they are propagated in the field-free region up to 8.6 ms after which the snapshot is taken. Molecules are decelerated from the initial forward velocity of 450 m/s down to the following final velocities: 450 m/s, 350 m/s, 250 m/s, 150 m/s and 50 m/s. Particles decelerated to different final velocities are indicated with a different color. From the figure, it can be seen that the considerable fraction of molecules is not efficiently decelerated. These are the molecules that are either too fast (slow) or spatially mismatched compared to the traveling wave and throughout the deceleration process are mostly experiencing a field-free expansion. Then, there are molecules that are efficiently decelerated to the target velocity. These can be seen in the figure as portions of the increased phase-space density that are centered around the target velocity. These molecules fall within the phase-space acceptance of the decelerator. Additionally, there are also molecules that are 'leaking' out of the phase-space stable region. These are the molecules that fall close to the phase-space stable region but are ultimately phase-space unstable. They are somewhat decelerated, but their deceleration is not stable and in turn are not decelerated to target velocity. From Figure 6.6 it can be noticed that for each final velocity, the phase-space distribution of decelerated molecules is tilted. This again comes from the fact that the decelerated molecules have a distribution of velocities, and after the field-free expansion, the molecules with differing velocities will spatially separate.

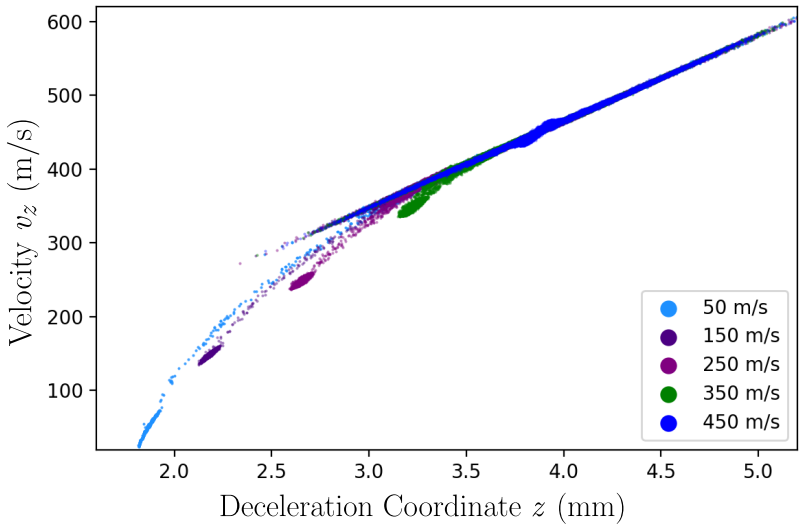

Figure 6.6: Phase-space distribution of OH molecules in the $X^2\Pi_{3/2}(m_J = 3/2)$ state 8.6 ms after the initialization of the simulation. Molecules are decelerated for a full length of the decelerator, after which they are propagated in the field-free region. Molecules are decelerated from initial velocity of 450 m/s down 450 m/s (guiding), 350 m/s, 250 m/s, 150 m/s and 50 m/s.

One of the best measures of the capabilities of a decelerator is evaluated by the phase-space acceptance at different decelerations. In order to characterize the proficiency of our deceleration method, first the longitudinal 2D phase-space acceptance as a function of deceleration is explore after which the 2D phase-space acceptance in both transverse directions, and also the full 6D phase-space capabilities of the deceleration method are inspected. Phase-space acceptance is calculated from the phase-space stability diagrams. First, for each deceleration, a phase-space stability diagram is calculated. Then, from the stability diagram, the border between the phase-space stable and unstable region is found after which the area enclosed by the border is numerically calculated. This is referred to as 2D longitudinal phase-space acceptance of the decelerator [208]. The phase-space acceptance is calculated for 9 different values of deceleration ranging from 0.25 km/s^2 to 55.83 km/s^2. This deceleration values correspond to a deceleration of the traveling wave from an initial forward velocity of 450 m/s down to a range of final velocities from 449 m/s down to 50 m/s final velocity in steps of 50 m/s. Results of these calculations are shown in Figure 6.7. The results are indicated

on a logarithmic plot with a black trace where black dots correspond to each data point. As expected, the maximum value of the longitudinal 2D phase-space acceptance is achieved for the lowest value of the deceleration and decreases with increasing deceleration while the minimum phase-space acceptance is achieved for the highest deceleration value. The maximum value of the longitudinal 2D phase-space acceptance is achieved for the guiding mode operation of the decelerator and equates to $\sim 1.3 \cdot 10^2$ mm[m/s].

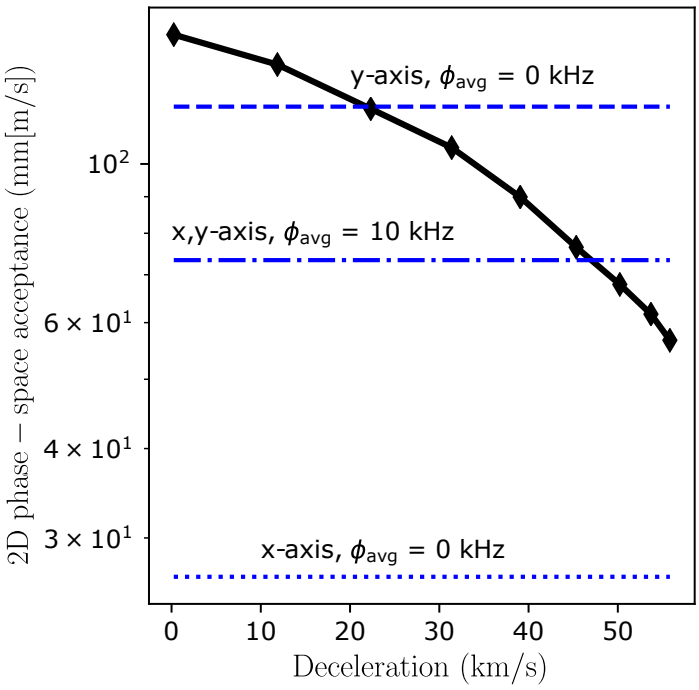

Figure 6.7: Longitudinal and transverse 2D phase-space acceptance of the traveling-wave Zeeman decelerator as a function of the deceleration. Phase-space acceptance is extracted by numerically calculating the area enclosed by a separatrix in the phase-space diagram in each case.

There are two ways in which longitudinal 2D phase-space acceptance of our deceleration technique can fundamentally be increased. One is to make a longer decelerator. The acceleration that the molecules experience during the deceleration process depends on the initial and the final velocity of the traveling wave and is given with the following relation: $a = (v_f^2 + v_i^2)/2L$, where v_f is the final velocity of the traveling wave, v_i is the initial velocity of the traveling wave and L is the length of the decelerator. Since the longitudinal 2D phase-space acceptance

of the traveling wave Zeeman decelerator mainly depends on the deceleration, by increasing the length of the decelerator the deceleration would be decreased and thereby would lead to an increase of the longitudinal 2D phase-space acceptance. The second way to increase the longitudinal 2D phase-space acceptance of the decelerator is to increase the currents that are supplied through the decelerator coils. The magnitude of the magnetic fields inside the coil geometry is proportional to the currents that are supplied to the coils, $B \sim I$. By increasing the currents by a factor, the magnitude of the magnetic field is increased by the same factor, and therefore the maximum Zeeman energy E_{max} that molecules can have and still remain trapped is also increased by the same factor.

6.2.2 Transverse motion in the trap and 6-dimensional phase-space stability

So far, the interest has been focused on the longitudinal 2D phase-space structure of the traveling-wave Zeeman decelerator. Here, the 2D phase-space structure in both transverse directions is explored in detail. As previously described, there are two modes of operations of the decelerator when talking about transverse confinement of the particles in the magnetic field. One when the rotational frequency is set $f_\theta = 0$ kHz and second one when it is set to $f_\theta > 0$ kHz. In the first case, the transverse trapping field is stationary, while in the second case it is rotating. The calculated transverse trapping potential for OH in $X^2\Pi_{3/2}(m_J = 3/2)$ state is depicted in Figure 6.1. Similarly, as in the longitudinal case, we proceed by calculating the phase-space structure in both transverse directions. Since ideally there is no coupling between longitudinal and transverse motion in our traveling-wave Zeeman decelerator model, the transverse motion is unaffected by the deceleration of the traveling wave. In that case, the energy that the molecule has in each of the transverse direction is given by:

$$E_x = \frac{mv_x^2}{2} + \mu_{eff}\mu_B B(x), \tag{6.7}$$

$$E_y = \frac{mv_y^2}{2} + \mu_{eff}\mu_B B(y). \tag{6.8}$$

Phase-space space stability regions are calculated from equations 6.7 and 6.8 for the stationary case, $f_\theta = 0$ kHz, and illustrated in Figure 6.8. Again, phase-space trajectories are stable up to a limiting energy $E_{max,x}$ and $E_{max,y}$, after which they become unstable. The border between phase-space stable trajectories and phase-space unstable trajectories is indicated with a red line. From the simulations, maximum energies of $E_{max,x} = 0.04$ cm^{-1} and $E_{max,y} = 0.30$ cm^{-1} are extracted for OH molecules in the $X^2\Pi_{3/2}(m_J = 3/2)$ state together with a magnitude of the magnetic field produced with $I = 300$ A of current in both layers. The phase-space structure with separatrices is depicted in Figure 6.8 a) for the x direction and 6.8 b) for the y direction. For the case of a rotating field and in the instance when the adiabatic condition $f_\theta > 1$ kHz is met, the maximum energy that the OH molecule can have in each direction is $E_{max,x,y} = 0.17$ cm^{-1}. The corresponding separatrix is shown in blue in each figure. From the given separatrices, the 2D transverse phase-space acceptance is calculated. The 2D transverse phase-space acceptance is illustrated in Figure 6.7 with horizontal blue lines.

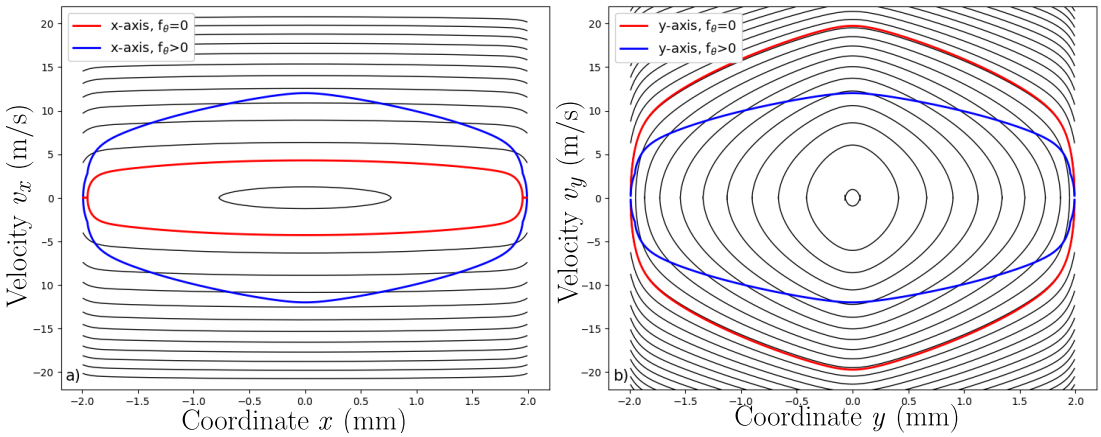

Figure 6.8: Transverse phase-space stability diagrams for OH in $X^2\Pi_{3/2}(m_J = 3/2)$ state. Phase-space stability diagram in a) x direction and b) y direction for a stationary transverse trap. Separatrices are depicted in red for stationary traps ($f_\theta = 0$ kHz) and blue for non-stationary traps ($f_\theta > 1$ kHz).

In order to confirm the phase-space calculations, a set of 1D particle trajectory simulations was performed for both transverse directions for OH molecules in the $X^2\Pi_{3/2}(m_J = 3/2)$ state and the phase-space structure was extracted from the simulations. Trajectory simulations were performed with the same initial param-

eters as in the case when the longitudinal phase-space structure was discussed, but in this case, two instances were explored: a stationary transverse trapping field, $f_\theta = 0$ kHz, and a rotating trapping field, $f_\theta = 10$ kHz. Particle trajectories were numerically calculated for 30 ms over which time the trapping fields were switched on. The reason for this is to allow the molecules to fully explore the phase space over the simulation time and to allow for the molecules for which $E > E_{max}$ enough time to be ejected from the trap. The results of the numerical trajectory simulations can be seen in Figure 6.9. The density of the molecules is shown with a color map, where lower densities of molecules are represented in blue and higher densities in red. The two figures in the upper row correspond to the cases of the stationary transverse trap for the x and y directions, respectively. The two figures in the lower row correspond to the cases of the rotating transverse trap for the x and y directions. The separatrices for each of the cases is shown with a white line. As expected, most of the density of the molecules fall inside the area enclosed by each separatrix.

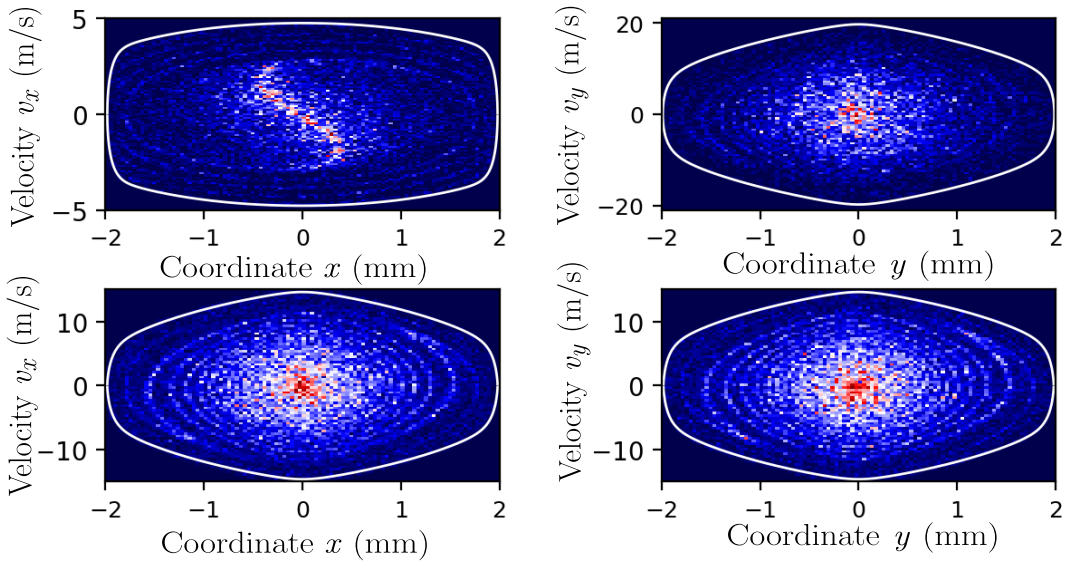

Figure 6.9: Phase-space distribution of OH molecules in the $X^2\Pi_{3/2}(m_J = 3/2)$ state in the transverse directions extracted from the numerical trajectory simulations 30 ms after the start of the simulation. The upper row shows the phase-space distribution of molecules in the x and y direction for the case of a stationary (f_θ = 0 kHz) transverse magnetic field. The lower row shows the phase-space distribution of molecules in x and y direction for a case of a rotating (f_θ = 10 kHz) transverse field. Separatrices are shown with a white line.

In order to fully characterize the traveling wave deceleration method, the full 6D phase-space acceptance description is required. 6D phase-space acceptance is calculated by a product of the 2D phase-space acceptances for each direction. This represents the maximum upper bound on the full 6D phase-space acceptance. Maximum 6D phase-space acceptances are calculated for two cases, namely for a stationary rotational trap, $f_\theta = 0$ kHz, and for a rotating transverse trap $f_\theta = 10$ kHz. As was previously realized with the 2D longitudinal phase-space acceptance, the 6D phase-space acceptance is calculated for 9 different decelerations of the traveling wave. The decelerations correspond to the deceleration of the traveling wave starting with an initial velocity of 450 m/s to a range of final velocities ranging in 449 m/s down to 50 m/s, in steps of 50 m/s. The results of the calculations are shown in Figure 6.11. The case of a stationary transverse trap is depicted with a dashed blue line, and the rotating transverse trap with a red dashed line. The respective data points are shown with blue dots and red triangles. The maximum values of the phase-space accepted volumes are achieved for the lowest acceleration values ($0.8 \cdot 10^5$ mm^3[m/s]^3 for $f_\theta = 10$ kHz and $0.5 \cdot 10^5$ mm^3[m/s]^3 for $f_\theta = 0$ kHz) and decreases with the increasing deceleration. Numerical trajectory simulations are used to extract the 6D phase-space acceptance. From the numerical trajectory simulations, the 6D phase-space volume is calculated at the end of the deceleration region. The phase-space distribution of molecules for each direction is extracted from the simulations and is then binned in a 2D histogram from which the area which the molecules are encompassing is extracted. This is shown in Figure 6.10. The area enclosed by the red line is the phase-space acceptance extracted from the simulation.

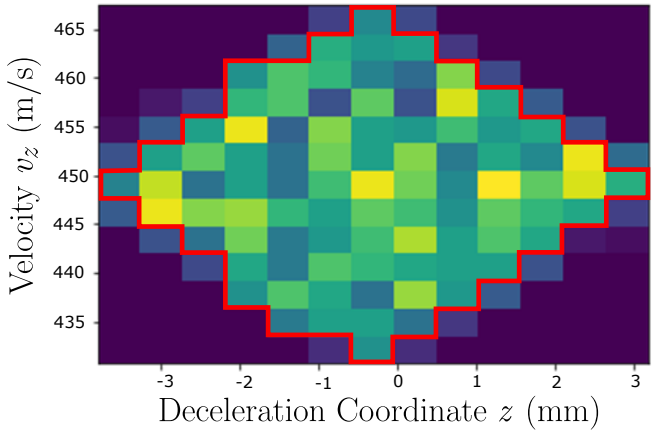

Figure 6.10: Phase-space acceptance extracted from numerical simulations. The phase-space distribution of molecules is extracted from simulation and binned in 2D histogram from which the phase-space acceptance is extracted (area enclosed by red line).

The full 6D phase-space acceptance is then calculated as a product of the respective 2D phase-space acceptances. The result of the calculations is shown in Figure 6.11 with full lines for the respective cases. The 6D phase-space acceptances fall in a similar range but below the calculated upper limits of the 6D acceptance. The difference between the calculated maximum phase-space volume and one obtained from the simulations was attributeed to three factors, namely inaccuracies in calculations of the phase-space acceptance from the numerical trajectory simulations, accumulated errors over the course of the simulations and to the weak coupling between the longitudinal and transverse motion inside the trap. The calculated values of the 6D phase-space acceptance refer to the phase-space accepted volume of a single trap. Depending on the initial phase-space distribution of molecules, multiple traps will be filled, and the total phase-space volume has to be multiplied by the number of filled traps. For comparison, the maximum phase-space accepted 6D volume of a typical Stark decelerator at 50 m/s is $0.8 \cdot 10^4$ $mm^3[m/s]^3$ [209, 210], and a 6D phase-space acceptance of another type of a travelling-wave Zeeman decelerator is $2 \cdot 10^7$ $mm^3[m/s]^3$ [211]. For comparison, in our analysis for the case of guiding mode, the maximum achieved 6D phase-space acceptance of OH molecules is $\approx 8 \cdot 10^5$ $mm^3[m/s]^3$. Taking into

account the fact that our trap depth is a factor of 5 lower than those realized in a typical Stark or Zeeman decelerator, the effective phase-space acceptance is comparable to or even higher than the most advanced decelerators. In the future the effects of the rotational frequency of the trap on the phase-space acceptance will be explored experimentally by examining relative intensities of the time-of-flight measurements.

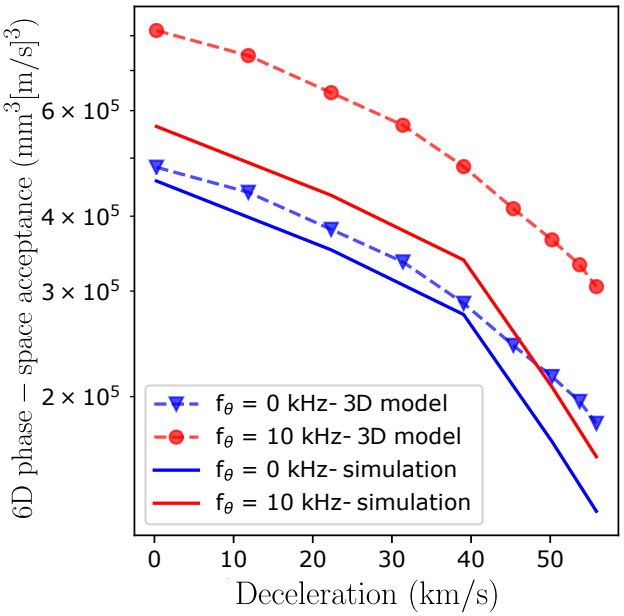

Figure 6.11: The 6D phase-space acceptance as a function of deceleration. The upper limit of the 6D phase-space acceptance is shown with a dashed line for two cases, namely for a stationary transverse trap (blue) and a rotating transverse trap (red). The 6D phase-space acceptances are extracted from the numerical trajectory simulations and depicted with a full line for their respective cases.

6.3 Guiding and deceleration of a molecular beam of OH radicals

6.3.1 Guiding of a molecular beam of OH radicals

A detailed description of the experimental setup, the Zeeman deceleration procedure and detection was given in the previous chapters. In short, a molecular beam of OH radicals with a mean longitudinal velocity of 445m/s and 50m/s velocity

spread (FWHM) was produced by the Nijmegen pulsed valve (NPV) by discharging H_2O seeded in Xe. In the supersonic expansion from the NPV, around 98% of the molecules were populated in the lowest rotational level ($J = 3/2$), of the vibrational ($v = 0$), and electronic ground state $X^2\Pi_{3/2}$ [150]. In the presence of the magnetic field, the degeneracy between different m_J levels ($m_J = \pm 3/2, \pm 1/2$) was split, and only particles in the low-field-seeking states ($m_J = 1/2, 3/2$) were amenable to Zeeman deceleration [212]. The effective magnetic moment of $m_J = 3/2$ state is $1.4\mu_B$, where μ_B denotes the Bohr magneton. Following the supersonic expansion, the molecular beam passed through a skimmer (Beam dynamics, 2 mm diameter) 7 cm downstream from the NPV and entered the deceleration chamber where it was coupled into the decelerator. Details on the production of the molecular beam can be found in [150]. Following Zeeman deceleration, the molecules arrived in the detection region, where they were detected by laser-induced fluorescence (LIF). OH molecules in $X^2\Pi_{3/2}(v = 0)$ state were excited by a 282 nm (1.2 mJ/pulse) laser radiation into the electronically and vibrationally excited state $A^2\Sigma(v = 1)$. Laser radiation was generated by the output of a frequency-doubled dye laser pumped by a Nd:YAG laser. Florescence from the off-resonant $A^2\Sigma(v = 1) \rightarrow X^2\Pi(v = 1)$ transition (720 ns lifetime) centered at 313 nm was then collected by a 50 mm focal length UV lens and detected by a photo-multiplier tube (Electron Tubes B2/RFI, 9813 QB).

Figure 6.12 shows time-of-flight experiments of freely expanding molecular package (i.e. the decelerator is switched off) of OH molecules in the $X^2\Pi_{3/2}$ state. The detection of the molecular packages were performed at two positions. Time-of-flight profile with a peak value at around 0.3 ms corresponds to the detection in the source chamber 100 mm downstream from the molecular source and the time-of-flight profile with a peak value at around 2.2 ms corresponds to the detection 36 mm downstream from the exit of the decelerator. Experimental traces are shown in red and results extracted from numerical trajectory simulations are shown in black, showing good agreement between the two. The time-of-flight profiles corresponding to the detection in the source chamber are scaled down by a factor of 100 for clarity.

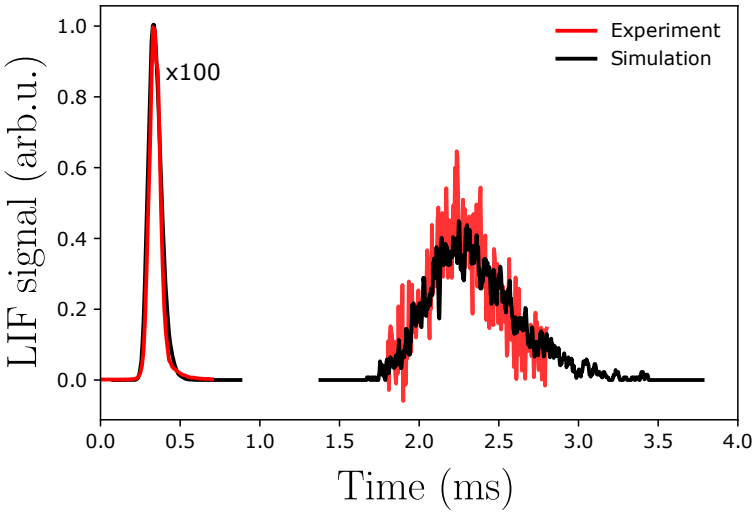

Figure 6.12: Time-of-flight experiments of freely expanding molecular package of OH molecules in the $X^2\Pi_{3/2}$ state. Detection is performed 100 mm downstream from the source (peak at 0.3 ms) and 36 mm downstream from the decelerator (peak at 2.2 ms). Time-of-flight profiles corresponding to the detection in the source chamber are scaled down by a factor of 100 for clarity.

Next, the operation of the decelerator in guiding mode is explored. In guiding mode, a packet of supersonically expanded OH molecules is coupled into the decelerator at the velocity of the package, which in our case was 445 m/s. The velocity of the travelling wave is matched to the velocity of the incoming package and is kept constant throughout the whole length of the decelerator. Results of the guiding experiments are shown in Figure 6.13. The black trace shows free-flight experiment. A supersonic beam of OH molecules was coupled into the decelerator while keeping the decelerator switched off. The incoming beam, after passing the decelerator, was detected by LIF in the detection region and time-of-flight traces were recorded. Each time-of-flight trace was recorded in the time range 1500 μs - 3000 μs when decelerator was switched off and 1800 μs - 2600 μs when decelerator was switched on. The time-of-flight timings were referenced to the opening time of the valve. The time separation between consecutive recorded data points was 2 μs, and each data point was averaged over 200 measurements. The red trace shows the results of the guiding experiments. After the expansion, the molecular beam was coupled into the decelerator, and the decelerator was switched on.

The time when the decelerator is switched on relative to the opening time of the valve is referred to as the incoupling time. The best incoupling time was chosen by recording the time-of-flight experiments by varying the incoupling time and maximizing the overall area under the time-of-flight profile. The incoupling times producing highest particle densities were in the range 100 μs-300 μs. The resulting time-of-flight profile from the numerical trajectory simulations is shown in blue. In the numerical trajectory simulations, the initial parameters were chosen to match those in the experiment. Initial parameters of the molecular beam in the simulations are: 445 m/s mean forward velocity with 20% longitudinal velocity spread and 10% transverse velocity spread with 11 mm spread in the position of the package along the deceleration axis. Details on the numerical trajectory simulations can be found in chapter 4. From Figure 6.13, a very good agreement between the experimental and simulated time-of-flight profiles can be observed. The time-of-flight profiles from the numerical simulations were corrected by 20 μs offset relative to the experimental profiles. This correction is ascribed to the dead time of the valve. The arrival time of the densest part of the molecular package was similar for both cases when the decelerator was off and on, arriving at $t \approx$2350 μs. From the time-of-flight profiles, a distinct increase in the overall OH signal in the instance when the decelerator was switched on relative to the case when it was switched off can be seen. At the highest density of particles, there is a factor of $\sim$9 increase in overall signal, while the total area under the time-of-flight profile is increased by a factor of $\sim$54.

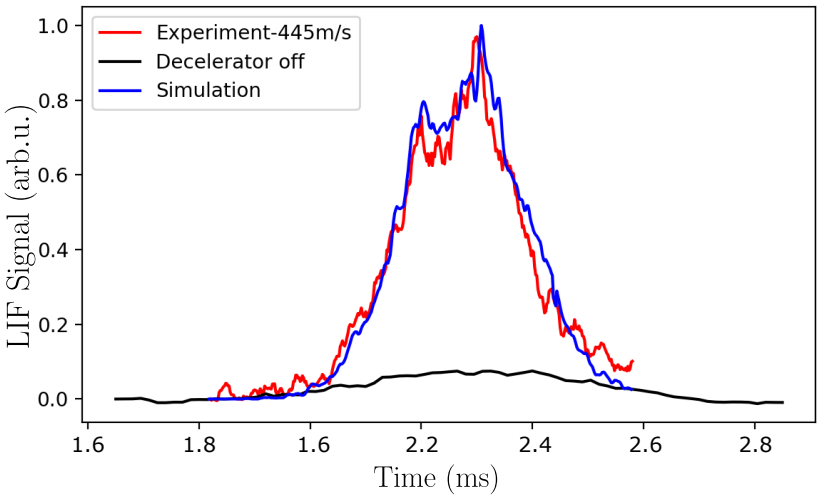

Figure 6.13: Experimental and simulated time-of-flight profiles resulting from the guiding of the OH molecules in the $X^2\Pi_{3/2}$ state. The time-of-flight profile when the decelerator is switched off is shown in black, red trace corresponds to the case when decelerator is switched on and the blue trace corresponds to a simulation. Comparing the case when the decelerator is switched off to the one when it is switched on, there is a factor of ~ 9 increase in the maximum OH signal and a factor of ~ 54 increase in the total area under the time-of-flight profile. The time-of-flight profile is well reproduced with the numerical trajectory simulations.

In Figure 6.14, results of the guiding experiments of OH molecules as a function of the incoupling time are presented. Time-of-flight traces were recorded for the following incoupling times: 50 μs, 100 μs , 150 μs , 170 μs and 290 μs. The inverted profiles correspond to the experimental results, while the upper profiles correspond to simulations. The time-of-flight profiles show that the overall area under each profile depends on the incoupling time. For low ($\leq$ 50 μs) and high ($\geq$ 290 μs) incoupling times an overall number of OH molecules that reach the detection region is decreased, while the incoupling time for which the number of OH molecules is highest is $\approx$ 150 μs. The central peak of the guided structure shifts in time depending on the incoupling time. If the incoupling time is changed, the timing of the coupling of the molecular beam into the decelerator is changed and also the portion of the molecular beam that couples into the decelerator is changed, this leads to the shifting in the timings when the trapped molecules arrive at the detection region.

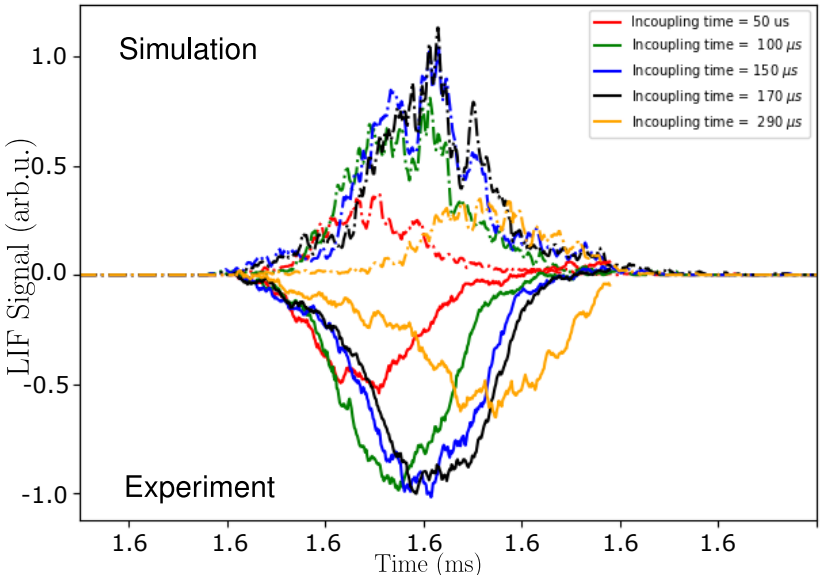

Figure 6.14: Experimental and simulated time-of-flight profiles resulting from the guiding of the OH molecules in the $X^2\Pi_{3/2}$ state as a function of the incoupling time. Time-of-flight traces were recorded for the following incoupling times: 50 μs, 100 μs, 150 μs, 170 μs and 290 μs. The lower pane illustrates experimentally recorded data while the upper pane illustrates results obtained from numerical trajectory simulations.

6.3.2 Deceleration of a molecular beam of OH radicals

Figure 6.15 shows results obtained from the time-of-flight measurements of a beam of OH molecules, detected by laser-induced-fluorescence 36 mm downstream from the decelerator. The initial velocity of the traveling wave was set to 445 m/s which was then tuned down to a predefined final velocity. Figure 6.15 a) shows time-of-flight measurements for different final velocities of the traveling wave. The blue trace corresponds to a measurement in guiding mode in which the final velocity of the traveling wave was kept the same as the initial velocity and molecules were being guided at 445 m/s around the node of the traveling magnetic field. The magenta and green traces correspond to the constant deceleration of the magnetic trap from the initial velocity down to 400 m/s and 350 m/s final velocities, respectively. The grey curve represents the time-of-flight profile when the decelerator is switched off. The inset of Figure 6.15 a) shows a 1D phase-space distribution of particles along the deceleration axis inside a single traveling trap.

The snapshot is taken at 2.2 ms after the molecules exit the nozzle which corresponds to the time when the effectively trapped molecules arrive at the laser position. The thick white curve is the separatrix corresponding to the trap depth of 0.24 cm^{-1}(0.34 K). Broken white lines in the inset correspond to isoenergetic phase-space trajectories, separated by 0.05 cm^{-1}. Particles are confined in a 7 mm region along the deceleration axis, which corresponds to the geometric size of the trap defined by $\lambda/2 = 7$ mm. In ref. [106] it was possible to discern in the time-of-flight profiles the contribution that comes from particles that are effectively trapped around the node of the magnetic wave. In our case, this was not possible due to experimental limitations. In order to obtain a single peak structure in the time-of-flight measurements, we would need to produce a well defined molecular beam with narrow positional spread along the deceleration axis so that only a single traveling trap would be populated with molecules. Due to geometry of the single module and the time dependent currents multiple traveling traps are created (> 8) and thus populated with molecules. This fact accounts for the broad distribution of the decelerated beam. We attempted to create a narrow molecular beam by limiting high voltage pulse duration for creating the discharge and bringing the NPV closer to the decelerator. At short pulse durations ($< 10\ \mu s$), the discharge was not effective anymore while by bringing the valve closer to the decelerator we were limited by skimmer interference [213] with the molecular beam. In the future, it would be possible to circumvent these limitations by employing laser dissociation of HNO_3 for the creation of a narrow beam of OH radicals [214].

Figure 6.15 b) and 6.15 c) illustrate a comparison of the experimentally obtained time-of-flight measurements to numerical particle trajectory simulations. The traces in red correspond to a numerical trajectory simulation that takes into the account the contribution from the LFS states. To help us understand how decelerated molecules contribute to the overall time-of-flight, the simulated time-of-flight was separated into the part whose contribution comes from the particles which are confined inside a traveling wave (black trace) and a contribution that comes from the traps with off-target velocities. An evolutionary algorithm was

developed for optimizing the initial parameters of the molecular beam in order to minimize the discrepancy between numerical simulations and experimental results. Details on the evolutionary algorithm can be found in Chapter 4.

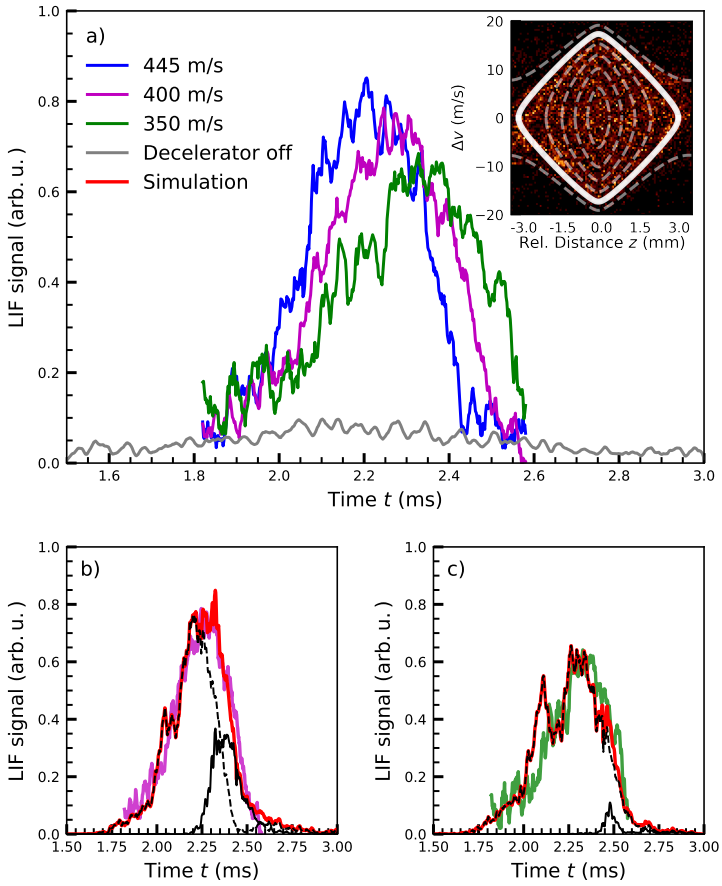

Figure 6.15: a) Time-of-flight measurements detected by LIF 36 mm downstream from the decelerator with an initial velocity of the traveling wave of 445 m/s and three different final velocities: 445 m/s (blue), 400 m/s (magenta), 350 m/s (green). The time-of-flight measurement when the decelerator is off is shown in grey. Inset: 1D phase-space distribution of particles along deceleration axis inside a single traveling trap with separatrix (0.24cm^{-1}) shown in with thick white line. b)-c) Comparison of experimentally obtained time-of-flight profiles to numerical simulations (red). Black traces show contributions to the overall time-of-flight profile from particles that are efficiently confined inside a traveling-wave during the deceleration process (full line), and ones that are not (broken line).

Figure 6.16 presents the phase-space distribution of particles arising from the

numerical trajectory simulation taken 2.5 ms after molecules exit the nozzle. Only the portion of the molecules which are effectively trapped during flight is shown. The normalized particle density is represented by a color map. Figure 6.16 a)-6.16 c) show the phase-space distribution of particles guided at 445 m/s, decelerated to a final velocity of 400 m/s and of 350 m/s. Each module consists of 8 geometrical traps but depending on when the time-dependent currents are switched on (off) in relation to arrival (departure) of the synchronous molecule to (out of) the decelerator, more effective traps can be created, leading to a higher fraction of the molecular beam being coupled into the decelerator. This can be seen in the phase-space distribution. In guiding mode, there are 10 effective traps that are propagated through the decelerator. A lower final velocity of the decelerator leads to a lower effective trap depth, which in turn leads to a smaller fraction of molecules being decelerated to the final velocity (Figure 6.16 b)- 6.16 c)). The phase-space distribution in Figure 6.16 a) and 6.16 b) is slanted towards one side. This effect comes from the fact that molecules guided at 445 m/s and decelerated to 400 m/s exit the decelerator at around 2.2 ms and 2.3 ms, respectively, and during free flight expansion, faster molecules are being separated from slower molecules, leading to a skewed phase-space distribution.

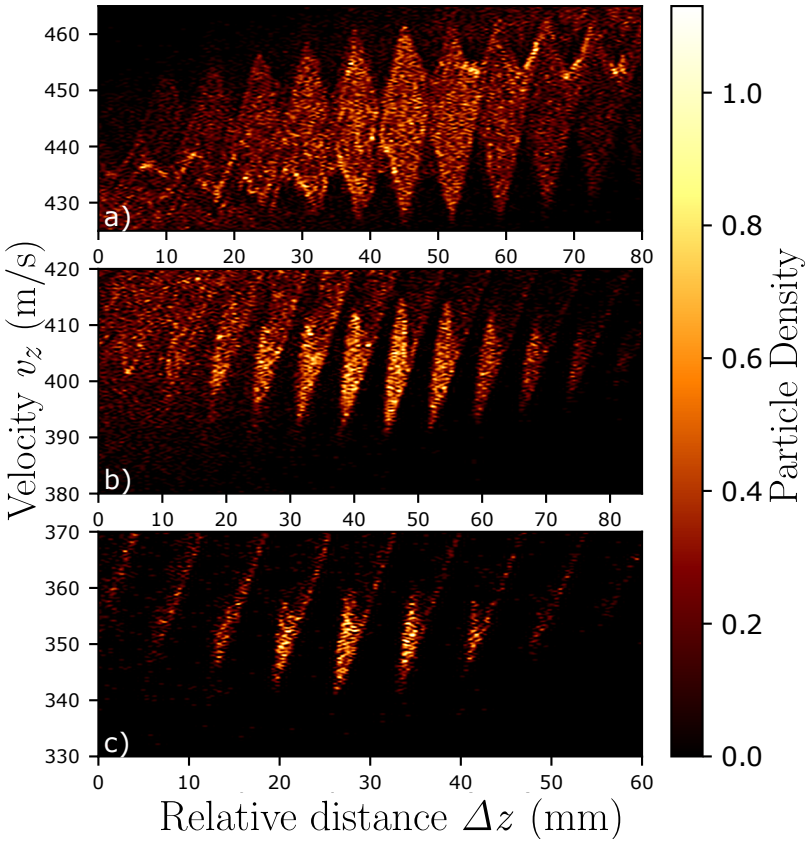

Figure 6.16: 1D phase-space distribution of particles along the deceleration axis 2.5 ms after molecules exit the nozzle. Molecules are decelerated from an initial velocity of 445 m/s down to 444 m/s (a), 400 m/s (b) and 350 m/s (c). The normalized particle density is represented by a color map.

6.4 Conclusions

In conclusion, we have demonstrated the operation of the traveling-wave Zeeman decelerator by decelerating OH molecules in their low-field seeking levels of the $X^2\Pi_{3/2}$ state from 450 m/s initial forward velocity down to 350 m/s final velocity. We have recorded experimental time-of-flight profiles and compared them to the time-of-flight profiles resulting from numerical particle trajectory simulations. We observed a significant increase in the number of molecules that are being transmitted through the decelerator operating both in the guiding mode and deceleration mode versus when the decelerator was switched off. An overall model for the 2D and 6D phase-space acceptance of the traveling-wave Zeeman

decelerator was developed and characterized. In addition, we used numerical trajectory simulations to confirm the models for the phase-space acceptance of the developed deceleration technique. Compared to the conventional Zeeman or Stark decelerators, our decelerator exhibits full three-dimensional confinement of the molecules at a full range of velocities starting from the initial forward velocity down to the arbitrary final velocity leading to an improved overall phase-space accepted volume compared to conventional Zeeman and Stark decelerators.

Chapter 7

Conclusions and outlook

In conclusion, we have designed, developed and tested a new type of travelling-wave Zeeman decelerator. The decelerator is able to decelerate species of atoms and molecules possessing a magnetic-dipole moment from initial forward velocity of 560 m/s down to in priciple arbitrary final velocities. We demonstrated successful operation of the decelerator by decelerating a molecular beam of OH molecules in the $X^2\Pi_{3/2}$ state from 450 m/s initial forward velocity down to the 350 m/s final velocity. Experimental time-of-flight traces were compared to the numerical trajectory simulations. Both 2D and 6D phase-space stability of the decelerator has been studied and compared to that of a conventional Zeeman and Stark decelerators as well as other travelling-wave Zeeman decelerators [106, 89, 107].

The decelerator is modular in design allowing for easy extension. The unique wire geometry of the solenoids allows us to create a travelling magnetic wave. Compared to conventional Zeeman or Stark decelerators, our decelerator exhibits full three-dimensional confinement of the molecules at a full range of velocities starting from initial forward velocities down to arbitrary final velocities leading to the improvement to the overall phase-space acceptance compared to the conventional Zeeman and Stark decelerators [215, 208, 185, 216]. For the purpose of producing the necessary time-dependent currents, we developed compact arbitrary waveform current generators, able to produce currents up to 300 A zero-peak, and 0-40 kHz in frequency. The decelerator is operated at 2 Hz repetition

rate, where by improving the cooling capability of the system the repetition rate could potentially be increased up to 10 Hz.

The decelerator in the current state consists of 16 stages. As presented, the decelerator is limited in the number of species that have a favourable magnetic-dipole-moment-to-mass ratio, μ_{eff}/m, that can be efficiently decelerated to low final velocities which is a disadvantage compared to some of the existing conventional and moving-trap Zeeman decelerators [101, 217, 94, 89]. Due to the complexity of the double-helix coil geometry and current generating system, from the engineering perspective the described decelerator is more challenging to implement relative to existing decelerators. One of the main features of this decelerators compared to other decelerators is the decoupling of the transverse and longitudinal motion, and capability of control of transverse orientation of the magnetic trap, which in the future will be used to explore mass selectivity of different species inside a trap during the deceleration process. The main bottleneck of the current decelerator was the inability to reach low final velocities. In the future, the decelerator will be extended by an additional 16 stages which will significantly improve on the deceleration capabilities and will allow for a wider range of species to be decelerated to a standstill in the laboratory frame. For example, a 32 stage decelerator would allow for deceleration of OH molecules to a standstill as shown in the simulations presented in Chapter 6. Additional improvements to the decelerator can be achieved by improving the power electronics. At present, the decelerator operation is limited to current pulses of up to 300 A amplitude and frequencies of up to 40 kHz. With the ever-improving technology for current switching devices, an enhancement of the deceleration capabilities can be envisioned. With the increase in the maximum amplitude of the current pulses, higher trap depths can be achieved, thereby increasing the phase-space acceptance of the decelerator. Additionally, with the increase in the frequency of the current pulses, species with higher initial velocities can be decelerated. The maximum initial velocity is given by $v_{max} = \lambda f_{max}$ where f_{max} is the maximum frequency of the current pulses allowed by the power electronics and λ is the periodicity of the double-helix geometry. Improvements on the power

electronics will also require additional improvements to the cooling system and the design of the modules. At the moment, one of the limiting factors of the decelerator is the heat dissipation during the operation of the decelerator. If the proficiency of the power electronics high-current switching capabilities are to be improved, additional improvements have to be made both in the module design and the cooling system in order to allow for switching of currents with high peak powers and efficient dissipation of the produced heat.

There are many molecular species which are suitable candidates for Zeeman deceleration, some of which are CH ($X^2\Pi_{3/2}$), O_2 ($X^3\Sigma_g^-$), NO ($X^2\Pi_{3/2}$), CaH ($X^2\Sigma^+$), SO ($X^3\Sigma^-$) and others [52]. One of the more interesting candidate molecules for Zeeman deceleration is the H_2 molecule. The hydrogen molecule is the most abundant molecule in interstellar space [218], and it is observed at redshifts up to z=4.2 providing observations of physical phenomena up to 12.5 billion years into the cosmic past [219]. Precision spectroscopy of H_2 molecules has been proposed as a possible probe into the physics beyond the Standard model [220]. Additionally, molecular hydrogen is the simplest neutral molecular system and as such serves as a standard for tests of quantum electrodynamics (QED) in molecular systems. Recently, measurements of the dissociation energy of ortho-H_2 have reached the precision below 1 MHz [221] making it one of the most precise dissociation energy measurements. At the same time, recent QED corrections to the dissociation energy of H_2 are in remarkable agreement with the aforementioned measurement [222]. Precision spectroscopy of hydrogen molecules can be further improved with Zeeman decelerated samples of H_2. In the ground state, the hydrogen molecule has no permanent magnetic or electric dipole moment and therefore it is not suitable for deceleration experiments. However, the metastable $c^3\Pi_u$ state has a magnetic dipole moment and can be decelerated with a Zeeman decelerator. g factors in the $N = 1$ state of the $c^3\Pi_u(\nu = 0)$ state of ortho and para hydrogen are given in Table 7.1 [118]. The existence of a metastable state in H_2 was first established by Lichten in 1960 [223] and the first lifetime measurements of the $c^3\Pi_u(\nu = 0)$ state yielded lifetime of $\tau = 1.02 \pm 0.05$ ms [224]. At present, the lifetimes of the $c^3\Pi_u$ state are not known with high precision and

could be additionally improved with a production of slow beams of H_2. One of the future plans of the travelling-wave Zeeman deceleration experiments will be to produce samples of cold metastable hydrogen molecules.

Table 7.1: g values for H_2 in the $c^3\Pi_u$ state.

N	J	g_J (para)	F	g_F (ortho)
1	0	...	1	-0.00304
	1	1.25115		
			0	...
			1	0.62405
			2	0.62405
	2	1.25115		
			1	1.87824
			2	1.0421
			3	0.83309

In the last decade, studies on the ion-neutral interactions at very low temperatures have seen significant progress with the developments of techniques for trapping of both cold neutral and ionic samples in the so-called hybrid traps [55, 225]. Typically, laser-cooled atomic ions are stored in a radiofrequency (RF) trap together with or without molecular ions. Over the ion trap, a magnetic trap for cold paramagnetic molecules or magneto-optical trap for laser-cooled atoms is superimposed. This type of experiments have paved the way for exploration of a range of phenomena related to ion-neutral collisions at low temperatures. For example, charge-exchange processes have been observed in specific systems [226, 227, 228], reaction rates were found to increase with the increase of the electronic state of the collision partners [229] and molecular ions can be formed by the radiative association under the cold and dilute conditions [230]. In the future, the traveling-wave Zeeman decelerator will serve as a source of cold paramagnetic molecules for hybrid trapping experiments.

Appendix A

Matrix elements of the effctive Hamiltonian for OH in $X^2\Pi$ state in the Hund's case (a) basis

Matrix elements for the effective Hamiltonian acquired from [120]:

(1) Spin-orbit coupling

$$\langle L\Lambda',S\Sigma',J'\Omega'M'_{J'},IM'_I|\, A_{\rm so}T^1_{q=0}(\mathbf{L})T^1_{q=0}(\mathbf{S})\,|L\Lambda,S\Sigma,J\Omega M_J,IM_I\rangle \tag{A.1}$$
$$= A_{\rm so}\Lambda\Sigma\delta_{\Lambda,\Lambda'}\delta_{\Sigma,\Sigma'}\delta_{J,J'}\delta_{\Omega,\Omega'}\delta_{M_J,M'_{J'}}\delta_{M_I,M'_{I'}}$$

(2) Molecular rotation

$$\langle L\Lambda',S\Sigma',J'\Omega'M'_{J'},IM'_I|\, B_N\mathbf{N}^2\,|L\Lambda,S\Sigma,J\Omega M_J,IM_I\rangle \tag{A.2}$$
$$= B_N\left[J(J+1)+S(S+1)-2\Omega\Sigma\right]\delta_{\Lambda,\Lambda'}\delta_{\Sigma,\Sigma'}\delta_{J,J'}\delta_{\Omega,\Omega'}\delta_{M_J,M'_{J'}}\delta_{M_I,M'_{I'}}$$
$$- 2B_N\delta_{\Lambda,\Lambda'}\delta_{J,J'}\delta_{M_J,M'_{J'}}\delta_{M_I,M'_{I'}}$$
$$\times(-1)^{J-\Omega'+S-\Sigma'}\sqrt{J(J+1)(2J+1)S(S+1)(2S+1)}\sum_{q=\pm1}\begin{pmatrix} J & 1 & J \\ -\Omega' & q & \Omega\end{pmatrix}\begin{pmatrix} S & 1 & S \\ -\Sigma' & q & \Sigma\end{pmatrix}$$

(3) Spin-molecular rotation coupling

$$\langle L\Lambda',S\Sigma',J'\Omega'M'_{J'},IM'_I|\,\gamma\,T^1(\mathbf{J}-\mathbf{S})\cdot T^1(\mathbf{S})\,|L\Lambda,S\Sigma,J\Omega M_J,IM_I\rangle \tag{A.3}$$

$$= \gamma\left[\Omega\Sigma - S(S+1)\right]\delta_{\Lambda,\Lambda'}\delta_{\Sigma,\Sigma'}\delta_{J,J'}\delta_{\Omega,\Omega'}\delta_{M_J,M'_{J'}}\delta_{M_I,M'_{I'}}$$

$$+\gamma\delta_{\Lambda,\Lambda'}\delta_{J,J'}\delta_{M_J,M'_{J'}}\delta_{M_I,M'_{I'}}$$

$$\times(-1)^{J-\Omega'+S-\Sigma'}\sqrt{J(J+1)(2J+1)S(S+1)(2S+1)}\sum_{q=\pm1}\begin{pmatrix} J & 1 & J \\ -\Omega' & q & \Omega\end{pmatrix}\begin{pmatrix} S & 1 & S \\ -\Sigma' & q & \Sigma\end{pmatrix}.$$

(4) Λ-doubling term

$$\langle L\Lambda',S\Sigma',J'\Omega'M'_{J'},IM'_I|\sum_{q=\pm1}\mathrm{e}^{-2\mathrm{i}q\phi}\left[-Q\,T^2_{2q}(\mathbf{J},\mathbf{J})+(P+2Q)T^2_{2q}(\mathbf{J},\mathbf{S})\right]|L\Lambda,S\Sigma,J\Omega M_J,IM_I\rangle \tag{A.4}$$

$$= \delta_{J,J'}\delta_{M_J,M'_{J'}}\delta_{M_I,M'_I}(-1)^{J-\Omega'}\sqrt{J(2J+1)}\sum_{q=\pm1}\delta_{\Lambda',\Lambda-2q}$$

$$\times\left\{\frac{Q}{2\sqrt{3}}\delta_{\Sigma,\Sigma'}\sqrt{(2J-1)(2J+2)(2J+3)}\begin{pmatrix} J & 2 & J \\ -\Omega' & -2q & \Omega\end{pmatrix}\right.$$

$$\left.+(P+2Q)(-1)^{S-\Sigma'}\sqrt{(J+1)S(S+1)(2S+1)}\begin{pmatrix} J & 1 & J \\ -\Omega' & -q & \Omega\end{pmatrix}\begin{pmatrix} S & 1 & S \\ -\Sigma' & q & \Sigma\end{pmatrix}\right\}.$$

(5) Magnetic hyperfine interaction (a)

$$\langle L\Lambda',S\Sigma',J'\Omega'M'_{J'},IM'_I|\,a\,T^1_{q=0}(\mathbf{I})T^1_{q=0}(\mathbf{L})\,|L\Lambda,S\Sigma,J\Omega M_J,IM_I\rangle \tag{A.5}$$

$$= a\Lambda\delta_{\Lambda,\Lambda'}\delta_{\Sigma,\Sigma'}(-1)^{M'_{J'}-\Omega'+I-M'_I}\sqrt{I(I+1)(2I+1)(2J'+1)(2J+1)}\begin{pmatrix} J' & 1 & J \\ -\Omega' & 0 & \Omega\end{pmatrix}$$

$$\times\sum_{p=0,\pm1}(-1)^p\begin{pmatrix} J' & 1 & J \\ -M'_{J'} & p & M_J\end{pmatrix}\begin{pmatrix} I & 1 & I \\ -M'_I & -p & M_I\end{pmatrix}.$$

(6) Magnetic hyperfine interaction (b)

$$\langle L\Lambda',S\Sigma',J'\Omega'M'_{J'},IM'_I|\, b_F T^1(\mathbf{I})\cdot T^1(\mathbf{S})\,|L\Lambda,S\Sigma,J\Omega M_J,IM_I\rangle \tag{A.6}$$
$$b_F\delta_{\Lambda,\Lambda'}(-1)^{M'_{J'}-\Omega'+I-M'_I+S-\Sigma'}\sqrt{(2J'+1)(2J+1)I(I+1)(2I+1)S(S+1)(2S+1)}$$
$$\times\sum_{p,q=0,\pm1}(-1)^p\begin{pmatrix} J' & 1 & J\\ -\Omega' & q & \Omega\end{pmatrix}\begin{pmatrix} J' & 1 & J\\ -M'_{J'} & p & M_J\end{pmatrix}\begin{pmatrix} I & 1 & I\\ -M'_I & -p & M_I\end{pmatrix}\begin{pmatrix} S & 1 & S\\ -\Sigma' & q & \Sigma\end{pmatrix}.$$

(7) Magnetic hyperfine interaction (c)

$$\langle L\Lambda',S\Sigma',J'\Omega'M'_{J'},IM'_I|\left\{\sqrt{\frac{2}{3}}c\,T^2_{q=0}(\mathbf{I},\mathbf{S})+d\sum_{q=\pm1}\mathrm{e}^{-2\mathrm{i}q\phi}\,T^2_{2q}(\mathbf{I},\mathbf{S})\right\}|L\Lambda,S\Sigma,J\Omega M_J,IM_I\rangle \tag{A.7}$$
$$=\ (-1)^{M'_{J'}-\Omega'+I-M'_I+S-\Sigma'}\sqrt{(2J'+1)(2J+1)I(I+1)(2I+1)S(S+1)(2S+1)}$$
$$\times\sum_{p=0,\pm1}(-1)^p\begin{pmatrix} J' & 1 & J\\ -M'_{J'} & p & M_J\end{pmatrix}\begin{pmatrix} I & 1 & I\\ -M'_I & -p & M_I\end{pmatrix}$$
$$\times\left\{\sqrt{\frac{10}{3}}c\,\delta_{\Lambda,\Lambda'}\sum_{q_1=0,\pm1}(-1)^{q_1}\begin{pmatrix} 1 & 2 & 1\\ -q_1 & 0 & q_1\end{pmatrix}\begin{pmatrix} J' & 1 & J\\ -\Omega' & q_1 & \Omega\end{pmatrix}\begin{pmatrix} S & 1 & S\\ -\Sigma' & q_1 & \Sigma\end{pmatrix}\right.$$
$$\left.+\,d\sum_{q=\pm1}\delta_{\Lambda',\Lambda-2q}\begin{pmatrix} J' & 1 & J\\ -\Omega' & -q & \Omega\end{pmatrix}\begin{pmatrix} S & 1 & S\\ -\Sigma' & q & \Sigma\end{pmatrix}\right\}.$$

(8) Magnetic hyperfine interaction (d)

$$\langle L\Lambda',S\Sigma',J'\Omega'M'_{J'},IM'_I|\, c_I T^1(\mathbf{I})\cdot T^1(\mathbf{J}-\mathbf{S})\,|L\Lambda,S\Sigma,J\Omega M_J,IM_I\rangle \tag{A.8}$$
$$=\ c_I\delta_{\Lambda,\Lambda'}(-1)^{I-M'_I}\sqrt{I(I+1)(2I+1)}\sum_{p=0,\pm1}(-1)^p\begin{pmatrix} J' & 1 & J\\ -M'_{J'} & p & M_J\end{pmatrix}\begin{pmatrix} I & 1 & I\\ -M'_I & -p & M_I\end{pmatrix}$$
$$\times\left\{\delta_{\Sigma,\Sigma'}\delta_{J,J'}\delta_{\Omega,\Omega'}(-1)^{J-M'_{J'}}\sqrt{J(J+1)(2J+1)}\right.$$
$$\left.-\,(-1)^{M'_{J'}-\Omega'+S-\Sigma'}\sqrt{(2J'+1)(2J+1)S(S+1)(2S+1)}\sum_{q=0,\pm1}\begin{pmatrix} J' & 1 & J\\ -\Omega' & q & \Omega\end{pmatrix}\begin{pmatrix} S & 1 & S\\ -\Sigma' & q & \Sigma\end{pmatrix}\right\}.$$

(9) Magnetic hyperfine interaction (e)

$$\langle L\Lambda',S\Sigma',J'\Omega'M'_{J'},IM'_I|\, c'_I \sum_{q=\pm1} \mathrm{e}^{-2\mathrm{i}q\phi}\, \frac{1}{2}\left[T^2_{2q}(\mathbf{I},\mathbf{J}-\mathbf{S}) + T^2_{2q}(\mathbf{J}-\mathbf{S},\mathbf{I})\right] |L\Lambda,S\Sigma,J\Omega M_J,IM_I\rangle \tag{A.9}$$

$$\begin{aligned}
&= -\frac{c'_I}{2}(-1)^{I-M'_I}\sqrt{I(I+1)(2I+1)(2J'+1)(2J+1)} \sum_{p=0,\pm1}(-1)^p \begin{pmatrix} I & 1 & I \\ -M'_I & -p & M_I \end{pmatrix}\begin{pmatrix} J' & 1 & J \\ -M'_{J'} & p & M_J \end{pmatrix} \\
&\times \sum_{q=\pm1}\delta_{\Lambda',\Lambda-2q}\Bigg\{2(-1)^{S-\Sigma'+M'_{J'}-\Omega'}\sqrt{S(S+1)(2S+1)}\begin{pmatrix} S & 1 & S \\ -\Sigma' & q & \Sigma \end{pmatrix}\begin{pmatrix} J' & 1 & J \\ -\Omega' & -q & \Omega \end{pmatrix} \\
&+ \delta_{\Sigma,\Sigma'}\theta(3/2-|\Omega'+q|)(-1)^{J+M'_{J'}}\sqrt{J(J+1)(2J+1)}\begin{pmatrix} J' & 1 & J \\ -\Omega' & -q & \Omega'+q \end{pmatrix}\begin{pmatrix} J & 1 & J \\ -\Omega'-q & -q & \Omega \end{pmatrix} \\
&+ \delta_{\Sigma,\Sigma'}\theta(3/2-|\Omega'+q|)(-1)^{J'+M'_{J'}}\sqrt{J'(J'+1)(2J'+1)}\begin{pmatrix} J' & 1 & J' \\ -\Omega' & -q & \Omega'+q \end{pmatrix}\begin{pmatrix} J' & 1 & J \\ -\Omega'-q & -q & \Omega \end{pmatrix}\Bigg\}.
\end{aligned}$$

(10) Orbital Zeeman effect

$$\langle L\Lambda',S\Sigma',J'\Omega'M'_{J'},IM'_I|\, g'_L\mu_B B_Z T^1_{p=0}(\mathbf{L})\, |L\Lambda,S\Sigma,J\Omega M_J,IM_I\rangle \tag{A.10}$$

$$= g'_L\mu_B B_Z \delta_{\Lambda,\Lambda'}\delta_{\Sigma,\Sigma'}\delta_{M_I,M'_I}\Lambda(-1)^{M'_{J'}-\Omega'}\sqrt{(2J'+1)(2J+1)}\begin{pmatrix} J' & 1 & J \\ -\Omega' & 0 & \Omega \end{pmatrix}\begin{pmatrix} J' & 1 & J \\ -M'_{J'} & 0 & M_J \end{pmatrix}.$$

(11) Electronic spin isotropic contribution to Zeeman effect

$$\langle L\Lambda',S\Sigma',J'\Omega'M'_{J'},IM'_I|\, g_S\mu_B B_Z T^1_{p=0}(\mathbf{S})\, |L\Lambda,S\Sigma,J\Omega M_J,IM_I\rangle \tag{A.11}$$

$$= g_S\mu_B B_Z \delta_{\Lambda,\Lambda'}\delta_{M_I,M'_I}(-1)^{M'_{J'}-\Omega'+S-\Sigma'}\sqrt{(2J'+1)(2J+1)S(S+1)(2S+1)}\begin{pmatrix} J' & 1 & J \\ -M'_{J'} & 0 & M_J \end{pmatrix} \tag{A.12}$$

$$\times \sum_{q=0,\pm1}\begin{pmatrix} J' & 1 & J \\ -\Omega' & q & \Omega \end{pmatrix}\begin{pmatrix} S & 1 & S \\ -\Sigma' & q & \Sigma \end{pmatrix}.$$

(12) Rotational magnetic moment contribution to Zeeman effect

$$
\begin{aligned}
&- \langle L\Lambda',S\Sigma',J'\Omega'M'_{J'},IM'_I|\, g_r\mu_B B_Z T^1_{p=0}(\mathbf{J}-\mathbf{L}-\mathbf{S})\,|L\Lambda,S\Sigma,J\Omega M_J,IM_I\rangle \qquad \text{(A.13)}\\
&= -g_r\mu_B B_Z \delta_{\Lambda,\Lambda'}\delta_{\Sigma,\Sigma'}\delta_{J,J'}\delta_{\Omega,\Omega'}\delta_{M_J,M'_{J'}}\delta_{M_I,M'_I}M_J\\
&+ g_r\mu_B B_Z \delta_{\Lambda,\Lambda'}\delta_{\Sigma,\Sigma'}\delta_{M_I,M'_I}\Lambda(-1)^{M'_{J'}-\Omega'}\sqrt{(2J'+1)(2J+1)}\begin{pmatrix} J' & 1 & J\\ -\Omega' & 0 & \Omega\end{pmatrix}\begin{pmatrix} J' & 1 & J\\ -M'_{J'} & 0 & M_J\end{pmatrix}\\
&+ g_r\mu_B B_Z \delta_{\Lambda,\Lambda'}\delta_{M_I,M'_I}(-1)^{M'_{J'}-\Omega'+S-\Sigma'}\sqrt{(2J'+1)(2J+1)S(S+1)(2S+1)}\begin{pmatrix} J' & 1 & J\\ -M'_{J'} & 0 & M_J\end{pmatrix}\\
&\quad\times\sum_{q_1=0,\pm1}\begin{pmatrix} J' & 1 & J\\ -\Omega' & q_1 & \Omega\end{pmatrix}\begin{pmatrix} S & 1 & S\\ -\Sigma' & q_1 & \Sigma\end{pmatrix}.
\end{aligned}
$$

(13) Nuclear spin Zeeman effect

$$
\begin{aligned}
&- \langle L\Lambda',S\Sigma',J'\Omega'M'_{J'},IM'_I|\, g_N\mu_N B_Z T^1_{p=0}(\mathbf{I})\,|L\Lambda,S\Sigma,J\Omega M_J,IM_I\rangle \qquad \text{(A.14)}\\
&= -g_N\mu_N B_Z \delta_{\Lambda,\Lambda'}\delta_{\Sigma,\Sigma'}\delta_{J,J'}\delta_{\Omega,\Omega'}\delta_{M_J,M'_{J'}}\delta_{M_I,M'_I}M_I
\end{aligned}
$$

(14) Electronic spin anisotropic contribution to Zeeman effect

$$
\begin{aligned}
&\langle L\Lambda',S\Sigma',J'\Omega'M'_{J'},IM'_I|\, g_\ell\mu_B B_Z \sum_{q=\pm1}\mathscr{D}^{(1)*}_{0,q}(\omega)T^1_q(\mathbf{S})\,|L\Lambda,S\Sigma,J\Omega M_J,IM_I\rangle \qquad \text{(A.15)}\\
&=\ g_\ell\mu_B B_Z \delta_{\Lambda,\Lambda'}\delta_{M_I,M'_I}(-1)^{M'_{J'}-\Omega'+S-\Sigma'}\sqrt{(2J'+1)(2J+1)S(S+1)(2S+1)}\begin{pmatrix} J' & 1 & J\\ -M'_{J'} & 0 & M_J\end{pmatrix}\\
&\times\sum_{q=\pm1}\begin{pmatrix} J' & 1 & J\\ -\Omega' & q & \Omega\end{pmatrix}\begin{pmatrix} S & 1 & S\\ -\Sigma' & q & \Sigma\end{pmatrix}.
\end{aligned}
$$

(15) Parity-dependent and non-cylindrical contribution to Zeeman effect (I)

$$
\begin{aligned}
&\langle L\Lambda',S\Sigma',J'\Omega'M'_{J'},IM'_I|\, g'_\ell\mu_B B_Z \sum_{q=\pm1}\mathrm{e}^{-2\mathrm{i}q\phi}\,\mathscr{D}^{(1)*}_{0,-q}(\omega)T^1_q(\mathbf{S})\,|L\Lambda,S\Sigma,J\Omega M_J,IM_I\rangle \qquad \text{(A.16)}\\
&= -g'_\ell\mu_B B_Z \delta_{M_I,M'_I}(-1)^{M'_{J'}-\Omega'+S-\Sigma'}\sqrt{(2J'+1)(2J+1)S(S+1)(2S+1)}\begin{pmatrix} J' & 1 & J\\ -M'_{J'} & 0 & M_J\end{pmatrix}\\
&\times\sum_{q=\pm1}\delta_{\Lambda',\Lambda-2q}\begin{pmatrix} J' & 1 & J\\ -\Omega' & -q & \Omega\end{pmatrix}\begin{pmatrix} S & 1 & S\\ -\Sigma' & q & \Sigma\end{pmatrix}.
\end{aligned}
$$

(16) Parity-dependent and non-cylindrical contribution to Zeeman effect (II)

$$-\langle\Lambda',\Sigma',J'\Omega'M'_{J'},M'_I|\, g_r^{e'}\mu_B B_Z \sum_{q=\pm1}\sum_{p=0,\pm1} \mathrm{e}^{-2\mathrm{i}q\phi}(-1)^p \mathscr{D}^{(1)*}_{-p,-q}(\omega) T^1_p(\mathbf{J}-\mathbf{S}) \mathscr{D}^{(1)*}_{0,-q}(\omega)\,|\Lambda,\Sigma,J\Omega M_J,M_I\rangle \tag{A.17}$$

$$= g_r^{e'}\mu_B B_Z \delta_{M_I,M'_I}\sqrt{(2J'+1)(2J+1)} \begin{pmatrix} J' & 1 & J \\ -M'_{J'} & 0 & M_J \end{pmatrix} \sum_{q=\pm1} \delta_{\Lambda',\Lambda-2q}$$

$$\times \left\{ \delta_{\Sigma,\Sigma'}(-1)^{J'+M'_{J'}} \sqrt{J'(J'+1)(2J'+1)} \begin{pmatrix} J' & 1 & J' \\ -\Omega' & -q & \Omega'+q \end{pmatrix} \begin{pmatrix} J' & 1 & J \\ -\Omega'-q & -q & \Omega \end{pmatrix} \right.$$

$$\left. \times\, \theta(3/2-|\Omega'+q|) \quad + (-1)^{M'_{J'}-\Omega'+S-\Sigma'} \sqrt{S(S+1)(2S+1)} \begin{pmatrix} J' & 1 & J \\ -\Omega' & -q & \Omega \end{pmatrix} \begin{pmatrix} S & 1 & S \\ -\Sigma' & q & \Sigma \end{pmatrix} \right\}.$$

Bibliography

[1] B. Yan, P. F. H. Claus, B. G. M. van Oorschot, L. Gerritsen, A. T. J. B. Eppink, S. Y. T. van de Meerakker, and D. H. Parker, "A new high intensity and short-pulse molecular beam valve," *Review of Scientific Instruments*, vol. 84, no. 2, p. 023102, 2013.

[2] N. Balakrishnan, "Perspective: Ultracold molecules and the dawn of cold controlled chemistry," *The Journal of Chemical Physics*, vol. 145, no. 15, p. 150901, 2016.

[3] M. T. Bell and T. P. Softley, "Ultracold molecules and ultracold chemistry," *Molecular Physics*, vol. 107, no. 2, pp. 99–132, 2009.

[4] B. K. Stuhl, M. T. Hummon, and J. Ye, "Cold state-selected molecular collisions and reactions," *Annual Review of Physical Chemistry*, vol. 65, no. 1, pp. 501–518, 2014.

[5] R. Krems, B. Friedrich, and W. C. Stwalley, *Cold Molecules : theory, experiment, applications*. S.l: CRC Press, 2019.

[6] I. W. M. Smith, *Low Temperatures and Cold Molecules*. Imperial Press, 2008.

[7] S. Willitsch, M. T. Bell, A. D. Gingell, S. R. Procter, and T. P. Softley, "Cold reactive collisions between laser-cooled ions and velocity-selected neutral molecules," *Physical Review Letters*, vol. 100, no. 4, 2008.

[8] M. Baranov, "Theoretical progress in many-body physics with ultracold dipolar gases," *Physics Reports*, vol. 464, no. 3, pp. 71–111, 2008.

[9] D. S. Jin and J. Ye, "Polar molecules in the quantum regime," *Physics Today*, vol. 64, no. 5, pp. 27–31, 2011.

[10] I. Bloch, J. Dalibard, and W. Zwerger, "Many-body physics with ultracold gases," *Reviews of Modern Physics*, vol. 80, no. 3, pp. 885–964, 2008.

[11] J. G. Danzl, M. J. Mark, E. Haller, M. Gustavsson, N. Bouloufa, O. Dulieu, H. Ritsch, R. Hart, and H. C. Nägerl, "Precision molecular spectroscopy for ground state transfer of molecular quantum gases," *Faraday Discussions*, vol. 142, p. 283, 2009.

[12] J. Veldhoven, J. Kopper, H. Bethlem, B. Sartakov, A. J. A. Roij, and G. Meijer, "Decelerated molecular beams for high-resolution spectroscopy," *The European Physical Journal D*, vol. 31, no. 2, pp. 337–349, 2004.

[13] H. Loh, K. C. Cossel, M. C. Grau, K. K. Ni, E. R. Meyer, J. L. Bohn, J. Ye, and E. A. Cornell, "Precision spectroscopy of polarized molecules in an ion trap," *Science*, vol. 342, no. 6163, pp. 1220–1222, 2013.

[14] M. S. Safronova, D. Budker, D. DeMille, D. F. J. Kimball, A. Derevianko, and C. W. Clark, "Search for new physics with atoms and molecules," *Rev. Mod. Phys.*, vol. 90, p. 025008, 2018.

[15] B. L. Augenbraun, Z. D. Lasner, A. Frenett, H. Sawaoka, C. Miller, T. C. Steimle, and D. J. M., "Laser-cooled polyatomic molecules for improved electron electric dipole moment searches," *New Journal of Physics*, vol. 22, no. 2, p. 022003, 2020.

[16] D. DeMille, "Diatomic molecules, a window onto fundamental physics," *Physics Today*, vol. 68, no. 12, pp. 34–40, 2015.

[17] M. Pospelov and A. Ritz, "Electric dipole moments as probes of new physics," *Annals of Physics*, vol. 318, no. 1, pp. 119–169, 2005.

[18] J. Engel, M. J. Ramsey-Musolf, and U. van Kolck, "Electric dipole moments of nucleons, nuclei, and atoms: The standard model and beyond," *Progress in Particle and Nuclear Physics*, vol. 71, pp. 21–74, 2013.

[19] ACME-collaboration, "Improved limit on the electric dipole moment of the electron," *Nature*, vol. 562, no. 7727, pp. 355–360, 2018.

[20] J. J. Hudson, D. M. Kara, I. J. Smallman, B. E. Sauer, M. R. Tarbutt, and E. A. Hinds, "Improved measurement of the shape of the electron," *Nature*, vol. 473, no. 7348, pp. 493–496, 2011.

[21] D. M. Kara, I. J. Smallman, J. J. Hudson, B. E. Sauer, M. R. Tarbutt, and E. A. Hinds, "Measurement of the electrons electric dipole moment using YbF molecules: methods and data analysis," *New Journal of Physics*, vol. 14, no. 10, p. 103051, 2012.

[22] D. DeMille, "Quantum computation with trapped polar molecules," *Physical Review Letters*, vol. 88, no. 6, 2002.

[23] L. Carr, D. DeMille, R. Krems, and J. Ye, "Cold and ultracold molecules: science, technology and applications," *New Journal of Physics*, vol. 11, no. 5, p. 055049, 2009.

[24] A. André, D. DeMille, J. M. Doyle, M. D. Lukin, S. E. Maxwell, P. Rabl, R. J. Schoelkopf, and P. Zoller, "A coherent all-electrical interface between polar molecules and mesoscopic superconducting resonators," *Nature Physics*, vol. 2, no. 9, pp. 636–642, 2006.

[25] S. F. Yelin, K. Kirby, and R. Côté, "Schemes for robust quantum computation with polar molecules," *Physical Review A*, vol. 74, no. 5, 2006.

[26] J. Argüello-Luengo, A. González-Tudela, T. Shi, P. Zoller, and J. Ignacio Cirac, "Analogue quantum chemistry simulation," *Nature*, vol. 574, no. 7777, pp. 215–218, 2019.

[27] P. O'Malley, R. Babbush, I. Kivlichan, J. Romero, J. McClean, R. Barends, J. Kelly, P. Roushan, A. Tranter, N. Ding, B. Campbell, Y. Chen, Z. Chen, B. Chiaro, A. Dunsworth, A. Fowler, E. Jeffrey, E. Lucero, A. Megrant, J. Mutus, M. Neeley, C. Neill, C. Quintana, D. Sank, A. Vainsencher, J. Wenner, T. White, P. Coveney, P. Love, H. Neven, A. Aspuru-Guzik, and

J. Martinis, "Scalable quantum simulation of molecular energies," *Physical Review X*, vol. 6, no. 3, 2016.

[28] G. Pupillo, A. Micheli, H.-P. Büchler, and P. Zoller, *Condensed matter physics with cold polar molecules*, pp. 421–470. 2009.

[29] L. Carr, D. DeMille, R. Krems, and J. Ye, "Cold and ultracold molecules: science, technology and applications," *New Journal of Physics*, vol. 11, no. 5, p. 055049, 2009.

[30] E. F. van Dishoeck, "Astrochemistry of dust, ice and gas: Introduction and overview," *Faraday Discuss.*, vol. 168, pp. 9–47, 2014.

[31] S. H. D. Hogan, "Cold atoms and molecules by Zeeman deceleration and Rydberg-Stark deceleration," 2012.

[32] A. B. Henson, S. Gersten, Y. Shagam, J. Narevicius, and E. Narevicius, "Observation of resonances in Penning ionization reactions at sub-Kelvin temperatures in merged beams," *Science*, vol. 338, no. 6104, pp. 234–238, 2012.

[33] C. Adams and E. Riis, "Laser cooling and trapping of neutral atoms," *Progress in Quantum Electronics*, vol. 21, no. 1, pp. 1–79, 1997.

[34] M. R. Tarbutt, "Laser cooling of molecules," *Contemporary Physics*, vol. 59, no. 4, pp. 356–376, 2018.

[35] E. S. Shuman, J. F. Barry, and D. DeMille, "Laser cooling of a diatomic molecule," *Nature*, vol. 467, no. 7317, pp. 820–823, 2010.

[36] S. Truppe, H. J. Williams, M. Hambach, L. Caldwell, N. J. Fitch, E. A. Hinds, B. E. Sauer, and M. R. Tarbutt, "Molecules cooled below the Doppler limit," *Nature Physics*, vol. 13, no. 12, pp. 1173–1176, 2017.

[37] S. Ding, Y. Wu, I. A. Finneran, J. J. Burau, and J. Ye, "Sub-Doppler cooling and compressed trapping of YO molecules at μk temperatures," *Physical Review X*, vol. 10, no. 2, 2020.

[38] I. Kozyryev, L. Baum, K. Matsuda, B. L. Augenbraun, L. Anderegg, A. P. Sedlack, and J. M. Doyle, "Sisyphus laser cooling of a polyatomic molecule," *Physical Review Letters*, vol. 118, no. 17, 2017.

[39] L. Baum, N. B. Vilas, C. Hallas, B. L. Augenbraun, S. Raval, D. Mitra, and J. M. Doyle, "1d magneto-optical trap of polyatomic molecules," *Physical Review Letters*, vol. 124, no. 13, 2020.

[40] D. Mitra, N. B. Vilas, C. Hallas, L. Anderegg, B. L. Augenbraun, L. Baum, C. Miller, S. Raval, and J. M. Doyle, "Direct laser cooling of a symmetric top molecule," 2020.

[41] J. Bahns, P. Gould, and W. Stwalley, "Formation of cold (T $\leqslant$ 1 K) molecules," in *Advances In Atomic, Molecular, and Optical Physics*, pp. 171–224, Elsevier, 2000.

[42] F. Masnou-Seeuws and P. Pillet, "Formation of ultracold molecules (T$\leq$200 μK) via photoassociation in a gas of laser-cooled atoms," in *Advances In Atomic, Molecular, and Optical Physics*, pp. 53–127, Elsevier, 2001.

[43] T. Köhler, K. Góral, and P. S. Julienne, "Production of cold molecules via magnetically tunable Feshbach resonances," *Reviews of Modern Physics*, vol. 78, no. 4, pp. 1311–1361, 2006.

[44] E. A. Donley, N. R. Claussen, S. T. Thompson, and C. E. Wieman, "Atom-molecule coherence in a Bose-Einstein condensate," *Nature*, vol. 417, no. 6888, pp. 529–533, 2002.

[45] J. D. Weinstein, R. de Carvalho, T. Guillet, B. Friedrich, and J. M. Doyle, "Magnetic trapping of calcium monohydride molecules at millikelvin temperatures," *Nature*, vol. 395, no. 6698, pp. 148–150, 1998.

[46] J. M. Bakker, M. Stoll, D. R. Weise, O. Vogelsang, G. Meijer, and A. Peters, "Magnetic trapping of buffer-gas-cooled chromium atoms and prospects for the extension to paramagnetic molecules," *Journal of Physics B: Atomic, Molecular and Optical Physics*, vol. 39, no. 19, pp. S1111–S1123, 2006.

[47] K. E. Strecker and D. W. Chandler, "Kinematic production of isolated millikelvin molecules," *Physical Review A*, vol. 78, no. 6, 2008.

[48] N. Liu and H. Loesch, "Kinematic slowing of molecules formed by reactive collisions," *Physical Review Letters*, vol. 98, no. 10, 2007.

[49] Y. Chang, K. Długołęcki, J. Küpper, D. Rösch, D. Wild, and S. Willitsch, "Specific chemical reactivities of spatially separated 3-aminophenol conformers with cold Ca^+ ions," *Science*, vol. 342, no. 6154, pp. 98–101, 2013.

[50] R. A. Phaneuf, C. C. Havener, G. H. Dunn, and A. Müller, "Merged-beams experiments in atomic and molecular physics," *Reports on Progress in Physics*, vol. 62, no. 7, pp. 1143–1180, 1999.

[51] S. A. Rangwala, T. Junglen, T. Rieger, P. W. H. Pinkse, and G. Rempe, "Continuous source of translationally cold dipolar molecules," *Physical Review A*, vol. 67, no. 4, 2003.

[52] S. Meerakker, H. L. Bethlem, N. Vanhaecke, and G. Meijer, "Manipulation and control of molecular beams," *Chemical Reviews*, vol. 112, no. 9, pp. 4828–4878, 2012.

[53] H. L. Bethlem, G. Berden, and G. Meijer, "Decelerating neutral dipolar molecules," *Physical Review Letters*, vol. 83, no. 8, pp. 1558–1561, 1999.

[54] W. Ketterle and W. E. Pritchard, "Atom cooling by time-dependent potentials," *Physical Review A*, vol. 46, no. 7, pp. 4051–4054, 1992.

[55] D. Haas, C. von Planta, T. Kierspel, D. Zhang, and S. Willitsch, "Long-term trapping of Stark-decelerated molecules," *Communications Physics*, vol. 2, p. 101, Aug 2019.

[56] D. Haas, S. Scherb, D. Zhang, and S. Willitsch, "Optimizing the density of Stark decelerated radicals at low final velocities: a tutorial review," *EPJ Techniques and Instrumentation*, vol. 4, no. 1, 2017.

[57] S. Y. T. van de Meerakker, P. H. M. Smeets, N. Vanhaecke, R. T. Jongma, and G. Meijer, "Deceleration and electrostatic trapping of OH radicals," *Physical Review Letters*, vol. 94, no. 2, 2005.

[58] J. R. Bochinski, E. R. Hudson, H. J. Lewandowski, G. Meijer, and J. Ye, "Phase space manipulation of cold free radical OH molecules," *Physical Review Letters*, vol. 91, no. 24, 2003.

[59] K. Wohlfart, F. Filsinger, F. Grätz, J. Küpper, and G. Meijer, "Stark deceleration of OH radicals in low-field-seeking and high-field-seeking quantum states," *Physical Review A*, vol. 78, no. 3, 2008.

[60] S. Hoekstra, M. Metsälä, P. C. Zieger, L. Scharfenberg, J. J. Gilijamse, G. Meijer, and S. Y. T. van de Meerakker, "Electrostatic trapping of metastable NH molecules," *Physical Review A*, vol. 76, no. 6, 2007.

[61] H. L. Bethlem, F. M. H. Crompvoets, R. T. Jongma, S. Y. T. van de Meerakker, and G. Meijer, "Deceleration and trapping of ammonia using time-varying electric fields," *Physical Review A*, vol. 65, no. 5, 2002.

[62] N. J. Fitch, L. P. Parazzoli, and H. J. Lewandowski, "Collisions between ultracold atoms and cold molecules in a dual electrostatic-magnetic trap," *Physical Review A*, vol. 101, no. 3, 2020.

[63] H. L. Bethlem, G. Berden, F. M. H. Crompvoets, R. T. Jongma, A. J. A. van Roij, and G. Meijer, "Electrostatic trapping of ammonia molecules," *Nature*, vol. 406, no. 6795, pp. 491–494, 2000.

[64] X. Wang, M. Kirste, G. Meijer, and S. Y. T. van de Meerakker, "Stark deceleration of NO radicals," 2013.

[65] T. E. Wall, J. F. Kanem, J. M. Dyne, J. J. Hudson, B. E. Sauer, E. A. Hinds, and M. R. Tarbutt, "Stark deceleration of CaF molecules in strong- and weak-field seeking states," *Physical Chemistry Chemical Physics*, vol. 13, no. 42, p. 18991, 2011.

[66] M. R. Tarbutt, H. L. Bethlem, J. J. Hudson, V. L. Ryabov, V. A. Ryzhov, B. E. Sauer, G. Meijer, and E. A. Hinds, "Slowing heavy, ground-state molecules using an alternating gradient decelerator," *Physical Review Letters*, vol. 92, no. 17, 2004.

[67] E. R. Hudson, C. Ticknor, B. C. Sawyer, C. A. Taatjes, H. J. Lewandowski, J. R. Bochinski, J. L. Bohn, and J. Ye, "Production of cold formaldehyde molecules for study and control of chemical reaction dynamics with hydroxyl radicals," *Physical Review A*, vol. 73, no. 6, 2006.

[68] O. Bucicov, M. Nowak, S. Jung, G. Meijer, E. Tiemann, and C. Lisdat, "Cold SO_2 molecules by Stark deceleration," *The European Physical Journal D*, vol. 46, no. 3, pp. 463–469, 2008.

[69] S. C. Mathavan, A. Zapara, Q. Esajas, and S. Hoekstra, "Deceleration of a supersonic beam of SrF molecules to 120 m /s," *ChemPhysChem*, vol. 17, no. 22, pp. 3709–3713, 2016.

[70] B. C. Sawyer, B. L. Lev, E. R. Hudson, B. K. Stuhl, M. Lara, J. L. Bohn, and J. Ye, "Magnetoelectrostatic trapping of ground state OH molecules," *Physical Review Letters*, vol. 98, no. 25, 2007.

[71] J. J. Gilijamse, S. Hoekstra, N. Vanhaecke, S. Y. T. van de Meerakker, and G. Meijer, "Loading Stark-decelerated molecules into electrostatic quadrupole traps," *The European Physical Journal D*, vol. 57, no. 1, pp. 33–41, 2010.

[72] T. de Jongh, M. Besemer, Q. Shuai, T. Karman, A. van der Avoird, G. C. Groenenboom, and S. Y. T. van de Meerakker, "Imaging the onset of the resonance regime in low-energy NO-he collisions," *Science*, vol. 368, no. 6491, pp. 626–630, 2020.

[73] S. N. Vogels, J. Onvlee, S. Chefdeville, A. van der Avoird, G. C. Groenenboom, and S. Y. T. van de Meerakker, "Imaging resonances in low-energy NO-he inelastic collisions," *Science*, vol. 350, no. 6262, pp. 787–790, 2015.

[74] J. J. Gilijamse, S. Hoekstra, S. Y. T. van de Meerakker, G. C. Groenenboom, and G. Meijer, "Near-threshold inelastic collisions using molecular beams with a tunable velocity," *Science*, vol. 313, no. 5793, pp. 1617–1620, 2006.

[75] H. J. Hudson and, E. R. Lewandowski, B. C. Sawyer, and J. Ye, "Cold molecule spectroscopy for constraining the evolution of the fine structure constant," *Physical Review Letters*, vol. 96, no. 14, 2006.

[76] S. Y. T. van de Meerakker, N. Vanhaecke, M. van der Loo, G. Groenenboom, and G. Meijer, "Direct measurement of the radiative lifetime of vibrationally excited OH radicals," *Physical Review Letters*, vol. 95, no. 1, 2005.

[77] J. H. Blokland, J. Riedel, S. Putzke, B. G. Sartakov, G. C. Groenenboom, and G. Meijer, "Producing translationally cold, ground-state CO molecules," *The Journal of Chemical Physics*, vol. 135, no. 11, p. 114201, 2011.

[78] Y. Yamakita, S. R. Procter, A. L. Goodgame, T. P. Softley, and F. Merkt, "Deflection and deceleration of hydrogen rydberg molecules in inhomogeneous electric fields," *The Journal of Chemical Physics*, vol. 121, no. 3, pp. 1419–1431, 2004.

[79] S. D. Hogan, C. Seiler, and F. Merkt, "Rydberg-state-enabled deceleration and trapping of cold molecules," *Physical Review Letters*, vol. 103, no. 12, 2009.

[80] S. D. Hogan, "Rydberg-Stark deceleration of atoms and molecules," *EPJ Techniques and Instrumentation*, vol. 3, no. 1, 2016.

[81] H. L. Bethlem, G. Berden, and G. Meijer, "Decelerating neutral dipolar molecules," *Phys. Rev. Lett.*, vol. 83, pp. 1558–1561, 1999.

[82] N. Vanhaecke, U. Meier, M. Andrist, B. H. Meier, and F. Merkt, "Multistage Zeeman deceleration of hydrogen atoms," *Physical Review A*, vol. 75, no. 3, 2007.

[83] S. D. Hogan, D. Sprecher, M. Andrist, N. Vanhaecke, and F. Merkt, "Zeeman deceleration of H and D," *Physical Review A*, vol. 76, no. 2, 2007.

[84] S. D. Hogan, A. W. Wiederkehr, H. Schmutz, and F. Merkt, "Magnetic trapping of hydrogen after multistage Zeeman deceleration," *Physical Review Letters*, vol. 101, no. 14, 2008.

[85] K. Dulitz, A. Tauschinsky, and P. T. Softley, "Zeeman deceleration of electron-impact-excited metastable helium atoms," *New Journal of Physics*, vol. 17, no. 3, p. 035005, 2015.

[86] T. Cremers, S. Chefdeville, N. Janssen, E. Sweers, S. Koot, P. Claus, and S. Y. T. van de Meerakker, "Multistage Zeeman decelerator for molecular-scattering studies," *Physical Review A*, vol. 95, no. 4, 2017.

[87] L. Semeria, P. Jansen, G. Clausen, J. A. Agner, H. Schmutz, and F. Merkt, "Molecular-beam resonance method with Zeeman-decelerated samples: Application to metastable helium molecules," *Physical Review A*, vol. 98, no. 6, 2018.

[88] A. W. Wiederkehr, M. Motsch, S. D. Hogan, M. Andrist, H. Schmutz, B. Lambillotte, J. A. Agner, and F. Merkt, "Multistage zeeman deceleration of metastable neon," *The Journal of Chemical Physics*, vol. 135, no. 21, p. 214202, 2011.

[89] E. Lavert-Ofir, S. Gersten, A. Henson, I. Shani, L. David, J. Narevicius, and E. Narevicius, "A moving magnetic trap decelerator: a new source of cold atoms and molecules," *New Journal of Physics*, vol. 13, no. 10, p. 103030, 2011.

[90] N. Akerman, M. Karpov, L. David, E. Lavert-Ofir, J. Narevicius, and E. Narevicius, "Simultaneous deceleration of atoms and molecules in a supersonic beam," *New Journal of Physics*, vol. 17, no. 6, p. 065015, 2015.

[91] K. Dulitz, J. Toscano, A. Tauschinsky, and T. P. Softley, "Zeeman deceleration of metastable nitrogen atoms," *Journal of Physics B: Atomic, Molecular and Optical Physics*, vol. 49, no. 7, p. 075203, 2016.

[92] A. W. Wiederkehr, H. Schmutz, M. Motsch, and F. Merkt, "Velocity-tunable slow beams of cold O_2 in a single spin-rovibronic state with full angular-momentum orientation by multistage Zeeman deceleration," *Molecular Physics*, vol. 110, no. 15-16, pp. 1807–1814, 2012.

[93] T. Cremers, S. Chefdeville, V. Plomp, N. Janssen, E. Sweers, and S. Y. T. van de Meerakker, "Multistage Zeeman deceleration of atomic and molecular oxygen," *Physical Review A*, vol. 98, no. 3, 2018.

[94] V. Plomp, Z. Gao, T. Cremers, and S. Y. T. van de Meerakker, "Multistage Zeeman deceleration of NH $X^3\Sigma^-$ radicals," *Physical Review A*, vol. 99, no. 3, 2019.

[95] V. Plomp, Z. Gao, T. Cremers, M. Besemer, and S. Y. T. van de Meerakker, "High-resolution imaging of molecular collisions using a Zeeman decelerator," *The Journal of Chemical Physics*, vol. 152, no. 9, p. 091103, 2020.

[96] Y. Liu, M. Vashishta, P. Djuricanin, S. Zhou, W. Zhong, T. Mittertreiner, D. Carty, and T. Momose, "Magnetic trapping of cold methyl radicals," *Physical Review Letters*, vol. 118, no. 9, 2017.

[97] T. Momose, Y. Liu, S. Zhou, P. Djuricanin, and D. Carty, "Manipulation of translational motion of methyl radicals by pulsed magnetic fields," *Phys. Chem. Chem. Phys.*, vol. 15, no. 6, pp. 1772–1777, 2013.

[98] Y. Segev, M. Pitzer, M. Karpov, N. Akerman, J. Narevicius, and E. Narevicius, "Collisions between cold molecules in a superconducting magnetic trap," *Nature*, vol. 572, no. 7768, pp. 189–193.

[99] A. W. Wiederkehr, S. D. Hogan, and F. Merkt, "Phase stability in a multistage Zeeman decelerator," *Physical Review A*, vol. 82, no. 4, 2010.

[100] K. Dulitz, N. Vanhaecke, and P. T. Softley, "Model for the overall phase-space acceptance in a Zeeman decelerator," *Physical Review A*, vol. 91, no. 1, 2015.

[101] J. Toscano, A. Tauschinsky, K. Dulitz, C. J. Rennick, B. R. Heazlewood, and P. T. Softley, "Zeeman deceleration beyond periodic phase space stability," *New Journal of Physics*, vol. 19, no. 8, p. 083016, 2017.

[102] J. Toscano, L. Y. Wu, M. Hejduk, and B. R. Heazlewood, "Evolutionary algorithm optimization of Zeeman deceleration: Is it worthwhile for longer decelerators?," *The Journal of Physical Chemistry A*, vol. 123, no. 25, pp. 5388–5394, 2019.

[103] S. A. Meek, H. L. Bethlem, H. Conrad, and G. Meijer, "Trapping molecules on a chip in traveling potential wells," *Physical Review Letters*, vol. 100, no. 15, 2008.

[104] A. Osterwalder, S. A. Meek, G. Hammer, H. Haak, and G. Meijer, "Deceleration of neutral molecules in macroscopic traveling traps," *Physical Review A*, vol. 81, no. 5, 2010.

[105] E. Narevicius, C. G. Parthey, A. Libson, M. F. Riedel, U. Even, and M. G. Raizen, "Towards magnetic slowing of atoms and molecules," *New Journal of Physics*, vol. 9, no. 4, pp. 96–96, 2007.

[106] A. Trimeche, M. N. Bera, J. P. Cromières, J. Robert, and N. Vanhaecke, "Trapping of a supersonic beam in a traveling magnetic wave," *The European Physical Journal D*, vol. 65, pp. 263–271, Nov 2011.

[107] L. A. McArd, A. Mizouri, P. A. Walker, V. Singh, U. Krohn, E. A. Hinds, and D. Carty, "A Moving-Trap Zeeman Decelerator," *arXiv e-prints*, p. arXiv:1807.10648, 2018.

[108] P. Zeeman, "Over de invloed eener magnetisatie op den aard van het door een stof uitgezonden licht," *Versl. Kon. Ak. Wet.*, vol. 5, p. 181, 1896.

[109] P. Zeeman *De Gids*, vol. 22, p. 105, 1925.

[110] A. Kox, "The discovery of the electron : II . the Zeeman effect," 1997.

[111] P. Zeeman, "XXXII. on the influence of magnetism on the nature of the light emitted by a substance," *The London, Edinburgh, and Dublin Philosophical Magazine and Journal of Science*, vol. 43, no. 262, pp. 226–239, 1897.

[112] P. Zeeman *Versl. Kon. Ak. Wet.*, vol. 6, p. 13, 1897.

[113] P. Zeeman *Versl. Kon. Ak. Wet.*, vol. 6, p. 99, 1897.

[114] C. J. Foot, *Atomic physics*. Oxford New York: Oxford University Press, 2005.

[115] E. Condon, *The theory of atomic spectra*. Cambridge: Cambridge University Press, 1951.

[116] M. Auzinsh, *Optically polarized atoms : Understanding light-atom interactions*. New York, NY: Oxford University Press, 2014.

[117] G. K. Woodgate, *Elementary atomic structure*. Oxford: Clarendon, 1980.

[118] J. Brown, *Rotational spectroscopy of diatomic molecules*. Cambridge New York: Cambridge University Press, 2003.

[119] J. Brown, E. Colbourn, J. Watson, and F. Wayne, "An effective hamiltonian for diatomic molecules," *Journal of Molecular Spectroscopy*, vol. 74, no. 2, pp. 294–318, 1979.

[120] K. Maeda, M. Wall, and L. Carr, "Hyperfine structure of the hydroxyl free radical (OH) in electric and magnetic fields," *New Journal of Physics*, vol. 17, no. 4, p. 045014, 2015.

[121] H. Wu, *Achieving a large density of hydroxyl radicals for cold collisions*. PhD thesis, Boulder, 2019.

[122] J. ter Meulen, W. Majewski, W. Meerts, and A. Dymanus, "Determination of the spin—rotation and hyperfine structure in the $A^2\Sigma^+_{12}$, $\nu = 0$ and $\nu = 1$ states of OH," *Chemical Physics Letters*, vol. 94, no. 1, pp. 25–28, 1983.

[123] J. T. Meulen, W. Ubachs, and A. Dumanus, "Observation of ρ-doublet transitions in OH($A^2\Sigma^+_{12}$) by UV-microwave double resonance in a molecular beam," *Chemical Physics Letters*, vol. 129, no. 6, pp. 533–537, 1986.

[124] S. van de Meerakker, *Deceleration and electrostatic trapping of OH radicals*. PhD Thesis, 2006.

[125] J. J. Gilijamse, J. Küpper, S. Hoekstra, N. Vanhaecke, S. Y. T. van de Meerakker, and G. Meijer, "Optimizing the Stark-decelerator beamline for the trapping of cold molecules using evolutionary strategies," *Physical Review A*, vol. 73, no. 6, 2006.

[126] J. J. Ter Meulen and A. Dymanus, "Beam-maser measurements of the ground-state transition frequencies of OH.," *The Astrophysical Journal*, vol. 172, p. L21, 1972.

[127] G. C. Dousmanis, T. M. Sanders, and C. H. Townes, "Microwave spectra of the free radicals OH and OD," *Physical Review*, vol. 100, no. 6, pp. 1735–1754, 1955.

[128] H. E. Radford, "Microwave Zeeman effect of free hydroxyl radicals," *Physical Review*, vol. 122, no. 1, pp. 114–130, 1961.

[129] H. Weaver, D. R. W. Williams, N. H. Dieter, and W. T. Lum, "Observations of a strong unidentified microwave line and of emission from the OH molecule," *Nature*, vol. 208, no. 5005, pp. 29–31, 1965.

[130] S. Weinerb, A. H. Barrett, M. L. Meeks, and J. C. Henry, "Radio observations of OH in the interstellar medium," *Nature*, vol. 200, no. 4909, pp. 829–831, 1963.

[131] A. L. Argon, M. J. Reid, and K. M. Menten, "A class of interstellar OH masers associated with protostellar outflows," *The Astrophysical Journal*, vol. 593, no. 2, pp. 925–930, 2003.

[132] F. Haber and J. Weiss, "The catalytic decomposition of hydrogen peroxide by iron salts," *Proceedings of the Royal Society of London. Series A - Mathematical and Physical Sciences*, vol. 147, no. 861, pp. 332–351, 1934.

[133] H. J. H. Fenton, "LXXIII.—oxidation of tartaric acid in presence of iron," *J. Chem. Soc., Trans.*, vol. 65, no. 0, pp. 899–910, 1894.

[134] P. Bernath and A. Dalgarno, "Spectra of atoms and molecules," *Physics Today*, vol. 49, no. 3, pp. 94–94, 1996.

[135] J. I. Steinfeld, *Molecules and Radiation*. 2005.

[136] A. J. C. Varandas and A. I. Voronin, "Calculation of the asymptotic interaction and modelling of the potential energy curves of OH and O^+," *Chemical Physics*, vol. 194, pp. 91–100, 1995.

[137] R. V. Krems, *Molecules in Electromagnetic Fields*. John Wiley & Sons, Inc., 2018.

[138] P. Andresen and E. Rothe, "Analysis of chemical dynamics via Λ doubling: Directed lobes in product molecules and transition states," *The Journal of Chemical Physics*, vol. 82, no. 8, pp. 3634–3640, 1985.

[139] D. Haas, S. Willitsch, and S. Y. van de Meerakker, *Towards hybrid trapping of cold molecules and cold molecular ions*. University of Basel, 2019.

[140] L. Ploenes, D. Haas, D. Zhang, S. Y. T. van de Meerakker, and S. Willitsch, "Cold and intense OH radical beam sources," *Review of Scientific Instruments*, vol. 87, no. 5, p. 053305, 2016.

[141] J. L. Kinsey, "Laser-induced fluorescence," *Annual Review of Physical Chemistry*, vol. 28, no. 1, pp. 349–372, 1977.

[142] W. J. Tango and R. Link, J. K.and Zare, "Spectroscopy of K_2 using laser-induced fluorescence," *The Journal of Chemical Physics*, vol. 49, no. 10, pp. 4264–4268, 1968.

[143] R. Zare, "My life with LIF: A personal account of developing laser-induced fluorescence," *Annual Review of Analytical Chemistry*, vol. 5, no. 1, pp. 1–14, 2012.

[144] L. Radziemski, *Laser spectroscopy and its applications*. New York: M. Dekker, 1987.

[145] T. Streibel and R. Zimmermann, "Resonance-enhanced multiphoton ionization mass spectrometry (REMPI-MS): Applications for process analysis," *Annual Review of Analytical Chemistry*, vol. 7, no. 1, pp. 361–381, 2014.

[146] S. L. Chin, "Multiphoton ionization of molecules," *Physical Review A*, vol. 4, no. 3, pp. 992–996, 1971.

[147] H. B. Bebb and A. Gold, "Multiphoton ionization of hydrogen and rare-gas atoms," *Physical Review*, vol. 143, no. 1, pp. 1–24, 1966.

[148] S. L. Chin, N. R. Isenor, and M. Young, "Multiphoton ionization of Hg and Xe," *Physical Review*, vol. 188, no. 1, pp. 7–8, 1969.

[149] W. C. Wiley and I. H. McLaren, "Time-of-flight mass spectrometer with improved resolution," *Review of Scientific Instruments*, vol. 26, no. 12, pp. 1150–1157, 1955.

[150] L. Ploenes, D. Haas, D. Zhang, S. Y. T. van de Meerakker, and S. Willitsch, "Cold and intense Oh radical beam sources," *Review of Scientific Instruments*, vol. 87, no. 5, p. 053305, 2016.

[151] G. Scoles, *Atomic and molecular beam methods*. New York: Oxford University Press, 1988.

[152] J. Jankunas and A. Osterwalder, "Cold and controlled molecular beams: Production and applications," *Annual Review of Physical Chemistry*, vol. 66, no. 1, pp. 241–262, 2015.

[153] F. White, *Fluid mechanics*. Boston Toronto: McGraw-Hill, 1999.

[154] R. Campargue, *Atomic and molecular beams : the state of the art 2000*. Berlin New York: Springer, 2001.

[155] N. Ramsey, *Molecular beams*. Oxford New York: Clarendon Press Oxford University Press, 1985.

[156] G. Sanna, *Introduction to molecular beams gas dynamics*. London Hackensack: Imperial College Press, 2005.

[157] H. Pauly, *Atom, molecule, and cluster beams I : basic theory, production and detection of thermal energy beams*. Berlin: Springer Berlin Heidelberg, 2000.

[158] O. Dulieu, *Cold chemistry : Molecular scattering and reactivity near absolute zero*. London, England: Royal Society of Chemistry,Royal Society of Chemistry, 2018.

[159] U. Even, "The Even-Lavie valve as a source for high intensity supersonic beam," *EPJ Techniques and Instrumentation*, vol. 2, no. 1, 2015.

[160] U. Even, "Pulsed supersonic beams from high pressure source: Simulation results and experimental measurements," *Advances in Chemistry*, vol. 2014, pp. 1–11, 2014.

[161] D. Irimia, D. Dobrikov, R. Kortekaas, H. Voet, D. A. van den Ende, W. A. Groen, and M. H. M. Janssen, "A short pulse (7 μs FWHM) and high repetition rate (dc-5khz) cantilever piezovalve for pulsed atomic and molecular beams," *Review of Scientific Instruments*, vol. 80, no. 11, p. 113303, 2009.

[162] J. Grzesiak, M. Vashishta, P. Djuricanin, F. Stienkemeier, M. Mudrich, K. Dulitz, and T. Momose, "Production of rotationally cold methyl radicals in pulsed supersonic beams," *Review of Scientific Instruments*, vol. 89, no. 11, p. 113103, 2018.

[163] H. Lewandowski, E. R. Hudson, J. Bochinski, and J. Ye, "A pulsed, low-temperature beam of supersonically cooled free radical OH molecules," *Chemical Physics Letters*, vol. 395, no. 1-3, pp. 53–57, 2004.

[164] M. Hillenkamp, S. Keinan, and U. Even, "Condensation limited cooling in supersonic expansions," *The Journal of Chemical Physics*, vol. 118, no. 19, pp. 8699–8705, 2003.

[165] K. Luria, W. Christen, and U. Even, "Generation and propagation of intense supersonic beams," *The Journal of Physical Chemistry A*, vol. 115, no. 25, pp. 7362–7367, 2011.

[166] D. Ostermayer, *Sources of Cold Hydroxyl Radicals.* University of Basel, 2018.

[167] E. Wagenaars, "Plasma breakdown of low-pressure gas discharges," 2006.

[168] A. Bogaerts and R. Gijbels, "Modeling of metastable argon atoms in a direct-current glow discharge," *Physical Review A*, vol. 52, no. 5, pp. 3743–3751, 1995.

[169] A. M. Howatson, *An Introduction to gas discharges.* Oxford New York: Pergamon Press, 1976.

[170] A. Fridman, *Plasma Chemistry.* Cambridge University Press, 2008.

[171] M. J. Druyvesteyn and F. M. Penning, "The mechanism of electrical discharges in gases of low pressure," *Reviews of Modern Physics*, vol. 12, no. 2, pp. 87–174, 1940.

[172] Y. Raizer, *Gas discharge physics.* Berlin New York: Springer, 1997.

[173] J. Luque and D. Crosley, "LIFbase: Database and spectral simulation," 1999.

[174] H. Photonics, *MCP assembly.*

[175] A. E. Cameron and D. F. Eggers, "An ion velocitron," *Review of Scientific Instruments*, vol. 19, no. 9, pp. 605–607, 1948.

[176] R. Cotter, *Time-of-flight mass spectrometry : instrumentation and applications in biological research.* Washington, DC: American Chemical Society, 1997.

[177] I. Ferrer, *Liquid chromatography/time-of-flight mass spectrometry : Principles, tools, and applications for accurate mass analysis.* Hoboken, NJ: Wiley, 2008.

[178] E. de Hoffmann, *Mass spectrometry : Principles and applications.* Chichester, England Hoboken, NJ: J. Wiley, 2007.

[179] E. Even and B. Dick, "Optimization of a one-dimensional time-of-flight mass spectrometer," *Review of Scientific Instruments*, vol. 71, no. 12, p. 4421, 2000.

[180] A. E. Kramida, "A critical compilation of experimental data on spectral lines and energy levels of hydrogen, deuterium, and tritium," *Atomic Data and Nuclear Data Tables*, vol. 96, no. 6, pp. 586–644, 2010.

[181] K. Battes, C. Day, and V. Hauer, "Outgassing behavior of different high-temperature resistant polymers," *Journal of Vacuum Science & Technology A: Vacuum, Surfaces, and Films*, vol. 36, no. 2, p. 021602, 2018.

[182] R. Bitter, T. Mohiuddin, and M. Nawrocki, *LabVIEW: Advanced programming techniques.* Crc Press, 2006.

[183] G. Van Rossum and F. L. Drake Jr, *Python reference manual.* Centrum voor Wiskunde en Informatica Amsterdam, 1995.

[184] J. Axelson, *Serial port complete : Programming and circuits for RS-232 and RS-485 links and networks*. Madison, WI: Lakeview Research, 1998.

[185] A. W. Wiederkehr, S. D. Hogan, and F. Merkt, "Phase stability in a multistage Zeeman decelerator," *Physical Review A*, vol. 82, no. 4, 2010.

[186] E. Majorana, "Atomi orientati in campo magnetico variabile," *Il Nuovo Cimento*, vol. 9, no. 2, pp. 43–50, 1932.

[187] L. Vattuone, G. Bracco, M. Smerieri, L. Savio, and M. Rocca, *Supersonic Molecular Beams Studies of Surfaces*, pp. 1–23. Berlin, Heidelberg: Springer Berlin Heidelberg, 2013.

[188] J. P. Toennies and K. Winkelmann, "Theoretical studies of highly expanded free jets: Influence of quantum effects and a realistic intermolecular potential," *The Journal of Chemical Physics*, vol. 66, no. 9, pp. 3965–3979, 1977.

[189] L. Verlet, "Computer "experiments" on classical fluids. I. thermodynamical properties of lennard-jones molecules," *Physical Review*, vol. 159, no. 1, pp. 98–103, 1967.

[190] W. C. Swope, H. C. Andersen, P. H. Berens, and K. R. Wilson, "A computer simulation method for the calculation of equilibrium constants for the formation of physical clusters of molecules: Application to small water clusters," *The Journal of Chemical Physics*, vol. 76, no. 1, pp. 637–649, 1982.

[191] S. K. Lam, A. Pitrou, and S. Seibert, "Numba," in *Proceedings of the Second Workshop on the LLVM Compiler Infrastructure in HPC - LLVM '15*, ACM Press, 2015.

[192] A. E. Eiben and J. E. Smith, *Introduction to Evolutionary Computing*. Springer Publishing Company, Incorporated, 2nd ed., 2015.

[193] D. B. Fogel, "An introduction to simulated evolutionary optimization," *IEEE Transactions on Neural Networks*, vol. 5, no. 1, pp. 3–14, 1994.

[194] J. J. Gilijamse, J. Küpper, S. Hoekstra, N. Vanhaecke, S. Y. T. van de Meerakker, and G. Meijer, "Optimizing the Stark-decelerator beamline for the trapping of cold molecules using evolutionary strategies," *Phys. Rev. A*, vol. 73, p. 063410, 2006.

[195] A. Williams, *Microcontroller projects using the Basic Stamp*. Boca Raton: CRC Press, 2017.

[196] G. Bianchi and R. Sorrentino, *Electronic Filter Simulation & Design*. McGraw-Hill Education, 2007.

[197] S. B. Dewan and A. Straughen, *Power Semiconductor Circuits*. 1975.

[198] S. Butterworth *et al.*, "On the theory of filter amplifiers," *Wireless Engineer*, vol. 7, no. 6, pp. 536–541, 1930.

[199] Z. Feng and J. Yu, "Design and implementation of RS485 bus communication protocol," *Computer Engineering*, pp. 221–224, 2012.

[200] R. Barnett, *Embedded C programming and the microchip PIC*. Clifton Park, NY: Thomson Delmar Learning, 2004.

[201] M. Barr, *Programming embedded systems : with C and GNU development tools*. Sebastopol, Calif: O'Reilly, 2006.

[202] M. T. I. Dsj, "Mplab ® c18 c compiler user's guide."

[203] J. Catsoulis, *Designing embedded hardware*. Sebastopol, CA: O'Reilly, 2005.

[204] A. Glaser, "The use of cyclic redundancy check (CRC-32) and Adler-32 checksums for source code verification," *Drug Information Journal*, vol. 37, no. 2, pp. 147–154, 2003.

[205] D. V. Sarwate, "Computation of cyclic redundancy checks via table look-up," *Communications of the ACM*, vol. 31, no. 8, pp. 1008–1013, 1988.

[206] B. Arazi, *A commonsense approach to the theory of error correcting codes*. Cambridge, Mass: MIT Press, 1988.

[207] H. J. W. Müller-Kirsten, *Basics of Statistical Physics.* World Scientific, 2013.

[208] K. Dulitz, N. Vanhaecke, and T. P. Softley, "Model for the overall phase-space acceptance in a Zeeman decelerator," *Physical Review A*, vol. 91, no. 1, 2015.

[209] D. Zhang, G. Meijer, and N. Vanhaecke, "Advanced switching schemes in a Stark decelerator," *Phys. Rev. A*, vol. 93, p. 023408, 2016.

[210] Y. Shyur, J. A. Bossert, and H. J. Lewandowski, "Pulsed operation of a ring Stark decelerator," *Journal of Physics B: Atomic, Molecular and Optical Physics*, vol. 51, no. 16, p. 165101, 2018.

[211] E. Lavert-Ofir, S. Gersten, A. Henson, I. Shani, L. David, J. Narevicius, and E. Narevicius, "A moving magnetic trap decelerator: a new source of cold atoms and molecules," *New Journal of Physics*, vol. 13, no. 10, p. 103030, 2011.

[212] N. Vanhaecke, U. Meier, M. Andrist, B. H. Meier, and F. Merkt, "Multistage zeeman deceleration of hydrogen atoms," *Phys. Rev. A*, vol. 75, p. 031402, 2007.

[213] G. A. Bird, "Transition regime behavior of supersonic beam skimmers," *Physics of Fluids*, vol. 19, no. 10, p. 1486, 1976.

[214] S. Y. T. van de Meerakker, P. H. M. Smeets, N. Vanhaecke, R. T. Jongma, and G. Meijer, "Deceleration and electrostatic trapping of oh radicals," *Phys. Rev. Lett.*, vol. 94, p. 023004, 2005.

[215] L. Scharfenberg, H. Haak, G. Meijer, and S. Y. T. van de Meerakker, "Operation of a Stark decelerator with optimum acceptance," *Physical Review A*, vol. 79, no. 2, 2009.

[216] H. L. Bethlem, G. Berden, A. J. A. van Roij, F. M. H. Crompvoets, and G. Meijer, "Trapping neutral molecules in a traveling potential well," *Physical Review Letters*, vol. 84, no. 25, pp. 5744–5747, 2000.

[217] S. D. Hogan, A. W. Wiederkehr, H. Schmutz, and F. Merkt, "Magnetic trapping of hydrogen after multistage zeeman deceleration," *Phys. Rev. Lett.*, vol. 101, p. 143001, 2008.

[218] K. M. Ferrière, "The interstellar environment of our galaxy," *Reviews of Modern Physics*, vol. 73, no. 4, pp. 1031–1066, 2001.

[219] J. Bagdonaite, W. Ubachs, M. T. Murphy, and J. B. Whitmore, "Constraint on a varying proton-electron mass ratio 1.5 billion years after the big bang," *Physical Review Letters*, vol. 114, no. 7, 2015.

[220] W. Ubachs, J. C. J. Koelemeij, K. S. E. Eikema, and E. J. Salumbides, "Physics beyond the standard model from hydrogen spectroscopy," *Journal of Molecular Spectroscopy*, vol. 320, pp. 1–12, 2016.

[221] N. Hölsch, M. Beyer, E. J. Salumbides, K. S. E. Eikema, W. Ubachs, C. Jungen, and F. Merkt, "Benchmarking theory with an improved measurement of the ionization and dissociation energies of H_2," *Physical Review Letters*, vol. 122, no. 10, 2019.

[222] M. Puchalski, J. Komasa, P. Czachorowski, and K. Pachucki, "Nonadiabatic QED correction to the dissociation energy of the hydrogen molecule," *Physical Review Letters*, vol. 122, no. 10, 2019.

[223] W. Lichten, "Metastable hydrogen molecules," *Physical Review*, vol. 120, no. 3, pp. 848–853, 1960.

[224] C. E. Johnson, "Lifetime of the $c^3\Pi_u$ metastable state of H_2, D_2, and HD," *Physical Review A*, vol. 5, no. 3, pp. 1026–1030, 1972.

[225] P. Eberle, A. D. Dörfler, C. von Planta, K. Ravi, and W. Willitsch, "A dynamic ion-atom hybrid trap for high-resolution cold-collision studies," *ChemPhysChem*, vol. 17, no. 22, pp. 3769–3775, 2016.

[226] F. H. J. Hall and S. Willitsch, "Millikelvin reactive collisions between sympathetically cooled molecular ions and laser-cooled atoms in an ion-atom hybrid trap," *Physical Review Letters*, vol. 109, no. 23, 2012.

[227] F. H. J. Hall, P. Eberle, G. Hegi, M. Raoult, M. Aymar, O. Dulieu, and S. Willitsch, "Ion-neutral chemistry at ultralow energies: dynamics of reactive collisions between laser-cooled Ca+ions and Rb atoms in an ion-atom hybrid trap," *Molecular Physics*, vol. 111, no. 14-15, pp. 2020–2032, 2013.

[228] F. H. J. Hall, M. Aymar, M. Raoult, O. Dulieu, and S. Willitsch, "Light-assisted cold chemical reactions of barium ions with rubidium atoms," *Molecular Physics*, vol. 111, no. 12-13, pp. 1683–1690, 2013.

[229] S. T. Sullivan, W. G. Rellergert, S. Kotochigova, and E. R. Hudson, "Role of electronic excitations in ground-state-forbidden inelastic collisions between ultracold atoms and ions," *Physical Review Letters*, vol. 109, no. 22, 2012.

[230] H. da Silva Jr., M. Raoult, M. Aymar, and O. Dulieu, "Formation of molecular ions by radiative association of cold trapped atoms and ions," *New Journal of Physics*, vol. 17, no. 4, p. 045015, 2015.